Functional and Structural Characterization of the Myocardium

Funktionelle und Strukturelle Charakterisierung des Myokardiums

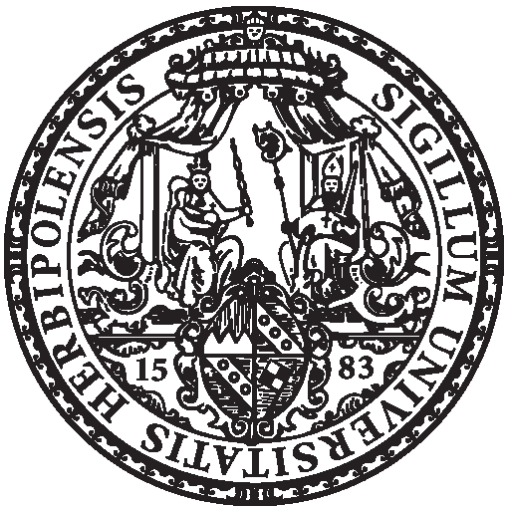

Doctoral thesis for a doctoral degree
at the Graduate School of Life Sciences,
Julius-Maximilians-Universität Würzburg,
Section Biomedicine

submitted by
David Lohr
from
Siegen

Würzburg 2020

COPYRIGHT

THESIS COMMITTEE

Submitted on:

Members of the Thesis Committee

Chairperson:
Prof. Dr. rer. nat. Peter Michael Jakob

(1) Supervisor:
Prof. Dr. rer. nat. et med. habil. Laura Maria Schreiber

(2) Supervisor:
Prof. Dr. rer. nat. Herbert Köstler

(3) Supervisor:
Prof. Dr. med. Dr. rer. nat. Wolfgang Rudolf Bauer

Date of Public Defense:

Date of Receipt of Certificates:

AFFIDAVIT

I hereby confirm that my thesis entitled “Functional and Structural Characterization of the myocardium” is the result of my own work. I did not receive any help or support from commercial consultants. All sources and / or materials applied are listed and specified in the thesis.

Furthermore, I confirm that this thesis has not yet been submitted as part of another examination process neither in identical nor similar form.

Würzburg, December 2020

David Lohr

EIDESSTATTLICHE ERKLÄRUNG

Hiermit erkläre ich an Eides statt, die Dissertation: „Funktionelle und Strukturelle Charakterisierung des Myokardiums“ eigenständig, d.h. insbesondere selbstständig und ohne Hilfe eines kommerziellen Promotionsberaters, angefertigt und keine anderen als die von mir angegebenen Quellen und Hilfsmittel verwendet zu haben.

Ich erkläre außerdem, dass die Dissertation weder in gleicher noch in ähnlicher Form bereits einem anderen Prüfungsverfahren vorgelegen hat.

Würzburg, Dezember 2020

David Lohr

SUMMARY

Clinical practice in CMR with respect to cardiovascular disease is currently focused on tissue characterization, and cardiac function, in particular. In recent years MRI based diffusion tensor imaging (DTI) has been shown to enable the assessment of microstructure based on the analysis of Brownian motion of water molecules in anisotropic tissue, such as the myocardium. With respect to both functional and structural imaging, 7T MRI may increase SNR, providing access to information beyond the reach of clinically applied field strengths. To date, cardiac 7T MRI is still a research modality that is only starting to develop towards clinical application.

In this thesis we primarily aimed to advance methods of ultrahigh field CMR using the latest 7T technology and its application towards the functional and structural characterization of the myocardium.

Regarding the assessment of myocardial microstructure at 7T, feasibility of *ex vivo* DTI of large animal hearts was demonstrated. In such hearts a custom sequence implemented for *in vivo* DTI was evaluated and fixation induced alterations of derived diffusion metrics and tissue properties were assessed. Results enable comparison of prior and future *ex vivo* DTI studies and provide information on measurement parameters at 7T.

Translating developed methodology to preclinical studies of mouse hearts, *ex vivo* DTI provided highly sensitive surrogates for microstructural remodeling in response to subendocardial damage. In such cases echocardiography measurements revealed mild diastolic dysfunction and impaired longitudinal deformation, linking disease induced structural and functional alterations. Complementary DTI and echocardiography data also improved our understanding of structure-function interactions in cases of loss of contractile myofiber tracts, replacement fibrosis, and LV systolic failure.

Regarding the functional characterization of the myocardium at 7T, sequence protocols were expanded towards a dedicated 7T routine protocol, encompassing accurate cardiac planning and the assessment of cardiac function via cine imaging in humans.

This assessment requires segmentation of myocardial contours. For that, artificial intelligence (AI) was developed and trained, enabling rapid automatic generation of cardiac segmentation in clinical data. Using transfer learning, AI models were adapted to cine data acquired using the latest generation 7T system. Methodology for AI based segmentation was translated to cardiac pathology, where automatic segmentation of scar tissue, edema and healthy myocardium was achieved.

Developed radiofrequency hardware facilitates translational studies at 7T, providing controlled conditions for future method development towards cardiac 7T MRI in humans.

In this thesis the latest 7T technology, cardiac DTI, and AI were used to advance methods of ultrahigh field CMR. In the long run, obtained results contribute to diagnostic methods that may facilitate early detection and risk stratification in cardiovascular disease.

ZUSAMMENFASSUNG

Bei kardiovaskulären Erkrankungen konzentriert sich die kardiale MRT aktuell auf die Gewebecharakterisierung und insbesondere die Herzfunktion. In den letzten Jahren hat sich gezeigt, dass MRT-basierte Diffusions-Tensor-Bildgebung (DTI) die Beurteilung der Mikrostruktur anhand der Analyse der Brownschen Bewegung von Wassermolekülen in anisotropem Gewebe, wie dem Myokardium, ermöglicht. In Bezug auf sowohl die funktionelle als auch die strukturelle Bildgebung kann 7T MRT SNR verbessern und Information messbar machen, die außerhalb der Reichweite von klinisch angewendeten Feldstärken liegt. Heute ist kardiale 7T MRT noch eine Forschungsmodalität, die sich Richtung klinischer Anwendung entwickelt.

Hauptziel dieser Dissertation war die Weiterentwicklung von Methoden der kardialen Ultrahochfeld-Bildgebung mittels der neuesten 7T-Technologie und dessen Anwendung für die funktionelle und strukturelle Charakterisierung des Myokardiums.

Für die Mikrostrukturcharakterisierung des Myokardiums bei 7T wurde die Durchführbarkeit von *ex vivo* DTI Messungen von Großtierherzen demonstriert. In solchen Herzen wurde eine Sequenz evaluiert, die für *in vivo* DTI etabliert wurde. Zudem wurden fixationsbedinge Veränderungen von Diffusionsparametern und Gewebeeigenschaften ermittelt. Die Ergebnisse erlauben den Vergleich von bestehenden und zukünftigen *ex vivo* Studien und geben Informationen zu Messparametern bei 7T.

Der Transfer von etablierten Methoden zu präklinischen Studien in Mäuseherzen demonstrierte, dass *ex vivo* DTI sensitive Marker für Mikrostruktur-Remodeling nach Subendokard-Schäden liefern kann. In solchen Fällen zeigte Echokardiographie eine leichte diastolische Dysfunktion und eingeschränkte Longitudinalverformung. Komplementäre DTI und Echokardiographie-Daten erweiterten zudem unser Verständnis von Struktur-Funktions-Interaktionen in Fällen von Verlust von kontraktilen Faserbündeln, Fibrose und linksventrikulärem, systolischem Versagen.

Für die funktionelle Charakterisierung des Myokardiums bei 7T wurde ein dediziertes 7T-Humanprotokoll erarbeitet, welches akkurate Schichtplanung und die Bestimmung der Herzfunktion mittels Cine-Bildgebung umfasst.

Die Herzfunktionsbestimmung erfordert die Segmentierung des Myokards. Hierfür wurde künstliche Intelligenz (KI) entwickelt, die eine schnelle, automatische Herzsegmentierung in klinischen Daten ermöglicht. Mittels Lerntransfer wurden KI-Modelle für Bilder angepasst, die mit der neuesten 7T-Technologie aufgenommen wurden. Methoden für die KI-basierte Segmentierung wurden zudem für die Bestimmung und Segmentierung von Narbengewebe, Ödemen und gesundem Myokard erweitert.

Entwickelte Radiofrequenz-Komponenten ermöglichen translationale 7T-Studien, welche kontrollierte Bedingungen für die Methodenentwicklung von kardialen 7T-Anwendungen für den Humanbereich liefern.

In dieser Arbeit werden die neueste 7T-Technologie, DTI am Herzen und AI genutzt, um Methoden der kardialen Ultrahochfeld-Bildgebung weiterzuentwickeln. Langfristig erweitern die erzielten Ergebnisse diagnostische Methoden, die Früherkennung und Risikoabschätzung in kardiovaskulären Erkrankungen ermöglichen können.

PUBLICATIONS

The following list shows all publications I authored and co-authored.

Original research publications and preprint, which are part of this thesis based on several published manuscripts (The medRxiv-preprint has been submitted to *MRM*; * indicates equal contributions):

1) **Lohr D**, Terekhov M, Weng AM, Schroeder A, Walles H, et al. Spin echo based cardiac diffusion imaging at 7T: An ex vivo study of the porcine heart at 7T and 3T. *PLOS ONE*. 2019;14(3):e0213994.
DOI: 10.1371/journal.pone.0213994

2) **Lohr D**, Terekhov M, Veit F, Schreiber LM. Longitudinal assessment of tissue properties and cardiac diffusion metrics of the ex vivo porcine heart at 7 T: Impact of continuous tissue fixation using formalin. *NMR in Biomedicine*. 2020;33(7):e4298.
DOI: 10.1002/nbm.4298

3) Beyhoff N, **Lohr D**, Foryst-Ludwig A, Klopfleisch R, Brix S, et al. Characterization of Myocardial Microstructure and Function in an Experimental Model of Isolated Subendocardial Damage. *Hypertension.* 2019;74(2):295-304.
DOI: 10.1161/HYPERTENSIONAHA.119.12956

4) Beyhoff N*, **Lohr D***, Thiele A, Foryst-Ludwig A, Klopfleisch R, et al. Myocardial Infarction after High-Dose Catecholamine Application - A Case Report from an Experimental Imaging Study. *Frontiers in Cardiovascular Medicine.* 2020;7(247)
DOI: 10.3389/fcvm.2020.580296

5) Elabyad IA, Terekhov M, **Lohr D**, Stefanescu MR, Baltes S, et al. A Novel Mono-surface Antisymmetric 8Tx/16Rx Coil Array for Parallel Transmit Cardiac MRI in Pigs at 7T. *Scientific Reports*. 2020;10(1):3117.
DOI: 10.1038/s41598-020-59949-6

6) Ankenbrand MJ*, **Lohr D***, Schlötelburg W, Reiter T, Wech T, et al. Deep Learning Based Cardiac Cine Segmentation - Transfer Learning Application to 7T Ultrahigh-Field MRI. *medRxiv*.2020.
DOI: 10.1101/2020.06.15.20131656

7) A Ankenbrand M, **Lohr D**, Schreiber LM. Exploring Ensemble Applications for Multi-sequence Myocardial Pathology Segmentation. In: Zhuang X et al. (eds) Myocardial Pathology Segmentation Combining Multi-Sequence Cardiac Magnetic Resonance Images. MyoPS 2020. Lecture Notes in Computer Science, vol 12554. Springer, Cham.
DOI: 10.1007/978-3-030-65651-5_6

Co-authored original research publications, which were not part of the original application for a dissertation based on several published manuscripts or are outside the scope of this thesis (publication 13 was resubmitted to *BMC Medical Imaging* following major revision, the DOI leads to the published preprint):

8) Elabyad IA, Terekhov M, Stefanescu MR, **Lohr D**, Fischer M, et al. Design of a novel antisymmetric coil array for parallel transmit cardiac MRI in pigs at 7 T. *Journal of magnetic resonance.* 2019;305:195-208.
DOI: 10.1016/j.jmr.2019.07.004

9) Elabyad IA, Terekhov M, Stefanescu MR, **Lohr D**, Fischer M, et al. Design and Evaluation of a Novel Symmetric Multichannel Transmit/Receive Coil Array for Cardiac MRI in Pigs at 7 T. *IEEE Transactions on Microwave Theory and Techniques*. 2019;67(9):3928-3945.
DOI: 10.1109/TMTT.2019.2913636

10) Hock M, Terekhov M, Stefanescu MR, **Lohr D**, Herz S, et al. B0 shimming of the human heart at 7T. *Magnetic Resonance in Medicine.*
DOI: 10.1002/mrm.28423

11) Teh I, Romero W, Dall'Armellina E, Ennis D, Ferreira PF, et al. Reproducibility of diffusion tensor imaging (DTI) on 12 clinical scanners: Towards validation of cardiac DTI sequences. *Journal of Cardiovascular Magnetic Resonance*. Submitted November 2020.

12) Reiter T**, Lohr D**, Hock M, Ankenbrand MJ, Stefanescu MR, et al. On the way to routine cardiac MRI at 7 Tesla - a pilot study on consecutive 84 examinations. *PLOS ONE*. Submitted November 2020.

13) Ankenbrand MJ, Shainberg L, Hock M, **Lohr D**, Schreiber LM. Sensitivity Analysis for Interpretation of Machine Learning Based Segmentation Models in Cardiac MRI. *BMC Medical Imaging.* 2020.
DOI: 10.21203/rs.3.rs-97535/v1

ACKNOWLEDGEMENTS

Finalizing the last pages of this thesis, I feel gratitude and admiration towards the people that have supported and guided me throughout these years. Without you, this thesis would not have been possible. This page is therefore dedicated to you as a token of my appreciation.

Throughout this thesis I had the privilege to work with numerous amazing people in various different projects, while also meeting scientists from different places all around the globe.

I would particularly like to thank Prof. Dr. Laura Schreiber, who has made this possible for me. The recent years have been an amazing learning experience, one that has shaped me and will accompany me for the rest of my life. I am deeply grateful that you have trusted me with this opportunity, thank you! I would also like to thank my other supervisors Prof. Dr. Herbert Köstler and Prof. Dr. Dr. Wolfgang Bauer, who have given me feedback and guidance at different time points in recent years. Thank you for having been part of this journey!

I want to acknowledge the Graduate School of Life Sciences for enabling scientists like me. In particular the staff has been incredibly motivated and helpful, thank you for this! Similarly I want to thank Anna Dorsch and Bettina Dammenhain, who supported me with everything I had to organize outside the scientific aspects of my thesis. Thank you for your patience!

I want to thank Niklas Beyhoff for the cooperation over the past two years. Thank you for all the insightful discussions!

I extend my gratitude to all my current and former colleagues, in particular at the Chair of Cellular and Molecular Imaging. A special thanks goes to Michael Hock, Johannes Martens, Tim Jedamzik, Ibrahim Elabyad, Maya Bille, Steven Nguyen, Markus Ankenbrand, and Maxim Terekhov. Working with you has been a privilege. Maxim, I am deeply grateful to you. Over the last 5 years you were my endless source of scientific knowledge, wherever and whenever I tried to make sense of things, thank you for that! Markus, thank you for sharing my excitement for all things related AI and deep learning, and the countless discussions on what to do next! I very much hope we will continue to find time for Kaggle challenges in the days to come.

At last, I want to thank my family, in particular my parents Bettina and Peter. It never ceases to amaze me with how much passion you follow whatever I do. Words cannot describe how grateful I am to you. Julia, the same applies to you. Thank you for your seemingly endless patience with me, but most of all, thank you for your love!

I can no other answer make but thanks, and thanks, and ever thanks.
– William Shakespeare

TABLE OF CONTENTS

LIST OF TABLES

ACRONYMS

ADC	apparent diffusion coefficient
AI	artificial intelligence
ANN	artificial neural network
ANP	atrial natriuretic peptide
CMR	cardiovascular magnetic resonance
CNN	convolutional neural network
CVD	cardiovascular disease
DL	deep learning
DTI	diffusion tensor imaging
EDV	end-diastolic volume
EF	ejection fraction
EM	electromagnetic
ESC	European Society of Cardiology
ESV	end-systolic volume
E2A	secondary eigenvector angle or sheetlet angle
FA	fractional anisotropy
HA	primary eigenvector angle, helix angle
HF	heart failure
HPC	high performance cluster
LGE	late gadolinium enhancement
LS	longitudinal strain
LSR	longitudinal strain rate
LV	left ventricle
MD	mean diffusivity
MI	myocardial infarction
MICCAI	Medical Image Computing and Computer Assisted Intervention
MRI	magnetic resonance imaging
MvMM	multivariate mixture model
RF	radio frequency
ROI	region of interest
RSD	relative standard deviation
RV	right ventricle
SAR	specific absorption rate
SE	spin echo
SNR	signal-to-noise ratio
STACOM	Statistical Atlases and Computational Modelling of the Heart
STE	stimulated echo
TE	echo time
TR	repetition time

1 INTRODUCTION

According to the World Health Organization cardiovascular diseases (CVDs) are globally the number one cause of death.[1] In 2016 alone CVDs led to an estimated 17.9 million lives lost, which corresponds to 31% of global deaths in that time. CVDs will eventually result in heart failure (HF), a disease development, where a ~50% 5-year mortality following initial diagnosis,[2] is still a harsh prognosis.

While the etiology of CVDs and HF is diverse with regard to world regions, advancing age has been identified as a powerful independent risk factor. This is particularly detrimental to developed countries (HF prevalence ≥ 10% among people older than 70 years),[3,4] where the quality of healthcare and the absence of wars and obesity have led to high average life expectations and shifts in demographics. In these countries, CVDs are still a main cause of death and HF a common cause for hospitalization. The average life expectancy after first hospitalization is only 2.5 years,[5] where present comorbidities predict adverse outcomes.[6]

Medical imaging has become a pillar of modern healthcare, enabling non-invasive clinical analysis, intervention, and diagnostic as well as treatment evaluation. The European Society of Cardiology (ESC) Guidelines for the treatment of acute and chronic heart failure[7] state that cardiovascular magnetic resonance (CMR) is the gold standard for measurements of mass and cardiac function via ejection fraction (EF) for both ventricles (LV, RV) and is the method of choice in patients with complex congenital heart disease.[8-10] Routine applications also encompass the assessment of myocardial fibrosis and scar visualization, and the differentiation between ischemic and non-ischemic origins of HF (etiology establishment[8,11]). Furthermore, they enable the characterization of myocardial tissue[8,10,11] of myocarditis, amyloidosis, sarcoidosis[12], Fabry disease, non-compaction cardiomyopathy and haemochromatosis.

In order to extract static anatomical and dynamic functional parameters such as myocardial mass, wall thickness, wall motion as well as LV and RV volumes and thus, EF, acquired MR images have to be segmented. This means that relevant pixels in each image have to be identified as part of the organ, a pathology (e.g. lesion or scar), or background, partitioning the image into semantically meaningful regions, which can be used to generate these quantitative measures. Manual segmentation of such regions is a rather tedious and time-consuming process that can be subject to non-negligible inter-observer variabilities.[13-16] In recent years, artificial intelligence (AI), more precisely, deep learning (DL) based segmentation

has been shown to outperform all prior automatic segmentation methods, leading to segmentation models for the ventricles,[17,18] the atria,[19,20] the aorta,[21] and the whole heart.[22,23] There has also been an increasing number of applications to pathologies such as scar and edema. While the quantity of scar tissue functions as an independent predictor of cardiovascular outcomes and mortality in patients with ischemic heart failure[24,25] and non-ischemic cardiomyopathies,[26,27] edema is connected to the assessment of the area at risk. Scar and edema volumes enable the assessment of myocardial viability and salvage,[28,29] which is essential in the diagnosis and treatment management for patients with MI. Rapid automatic data evaluation based on deep learning segmentation may increase the value of CMR, where long examination times are considered as a disadvantage to other imaging modalities.

While CMR is already quite established with respect to CVDs and their impact on cardiac tissue, clinical practice is currently solely focusing on macroscopic alterations. Using pulsed gradient fields, magnetic resonance imaging (MRI) is able to acquire images of biological tissue sensitized to molecular diffusion, also called Brownian motion, which refers to the random motion of molecules induced by their thermal energy. Molecular diffusion in isotropic tissue can be described using a single scalar value, the apparent diffusion coefficient (ADC). However, this is insufficient for highly anisotropic tissue such as skeletal and cardiac muscle,[30,31] where molecular diffusion interacts with tissue boundaries and measured diffusivity depends upon tissue anisotropy. In order to fully characterize this orientation-dependent displacement of water molecules in 3D space, the scalar value was replaced by a slightly more complex model of diffusion, the symmetric effective diffusion tensor.[32] MRI based cardiac diffusion tensor imaging (DTI) has become an established technique for the visualization of the myocardial microstructure both *ex vivo* and *in vivo*, offering new insights into ventricular contraction and thus, the mechanical aspects of cardiac function and cardiac disease on a microscopic level. Physiological interpretation of the diffusivity of water in healthy myocardium states that cardiac DTI enables visualization of helical cardiomyocyte configurations,[33-35] and so-called sheetlets,[36-38] which are functional units of connecting and branching cardiomyocytes, separated by shear layers. Functionally, cardiomyocyte helices are thought to facilitate rotation and torsion, while ventricular thickening[39,40] and base-to-apex shortening are attributed to sheetlet re-orientation during contraction. Next to non-destructive visualization of microstructures first discovered using histology, DTI demonstrated abnormal myocyte or sheetlet orientation in congenital heart disease, hypertrophic[38,41,42] as well as dilative cardiomyopathies,[38,43] and MI,[44,45] providing unique information about microstructure integrity and pathologic alterations. Myocardial disarray, impaired sheetlet mobility, and structure loss with respect to cardiomyocyte bundles, are potential non-invasive, early markers for contractile dysfunction, ventricular remodeling and underlying structural changes. Based on such features cardiac DTI may facilitate early detection of adverse remodeling in endocardial layers in response to multiple cardiovascular risk factors,[46-48] allow risk stratification in asymptomatic disease states, and enable

treatment validation on a microstructural level. Increasing numbers of *in vivo* applications[38,41,43,49-52] demonstrate that cardiac DTI may play an essential role in improving our understanding of functional and structural alterations in one of today's major health burdens, namely CVDs.

Since DTI is intrinsically limited in signal-to-noise ratio (SNR) and particularly susceptible to cardiac and breathing motion, initial research and validation was and still is performed in translational *ex vivo* studies.[38,53-56] Without limiting factors such as motion, strain and flow, long scan times are enabled using fixed tissue specimen, allowing the generation of high fidelity, high resolution whole heart data.

Clinical CMR assessments are run on 1.5T and 3T systems, but early studies have demonstrated that ultrahigh field MRI (7T) may improve SNR[57-61] and thus, provide new, prognostic information on cardiac diseases. Next to already established CMR applications, MRI at ultrahigh field strengths may improve SNR in cardiac DTI measurements, enabling higher image quality, improved volume coverage and faster acquisitions.

However, the higher field strength also leads to shorter wavelengths in tissue, inducing B_1-non-uniformity, and thus difficulties regarding power deposition, and the specific absorption rate (SAR). Dedicated radio frequency (RF) hardware based on parallel transmit technology has been introduced to address these issues. Here, multiple transmit elements are used to actively shape the transmission field, a process known as B_1^+ shimming. Depending on the shimming process the transmission field can be optimized with regard to field homogeneity, transmission efficiency, and SAR-safety. This process may facilitate homogeneous RF excitation and enables the potential of high SNR imaging at ultrahigh field strengths.

To date, there is no 7T system with CE certification for cardiac MRI and no sequence protocols dedicated to ultrahigh field cardiac MRI are provided by the vendors. In that sense, cardiac 7T MRI is currently a research modality that is starting to develop towards clinical application. This is one of the first dissertations, where MR image acquisition and method development was mainly done using the latest generation 7T ultrahigh field MRI system.

Primary aim of this thesis was the methodological advancement of ultrahigh field CMR using this latest 7T technology and its application for the functional and structural characterization of the myocardium. Since the 7T system did not come with options dedicated towards ultrahigh field cardiac MRI and sequence protocols applied on clinical systems of earlier generations were not simply transferable, dedicated sequence protocols had to be created. Next to the generation of a custom *in vivo* DTI sequence, the primary aim therefore encompassed the expansion of vendor sequences towards 7T cardiac protocols as well as the development of dedicated RF hardware for translational studies. Due to B_1-non-uniformity, increased B_0 inhomogeneity, and limited RF hardware at 7T, we aimed to implement the custom diffusion sequence on a clinical 3T system first. Moving to diffusion measurements at 7T in controlled *ex vivo* studies, we aimed to validate feasibility and effects of ultrahigh field MRI on both image acquisition and DTI

metrics. In addition to applications in humans we aimed to facilitate translational studies based on DTI for both large and small animals. Secondary aim of this thesis was the development of DL models for rapid automatic segmentation of clinical CMR data and its transfer towards images acquired at 7T. As indicated above, image segmentation is of paramount importance for the assessment of quantitative metrics and accurate segmentation thus an essential step towards future clinical application. Holistically, methods developed in this thesis may be applied for the assessment of functional and microstructural changes in CVDs at 7T, which may also improve our understanding thereof.

Since this is a thesis based on several published manuscripts, the following chapter (Materials and Methods) presents an overview over key materials and methods relevant to the respective publications. Brief summaries of these publications in the chapter "Published Results" are meant to provide the reader with a comprehensive review on individual aims, study motivation as well as key findings. The summaries are followed by the full publications. Thematically publications of this thesis can be sorted into three categories:

1. *ex vivo* cardiac DTI at 7T:
   chapters 3.1, 3.2, 3.3, and 3.4 (pages 11, 33, 49, and 61)
2. hardware development for translational cardiac MRI at 7T:
   chapter 3.5 (page 69)
3. deep learning based segmentation for cardiac MRI data:
   chapters 3.6 and 3.7 (page 89 and 117)

Individual results and their relevance with respect to cardiovascular magnetic resonance imaging and deep learning in medical imaging, are discussed in the overarching chapter "discussion".

2 MATERIALS AND METHODS

This section is meant to give an overview over the key materials and methods applied in the publications of this thesis, while simultaneously providing some additional background information. All content will be divided into the sections hardware, data, and software. A detailed description for materials and methods is given in the individual publications in Chapter 3.

2.1 Hardware

2.1.1 MRI Data Acquisition

MRI systems and hardware specifications used for image acquisition were:

1. Siemens MAGNETOM™ Terra
    i. 7 T
    ii. 80 mT/m, 200 T/m/s
    iii. 1Tx/32Rx head coil (Noval Medical),
    1Tx/16Rx cardiac coil (MRI Tools, Berlin, Germany)
    iv. 8Tx/16Rx parallel transmit cardiac array

2. Siemens MAGNETOM™ Prisma Fit (Cooperation with the Department of Diagnostic and Interventional Radiology, Würzburg)
    i. 3 T
    ii. 80 mT/m, 200 T/m/s
    iii. 1Tx/20Rx head coil

3. Bruker PharmaScan™ 70/16 (Paravision 6.01 interface)
    i. 7 T
    ii. 570 mT/m, 5130 T/m/s
    iii. 1Tx/2Rx ^{1}H-CryoProbe (Bruker BioSpin)

4. Legend:
    i. field strength - B_0
    ii. maximum gradient strength [mT/m], maximum slew rate [T/m/s]
    iii. commercial coils [channels: Tx – transmit/Rx - receive]
    iv. in-house built coil [channels: Tx/Rx]

2.1.2 Data Processing and Deep learning

While most data processing was run on the personal desktop, DL approaches were generally realized using GPU hardware on high performance clusters (HPC) to achieve acceptable time frames. Depending on the task, a hardware setup was chosen from the following selection:

1. Personal desktop:
    i. 1x Intel® Core™ i7-4790 CPU @ 3.60 GHz
    ii. 32 GB of memory
    iii. 1x NVIDIA® GeForce® RTX 2070 Super with 8 GB of memory
2. Local HPC of the Chair of Cellular and Molecular Imaging:
    i. 8x Intel® Xeon® CPU E5-2630 v3 @ 2.40GHz
    ii. 512 GB of memory
    iii. 1x NVIDIA® Tesla® K80 with 12 GB of memory
3. GPU node of the Julia HPC of the University of Würzburg:
    i. 2x Intel® Xeon® Gold 6134 Processor
    ii. 384 GB of memory
    iii. 2x NVIDIA® Tesla® P100 with 16 GB of memory
4. Google Colab

All data underlying data protection terms of the University Hospital Würzburg were computed in-house, using the personal desktop or the local HPC of the Chair of Cellular and Molecular Imaging.

2.2 Data

Training of supervised deep learning methods requires large amounts of so-called ground truth input data. For image segmentation tasks, ground truth means that we have labels that indicate the class of each pixel in each image. In cardiac MRI classes are typically tissue related such as LV blood pool, LV myocardium, or some kind of pathology, for example scar, edema, or fibrosis.

2.2.1 Deep learning Based Cardiac Cine Segmentation

Kaggle (www.kaggle.com) is an online platform and community for topics related to data analysis, machine learning, DL, data mining and “big data” that enables knowledge exchange between data scientists, corporations, and organizations from a variety of different fields. In addition, the platform allows members to host challenges, such as the Data Science Bowl Cardiac Challenge,[62] which summoned participants to write an algorithm for the automated assessment of end-systolic and end-diastolic volumes (ESV and EDV) as well as ejection fraction from cardiovascular MRI data. The data provided for this challenge contained 1140 cardiac MRI examinations (cine images) of normal and abnormal cardiac function as well as corresponding ground truth values for ESV and EDV in milliliter, but no

segmentation labels. Details regarding the MRI examinations and the use of this data set are described in the respective publication (page 89).

2.2.2 Multi-Sequence Myocardial Pathology Segmentation

In conjunction with the conferences STACOM (Statistical Atlases and Computational Modelling of the Heart) and MICCAI (Medical Image Computing and Computer Assisted Intervention 2020), a challenge for myocardial pathology segmentation (MyoPS 2020[63]) was hosted. Participants were tasked to combine multi-sequence CMR data to classify myocardial pathology, such as scar and edema. Pre-processed clinical cine, late gadolinium enhancement (LGE), and T_2-weighted images for 45 patients were provided. Sequences parameters were:

1. balanced steady-state free precession for cine
    i. 8-12, 8-13 mm
    ii. 1.4/2.7

2. Inversion-Recovery gradient-echo for LGE
    i. 10-18, 5 mm
    ii. 1.8/3.6

3. black blood Spectral Attenuated Inversion-Recovery for T_2
    i. 3-7, 12-20 mm
    ii. 90/2000

4. Legend
    i. number of slices, slice thickness [mm]
    ii. TE/TR [ms]

Prior to release, images were processed using Multivariate Mixture Model (MvMM) methods,[64,65] aligning them in common space with identical spatial resolution. In addition to images, the organizers provided ground truth labels on pixel by pixel basis for the following classes:

- LV blood pool
- RV blood pool
- LV healthy myocardium
- LV myocardial edema
- LV myocardial Scar

Details regarding data use are described in the respective publication (page 89).

2.3 Software

2.3.1 Data and Image Processing

A pipeline for data processing including denoising, image registration, and estimation of the diffusion tensor as well as derived diffusion metrics was set up simultaneously to data acquisition throughout this thesis. All data and image processing, unless stated otherwise, was performed using MATLAB[66] with the following toolboxes:

- image processing
- curve fitting
- optimization
- statistics and machine learning.

Denoising of diffusion-weighted image data was performed using overcomplete local partial component analysis as described by Manjon et al.[67] Reconstruction of the diffusion tensor was achieved using methodology by Jiang et al[68] in DSI Studio.[69]

All sequence programming developments were done using the Siemens IDEA environment. Software baselines for the 7T MAGNETOM™ Terra and the 3T MAGNETOM™ Prisma were VE12U and VE11C, respectively.

2.3.2 Deep Learning Based Cardiac Cine Segmentation

This is a list of all the software applied by Ankenbrand et al[70] (page 89) All models were built using an open source software environment based on:

- Python 3.8.3 (www.python.org/)
- Pytorch[71] 1.4.0 (pytorch.org/)
- fastai[72] V1 1.0.60 (docs.fast.ai/)
- juypter 1.0.0 (jupyter.org/).

Further Python software, including its dependencies, was:

- NiBabel 3.1.0 (nipy.org/nibabel/)
- numpy[73] 1.13.3 (numpy.org/)
- pandas 1.0.3 (pandas.pydata.org/)
- pydicom 1.4.2 (pydicom.github.io/)
- scikit-image 0.16.2 (scikit-image.org/)
- SciPy 1.4.1 (www.scipy.org/)
- seaborn 0.10.1 (seaborn.pydata.org/)
- tqdm 4.46.0 (tqdm.github.io/)
- ukbb_cardiac v2.0 (github.com/baiwenjia/ukbb_cardiac).

Next to Python we used software moduls in R 3.6.1 for data analysis:

- Tidyverse 1.2.1 (www.tidyverse.org/)
- Patchwork 1.0.0 (rdocumentation.org/packages/patchwork/)
- ggfortify 0.4.10 (rdocumentation.org/packages/ggfortify)

and the following implementations for data processing:

- med2image 2.0.1 (github.com/FNNDSC/med2image)
- mitools 2.0.3 (neuro.debian.net/pkgs/mitools.html)
- dos2unix 7.4.0 (sourceforge.net/projects/dos2unix/).

Initial labelling of the Kaggle data (page 6) was done using the publicly available model by Bai et al.[74]

In order to provide transparency and to facilitate reproducibility of our results all models and code were made publicly available:

- github.com/chfc-cmi/cmr-seg-tl
- doi.org/10.5281/zenodo.3876351

2.3.3 Multi-Sequence Myocardial Pathology Segmentation

We built all models in Ankenbrand et al[75] (page 117) using the previously mentioned (page 8) open source software environment with slight modifications:

- Python 3.7.7 (www.python.org/)
- Pytorch[71] 1.5.1 (pytorch.org/)
- fastai[72] V2 0.0.17 (docs.fast.ai/)
- NiBabel 3.0.1 (nipy.org/nibabel/)
- numpy[73] 1.19.0
- scikit-image 0.15.0
- tqdm 4.47.0
- R Tidyverse 1.3.0

and minor software additions:

- MONAI 0.2.0 (www.python.org/)
- TorchIO[71] 0.15.5 (pytorch.org/).

For calculations in Google Colab we used pre-installed libraries and added TorchIO, fastai V2, and MONAI, as listed above, including their dependencies.
Again, models and code were made openly available:

- https://github.com/chfc-cmi/miccai2020-myops
- doi.org/10.5281/zenodo.3982324
- doi.org/10.5281/zenodo.3985837

3 PUBLISHED RESULTS

This is a thesis based on several published manuscripts. This chapter includes information on individual publication licenses to publications listed on page ix, a one page summary of these publications, followed by the corresponding publications. Abbreviations used in the summaries are explained in the full publication. Chapter titles are publication titles. For the printed version of this thesis published supplementary material can be found on the added CD. For the digital version there is a separate PDF document "Published Supplemental Material".

3.1 Spin echo based cardiac diffusion imaging at 7T: An ex vivo study of the porcine heart at 7T and 3T

〉 Published in *PLOSONE* – 2019[76]

These citations have been applied in this publication.[34,38,41,49,50,53,54,67-69,76-121]

Due to cardiac and breathing motion as well as intrinsically limited signal-to-noise ratio, angular and spatial resolution in *in vivo* DTI scans remain low, emphasizing the importance of *ex vivo* measurements for research and validation. MRI at ultrahigh field strengths may provide improved SNR in such measurements, enabling increased spatial and/or angular resolution, higher b-values, better image quality and consistency of diffusion metrics.

In this study we aimed to assess the feasibility of cardiac DTI at ultrahigh field strengths using commercial apparatus and software.

Whole heart DTI data was acquired at both 3T and 7T in a set (n=11) of healthy, unfixed porcine hearts shortly after excision. In order to demonstrate sample stability, we continuously measured changes in T_2*, T_1, and diffusion metrics in two freshly excised hearts for 12 hours. Derived diffusion metrics were compared to the 3T reference scan, following manual segmentation according to the 17 segment model of the American Heart Association. Various parallel imaging factors (R=2, 3, 4) were used at 7T to assess, if the increase in field strengths sufficiently compensates the SNR loss.

Sample stability measurements demonstrated that T_2* and T_1 changes were within 2-5% and 2-6% and mean standard deviation over time for FA and MD were ≤0.03 and ≤0.02, respectively. Using the same sequence protocol at 3T and 7T, SNR in b_0 images was 29±3 and 44±6, respectively, and diffusion metrics, such as ADC, FA and |E2A| were significantly different. Susceptibility effects were most pronounced at epicardial and papillary muscle boundaries. Parallel imaging improved data consistency with the 3T reference and no statistically significant differences were found using R=3. SNR in b_0 images using R=2, R=3, and R=4 was 17±6, 19±5, 13±2.

In this study we demonstrate that essential DTI features such as HA, |E2A|, FA, and ADC, do not significantly change with B_0 field strength, given sufficiently high SNR and geometrically undistorted images. Commercial hardware at 7T can lead to improved SNR compared to 3T and parallel imaging is required to reduce susceptibility induced distortions. For the coil used, we conclude that a minimum of R=3 will provide the best compromise between the effects of susceptibility induced distortions and SNR losses.

PLOS ONE

RESEARCH ARTICLE

Spin echo based cardiac diffusion imaging at 7T: An ex vivo study of the porcine heart at 7T and 3T

David Lohr[1]*, Maxim Terekhov[1], Andreas Max Weng[2], Anja Schroeder[3], Heike Walles[4], Laura Maria Schreiber[1]

1 Chair of Cellular and Molecular Imaging, Comprehensive Heart Failure Center (CHFC), University Hospital Wuerzburg, Wuerzburg, Germany, **2** Department of Diagnostic and Interventional Radiology, University of Wuerzburg, Wuerzburg, Germany, **3** Chair Tissue Engineering and Regenerative Medicine (TERM), University Hospital Wuerzburg, Wuerzburg, Germany, **4** Translational Center Regenerative Therapies (TLC-RT), Fraunhofer Institute for Silicate Research (ISC), Wuerzburg, Germany

* e_lohr_d@ukw.de

Citation: Lohr D, Terekhov M, Weng AM, Schroeder A, Walles H, Schreiber LM (2019) Spin echo based cardiac diffusion imaging at 7T: An ex vivo study of the porcine heart at 7T and 3T. PLoS ONE 14(3): e0213994. https://doi.org/10.1371/journal.pone.0213994

Editor: Wolfgang Rudolf Bauer, Universitatsklinikum Wurzburg, GERMANY

Received: October 4, 2018

Accepted: March 5, 2019

Published: March 25, 2019

Data Availability Statement: All relevant data are within the manuscript and its Supporting Information files.

Funding: This work was supported by the German Ministry of Education and Research (grant numbers 01EO1004, 01EO1504). This publication was funded by the German Research Foundation (DFG) and the University of Wuerzburg in the funding programme Open Access Publishing.

Competing interests: The authors have declared that no competing interests exist.

Abstract

Purpose of this work was to assess feasibility of cardiac diffusion tensor imaging (cDTI) at 7 T in a set of healthy, unfixed, porcine hearts using various parallel imaging acceleration factors and to compare SNR and derived cDTI metrics to a reference measured at 3 T. Magnetic resonance imaging was performed on 7T and 3T whole body systems using a spin echo diffusion encoding sequence with echo planar imaging readout. Five reference (b = 0 s/mm^2) images and 30 diffusion directions (b = 700 s/mm^2) were acquired at both 7 T and 3 T using a GRAPPA acceleration factor R = 1. Scans at 7 T were repeated using R = 2, R = 3, and R = 4. SNR evaluation was based on 30 reference (b = 0 s/mm^2) images of 30 slices of the left ventricle and cardiac DTI metrics were compared within AHA segmentation. The number of hearts scanned at 7 T and 3 T was n = 11. No statistically significant differences were found for evaluated helix angle, secondary eigenvector angle, fractional anisotropy and apparent diffusion coefficient at the different field strengths, given sufficiently high SNR and geometrically undistorted images. R≥3 was needed to reduce susceptibility induced geometric distortions to an acceptable amount. On average SNR in myocardium of the left ventricle was increased from 29±3 to 44±6 in the reference image (b = 0 s/mm^2) when switching from 3 T to 7 T. Our study demonstrates that high resolution, ex vivo cDTI is feasible at 7 T using commercial hardware.

Introduction

Mechanical [1] and electrical [2] properties of the heart are linked to the myocardial microarchitecture, which exhibits alterations in a broad range of cardiovascular pathologies. In the past years cardiac diffusion imaging, especially cardiac DTI (cDTI), has been established as a nondestructive and non-invasive method for analysis of the microstructure of myocardial tissue. Helical configuration of myofiber bundles [3–6] and sheet [7–9] formation of connecting

and branching myocytes have been described in ex vivo studies and shown to have high consistency to histological correlation, enabling this method to expand our knowledge of the microstructural basis and progression of cardiovascular diseases.

While technical and methodical advances in cDTI gave rise to in vivo applications [10–13], scan time remains a limiting factor for both angular and spatial resolution. Additionally, DTI is intrinsically limited by signal-to-noise-ratio (SNR) [14–17] and derived metrics are affected by partial volume effects. Thus, ex vivo studies, where scan times are unrestricted and no motion and flow factors exist, remain an important research and validation tool in cDTI applications [18–21].

MRI at ultra-high field strengths ($\geq$7 T) may provide improved SNR, allowing for improvement of the spatial and/or angular resolution, higher b-values, better image quality as well as consistency of diffusion metrics. While there are demonstrations [22, 23] of DTI benefitting from the 7T field in neurological applications, it remains unclear if the SNR advantage will outweigh influences of shortened T_2, T_2^*, and increased B_0 and B_1 inhomogeneity in DTI of the heart.

To date in vivo DTI studies of porcine or human hearts have been limited to field strength of 1.5 T or 3 T, where, due to limited SNR, multiple averages [24–28] are required to ensure consistent results.

Ex vivo studies so far use fixed myocardial tissue to enable the long scan times and/or multiple experiments with parameter variations. In order to produce diffusion data, which is easily reproducible and comparable, we minimized additional tissue treatment and therefore omitted tissue fixation, which shortens the T_2 relaxation time, a critical parameter in diffusion measurements at ultra-high field strengths.

The main aim of this study was to assess feasibility of cDTI using commercial apparatus and software in a set of healthy, unfixed, porcine hearts at 7 T shortly after excision and to compare derived diffusion metrics to a reference data set measured at 3 T. This will allow the comparison of data consistency between cDTI at 3 T and 7 T. Secondary aim of this study was to assess if SNR loss due to increasing acceleration factors can be sufficiently compensated for by the higher field strength. The analysis of consistency of diffusion metrics, susceptibility induced distortions, and SNR derived from scans with various parallel imaging factors and echo times should further allow adaptation and adjustment of established 3T cDTI techniques to the usage at ultra-high fields in vivo.

Materials and methods

Study protocol

Hearts were collected in cooperation with the Translational Center Regenerative Therapies. Animal experiments were approved (reference number: 55.2 2532-2-256) by the District Government of Lower Franconia and the local animal welfare committee and performed according to the German Animal Welfare Act and the EU Directive 2010/63/EU. Male German Landrace piglets, all obtained from the same breeder, and with body weights between 19 and 23.5 kg, were used. More detailed information on the study animals is listed in the S1 Table.

The ratio of heart weight to body weight in 20-30kg pigs (5g/kg) is identical to that of adult humans [29]. The left chambers in porcine hearts are more dominant than in the human heart and the left ventricular wall is much thicker. The interventricular septum in porcine hearts is located more to the right of the heart, while the interventricular septum in the human heart is located in a more central position. This means that the porcine apex is only composed of left ventricular musculature.

For euthanasia, piglets were sedated with azaperone (Stresnil, 2–6 mg/kg) and anesthetized with ketamine (Ursotamin 20–25 mg/kg) intramuscularly in the neck muscle caudal to the base of the ear, before T61 (Embutramid, Mebezoniumiodid, Tetracainhydrochlorid, 0.3–0.4 ml/kg) was administered intravenously via the marginal ear vein.

Immediately after euthanasia the hearts were collected, rinsed and stored in physiological saline solution. They were not fixed in Formalin or other substances. Hearts were centered in plastic containers filled with saline solution using surgical threads. MRI was performed at bore temperature (~19˚) on 7T and 3T whole body MRI systems (Siemens MAGNETOM Terra and Prisma, respectively, Erlangen, Germany) within 10 hours after euthanasia using a 1Tx/32Rx head coil. All measurements were therefore performed in a state of rigor mortis. On measurement days we received two hearts, which were excised in one setting. Data for the two hearts was acquired in consecutive measurements in five out of six cases (n = 11). Sample stability measurements were done on separate occasions, since they blocked the scanner for a duration of 12 hours.

Sample stability

Tissue-stability measurements were made to monitor possible changes in tissue structure, which may occur within the time period between scans at 7 T and 3 T. For this purpose, a mid-cavity slice was imaged continuously in two hearts over a period of 12 hours. The delay between the last excision and the start of imaging was roughly 45 minutes. Myocardial T_2^* and T_1 values as well as diffusion parameters, such as FA and ADC were measured interleaved in an uninterrupted cycle.

T_2^* was evaluated based on a 2D gradient multi-echo sequence with the following imaging parameters: slice thickness: 5 mm, matrix size: 68 × 176, field of view (FOV): 131 mm × 176 mm, number of averages: 6, TR: 150 ms. Nine echoes per excitation were acquired with TE values between 2.07 ms and 18 ms.

T_1 was evaluated using the DESPOT1 method [30] with the flip angles: 15˚, 30˚, and 45˚. Ten averages were acquired with TE: 3.69 ms. A supporting B_1 map for DESPOT1 was derived from additional double flip angle measurements using 6 averages and TR: 2000 ms. FOV and the matrix size remained the same as listed for T_2^* acquisitions.

Twenty diffusion directions according to Skare [31] (b = 700 s/mm^2) and five reference images (b = 0 s/mm^2) were acquired using a single refocused spin-echo sequence with Stejskal-Tanner diffusion preparation, EPI readout and a GRAPPA acceleration factor R = 3. Measurement parameters were: slice thickness: 5 mm, TE/TR: 55/3000 ms, matrix size: 100 x 128, FOV: 132x170 mm^2, bandwidth: 2300 Hz/Pixel (readout) and 1299 Hz/Pixel (phase-encode).

DTI acquisition

At 7 T: Prior to measurements we applied 3rd order shims for a volume covering the whole organ. Whole heart diffusion data sets (n = 11) were acquired with an isotropic resolution of 1.3x1.3x1.3 mm^3 using a Stejskal-Tanner diffusion preparation and EPI readout (described above). Further parameters were TE/TR: 55/15000 ms, 65 interleaved slices (no gaps), bandwidth: 1302 Hz/Pixel (readout) and 1000 Hz/Pixel (phase-encode), non-accelerated (R = 1) echo train length: 55, matrix size: 84x128, FOV: 111x170 mm^2 and 5/8 partial-Fourier. 30 diffusion directions (b = 700 s/mm^2) [31] and 5 reference (b = 0 s/mm^2) images were acquired in a total scan time of nine minutes. Measurements with the parameters above were originally chosen for measurements at 3 T [32] and were used here as a first point for comparison between scans at 7 T and 3 T. Measurements with these parameters will be referred to as the reference scan at 7 T (R = 1).

The scan was repeated with GRAPPA acceleration factors R = 2 (n = 7), R = 3 (n = 11) and R = 4 (n = 11), 3/4 partial-Fourier, and an increased readout bandwidth of 2300 Hz/Pixel resulting in minimal TEs and echo train lengths of 50/47/43 ms and 33/21/ 16, respectively. The bandwidth in phase-encode direction was 1299 Hz/Pixel. Total measurement time for the 7T scans was ~65 minutes.

AT 3 T: Whole heart (n = 11) diffusion data sets were acquired at 3T. Reference scan parameters described above were used for image acquisition. The parameters were chosen to optimize for a high isotropic resolution and minimal susceptibility induced distortions in diffusion weighted images at 3 T, while maintaining SNR>25db, which is considered to be in the clinical SNR regime [15].

DTI data analysis

All Processing was based on images using the vendor reconstruction pipeline. For whole heart scans, motion correction was applied to account for eddy-current induced geometrical distortions. Tensor reconstruction using DSI Studio [33, 34] was achieved as described in [35]. For the Stejskal-Tanner sequence and isotropic samples the observed signal intensity S, following diffusion weighting, is:

$$S = S_0 e^{-bg^t Dg} = S_0 e^{-b\sum_{i,j=x,y,z}(g_i g_j)D_{ij}} \tag{1}$$

where S_0 corresponds to the observed signal without diffusion weighting, g to the normalized diffusion gradient directions, b to the diffusion weighting factor, which, for rectangular gradients, is defined by:

$$b = \gamma^2\delta^2G^2\left(\Delta - \frac{\delta}{3}\right) \tag{2}$$

and D to a 3x3 diffusion Tensor (laboratory frame):

$$D = \begin{bmatrix} D_{xx} & D_{xy} & D_{xz} \\ D_{yx} & D_{yy} & D_{yz} \\ D_{zx} & D_{zy} & D_{zz} \end{bmatrix} \tag{3}$$

In the definition of the diffusion weighting factor, γ corresponds to the gyromagnetic ratio, δ and G to the duration and amplitude of the applied diffusion gradient in a given direction, and Δ to the separation between the applied diffusion gradients. With the introduction of the following two vectors:

$$\bar{D} = [D_{xx}\ D_{yy}\ D_{zz}\ D_{xy}\ D_{xz}\ D_{yz}]^T \tag{4}$$

$$\bar{g} = [g_x^2\ g_y^2\ g_z^2\ 2g_xg_y\ 2g_xg_z\ 2g_yg_z]^T \tag{5}$$

Eq (1) can be rewritten as:

$$\sum_{i,j=x,y,z}(g_ig_j)D_{ij} = \bar{g}^t \cdot \bar{D} = ln\frac{(S/S_0)}{b} \tag{6}$$

Since the tensor is symmetric ($D_{ij} = D_{ji}$), it can be calculated based on the acquisition of $\geq$7 images (six or more diffusion weighted images S_k using the diffusion gradients g_k and one

reference S_0). The resulting system of equations:

$$\bar{g}_k^t \cdot \bar{D} = ln\frac{(S_k/S_0)}{b_k} \quad (k = 1, \ldots, K; K \geq 6) \tag{7}$$

is solved in matrix form:

$$A\bar{D} = B \tag{8}$$

where A is a K x 6 matrix:

$$A = \begin{bmatrix} \bar{g}_1^t \\ \vdots \\ \bar{g}_K^t \end{bmatrix} = \begin{bmatrix} g_{1x}^2 & g_{1y}^2 & g_{1z}^2 & 2g_{1x}g_{1y} & 2g_{1x}g_{1y} & 2g_{1y}g_{1z} \\ \vdots & \vdots & \vdots & \vdots & \vdots & \vdots \\ g_{Kx}^2 & g_{Ky}^2 & g_{Kz}^2 & 2g_{Kx}g_{Ky} & 2g_{Kx}g_{Kz} & 2g_{Ky}g_{Kz} \end{bmatrix} \tag{9}$$

and B a K-dimensional vector:

$$B = \begin{bmatrix} ln\frac{(S_1/S_0)}{b_1} & \ldots & ln\frac{(S_K/S_0)}{b_K} \end{bmatrix}^T \tag{10}$$

The solution is found using the pseudo-inverse (A^+) of the matrix A:

$$\bar{D} = A^+B = (A^TA)^{-1}A^TB \tag{11}$$

The calculated tensor was used for visualization of fiber bundle tracts, eigenvalue analysis on a voxel-by-voxel-basis and the calculation of fractional anisotropy (FA) and the apparent diffusion coefficient (ADC) using:

$$FA = \frac{\sqrt{3}}{\sqrt{2}}\frac{\sqrt{(\lambda_1 - \lambda)^2 + (\lambda_2 - \lambda)^2 + (\lambda_3 - \lambda)^2}}{\sqrt{\lambda_1^2 + \lambda_2^2 + \lambda_3^2}} \tag{12}$$

and

$$ADC = \frac{\lambda_1 + \lambda_2 + \lambda_3}{3} \tag{13}$$

Here, λ_1, λ_2, λ_3 are eigenvalues of the diffusion tensor sorted by size and λ their mean value. All other post processing was accomplished using MATLAB (MathWorks, Natick, USA). First, images were converted to NIfTI format and denoised using the local PCA-denoising algorithm described in [36]. Manual segmentation of the whole heart scans was done according to the 17 segment model [37] of the American Heart Association (AHA). Representative distribution of the segments: basal, mid-cavity, apical and apex is displayed in Fig 1. Resulting myocardial contours were applied to all whole heart scans of the same heart. A local orthogonal coordinate system with longitudinal, circumferential, and radial axes was established and the primary eigenvector (E_1) was projected in the plane given by circumferential and longitudinal vectors. As illustrated in Fig 2A and 2B the angle between the projected eigenvector and the circumferential direction was defined as the primary eigenvector angle or helix angle (HA) [3, 38]. The orientation of the primary eigenvector depends on localization in the myocardium, describing a smooth transmural progressing from positive right-handed angles in the endocardium to negative left-handed angles in the epicardium (Fig 2D). Analysis of this pattern was done using profile lines between the LV center and epicardial voxels. Profiles were averaged for apical, mid-cavity, and basal parts as well as multiple hearts. The stability of the transmural

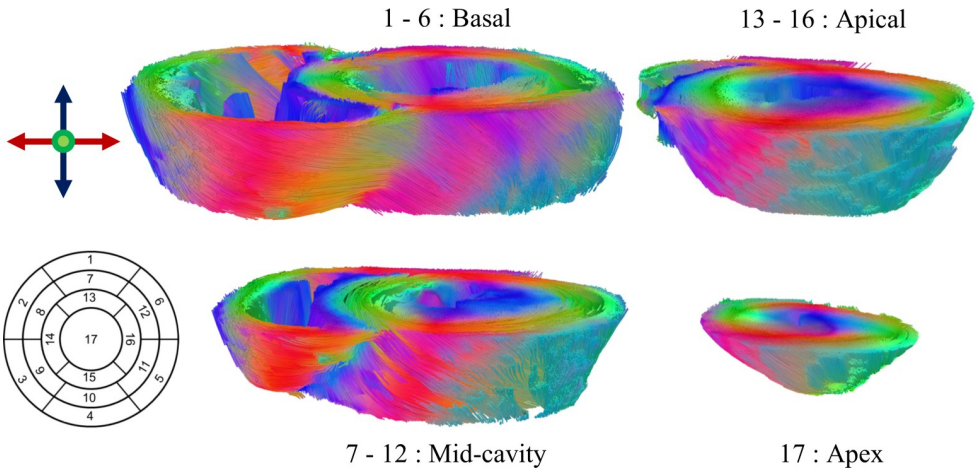

Fig 1. Orientation of the main eigenvector of the diffusion tensor within apex, apical, mid-cavity, and basal parts. Values were calculated from cDTI data measured at 7T and mapped onto fiber tractography of the left and right ventricle. Segmentation was done according to the 17 segment AHA model.

https://doi.org/10.1371/journal.pone.0213994.g001

gradient was assessed using the standard deviation of values at the five myocardial layers: endocardial, sub-endocardial, mid-wall, sub-epicardial, and epicardial.

The secondary eigenvector is associated with sheetlet orientation [7, 38]. As shown in Fig 2C, a cross-myocyte plane was calculated perpendicular to E_1 for every voxel. The secondary

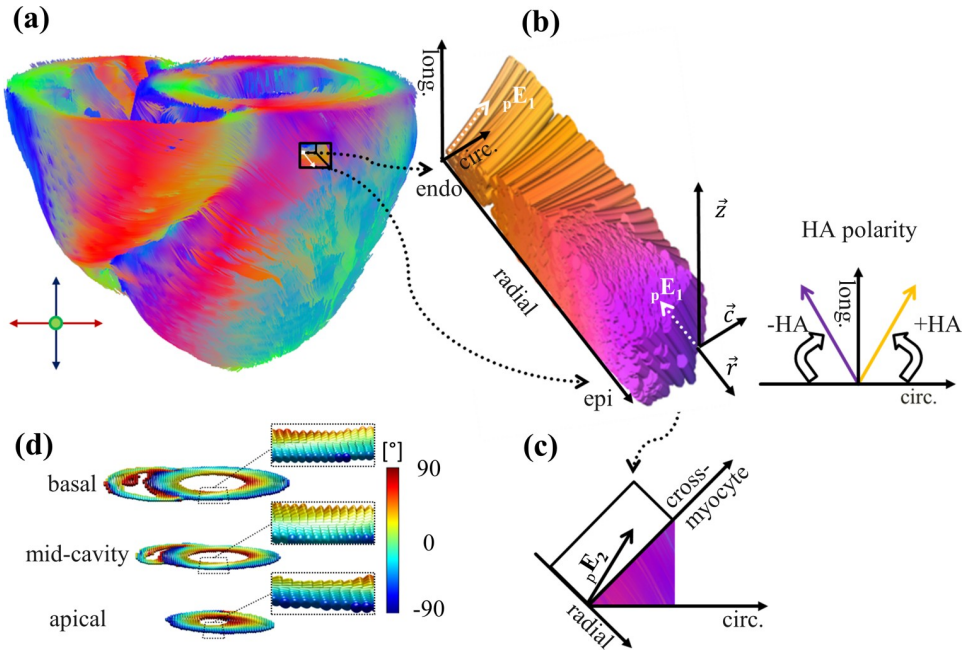

Fig 2. Orientation of primary and secondary eigenvector of diffusion and derived metrics helix angle and E2A. (a) Main eigenvector of diffusion mapped onto fiber tractography of the left and right ventricle. (b) Cut transmural block of reconstructed fibers from a) used to illustrate the parameter helix angle and assignment of its polarity within the local coordinate system of longitudinal $\vec{z}$, radial $\vec{r}$ and circumferential $\vec{c}$ axes. (c) Projected secondary eigenvector angle. (d) Tensor visualization as superquadric glyphs in basal, mid-cavity and apical parts of (a). Color coding resembles helix angle values for single voxels. Zoomed areas show the typical smooth progression of positive right handed fibers in the endocardium to negative left handed fibers in the epicardium.

https://doi.org/10.1371/journal.pone.0213994.g002

eigenvector was projected onto this plane and the angle between projection and cross-myocyte direction defined as secondary eigenvector angle (E2A).

Comparison between the reference scan at 3 T and 7 T, as well as 7T measurements with GRAPPA factors R = 2, R = 3, and R = 4 was done for medians of ADC, FA, and |E2A| using a Wilcoxon test with a significance level of $P<0.05$. This analysis was performed for apical, mid-cavity, basal parts, and the entire left ventricle. Maximal and minimal deviations of ADC [10^{-3} mm^2/s] and FA within the AHA segments were used to define a bias range for 7T acquisitions relative to the median 3T reference.

Visualization of diffusion in 3D was done using superquadric glyphs [39] as representations of the primary eigenvector. A generalized version of the deterministic fiber tracking algorithm in [33] was used in DSI studio in order to generate fiber visualization from DT-data. After calculation in Matlab, helix angle values were reintegrated back into DSI Studio, in order to generate a color coded mapping of the parameter as local indices onto reconstructed fibers of the right and left ventricle. The same was done for SNR values within myocardial contours. All fiber tracking was based on a ROI, containing the left and right ventricle from base to apex. Segmentation of this ROI was done using the R = 3 scan and copied to other 7T scans, where applicable. Segmentation of the 3T scan was done separately. An anisotropy threshold of 0.1 was used for fiber termination, filtering out all voxels with FA<0.1. The angular threshold was set to 60˚ and the step size to 0.5 voxels. Only tracks ranging from 10 mm to 300 mm were accepted and initially a total of 100000 tracks was reconstructed.

SNR analysis

For the assessment of SNR (n = 9) as a function of parallel imaging we acquired 30 b = 0 s/mm^2 images of 30 slices of the left ventricle (LV) using the reference scan parameters as well as GRAPPA acceleration factors R = 2, R = 3, and R = 4. No partial Fourier technique was used in GRAPPA accelerated scans. Echo train lengths were 55, 41, 27, and 21, respectively. A region of interest (ROI) was drawn for myocardial tissue of the LV in all 30 slices of the acquired b = 0 images. SNR was calculated according to the multiple acquisition method described by Reeder et al. [40]. Multiple acquisitions with identical scan parameters are used to form a pseudo-time dependent data set. The mean ($\bar{x}$) and standard deviation (σ) of every voxel (r) can be calculated over "time" (t), allowing the measurement of SNR on a pixel-by-pixel basis:

$$SNR(r) = \frac{\bar{x}_t(r)}{\sigma_t(r)} \tag{14}$$

Resulting values were averaged for the previously defined myocardial ROI. SNR in scans with R≥2 and increased bandwidth was compensated using the following two factors, in order to normalize GRAPPA accelerated scans:

$$1 : \sqrt{\frac{N_{PE}(R=1)}{N_{PE}(R=k)}} \quad 2 : \sqrt{\frac{bw(R \geq 2)}{bw(R=1)}} \tag{15}$$

where N_{PE} corresponds to the number of phase encodings in scans using varying parallel imaging factors k and bw to the bandwidth. No pre-processing, such as denoising, was applied prior to SNR analysis.

Results

Sample stability

Experiments monitoring tissue stability over a period of 12 hours showed little sign of change in the measured mid-cavity slice. Time curve developments for relative changes in T_2^*, T_1, FA, and ADC over the time period of 12 hours are shown in Fig 3. Corresponding changes in absolute values can be found in S1 Fig. Any tissue changes immediately after excision could not be assessed, since scans started approximately 45 min after the second organ excision, due to the transport and preparation time required. No change in LV wall thickness was observed during the measurements. Initial myocardial T_2^* values for the two hearts changed 2% and 5% over the time course of 12 hours, remaining stable with mean ± error of the mean of 20.45 ± 0.15 ms and 20.47 ± 0.28 ms. Relative T_1 changes over this time period were 2–6%. Mean ± error of the mean for FA and ADC for the two hearts were 0.45±0.01 and 0.45±0.02 and 0.63±0.02 [10^{-3} mm^2/s] and 0.69±0.03 [10^{-3} mm^2/s], respectively. ADC values for one heart decreased during the first 4–5 hours of scan time, but remained within measurement precision during typical acquisition times in this study.

DTI

SNR in b = 0 images of reference scans (R = 1) at 3 T and 7 T was 29±3 and 44±6, respectively. While B_1 destructive interferences were apparent in saline solution in all 7T acquisitions, such

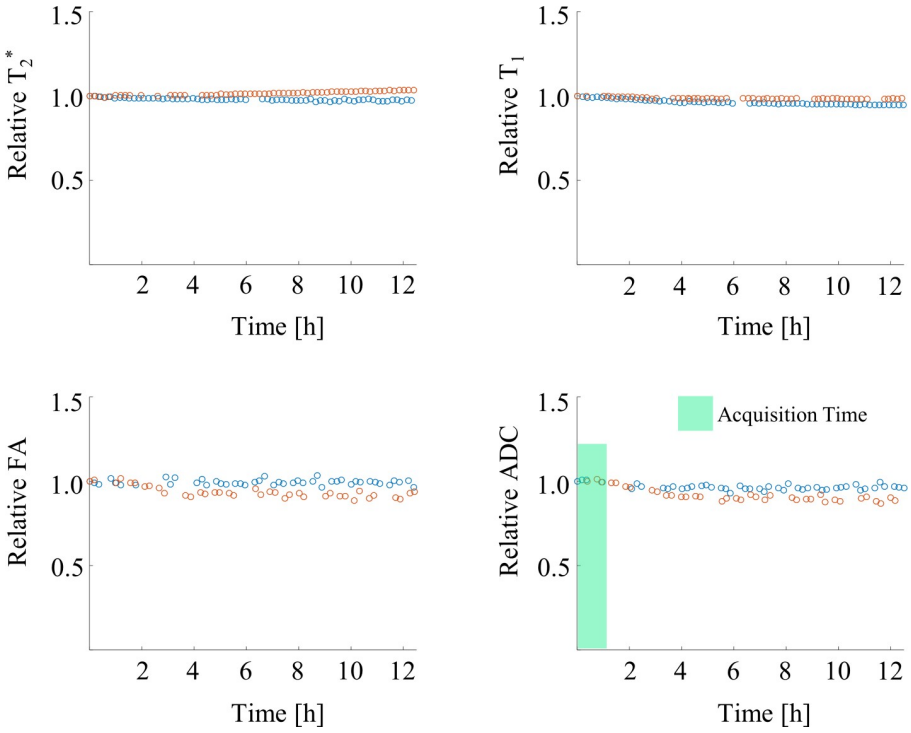

Fig 3. Temporal evolution of sample stability using measures of T2*, T_1, FA, and ADC. Values are plotted relative to time point t = 0 over a period of 12 hours for two hearts (blue, red). Changes in myocardial T_2^* and T_1 over this time period for the two hearts were 2–5% and 2–6%, respectively. Mean ± single standard deviation were 0.45±0.01 and 0.45±0.02 for FA and 0.63±0.02 [10^{-3} mm^2/s] and 0.69±0.03 [10^{-3} mm^2/s] for ADC respectively. The green area marks the time interval, were the diffusion measurements at 7T would take place. Derived diffusion parameters measured within this time interval were stable.

https://doi.org/10.1371/journal.pone.0213994.g003

artefacts were mostly not observed within myocardial tissue. Representative images for the various protocols can be found in S2 Fig.

Statistical DTI analysis was performed for 4±1 slices of the apical cap, 10±1 apical, 10±1 mid-cavity, and 11±1 basal slices. A typical segment distribution as well as main eigenvector orientation for fibers of the left and right ventricle reconstructed by tractography is shown in Fig 1.

Fig 4A displays median values of diffusion metrics for the 17 segments of the AHA model for all DTI acquisitions. The biggest differences can be found between the reference scan at 3 T and 7 T, particularly for the metrics ADC and FA. Eigenvector orientations appear robust to increasing acceleration at 7 T. The absolute bias ranges of the examined parameters between 3 T and 7 T were as follows: 3–45% (ADC) and 3–26% (FA) using values of the reference at 7 T; 1–12% (ADC) and 1–13% (FA) for GRAPPA factor R = 2; 1–11% (ADC) and 1–12% (FA) for GRAPPA factor R = 3; 1–15% (ADC) and 1–12% (FA) using GRAPPA factor R = 4.

Median ADC, FA, and |E2A| values averaged for apex, apical, mid-cavity, and basal parts as well as the entire left ventricle are displayed in Fig 4B. All metrics measured at 7T exhibit higher standard deviation when compared to the 3T reference. Statistically significant differences in some segments were found for all parameters derived from the 7T R = 1 and R = 4 scans. While calculated metrics from scans using GRAPPA factor R = 2 showed significant differences in the apex for ADC and |E2A| in mid-cavity and basal parts, there were no significant differences for data derived from scans with R = 3.

Fig 5 shows helix angle profiles averaged for apical, mid-cavity, and basal parts in comparison to the reference (R = 1) data at 3T. Transmural profiles follow the same trend for all acquisitions. Helix angle standard deviations in apical, mid-cavity, and basal segments are displayed in Table 1 for all scans. With 8.7˚ and 8.6˚, averaged over apical, mid-cavity, and basal segments, transmural profiles based on the reference scan at 7 T and scans using R = 4 exhibited the highest variation. Mean values for scans using R = 2 and R = 3 were within a 2˚ deviation with respect to the 3T reference. GRAPPA factors R>2 lead to an increase in standard deviation relative to R = 2. Compared to the 3T reference, profiles based on the reference scan at 7 T have shown the highest deviation in mean values at different transmural points, particularly in the mid-cavity segment ($\leq$9.1˚). The lowest deviation in mean values relative to the 3T reference was found for the scans using R = 2.

Transmural helix angle gradients in degrees per percentage of transmural depth are presented in Fig 6. The highest variation in determined gradient values was found in the apical region. Scans using the reference parameters at 7 T lead to the biggest difference in mean gradients for apical and basal regions, while showing the smallest difference in mid-cavity regions. Averaged over all regions the reference at 3 T and the R = 3 scan exhibited the lowest standard deviations. The smallest difference in mean values in relation to the 3T reference was found for R = 2.

Fig 7 shows an excerpt of fiber tractography of the left ventricle and the diffusion tensor represented as superquadric glyphs in apical, mid-cavity, and basal slices for the same heart of both the reference scan at 3 T and GRAPPA accelerated scans at 7 T. Helix angle values across the myocardium of reconstructed fibers transition smoothly in the 3T reference and the scan using GRAPPA factor R = 4. Transitions, particularly in the epicardium, are less smooth for the scans using GRAPPA factors R = 2,3 and appear patchy. The highest variation for helix angle values was found for epicardial voxels and areas within the left ventricle involving papillary muscle. In addition there are areas with varying glyph form (black arrows), indicating variations in the underlying diffusion tensor for scans at 7 T. These changes are severe for scans using GRAPPA factor R = 1 and become less severe with increasing acceleration.

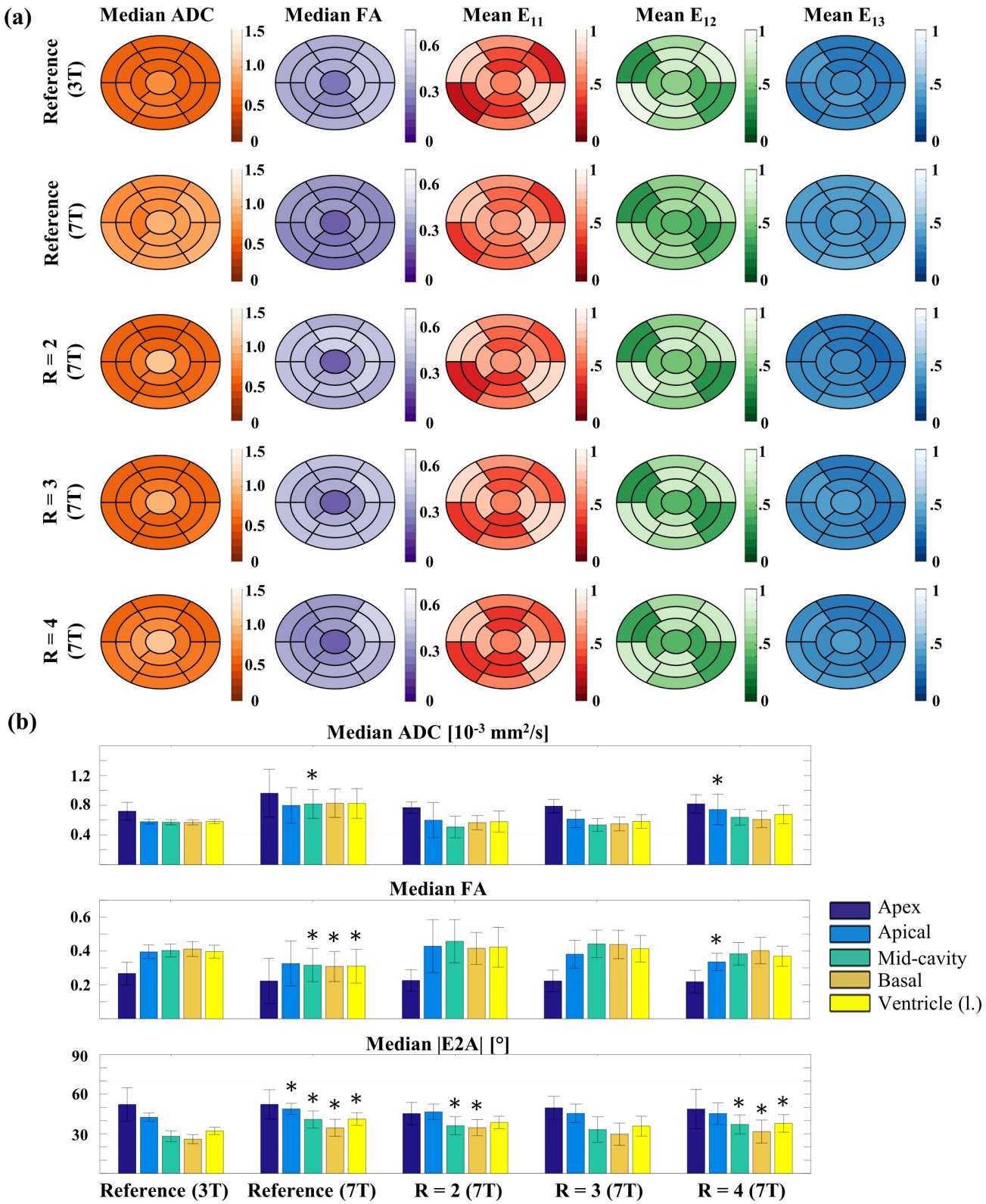

Fig 4. 17 segment distributions of diffusion metrics at 3 T and 7 T using varying parallel imaging factors. (a) Median ADC [10^{-3} mm^2/s], FA, and the three main eigenvector E_1 components E_{11}, E_{12}, E_{13} for all 17 segments. Color coding of the vector components corresponds to the "RGB" encoding of spatial orientation for diffusion tensor main axes typically used in DTI (see Fig 1). (b) Values of median ADC, FA and |E2A| averaged for apex, apical,

mid-cavity, and basal parts as well as the whole left ventricle A significant difference in Wilcoxon test ($P < 0.05$) compared to the 3T reference is indicated by *.

https://doi.org/10.1371/journal.pone.0213994.g004

SNR

Fig 8A displays average SNR, normalized using the factors in Eq (15), in myocardial tissue in unaveraged b = 0 s/mm^2 images acquired for this study. Means of SNR were 29±3, 44±6, 17±6, 19±5, 13±2 for the reference at 3 T, the reference at 7 T, and scans using GRAPPA factors R = 2–4, respectively. Representative, for the same heart, calculated values, mapped to fiber tractography of the 3T and the 7T reference scan are shown in Fig 8B and corresponding tractography for GRAPPA accelerated scans in Fig 8C. Mapped SNR values illustrate the distribution within the myocardium of the left ventricle. The SNR gain at 7 T is clearly visible. Incomplete or diffuse reconstructions in the reference scan at 7 T and the scan using GRAPPA acceleration factor R = 2 are indicated by black arrows.

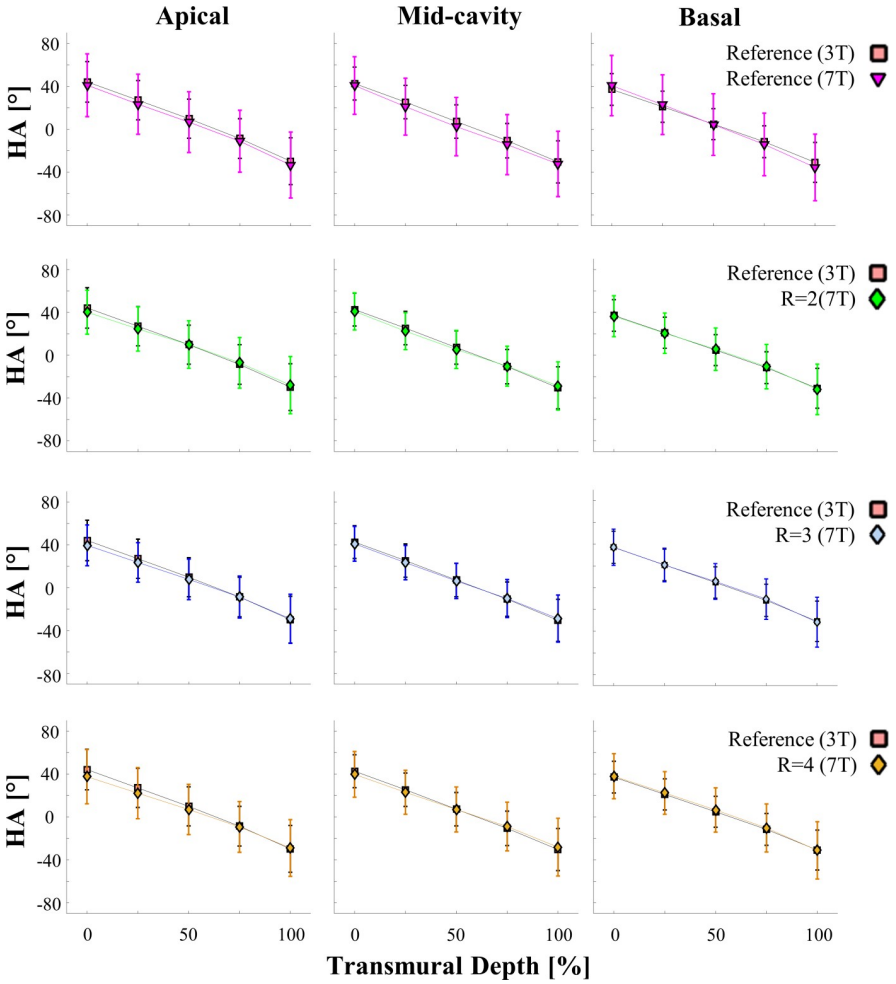

Fig 5. Average transmural helix angle profiles at 7 T and 3 T for apical, mid-cavity, and basal segments. Data was derived from the reference scan at 3 T, the reference scan at 7 T and scans with increasing GRAPPA factors R = 2, R = 3, and R = 4 at 7 T. Data points are displayed for five myocardial layers endocardial, sub-endocardial, mid-wall, sub-epicardial, and epicardial as mean ± one standard deviation. Profiles show helix angle values as a function of transmural depth (%).

https://doi.org/10.1371/journal.pone.0213994.g005

Table 1. Helix angle standard deviation within apical, mid-cavity and basal parts of the left ventricle.

	Reference (3T)	Reference (7T)	R = 2 (7T)	R = 3 (7T)	R = 4 (7T)
Apical	7.3	9.0	5.8	5.9	8.3
Mid-cavity	4.4	9.1	6.0	7.0	8.8
Basal	3.7	8.0	4.4	5.8	8.6
Mean	5.1	8.7	5.4	6.2	8.6

Values were measured at the 5 transmural layers: endocardial, sub-endocardial, mid-wall, sub-epicardial, and epicardial

https://doi.org/10.1371/journal.pone.0213994.t001

Discussion

Our results demonstrate that cDTI in unfixed porcine hearts at 7 T is feasible and can lead to improved SNR in DTI acquisitions of myocardial tissue. Comparison to a reference data set of the same hearts measured at 3 T shows that essential DTI features such as HA, |E2A|, FA, and ADC, do not significantly change with B_0 field strength, given sufficiently high SNR and geometrically undistorted images. This is an important finding with regard to future studies.

Measurements in vivo will require additional measures to reduce susceptibility in areas close to the lung. This can be accomplished via dedicated shimming methods [41] and/or further reduction of the echo train using reduced field-of-view approaches [13, 42].

Obtained FA values in the unfixed heart using b = 700 s/mm^2 are 0.41±0.04 at 3 T (R = 1), 0.43±0.07 at 7 T (R = 2) and 0.42±0.06 at 7 T (R = 3). Using a similar b value (b = 800 s/mm^2) in porcine hearts at 3T, Wu et al. [21] reported FA = 0.32±0.01 and Pashakhanloo et al. [43] FA = 0.37±0.04. Literature values above refer to formalin based tissue fixation prior to DTI measurements. FA discrepancy observed in our study with respect to values cited above are in agreement with studies analyzing the impact of tissue fixation on diffusion metrics. Mazumder et al. [44] reported FA values of 0.42 ± 0.028 in porcine hearts prior to formalin fixation, which dropped to 0.26 ± 0.034 after fixation. A similar observation was made in [45], which reports a fixative concentration dependent decrease in FA compared to unfixed myocardial tissue.

Median ADC values for apical to basal segments in our study range from 0.53–0.62 [10^{-3} mm^2/s] (3T) and 0.51–0.66 [10^{-3} mm^2/s] (7T, R = 3). While the corresponding values of 0.671 ± 0.106 and 0.633 ±0.04 [10^{-3} mm^2/s] reported by Wu and Pashakhanloo et al. in fixed hearts are higher, our results are in good agreement with Mazumder et al., who reported an

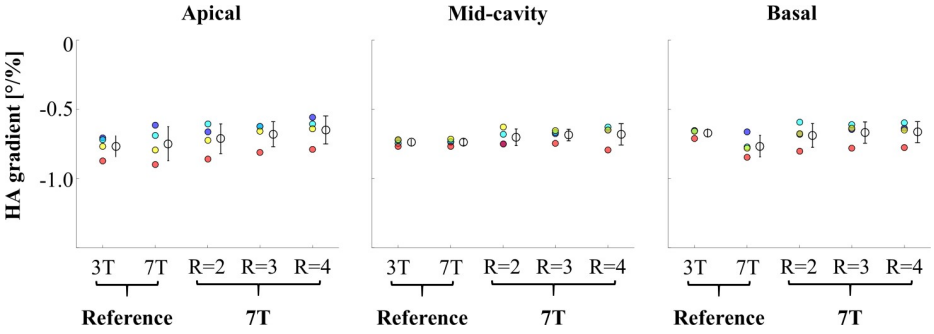

Fig 6. Transmural helix angle gradients between transmural layers. Endocardial, sub-endocardial, mid-wall, sub-epicardial, and epicardial. Gradients were calculated based on the data displayed in Fig 4. Color coding: Endo- to sub-endocardial gradient (blue), sub-endocardial to mid-wall gradient (light blue), mid-wall to sub-epicardial gradient (yellow), and sub-epicardial to epicardial gradient (red). The complete transmural gradient is displayed with mean ± one standard deviation.

https://doi.org/10.1371/journal.pone.0213994.g006

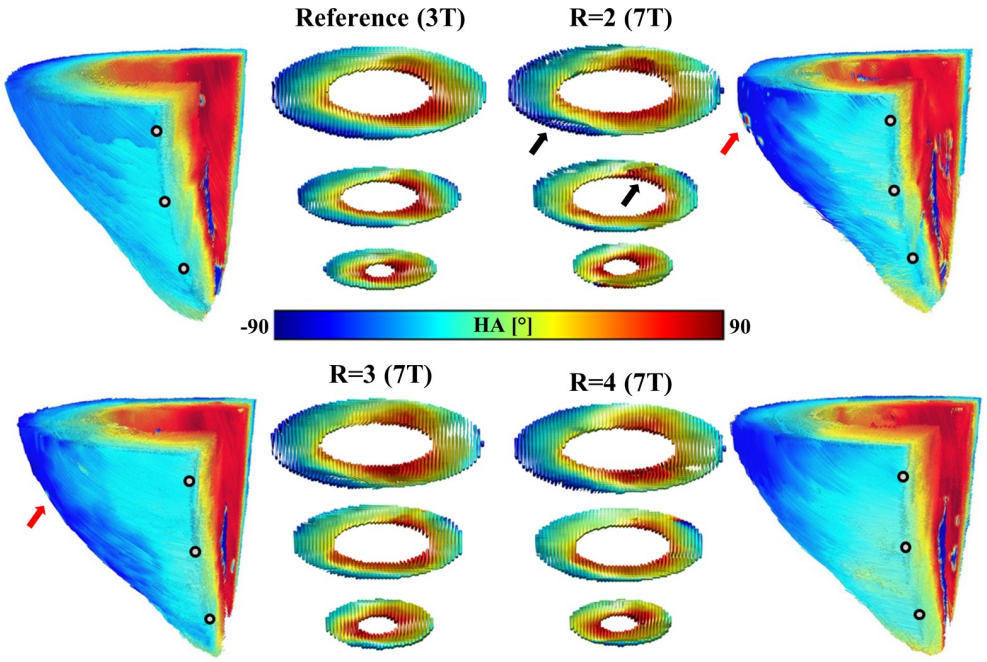

Fig 7. Tractography and helix angle comparison between the 3T reference and GRAPPA accelerated scans at 7 T. Examples of left ventricle tractography from the same heart are displayed for the 3T reference and GRAPPA accelerated scans at 7 T showing differences in resulting tractography and helix angle values. Grey points indicate the position of selected apical, mid-cavity and basal slices. The diffusion tensor within the myocardium of the left ventricle in these slices is visualized as a superquadric glyph. Areas with glyph variation and underlying changes in the diffusion tensor are indicated by a black arrow and areas of helix angle variation in the epicardium with a red arrow.

https://doi.org/10.1371/journal.pone.0213994.g007

ADC of 0.52 ± 0.026 [10^{-3} mm^2/s] in unfixed tissue, and observed an increase in ADC following tissue fixation. In addition to different tissue preparation, the age and breed of the pigs may have an influence on derived ADC and FA values as well. Compared to heart regions in the middle of the ventricle, the number of analyzed voxels in the apex is relatively low. Differences in FA and ADC compared to the other regions may therefore be caused by a mix of structural differences and an increased role of partial volume effects.

ADC, |E2A|, and helix angle values were used for validation versus the 3T reference. Standard deviations were particularly high for the reference scan at 7T, resulting in a significant difference compared to the 3T reference in ADC of mid-cavity segments, despite systematic overestimation of this metric, and multiple significant differences for the metrics FA and |E2A|. DTI measurements using EPI readout without reduction in the number of phase encoding steps, due to parallel imaging acceleration, do not seem feasible at 7T, leading to a strong bias in derived diffusion metrics. While ADC is influenced by low SNR (<20db), there was only one significant difference between GRAPPA accelerated scans at 7T using R = 4 and the 3T reference in apical segments. FA was similarly affected, while main eigenvector orientations appeared robust for GRAPPA accelerated scans. Simulations [46] have shown that FA and parametric angles are largely independent of the trade-off between the number of acquired directions and SNR in b = 0 images. However, the acquisition of 30 diffusion directions leads to an increased robustness of measured FA and decreases the probability of a measured FA bias caused by extreme cases of underlying tissue orientation. In addition to the ADC, |E2A| is also affected by low SNR (<20db). In R = 4 scans this leads to significant differences compared to the reference at 3 T and scans using R = 3. This is in agreement with recent work of Scott

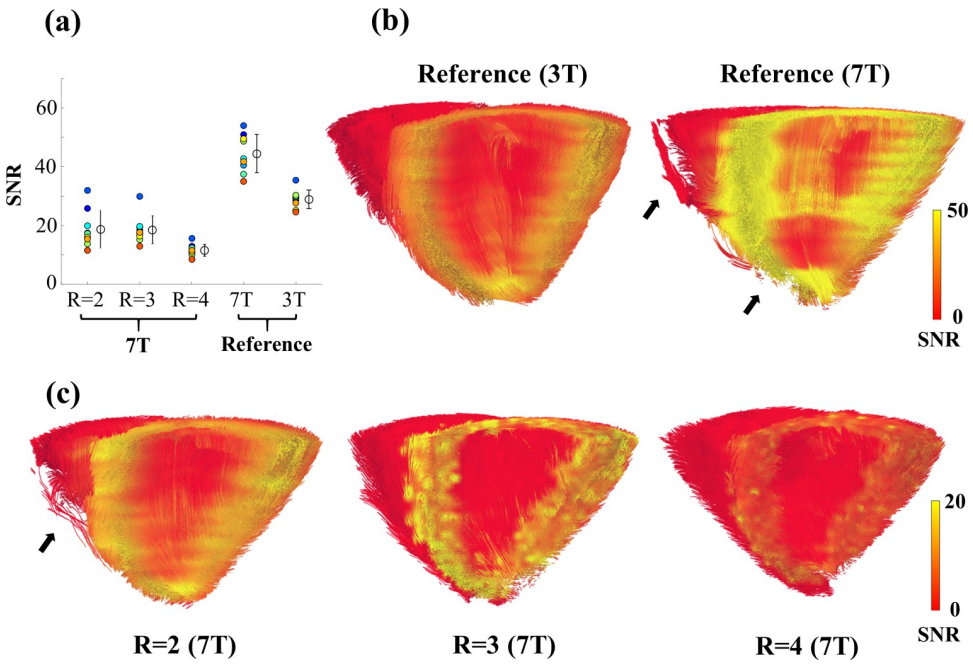

Fig 8. Calculated SNR in the 3T reference, the 7T reference and GRAPPA accelerated scans at 7 T. (a) Shown are average SNR (normalized) values of the hearts measured at 7 T, the reference hearts measured at 3 T and their mean ± single standard deviation. (b) A tractography excerpt of the left and right ventricle from the same heart is displayed for 30 slices of the 3T reference and the 7T reference. Mapped to reconstructed fibers are the measured SNR values. (c) Tractography volumes identical to the 7T reference in (b) are shown for GRAPPA accelerated scans and resulting SNR. Areas of incomplete or diffuse fiber reconstructions are indicated by a black arrow. SNR values were only calculated for myocardial contours of the left ventricle, setting voxels within the right ventricle and papillary muscle to 0. Threshold for tractography was set to a FA value 0.1 for all visualizations.

https://doi.org/10.1371/journal.pone.0213994.g008

et al. [16] demonstrating that noise leads to a loss of both precision and accuracy in derived |E2A| values.

Acceleration of image acquisition using parallel imaging at 7 T is a trade-off between susceptibility effects for long echo trains at low acceleration, SNR loss as acceleration penalty, and an SNR gain for shortened EPI readouts due to lower T_2^* induced losses. Undersampling-effects on the k-space filter, and thus point spread function, were outside the scope of this work and are most likely masked by the applied denoising algorithm. For the tested conditions, we found that GRAPPA acceleration factor R = 3 was optimal for several derived DT-features. Taking the number of phase encoding steps into account, SNR comparison showed, that scans using R = 3 benefitted from the shorter EPI readout leading to an increase in relative SNR compared to R = 2. We observed a significant loss in SNR compared to the reference (R = 1) at 7 T when using R = 2, even when taking into account SNR penalty normalization. Most likely this is due to the relatively small size of the piglet heart in comparison to the size of the coil elements, which leads to an enhanced effect of the g-factor on noise amplification [47, 48] in GRAPPA reconstructed images. Additionally, as shown in [49], SNR decreases for high acceleration factors at ultra-high field strength due to fundamental electromagnetic factors, even considering optimal coil sensitivity profiles. For our setup this effect may already occur for the moderate acceleration factors used. A systematic evaluation of different coil combinations (sum of squares vs adaptive combine) and a comparison of GRAPPA versus SENSE acceleration may be subject of future studies.

The results also show that long echo times and readouts at 7 T lead to susceptibility effects, causing deformation of the reconstructed diffusion tensor. While ADC and FA values are changed significantly, main eigenvector orientation appears to be robust in the presence of susceptibility induced geometrical distortions. This is in agreement with observations made in our previous work [50], where susceptibility effects on the main eigenvector were analyzed at 3 T. It was demonstrated, that, while there are changes in the eigenvector components, the ratio between them stays similar, resulting in small orientation changes of the main eigenvector of diffusion. As shown in Fig 4B changes in the |E2A| are more pronounced, resulting in significant deviations, when compared to our 3T reference. The need for highly parallel imaging reported [22] for DTI in the brain at 7 T, holds true for ex vivo cDTI at 7 T as well.

Despite the observed advantages in SNR, the increased B_0 (7 T) also increases demands on the measurement setup and introduces additional limitations in comparison to lower field strengths ($\leq$3T). For fixed hearts and certain scan times proton-free and low electrical permittivity synthetic oils such as perfluorpolyether (e.g. Fomblin) can be used to minimize both B_0 and B_1 effects of the surrounding on image quality of myocardial tissue, without effecting T_1, T_2, and targeted histo-architecture [51]. While the effects of Fomblin on T_2 and T_2^* in unfixed tissue have been shown to be insignificant [52], diffusion metrics may still vary depending on the sample preparation. The use of Fomblin was therefore omitted in this study. Additional advantages may be gained using B_0 correction techniques, enabling imaging with lower acceleration factors, and thus maintaining higher SNR. However, in our experience, non-negligible second and third order shim terms are necessary to correct B_0 field inhomogeneity in the heart at 7 T. Established correction techniques might therefore show weaker performance at ultra-high fields. Achieving stable solutions of optimization-based distortion correction methods is additionally limited by the smaller organ size compared to the brain, which results in smaller numbers of available pixels to solve the minimization problem. Exploration of the limits of existing techniques might be subject of a future ex vivo study, but were outside the scope of this work.

|E2A| has been shown to depend on the heart phase and therefore the contraction state of the organ, which is why hearts are often forced into a set contraction state prior to fixation and following ex vivo analysis of laminar structure. The question whether tissue fixation, which is predominantly used at lower fields for ex vivo DTI, is reasonable for DTI of the porcine heart at 7 T, is still open, and may be subject to future studies. However the reduced T_2^* due to tissue fixation will further the need for higher parallel imaging factors. The contraction state of hearts in this study was not controlled. The evaluation of |E2A| was therefore exclusively to analyze reproducibility using varying acquisition protocols.

Optimization of different components of the measurement setup may lead to improved robustness and precision of high resolution scans with long acquisition time. For the high acceleration factors (R$\geq$3) required, it is beneficial to use a dedicated multi-channel array, e.g. a 64 element array as used in [53]. The heart should be placed in a dedicated spherical container filled with liquid (magnetic susceptibility and electric permittivity similar to tissue), in order to achieve optimal 3rd order shimming results and minimize SNR degradation due to inhomogeneous B_1. Prior to measurements the influence of such liquids on DTI metrics should be tested.

Additional advantages in diffusion imaging may be gained using pulse sequence optimization. Long echo times required for diffusion encoding reduce available SNR at 7 T and increase the influence of susceptibility effects. A stimulated echo approach may, despite the factor two disadvantage in SNR compared to the standard spin echo sequence, increase SNR in two ways: 1) Signal during the mixing time, where magnetization is stored in the longitudinal direction, decays with T_1 time, which is increased at 7 T. 2) The mixing time also contributes to diffusion

encoding and thus enables to shorten periods affected by T_2 relaxation, which is short at 7 T. Both factors become particularly pronounced in in vivo measurements where the mixing time is equal to the RR-interval.

While an increase in field strength can lead to increased SNR, it will also lead to changes in the distribution of field inhomogeneity introduced by locally varying orientations of fiber bundles within the heart. In addition to studies that leverage ultra-high field strengths for resolution [54], this has led to studies exploring high resolution T_2^* imaging [55, 56], quantitative susceptibility mapping, or even measurements of a susceptibility tensor [57] as alternative methods to diffusion imaging. While the feasibility of these methods has been demonstrated for beating, isolated hearts and fixed, ex vivo hearts, there have been no demonstrations in vivo. Macroscopic field inhomogeneity and variations of susceptibility due to changing blood oxygenation levels may limit a direct translation to in vivo applications. Additionally, in order to get sufficient orientation information for the reconstruction of a susceptibility tensor, the specimen needs to be rotated with respect to the magnetic field, which complicates a practical translation to in-vivo measurements.

We obtained DTI data of the fresh hearts at 7 T within 1–3 hours after euthanasia. The 3T MRI system is predominantly clinically used, which limited the time slots for acquisition of our reference data set to 5–10 hours after euthanasia. Usually, 3T and 7T scans should be performed in random order to minimize systematic errors. Considering our results that T_2^*, T_1, and diffusion metrics are constant over 12 hours, we believe that the time between scans and the missing randomization are no critical factors for the results.

Conclusions

In this study we demonstrate feasibility of whole heart, high resolution DTI acquisitions of the healthy, unfixed porcine heart at 7 T using commercial hardware. For the coil used, we conclude that a minimum of R = 3 will provide the best compromise between the effects of susceptibility induced distortions and SNR losses. We also conclude that a dedicated coil setup for ex vivo measurements of organs the size of a piglet heart is necessary to enable the use of acceleration factors $\geq$4.

Supporting information

S1 Fig. Temporal evolution of sample stability using measures of absolute T2*, T_1, FA, and ADC. Values are plotted relative to time point t = 0 over a period of 12 hours for two hearts (blue, red). The green area marks the time interval, were the diffusion measurements at 7T would take place.
(TIF)

S2 Fig. Representative reference and diffusion weighted images for the various acquisition protocols used. Diffusion weighted images #1–4 correspond to the first 4/30 gradient orientations according to Skare (31).
(TIF)

S1 Table. Information on study animals and corresponding estimates of left ventricle size and heart weight. Heart size and weight were not measured within this study. Shown values for the size are estimates of the size of the left ventricle based on the number of slices included in the AHA segmentation and the slice thickness during data acquisition. Values for the heart weight are estimates for the total heart weight based on the heart weight to body weight ratio of 5g/kg reported by Lelovas et al (29).
(DOCX)

Acknowledgments

We thank Sebastian Kress and Franziska Veit for the cooperation regarding the collection of the ex vivo hearts.

Data of this work will be used in the doctoral thesis of David Lohr.

Author Contributions

Conceptualization: David Lohr, Maxim Terekhov, Laura Maria Schreiber.

Data curation: David Lohr.

Formal analysis: David Lohr.

Funding acquisition: Laura Maria Schreiber.

Methodology: David Lohr, Anja Schroeder.

Project administration: David Lohr.

Resources: Anja Schroeder, Heike Walles.

Software: David Lohr, Maxim Terekhov.

Supervision: Maxim Terekhov, Andreas Max Weng, Heike Walles, Laura Maria Schreiber.

Validation: David Lohr.

Visualization: David Lohr.

Writing – original draft: David Lohr.

Writing – review & editing: David Lohr, Maxim Terekhov, Andreas Max Weng, Anja Schroeder, Laura Maria Schreiber.

References

1. Waldman LK, Nosan D, Villarreal F, Covell JW. Relation between transmural deformation and local myofiber direction in canine left ventricle. Circ Res. 1988;63. https://doi.org/10.1161/01.res.63.3.550
2. Kanai A, Salama G. Optical Mapping Reveals That Repolarization Spreads Anisotropically and Is Guided by Fiber Orientation in Guinea Pig Hearts. Circulation Research. 1995; 77(4):784–802. https://doi.org/10.1161/01.res.77.4.784 PMID: 7554126
3. Streeter DD, Spotnitz HM, Patel DP, Ross J, Sonnenblick EH. Fiber orientation in the canine left ventricle during diastole and systole. Circ Res. 1969;24. https://doi.org/10.1161/01.res.24.3.339
4. Greenbaum RA, Ho SY, GIbson DG, Becker AE, Anderson RH. Left ventricular fibre architecture in man. Br Heart J. 1981;45. https://doi.org/10.1136/hrt.45.3.248
5. Scollan DF, Holmes A, Winslow R, Forder J. Histological validation of myocardial microstructure obtained from diffusion tensor magnetic resonance imaging. American Journal of Physiology—Heart and Circulatory Physiology. 1998; 275(6):H2308–H18.
6. Schmid P, Jaermann T, Boesiger P, Niederer PF, Lunkenheimer PP, Cryer CW, et al. Ventricular myocardial architecture as visualised in postmortem swine hearts using magnetic resonance diffusion tensor imaging. European Journal of Cardio-Thoracic Surgery. 2005; 27(3):468–72. https://doi.org/10.1016/j.ejcts.2004.11.036 PMID: 15740957
7. LeGrice IJ, Smaill BH, Chai LZ, Edgar SG, Gavin JB, Hunter PJ. Laminar structure of the heart: ventricular myocyte arrangement and connective tissue architecture in the dog. Am J Physiol. 1995;269.
8. Helm PA, Tseng HJ, Younes L, McVeigh ER, Winslow RL. Ex vivo 3D diffusion tensor imaging and quantification of cardiac laminar structure. Magnetic resonance in medicine. 2005;54. https://doi.org/10.1002/mrm.20622 PMID: 16149057
9. Kung GL, Nguyen TC, Itoh A, Skare S, Ingels NB, Miller DC. The presence of two local myocardial sheet populations confirmed by diffusion tensor MRI and histological validation. Journal of magnetic resonance imaging: JMRI. 2011; 34. https://doi.org/10.1002/jmri.22725 PMID: 21932362

10. Tseng W-YI, Reese TG, Weisskoff RM, Wedeen VJ. Cardiac diffusion tensor MRI in vivo without strain correction. Magnetic resonance in medicine. 1999; 42(2):393–403. https://doi.org/10.1002/(SICI)1522-2594(199908)42:2<393::AID-MRM22>3.0.CO;2-F PMID: 10440965

11. Dou J, Reese TG, Tseng WY, Wedeen VJ. Cardiac diffusion MRI without motion effects. Magnetic resonance in medicine. 2002; 48(1):105–14. https://doi.org/10.1002/mrm.10188 PMID: 12111937.

12. Gamper U, Boesiger P, Kozerke S. Diffusion imaging of the in vivo heart using spin echoes–considerations on bulk motion sensitivity. Magnetic resonance in medicine. 2007; 57(2):331–7. https://doi.org/10.1002/mrm.21127 PMID: 17260376

13. Nielles-Vallespin S, Mekkaoui C, Gatehouse PD, Reese TG, Keegan J, Ferreira PF, et al. In vivo diffusion tensor MRI of the human heart: reproducibility of breath-hold and navigator-based approaches. Magnetic resonance in medicine. 2013; 70(2):454–65. https://doi.org/10.1002/mrm.24488 PMID: 23001828; PubMed Central PMCID: PMC3864770.

14. Bastin ME, Armitage PA, Marshall I. A theoretical study of the effect of experimental noise on the measurement of anisotropy in diffusion imaging. Magnetic resonance imaging. 1998; 16(7):773–85. Epub 1998/11/12. PMID: 9811143.

15. Landman BA, Farrell JA, Huang H, Prince JL, Mori S. Diffusion tensor imaging at low SNR: nonmonotonic behaviors of tensor contrasts. Magnetic resonance imaging. 2008; 26(6):790–800. Epub 2008/05/24. https://doi.org/10.1016/j.mri.2008.01.034 PMID: 18499378; PubMed Central PMCID: PMCPMC2583784.

16. Scott AD, Nielles-Vallespin S, Ferreira PF, McGill L-A, Pennell DJ, Firmin DN. The effects of noise in cardiac diffusion tensor imaging and the benefits of averaging complex data. NMR in biomedicine. 2016; 29(5):588–99. https://doi.org/10.1002/nbm.3500 PMID: 26891219

17. McClymont D, Teh I, Schneider JE. The impact of signal-to-noise ratio, diffusion-weighted directions and image resolution in cardiac diffusion tensor imaging–insights from the ex-vivo rat heart. Journal of Cardiovascular Magnetic Resonance. 2017; 19(1):90. https://doi.org/10.1186/s12968-017-0395-x PMID: 29157268

18. Hsu EW, Muzikant AL, Matulevicius SA, Penland RC, Henriquez CS. Magnetic resonance myocardial fiber-orientation mapping with direct histological correlation. American Journal of Physiology—Heart and Circulatory Physiology. 1998; 274(5):H1627–H34.

19. Tseng WY, Wedeen VJ, Reese TG, Smith RN, Halpern EF. Diffusion tensor MRI of myocardial fibers and sheets: correspondence with visible cut-face texture. Journal of magnetic resonance imaging: JMRI. 2003;17. https://doi.org/10.1002/jmri.10223 PMID: 12500272

20. Helm P, Beg MF, Miller MI, Winslow RL. Measuring and mapping cardiac fiber and laminar architecture using diffusion tensor MR imaging. Ann N Y Acad Sci. 2005; 1047. https://doi.org/10.1196/annals.1341.026 PMID: 16093505

21. Wu EX, Wu Y, Nicholls JM, Wang J, Liao S, Zhu S, et al. MR diffusion tensor imaging study of postinfarct myocardium structural remodeling in a porcine model. Magnetic resonance in medicine. 2007; 58 (4):687–95. https://doi.org/10.1002/mrm.21350 PMID: 17899595

22. Choi S, Cunningham DT, Aguila F, Corrigan JD, Bogner J, Mysiw WJ, et al. DTI at 7 and 3 T: systematic comparison of SNR and its influence on quantitative metrics. Magnetic resonance imaging. 2011; 29 (6):739–51. https://doi.org/10.1016/j.mri.2011.02.009 PMID: 21571473

23. Vu AT, Auerbach E, Lenglet C, Moeller S, Sotiropoulos SN, Jbabdi S, et al. High resolution whole brain diffusion imaging at 7 T for the Human Connectome Project. NeuroImage. 2015; 122:318–31. https://doi.org/10.1016/j.neuroimage.2015.08.004 PMC4618066. PMID: 26260428

24. McGill LA, Ismail TF, Nielles-Vallespin S, Ferreira PF, Scott AD, Roughton M, et al. Reproducibility of in-vivo diffusion tensor cardiovascualar magnetic resonance in hypertrophic cardiomyopathy. Journal of cardiovascular magnetic resonance: official journal of the Society for Cardiovascular Magnetic Resonance. 2012;14.

25. Scott AD, Ferreira PF, Nielles-Vallespin S, Gatehouse P, McGill LA, Kilner P, et al. Optimal diffusion weighting for in vivo cardiac diffusion tensor imaging. Magnetic resonance in medicine. 2015; 74 (2):420–30. Epub 2014/08/27. https://doi.org/10.1002/mrm.25418 PMID: 25154715.

26. von Deuster C, Stoeck CT, Genet M, Atkinson D, Kozerke S. Spin echo versus stimulated echo diffusion tensor imaging of the in vivo human heart. Magnetic resonance in medicine. 2016; 76(3):862–72. https://doi.org/10.1002/mrm.25998 PMID: 26445426

27. Mekkaoui C, Reese TG, Jackowski MP, Cauley SF, Setsompop K, Bhat H, et al. Diffusion Tractography of the Entire Left Ventricle by Using Free-breathing Accelerated Simultaneous Multisection Imaging. Radiology. 2017; 282(3):850–6. https://doi.org/10.1148/radiol.2016152613 PMID: 27681278.

28. Nielles-Vallespin S, Khalique Z, Ferreira PF, de Silva R, Scott AD, Kilner P, et al. Assessment of Myocardial Microstructural Dynamics by In Vivo Diffusion Tensor Cardiac Magnetic Resonance. Journal of

the American College of Cardiology. 2017; 69(6):661–76. https://doi.org/10.1016/j.jacc.2016.11.051 PMID: 28183509

29. Lelovas PP, Kostomitsopoulos NG, Xanthos TT. A comparative anatomic and physiologic overview of the porcine heart. Journal of the American Association for Laboratory Animal Science: JAALAS. 2014; 53(5):432–8. Epub 09/. PMID: 25255064.

30. Deoni SC, Rutt BK, Peters TM. Rapid combined T1 and T2 mapping using gradient recalled acquisition in the steady state. Magnetic resonance in medicine. 2003; 49(3):515–26. Epub 2003/02/21. https://doi.org/10.1002/mrm.10407 PMID: 12594755.

31. Skare S, Hedehus M, Moseley ME, Li T-Q. Condition Number as a Measure of Noise Performance of Diffusion Tensor Data Acquisition Schemes with MRI. Journal of magnetic resonance. 2000; 147 (2):340–52. https://doi.org/10.1006/jmre.2000.2209 PMID: 11097823

32. Lohr D, Terekhov M, Weng AM, Schroeder A, Walles H, Schreiber LM. High Resolution Cardiac DTI—Fiber Tractography Statistics of the ex Vivo pig Heart. In Proceedings of the 25th Annual Meeting of ISMRM, Honolulu, Hawaii, USA, 2017 p 1841.

33. Yeh F-C, Verstynen TD, Wang Y, Fernández-Miranda JC, Tseng W-YI. Deterministic Diffusion Fiber Tracking Improved by Quantitative Anisotropy. PloS one. 2013; 8(11):e80713. https://doi.org/10.1371/journal.pone.0080713 PMID: 24348913

34. Yeh F-C. DSI Studio. http://dsi-studio.labsolver.org. Accessed April 22, 2016.

35. Jiang H, van Zijl PC, Kim J, Pearlson GD, Mori S. DtiStudio: resource program for diffusion tensor computation and fiber bundle tracking. Computer methods and programs in biomedicine. 2006; 81(2):106–16. Epub 2006/01/18. https://doi.org/10.1016/j.cmpb.2005.08.004 PMID: 16413083.

36. Manjon JV, Coupe P, Concha L, Buades A, Collins DL, Robles M. Diffusion Weighted Image Denoising Using Overcomplete Local PCA. PloS one. 2013; 8(9). https://doi.org/10.1371/journal.pone.0073021.g001 10.1371/journal.pone.0073021.g002.

37. Cerqueira MD, Weissman NJ, Dilsizian V, Jacobs AK, Kaul S, Laskey WK. Standardized myocardial segmentation and nomenclature for tomographic imaging of the heart. A statement for healthcare professionals from the cardiac imaging committee of the council on clinical cardiology of the american heart association. Circulation. 2002; 105. https://doi.org/10.1161/hc0402.102975

38. Ferreira PF, Kilner PJ, McGill LA, Nielles-Vallespin S, Scott AD, Ho SY, et al. In vivo cardiovascular magnetic resonance diffusion tensor imaging shows evidence of abnormal myocardial laminar orientations and mobility in hypertrophic cardiomyopathy. Journal of cardiovascular magnetic resonance: official journal of the Society for Cardiovascular Magnetic Resonance. 2014; 16:87. Epub 2014/11/13. https://doi.org/10.1186/s12968-014-0087-8 PMID: 25388867; PubMed Central PMCID: PMCPMC4229618.

39. Ennis DB, Kindlman G, Rodriguez I, Helm PA, McVeigh ER. Visualization of Tensor Fields Using Superquadric Glyphs. Magnetic resonance in medicine. 2005; 53(1):169–76. https://doi.org/10.1002/mrm.20318 PMID: 15690516

40. Reeder SB, Wintersperger BJ, Dietrich O, Lanz T, Greiser A, Reiser MF, et al. Practical approaches to the evaluation of signal-to-noise ratio performance with parallel imaging: Application with cardiac imaging and a 32-channel cardiac coil. Magnetic resonance in medicine. 2005; 54(3):748–54. https://doi.org/10.1002/mrm.20636 PMID: 16088885

41. Juchem C, Rudrapatna SU, Nixon TW, de Graaf RA. Dynamic Multi-Coil Technique (DYNAMITE) Shimming for Echo-Planar Imaging of the Human Brain at 7 Tesla. NeuroImage. 2015; 105:462–72. https://doi.org/10.1016/j.neuroimage.2014.11.011 PMC4262558. PMID: 25462795

42. Scott AD, Ferreira PFADC, Nielles-Vallespin S, Gatehouse P, McGill L-A, Kilner P, et al. Optimal diffusion weighting for in vivo cardiac diffusion tensor imaging. Magnetic resonance in medicine. 2015; 74 (2):420–30. https://doi.org/10.1002/mrm.25418 PMID: 25154715

43. Pashakhanloo F, Herzka DA, Mori S, Zviman M, Halperin H, Gai N, et al. Submillimeter diffusion tensor imaging and late gadolinium enhancement cardiovascular magnetic resonance of chronic myocardial infarction. Journal of cardiovascular magnetic resonance: official journal of the Society for Cardiovascular Magnetic Resonance. 2017; 19(1):9. Epub 2017/01/27. https://doi.org/10.1186/s12968-016-0317-3 PMID: 28122618; PubMed Central PMCID: PMCPMC5264305.

44. Mazumder R, Choi S, Clymer BD, White RD, Kolipaka A. Diffusion Tensor Imaging of Healthy and Infarcted Porcine Hearts: Study on the Impact of Formalin Fixation. Journal of medical imaging and radiation sciences. 2016; 47(1):74–85. https://doi.org/10.1016/j.jmir.2015.10.007 PMID: 26989451.

45. Watson BR, Hsu EW. Effects of Formalin Fixation on Diffusion Tensor Imaging of Myocardial Tissues. In Proceedings of the 20th Annual Meeting of ISMRM, Melborune, Victoria, Australia, 2012 p 1114.

46. Gahm JK, Kindlmann G, Ennis DB. The effects of noise over the complete space of diffusion tensor shape. Medical Image Analysis. 2014; 18(1):197–210. https://doi.org/10.1016/j.media.2013.10.009 PMID: 24239734

47. Robson PM, Grant AK, Madhuranthakam AJ, Lattanzi R, Sodickson DK, McKenzie CA. Comprehensive quantification of signal-to-noise ratio and g-factor for image-based and k-space-based parallel imaging reconstructions. Magnetic resonance in medicine. 2008; 60(4):895–907. Epub 2008/09/26. https://doi.org/10.1002/mrm.21728 PMID: 18816810; PubMed Central PMCID: PMCPMC2838249.

48. Breuer FA, Kannengiesser SAR, Blaimer M, Seiberlich N, Jakob PM, Griswold MA. General formulation for quantitative G-factor calculation in GRAPPA reconstructions. Magnetic resonance in medicine. 2009; 62(3):739–46. https://doi.org/10.1002/mrm.22066 PMID: 19585608

49. Ohliger MA, Grant AK, Sodickson DK. Ultimate intrinsic signal-to-noise ratio for parallel MRI: electromagnetic field considerations. Magnetic resonance in medicine. 2003; 50(5):1018–30. Epub 2003/10/31. https://doi.org/10.1002/mrm.10597 PMID: 14587013.

50. Terekhov M, Lohr D, Schreiber LM. Myocardium tissue DTI with stimulated echo at large susceptibility induced B0 gradients: examination of the shimming strategies efficiency and errors. In Proceedings of the 25th Annual Meeting of ISMRM, Honolulu, Hawaii, USA, 2017 p 1841.

51. Hales PW, Burton RAB, Bollensdorff C, Mason F, Bishop M, Gavaghan D, et al. Progressive changes in T1, T2 and left-ventricular histo-architecture in the fixed and embedded rat heart. NMR in biomedicine. 2011; 24(7):836–43. https://doi.org/10.1002/nbm.1629 PMID: 21834007

52. Chang EY, Du J, Bae WC, Statum S, Chung CB. Effects of achilles tendon immersion in saline and perfluorochemicals on T2 and T2*. Journal of Magnetic Resonance Imaging. 2014; 40(2):496–500. https://doi.org/10.1002/jmri.24360 PMID: 24155129

53. Schuppert M, Kreitner K-F, Fischer S, Wein S, Keil B, Wald LL, et al. Determination of the optimal number of coil elements: A semi-theoretical approach In Proceedings of the 23rd Annual Meeting of ISMRM, Toronto, Ontario, Canada, 2015 p 1779.

54. Köhler S, Hiller K-H, Griswold M, Bauer WR, Haase A, Jakob PM. NMR-microscopy with TrueFISP at 11.75T. Journal of magnetic resonance. 2003; 161(2):252–7. https://doi.org/10.1016/S1090-7807(03)00013-2. PMID: 12713977

55. Köhler S, Hiller K-H, Waller C, Jakob PM, Bauer WR, Haase A. Visualization of myocardial microstructure using high-resolution T imaging at high magnetic field. Magnetic resonance in medicine. 2003; 49(2):371–5. https://doi.org/10.1002/mrm.10346 PMID: 12541258

56. Köhler S, Hiller K-H, Waller C, Bauer WR, Haase A, Jakob PM. Investigation of the microstructure of the isolated rat heart: A comparison between T*2- and diffusion-weighted MRI. Magnetic resonance in medicine. 2003; 50(6):1144–50. https://doi.org/10.1002/mrm.10636 PMID: 14648562

57. Dibb R, Liu C. Joint eigenvector estimation from mutually anisotropic tensors improves susceptibility tensor imaging of the brain, kidney, and heart. Magnetic resonance in medicine. 2017; 77(6):2331–46. https://doi.org/10.1002/mrm.26321 PMID: 27385561

3.2 Longitudinal assessment of tissue properties and cardiac diffusion metrics of the ex vivo porcine heart at 7 T: Impact of continuous tissue fixation using formalin

〉 Published in *NMR in Biomedicine* – 2020[122]

These citations have been applied in this publication.[38,41-43,45,49,53-56,68,69,76,98,101,102,105,106,111,120,123-148]

Due to limited scan time, cardiac and breathing motion as well as intrinsically low SNR lead to low spatial and angular resolution in *in vivo* DTI scans. *Ex vivo* measurements in controlled environments, that enable long scan times and the acquisition of high resolution and high-fidelity data thus remain an important research tool. Tissue fixation, often achieved using formalin, is applied to prevent autolytic effects after the organ harvest, preserving physiological diffusion properties and tissue microstructure for these long measurements. While continuous formalin fixation has been shown to shorten T_1 and T_2 relaxation times and significantly decrease diffusivity in the brain, there is a lack of such data for the heart.

Primarily we aimed to assess the impact of formalin immersion fixation on diffusion metrics of the *ex vivo* porcine heart at 7T. As a secondary aim of this study we evaluated changes in T_2 and T_2* and their impact on SNR in diffusion MRI at ultrahigh field strength.

MRI was performed on a 7T system for n=8 excised porcine hearts. The protocol included SNR (diffusion), relaxometry (T_2 and T_2*), and diffusion (spin echo and a custom written stimulated echo sequence) measurements. Scans were performed within 3 hours of excision and 7, 15, 50, 100, and 200 days post immersion fixation using formalin.

In the first 7 days post fixation average T_2 and T_2* dropped from 49.3 ms to 32.1 ms and 25.1 ms to 19.8 ms. Over 200 days T_2* values gradually recovered (Δ5%) and T_2 values remained lowered (Δ26%). SNR in b_0 images followed a similar trend, initially dropping 32% and 19% in spin echo and stimulated echo data and recovering to Δ20% and Δ 10%, respectively. ADC and FA values 7 and 200 days post fixation were 78% and 92% as well as 90% and 80% relative to fresh hearts. Average standard deviations over time in mean helix angle and sheetlet angle values were small 3.4° and 6.5° and no systematic alterations post tissue fixation were found.

In this study we demonstrate that continuous immersion fixation using formalin significantly alters T_2, T_2*, ADC and FA. In addition to tissue fixation durations, storage and sample preparation need to be considered when interpreting the impact of diseases. The longitudinal setup of this study facilitates proper placement of previously published diffusion metrics with respect to disease induced alterations. Anisotropy and overall microstructure are preserved, even after long periods of immersion, enabling studies on ventricular remodeling of cardiac microstructure in various cardiac pathologies.

Received: 20 November 2019 | Revised: 18 February 2020 | Accepted: 5 March 2020

DOI: 10.1002/nbm.4298

RESEARCH ARTICLE

NMR IN BIOMEDICINE WILEY

Longitudinal assessment of tissue properties and cardiac diffusion metrics of the ex vivo porcine heart at 7 T: Impact of continuous tissue fixation using formalin

David Lohr[1] | Maxim Terekhov[1] | Franziska Veit[2] | Laura Maria Schreiber[1]

[1]Cellular and Molecular Imaging, Comprehensive Heart Failure Center (CHFC), University Hospital Wuerzburg, Wuerzburg, Germany

[2]Tissue Engineering and Regenerative Medicine (TERM), University Hospital Wuerzburg, Wuerzburg, Germany

Correspondence
David Lohr, Chair of Cellular and Molecular Imaging, Comprehensive Heart Failure Center (CHFC), University Hospital Wuerzburg, Am Schwarzenberg 15, 97078, Wuerzburg, Germany.
Email: e_lohr_d@ukw.de

Funding information
Federal Ministry of Education and Research, Grant/Award Number: 01EO1504

In this study we aimed to assess the effects of continuous formalin fixation on diffusion and relaxation metrics of the ex vivo porcine heart at 7 T. Magnetic resonance imaging was performed on eight piglet hearts using a 7 T whole body system. Hearts were measured fresh within 3 hours of cardiac arrest followed by immersion in 10% neutral buffered formalin. T_2^* and T_2 were assessed using a gradient multi-echo and multi-echo spin echo sequence, respectively. A spin echo and a custom stimulated echo sequence were employed to assess diffusion time-dependent changes in metrics of cardiac diffusion tensor imaging. SNR was determined for b = 0 images. Scans were performed for 5 mm thick apical, midcavity and basal slices (in-plane resolution: 1 mm) and repeated 7, 15, 50, 100 and 200 days postfixation. Eigenvalues of the apparent diffusion coefficient (ADC) and fractional anisotropy (FA) decreased significantly ($P < 0.05$) following fixation. Relative to fresh hearts, FA values 7 and 200 days postfixation were 90% and 80%, while respective relative ADC values at those fixation stages were 78% and 92%. Statistical helix and sheetlet angle distributions as well as respective mean and median values showed no systematic influence of continuous formalin fixation. Similar to changes in the ADC, values for T_2, T_2^* and SNR dropped initially postfixation. Respective relative values compared with fresh hearts at day 7 were 64%, 79% and 68%, whereas continuous fixation restored T_2, T_2^* and SNR leading to relative values of 74%, 100%, and 81% at day 200, respectively. Relaxation parameters and diffusion metrics are significantly altered by continuous formalin fixation. The preservation of microstructure metrics following prolonged fixation is a key finding that may enable future studies of ventricular remodeling in cardiac pathologies.

KEYWORDS
cardiovascular MR methods, diffusion tensor imaging, heart structure, relaxometry

Abbreviations used: |E2A|, absolute sheetlet angle; ADC, apparent diffusion coefficient; cDTI, cardiac diffusion tensor imaging; DTI, diffusion tensor imaging; E2A, secondary eigenvector angle, sheetlet angle; FA, fractional anisotropy; HA, primary eigenvector angle, helix angle; LV, left ventricle; ROI, region of interest; SE, spin echo; SNR, signal-to-noise ratio; STE, stimulated echo; λ_1, primary eigenvalue; λ_2, secondary eigenvalue; λ_3, tertiary eigenvalue.

1 | INTRODUCTION

Cardiac diffusion tensor imaging (cDTI) has become an emerging application in the characterization of cardiac tissue and its functional and structural integrity. It has since been applied in a variety of cardiovascular pathologies, such as hypertrophic[1–3] and dilative cardiomyopathy[3,4] as well as myocardial infarction.[5] In recent years the number of in vivo studies in humans[6–8] and animals[3,9] has increased. But, due to cardiac motion, breath holds, intrinsically low SNR,[10–12] and limited scan times, spatial and angular resolution as well as spatial coverage remain low. Many cardiac studies using DTI have therefore been performed on ex vivo specimens. Usually rapid chemical fixation is applied to prevent autolytic effects after the organ harvest,[13,14] preserving physiological diffusion properties and tissue microstructure as best as possible. This tissue fixation, often performed using formalin, enables long scan times and, thus, ex vivo measurements remain an important scientific tool which provides high resolution and high fidelity, ground truth data. Historically, such data allowed validation of DTI against histology,[9,15–17] proof of concept studies,[18–20] as well as validation of in vivo results.[3,21] Furthermore, cardiac tissue samples can often be gained as a byproduct of other scientific or biomedical studies. The site of cardiac experimentation and fixation, and the site for subsequent DTI measurement may be separated by hundreds of miles.[19] Thus, tissue specimens may be shipped before the MR measurements.

In order to allow an accurate comparison between in vivo and ex vivo measurements it is paramount to assess fixation-induced changes of tissue properties. While there are studies analyzing the impact of tissue fixation on diffusion metrics of the heart,[18,20,22] methodology in studies throughout the years remained highly heterogeneous with regard to the procedure of fixation, storage times and temperature, the fixative itself, and the overall fixation duration.

There is a lack of data on variations of cardiac MRI and DTI parameters following excision of the heart combined with subsequent formalin fixation. For brain tissue, studies have shown that continuous formalin fixation shortens T_1 and T_2 relaxation times compared with the in vivo values[23–29] and that diffusivity is significantly decreased following fixation.[13,30,31]

In a study comparing different fixation methods on the porcine heart, Agger et al[18] concluded that immersion fixation using formalin yielded the diffusion profile most similar to that of "fresh" tissue. In addition, they state that the process of perfusion fixation, in dependence of the perfusion pressure, may possibly inflict tissue damage, resulting in changes of both mean diffusivity and components of the diffusion tensor.

Therefore, the main aim of this study was to assess the impact of formalin immersion fixation on diffusion metrics of the ex vivo porcine heart at 7 T. Diffusion properties for various fixation durations are assessed in dependence of the diffusion time using a stimulated echo diffusion sequence. The secondary aim of this study was to assess fixation-induced alterations in T_2 and T_2^* at ultrahigh field strength and their impact on SNR in diffusion MRI. Results of this study will benefit future ex vivo diffusion experiments regarding fixation, measurement and sequence protocols. In addition, changes in diffusion metrics in dependence of the fixation duration will ease comparison of existing and upcoming studies.

2 | METHODS

2.1 | Porcine heart samples

Hearts (n = 8) were kindly provided by the Translational Center for Regenerative Therapies Wuerzburg, following the animals approved use (55.2 2532–2-256, District Government of Lower Franconia, Germany) in another study. All experiments were performed according to the German Animal Welfare Act and the EU Directive 2010/63/EU. Euthanasia was achieved as described in[32] and hearts were collected, rinsed and stored in physiological saline solution. The eight hearts were harvested in four experiments, where two hearts each were excised with ~20 minutes temporal difference. All samples in this study were harvested from male German Landrace piglets, which were obtained from the same breeder. Body weights ranged from 20-22 kg. Details regarding age and body weight are shown in Table S1.

3 | SAMPLE PREPARATION

Prior to MR measurements and subsequent tissue fixation, both atria were removed, easing the release of air trapped in the ventricles. Sample transport and preparation required ~45–60 minutes before measurement of the first heart (set of two). We always started with MRI measurements of the heart that was excised second, in order to minimize the time differences from excision to measurement between hearts within one set. Hearts were centered in a plastic container filled with physiological saline solution and the sample position was fixed using surgical threads. Directly after the initial MR measurement of the fresh heart, each heart was fixed via immersion in 10% phosphate buffered formalin solution. Before MR measurements of fixed specimens, hearts were briefly (~3-5 minutes) rinsed to remove excess formalin. Throughout the study, hearts were stored immersed in formalin in the scanner operating room. This room is temperature-controlled, allowing storage at a consistent 21 ± 1°C.

3.1 | MRI measurements

3.1.1 | General experimental setup

MRI was performed at bore temperature on a 7 T whole body MRI system (Siemens MAGNETOM Terra, Erlangen, Germany) using a 1/32 Tx/Rx head coil (Nova Medical). Data for the two hearts were acquired in consecutive measurements. Figure 1 shows an illustration of the whole study protocol. Initial measurements on the day of excision were performed on fresh hearts.

For MRI measurements, three short axis slices were positioned in relation to the valves in order to reproduce the slice position in subsequent measurements. The distance between 5 mm slices was set to 15 mm, resulting in single basal, midcavity and apical slices. All scans were performed with an in-plane resolution of 1 mm. Prior to measurements we applied third-order B_0-shimming using the scanner-integrated 3D-shimming algorithm covering the whole three-slice volume. The scan protocol consisted of relaxometry (T_2, T_2^*), diffusion (SE and STE) and SNR (diffusion) measurements. An overview of all sequence parameters is displayed in Table S3. Total acquisition time for the protocol was 63 minutes. Scans for both hearts were therefore completed within 3 hours after excision. Data was postprocessed using MATLAB (MathWorks, Natick, MA) and DSI Studio.[33] Measurements were repeated 7, 15, 50, 100 and 200 days after immersion.

3.1.2 | SNR

In order to evaluate peak SNR in diffusion measurements for the parameters used, we acquired 30 b = 0 images with the spin-echo sequence as well as the stimulated echo sequence (t_{Mix} = 100 ms) for the basal, midcavity and apical slice. Due to a longer diffusion time, the applied spoiler gradients amount to a diffusion weighting of b~18 s/mm^2 in the stimulated echo sequence. Other sequence parameters are described in more detail in the diffusion section below.

3.1.3 | Relaxometry

T_2^* was evaluated based on a 2D multi-gradient-echo sequence with the following imaging parameters, field of view (FOV): 131 mm × 176 mm, number of averages: 8, FA: 30°, bandwidth: 1095 Hz/pixel, TR: 150 ms. Nine echoes per excitation were acquired with TE values distributed between 2.07 and 18.0 ms.

Measurements for T_2 evaluation were performed using a multi-spin-echo spin echo sequence acquiring four averages with bandwidth: 465 Hz/pixel and TR: 2000 ms. Thirty-two images with TE values, distributed equally between 7.5 and 240 ms, were measured. The FOV remained identical with the respective T_2^* acquisition.

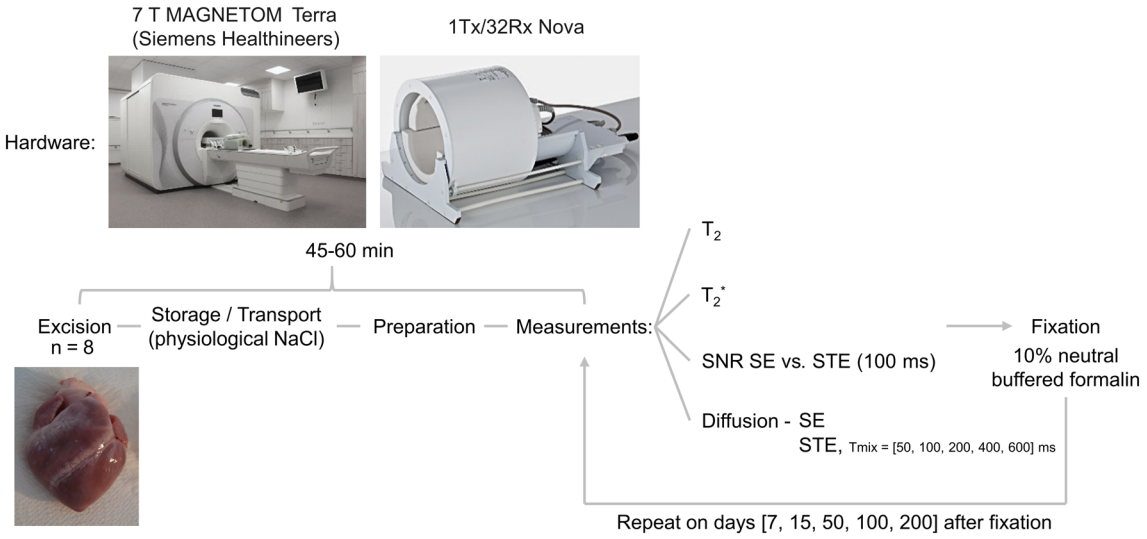

FIGURE 1 Study protocol for the assessment of changes in tissue properties and diffusion metrics in the ex vivo porcine heart due to continuous formalin fixation

3.1.4 | Diffusion

Diffusion data were acquired using a Stejskal-Tanner spin-echo sequence and an in-house written stimulated echo pulse sequence. Both pulse sequences used a monopolar diffusion preparation, EPI readout and a GRAPPA acceleration factor of R = 3. In order to minimize TE we used a bandwidth of 2442 Hz/pixel, leading to a bigger FOV. Further measurement parameters were: TR: 3500 ms, FOV: 208 mm x 256 mm, bandwidth: 2440 Hz/pixel, vendor-supplied diffusion directions (b = 1000 s/mm^2): 6 (averages: 12), reference images (b = 150 s/mm^2): 6 (averages: 12). In order to gain additional information about changes in diffusivity and microstructure, we used varying mixing times (t_{Mix} = 50, 100, 200, 400 and 600 ms) in the stimulated echo sequence, probing diffusion metrics in dependence of the diffusion time. Prolonging the diffusion time allowed shortening of the diffusion gradients, which resulted in shorter echo times. TE for the spin-echo sequence was 44 ms, while TEs for the stimulated echo sequences (t_{Mix}) were 37, 36, 35, 32 and 32 ms.

3.2 | Data processing

All postprocessing was based on DICOM-images created using the vendor's reconstruction pipeline and MATLAB, if not indicated otherwise.

3.2.1 | SNR

Myocardial contours of the left ventricle (LV) were manually segmented and SNR calculated according to the multiple acquisition method.[34] The 30 images were evaluated as a "pseudo" time-dependent dataset, where SNR can be calculated for each voxel (r) using the mean ($\bar{x}$) and standard deviation (σ) over time (t):

$$SNR(r) = \frac{\bar{x}_t(r)}{\sigma_t(r)} \tag{1}$$

The resulting values were averaged for the previously created LV ROI.

In addition, we assessed background noise and SNR in the saline solution as a reference, ensuring coil functionality. As described by Reeder et al[34] noise, assessed in a signal-free area, was corrected for Rayleigh distribution.

3.2.2 | Relaxometry

T_2^* and T_2 maps were reconstructed on a pixel basis using an in-house developed MATLAB script. Here a mono-exponential model fit:

$$S(TE) = S_0 e^{\left(-TE/T_2^*\right)} \tag{2}$$

with the free parameters (T_2^* and S_0) was applied to a preliminary normalized data vector S (TE). T_2 decay was fit the same way. Margins for the fitting parameters of the nonlinear solver were set to 1-50 ms for T_2^* and 1-80 ms for T_2. Providing manually segmented epicardial contours accelerated the fitting process.

3.2.3 | Diffusion

Motion correction was applied in order to correct for eddy current-induced geometrical distortions and DSI Studio[33] was used for reconstruction of the diffusion tensor as described by Jiang et al.[35] All the following processing steps were performed using MATLAB. Eigenvalues (λ_1, λ_2, λ_3), fractional anisotropy (FA) and the apparent diffusion coefficient (ADC) were derived from the diffusion tensor using eigenvalue analysis and the following two equations:

$$FA = \frac{\sqrt{3}}{\sqrt{2}} \frac{\sqrt{(\lambda_1 - \lambda)^2 + (\lambda_2 - \lambda)^2 + (\lambda_3 - \lambda)^2}}{\sqrt{\lambda_1^2 + \lambda_2^2 + \lambda_3^2}} \tag{3}$$

$$ADC = \frac{\lambda_1 + \lambda_2 + \lambda_3}{3} \tag{4}$$

where λ corresponds to the mean eigenvalue of the diffusion tensor.

In addition, we assessed cardiac diffusion metrics such as the primary eigenvector or helix angle (HA) and secondary eigenvector angle (E2A), which correspond to the fiber bundle and sheetlet orientation, respectively. Changes in HA or |E2A| distribution due to fixation were assessed using histograms. Endocardial and epicardial contours of the LV were segmented for subsequent data analysis of diffusion metrics. This also enabled determination of the LV center, which was used to calculate primary and secondary eigenvector angles as described by Ferreira et al.[2] The LV center was recalculated for each time point. Changes in these metrics were also assessed in dependence of the diffusion time up to 600 ms. In order to demonstrate temperature independence, we placed a 20 x 20 pixel ROI in the saline solution for all ADC maps based on the spin echo sequence. This was done for all time points of this study (0, 7, 15, 50, 100, 200 days).

3.2.4 | Statistics

All statistical testing was done using MATLAB. Prior to statistical tests, data were checked for normal distribution using Shapiro–Wilk tests with a significance level of $P < 0.05$. Fixation-induced changes in T_2, T_2^*, eigenvalues of the diffusion tensor, ADC and FA were then assessed using a paired t-test with $P < 0.05$. Bonferroni correction was applied to account for multiple testing.

4 | RESULTS

4.1 | SNR

Figure 2 displays SNR values in the LV in dependence of the tissue fixation duration comparing the spin echo (TE = 44 ms, t_{Mix} = 21 ms) and stimulated echo (TE = 36 ms, t_{Mix} = 100 ms) sequence. For both pulse sequences, the SNR follows a similar trend. There is an initial drop of SNR in the first 7 days of fixation (Δ_{SE}: 32%, Δ_{STE}: 19%) followed by another week of approximately consistent SNR. With longer tissue fixation duration SNR recovers compared with fresh tissue values (Δ_{SE}: 20%, Δ_{STE}: 10%). The use of a stimulated echo approach resulted in a loss of ~33% SNR in the fresh heart. With decreased T_2 and T_2^* this difference was 31% on day 7 after fixation and 25% on day 200 after fixation. Results of the paired t-test are listed in Table S4 and histograms of the SNR distribution are shown in Figure S1. Using the STE sequence resulted in narrower histograms with sharper modes. Destructive B_1 interference, as illustrated in Figure S2, was present in the saline solution in all diffusion scans. Despite this signal variation, the saline SNR reference was consistent throughout this study. In addition, there were no variations in the noise floor.

4.2 | Relaxometry

Representative image contrasts for the varying echo times in T_2^* and T_2 measurements are displayed in Figures S3 and S4 for a midcavity slice of one heart. Alterations of the transverse and the effective transverse relaxation times due to continuous tissue fixation are shown in Figure 3. As visualized by the parameter maps of a representative midcavity slice, both T_2 (see Figure 3A) and T_2^* (see Figure 3B) drop significantly in the first 7 days. Afterwards, we observe slightly increasing values for both T_2 and T_2^*. Mean values of individual hearts as well as their mean ± single standard deviation show that this trend was present in basal, midcavity and apical slices of all hearts. Average values for the initial drop as well as the relative difference after 200 days of continuous fixation are listed in Table 1. On average, T_2 dropped from 49.3 to 32.1 ms (35%) and T_2^* from 25.1 to 19.8 ms (~21%) in the LV in the first 7 days. While T_2^* values almost recovered after 200 days of continuous fixation (<5% mean difference to fresh hearts), T_2 values remain lowered (26% mean difference to fresh hearts). Results of the paired t-test are listed in Table S4.

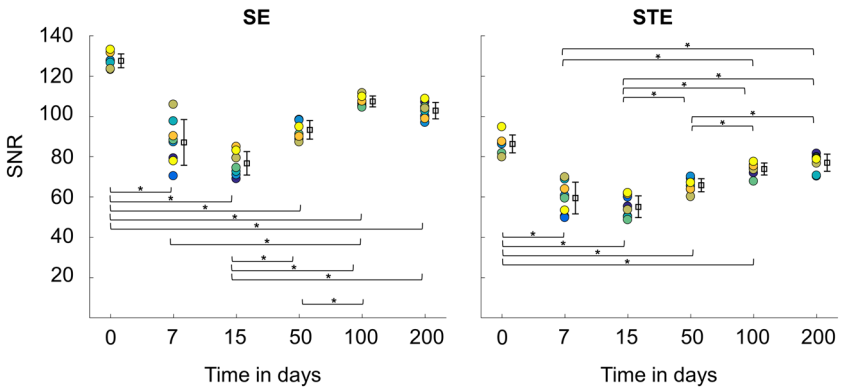

FIGURE 2 SNR in reference scans of the spin echo and stimulated echo (t_{Mix} = 100 ms) sequence for all hearts. Color coding: Hearts 1–8. Displayed are mean values for individual hearts and their mean ± single standard deviation for the different time points prior to and after fixation. Significant differences in paired t-test ($P < 0.05$) are indicated by *

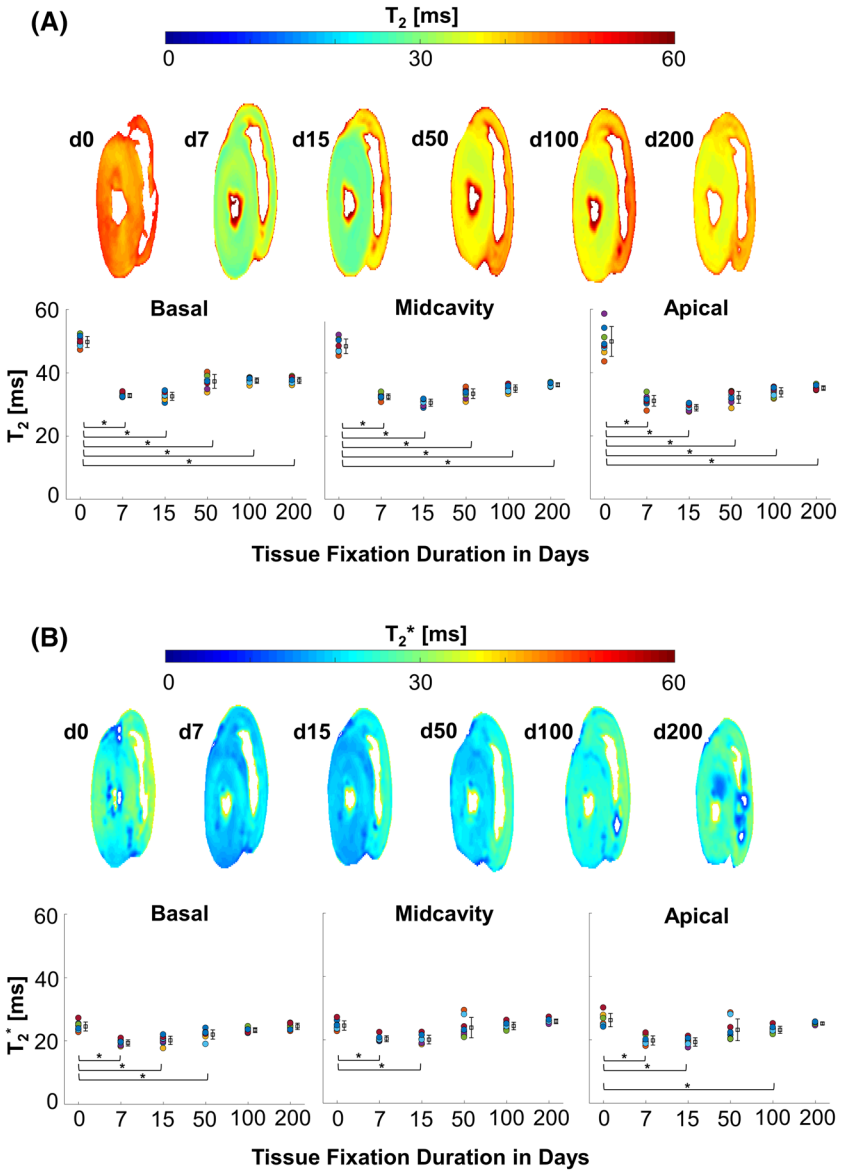

FIGURE 3 T_2 and T_2^* prior to fixation and 7, 15, 50, 100 and 200 days after (A) representative T_2 maps for a single midcavity slice for the different time points prior to and after fixation. Below are mean values for individual hearts and their mean ± single standard deviation. A significant difference in paired t-test ($P < 0.05$) relative to day 0 is indicated by *. Color coding: Hearts 1–8. (B) Corresponding visualization of T_2^*

TABLE 1 Alterations of T_2 and T_2^* due to tissue fixation compared with fresh hearts

	T_2 fresh [ms]	T_2 day-7 [ms]	Δ [%]	T_2 day-200 [ms]	Δ [%]
Apical	49.8 ± 4.7	31.1 ± 1.7	38	35.2 ± 0.7	30
Midcavity	48.3 ± 2.3	32.4 ± 0.9	33	36.3 ± 0.6	25
Basal	49.7 ± 1.7	31.1 ± 0.7	34	37.6 ± 1.0	24
	T_2^* fresh [ms]	T_2^* day-7 [ms]	Δ [%]	T_2^* day-200 [ms]	Δ [%]
Apical	26.2 ± 2.1	19.8 ± 1.5	25	25.1 ± 0.4	4
Midcavity	24.5 ± 1.4	19.3 ± 1.0	21	25.8 ± 0.7	-5
Basal	24.5 ± 1.5	20.3 ± 0.9	17	24.6 ± 1.0	–0.1

4.3 | Diffusion

Mean temporal changes in the eigenvalues of the diffusion tensor, the ADC and FA are shown in Figure 4. All eigenvalues and therefore the ADC decreased, similarly to T_2 and T_2^*, within 7 days following fixation. Changes in λ_2 and λ_3 were rather small. After this initial drop, eigenvalues slightly increased with fixation duration. After 100 days of fixation this led to significant differences compared with first week λ_1 and ADC values.

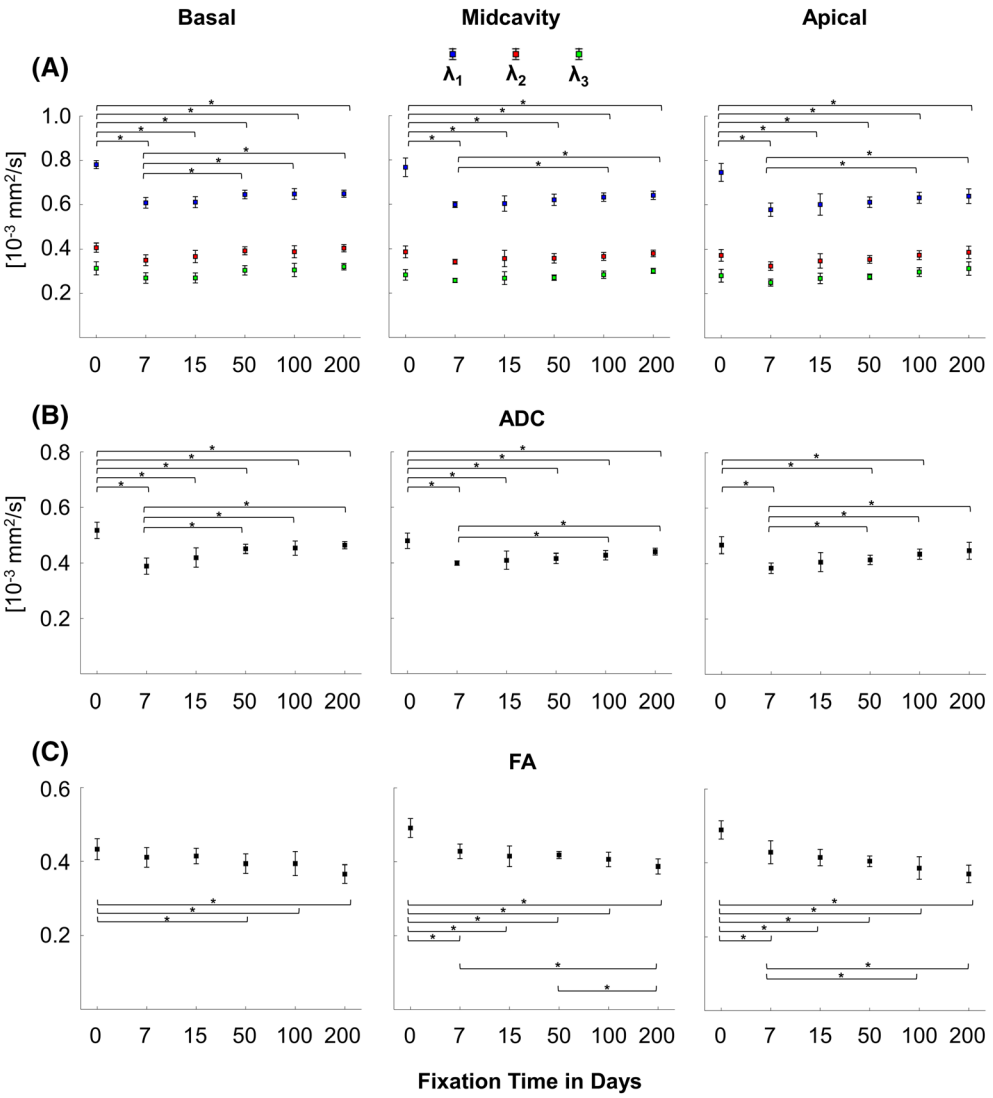

FIGURE 4 Mean ± single standard deviation of diffusion metrics of the left ventricle prior to fixation and 7, 15, 50, 100 and 200 days after fixation for basal, midcavity and apical slices. (A) eigenvalues λ_1 (blue), λ_2 (red), λ_3 (green) of the diffusion tensor. (B) ADC. (C) FA. Standard deviations are of averages across all hearts. A significant difference in paired t-test ($P < 0.05$) is indicated by *. For visibility reasons, test results for the eigenvalues are only shown for λ_1

FA was altered significantly postfixation. However, contrary to the eigenvalue evolution, values decreased with fixation time, leading to significant differences in first week values in midcavity and apical slices after 200 days of fixation. Initial changes in FA due to tissue fixation or tissue fixation duration were smaller and insignificant for basal slices.

Reference values for the ADC are depicted in Figure S5. The average ADC in saline solution was 1.740 ± 0.022 [10^{-3} mm^2/s], with the standard deviation being lower than 2%.

Representative fixation-induced alterations of the main eigenvector orientation and therefore microstructure for heart #5 are displayed in Figure 5. Data were acquired using the spin echo sequence and the diffusion tensor and HA visualized as superquadric glyphs for a basal slice. The expected smooth progression from positive values in the endocardium to negative values in the epicardium is present at all fixation stages. Differences at various fixation stages can be found at the insertion point of the left and right ventricles. Mean HA values (in degrees) for the heart shown in Figure 5 at the time points 0, 7, 15, 50, 100 and 200 days were −1.0°, −0.1°, −2.5°, 2°, −1.6° and 1.25°, respectively. Histograms showing the distribution of HA values for this heart within LV segmentation at different time points after fixation compared with the distribution in unfixed tissue are displayed in Figure S6. There is no systematic shift in the main eigenvector orientation. Respective HA distributions for the remaining seven hearts prior and after 7, 15 and 100 days of fixation are shown in Figure S7. The average standard deviation (over time) in mean values for all hearts was 3.4°.

Figure 6 demonstrates representative variations of the secondary eigenvector orientation for the same basal slice of heart #5. Superquadric glyphs are used to visualize the diffusion tensor and the secondary eigenvector angle (|E2A|). Since the secondary eigenvector orientation is not linked to a certain position in the myocardium, the visual assessment of changes turned out to be difficult compared with the main eigenvector. However, similar to Figure 5, the main difference at different fixation stages was found at the insertion point of the left and right ventricles. While the LV cavity looks similar for scans at days 7, 15, 50, 100 and 200, there is a distinct structural difference compared with day 0. Median |E2A| values (in degrees) for the heart shown in Figure 6 at the time points 0, 7, 15, 50, 100 and 200 days were 64.6°, 64.5°, 65.1°, 65.2°, 64.6° and

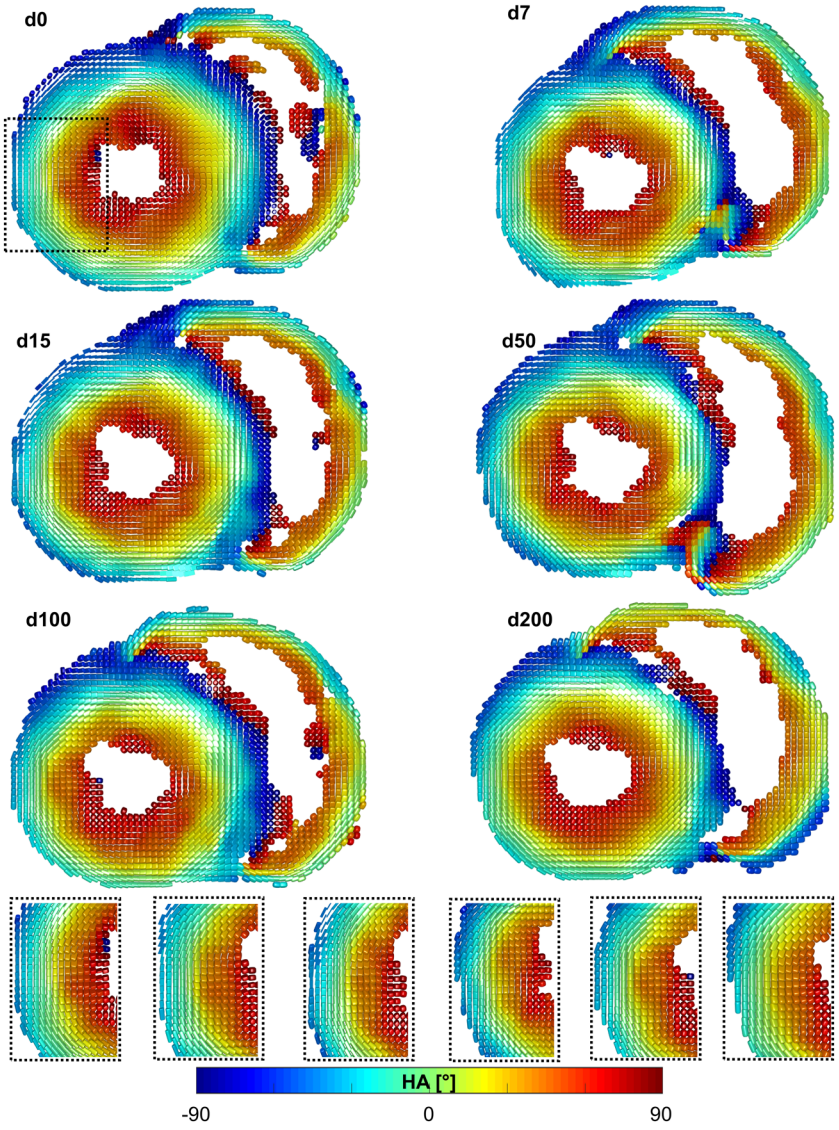

FIGURE 5 Representative helix angle distribution for one heart prior to fixation and 7, 15, 50, 100 and 200 days after fixation. The diffusion tensor for a basal slice is visualized as a superquadric glyph for each pixel. Color-coding of each glyph corresponds to HA values. Dotted line: example section at day 0 and respective zoomed images for the various time points. Threshold for visualization of a pixel as superquadric glyph was set to a FA value of 0.2

64.6°, respectively. Histograms showing the respective |E2A| distribution within LV segmentation at different time points after fixation are presented in Figure S8. |E2A| distributions for the remaining seven hearts prior and after 7, 15 and 100 days of fixation are shown in Figure S9. The average standard deviation (over time) in mean values for all hearts was 6.5°.

Figure 7 shows tissue fixation-induced changes in diffusion metrics (λ_1, λ_2, λ_3, ADC and FA) of the midcavity slice averaged over all eight hearts in dependence of the diffusion time. Values for the diffusion time of 21 ms were acquired using the spin echo sequence. All longer measurements with diffusion times longer than 21 ms were performed using the stimulated echo sequence. Values for individual hearts are displayed in Figure S10.

While λ_1 continually decreased with increasing diffusion time in the unfixed heart, this trend was not apparent after fixation. Values of λ_1 appear rather consistent with increasing diffusion time. As described above, the main eigenvalue of the diffusion tensor drops following fixation. In addition, there is a slight increase with increasing fixation duration. Thus, the difference between λ_1 in fixed and unfixed cardiac tissue is smallest for longer diffusion times and tissue fixation durations (<10%).

Differences of the secondary and tertiary eigenvalues following fixation were small compared with the main eigenvalue. Both λ_2 and λ_3 initially decreased with increasing diffusion time, resulting in a rather consistent state for longer diffusion times (>200 ms). This diffusion time-dependent decrease was highest in unfixed hearts and on average became less impactful for longer tissue fixation durations. ADC curves exhibit the same diffusion time dependency with smaller differences between fixed and unfixed tissue.

FA values increased with increasing diffusion time. This trend was present for all fixation stages and most prominent in the unfixed heart. On average, longer fixation durations led to lower FA values. An initial drop of FA following fixation was present in all hearts.

For all metrics curves reached a plateau between 200 and 400 ms diffusion time.

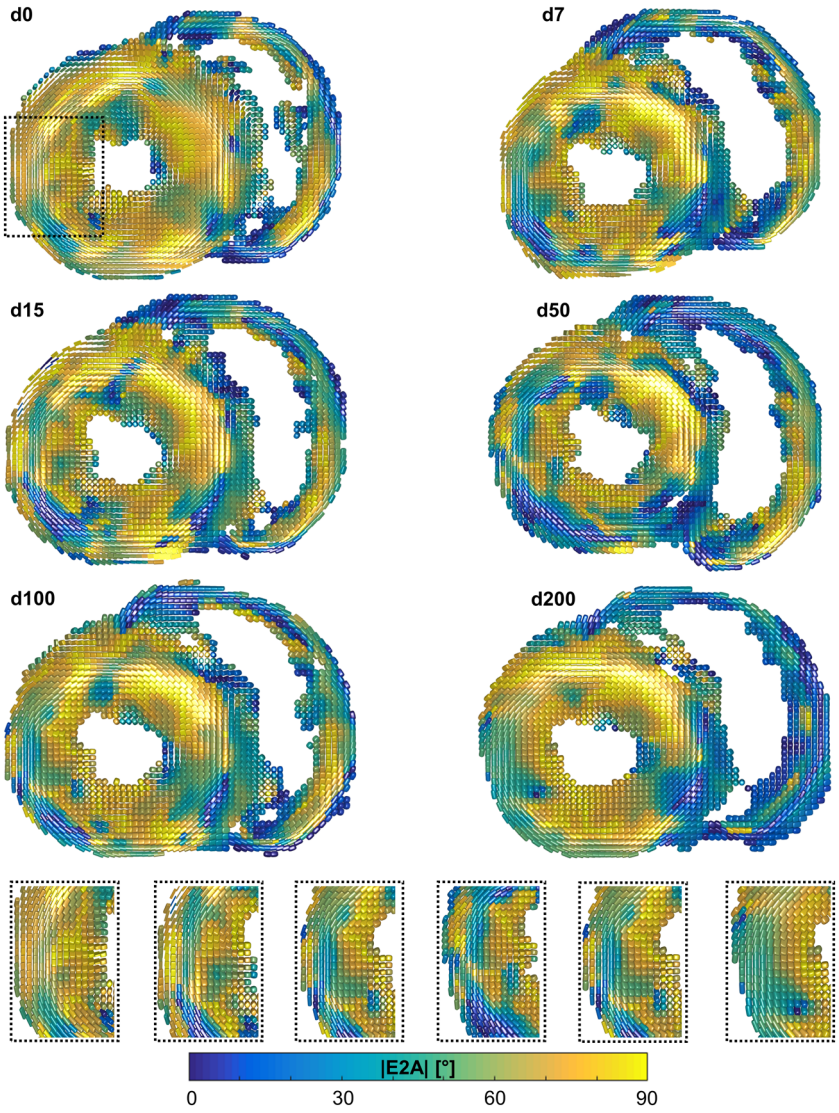

FIGURE 6 Representative secondary eigenvector angle distribution for one heart prior to fixation and 7, 15, 50, 100 and 200 days after fixation. The diffusion tensor for a basal slice is visualized as a superquadric glyph for each pixel. Color-coding of each glyph corresponds to |E2A| values. Dotted line: example section at day 0 and respective zoomed images for the various time points. Threshold for visualization of a pixel as superquadric glyph was set to a FA value of 0.2

5 | DISCUSSION

We have demonstrated tissue fixation and fixation duration-dependent alterations of various MRI (T_2, T_2^*, SNR) and diffusion metrics (ADC, λ_1, λ_2, λ_3, FA, HA, |E2A|) in the LV of the porcine heart at 7 T. Our results show that T_2 and T_2^* relaxation times were continuously altered by immersion fixation in formalin and that SNR values strongly correlated with the respective changes in T_2 and T_2^*. In addition, we found that tissue fixation significantly changed the main eigenvalue of the diffusion tensor, ADC and FA, and that continuous changes in the main eigenvalues, ADC and FA after a fixation duration of 15 days were not significant. By contrast, no systematic changes in structural parameters, such as HA and |E2A|, were introduced by fixation, independent of the immersion duration. This is an important finding for studies assessing ventricular remodeling of cardiac microstructure in various cardiac pathologies.

SNR in diffusion MRI directly influences the data fidelity[11,12] of derived diffusion parameters. Most ex vivo studies use a Stejskal-Tanner diffusion preparation and EPI readout. Thus, SNR strongly depends on both T_2 and T_2^*. Since ex vivo studies are usually performed to achieve high quality and high fidelity data, study protocols should be optimized with respect to SNR. Our results show that SNR decreases (mean: ~32%) initially after tissue fixation and that SNR was somewhat restored (mean: ~20%) with prolonged tissue fixation. This change in SNR is mainly due to the changes observed in T_2 and T_2^* relative to the used echo times as well as subsequent k-space filter effects. Special care needs to be taken in order to avoid further reduction of T_2^* due to increased B_0 inhomogeneity at ultrahigh field strengths (≥7 T).

Many studies have reported a decrease in T_2 in nervous tissue or other organs following tissue fixation using formalin.[23–29] To our knowledge such changes in relaxation parameters have not been yet reported for the heart. Initial T_2 changes following tissue fixation observed in this study fit well to the literature values for brain tissue listed above. T_2 shortening in nervous tissue has been described in many studies and has been attributed to multiple causes, such as increased tissue rigidity due to protein cross-linking, interactions of water molecules and myelin lipids in

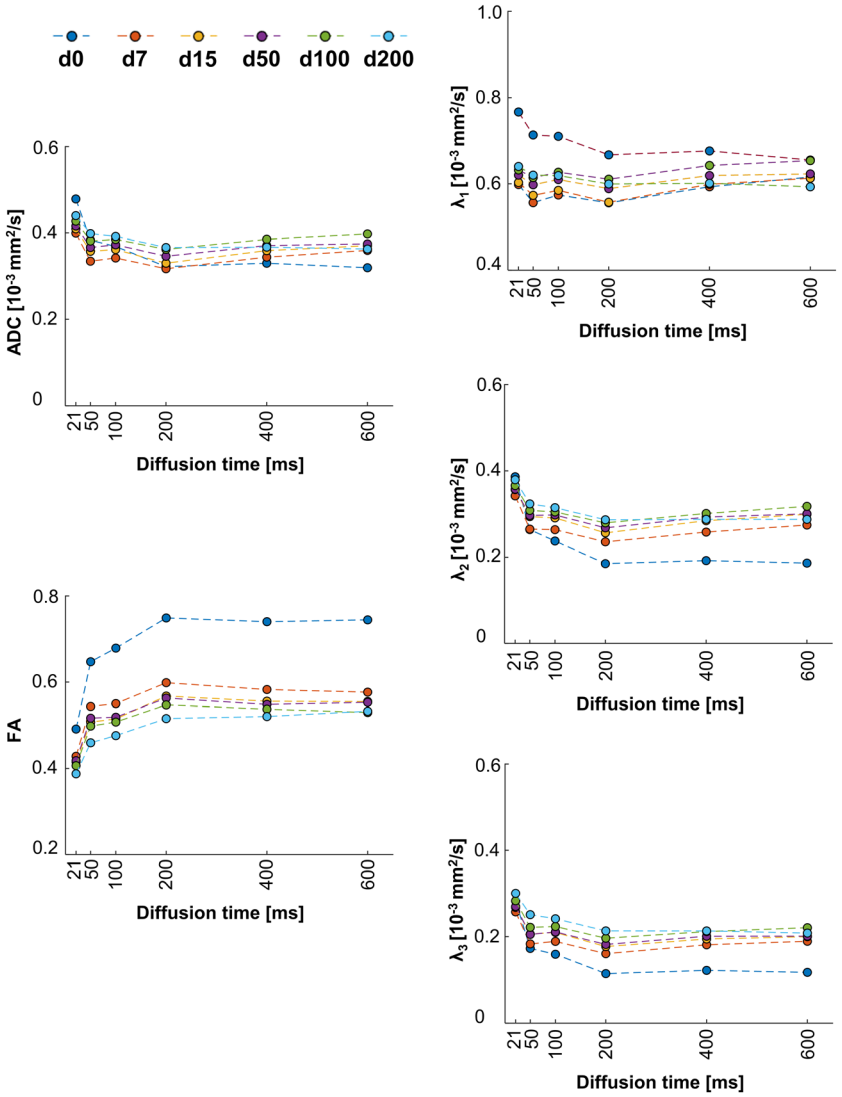

FIGURE 7 Average diffusion time-dependent changes of λ_1, λ_2, λ_3, ADC and FA in the midcavity slice in dependence of the fixation duration

tissue compartments,[36] changes in diffusion rates,[37] intra/extra-cellular water components,[25] tissue dehydration[28,38] and regular replacements of formalin solution.[27] The analysis of the mechanisms of T_2 shortening and their application to heart tissue was outside the scope of this study.

We rather focused on changes in MR and diffusion metrics induced by continuous tissue fixation in order to (1) ease optimization of future study protocols and (2) enable comparisons of past and future studies regarding fixed versus unfixed tissue, fixation duration, and spin echo versus stimulated echo data.

Dawe et al[23] reported a gradual increase (20%, 60-90 days postmortem) of T_2 values in "deep" brain tissue for longer fixation durations, following the initial decrease after formalin immersion. We observed an increase (~13%) in T_2 between 15 and 50 days of fixation. Dawe et al[23] argue that this recovery in T_2 values is connected to latent tissue decomposition.

In our study, we removed the atria from all hearts in order to ease the removal of trapped air and fixative distribution, allowing penetration of the myocardial wall from both sides. Aldehyde fixation penetration occurs with a rate of 0.5 to 1 mm/hour at room temperature and we observed the pale yellow color change, which indicates penetration, shortly after immersion. Multiple studies have shown that autolytic effects on cardiac tissue are very slow.[14,32,39] It is therefore unlikely that the gradual increase in T_2 at later stages of fixation is related to latent effects of tissue decomposition. During the fixation process cells move through stages of (1) shrinkage, (2) prolonged swelling and (3) secondary shrinkage. As mentioned above, changes in T_2 have been attributed to changes in intra- and extra-cellular volume components.[25] In this study we apply formalin, a neutral buffered, aqueous solution of formaldehyde (systematic name: methanal), with a formaldehyde concentration of 4%. Formaldehyde concentrations below 5% only cause very minimal initial shrinkage followed by extensive swelling[40] and later on shrinkage. Observed decreases and increases in T_2 may thus be caused by cell swelling and shrinkage, respectively. A dedicated study resolving the fixation process itself will be necessary to completely exclude influences of tissue decomposition and variations in both heart size and contraction state. In addition to SNR, alterations in T_2 may possibly change T_2 weightings in the diffusion-weighted images acquired.

Since we did not observe any interference patterns in images for T_2 quantification due to imperfect inversions, normalized the signal-time curves and checked for mono-exponential decay via goodness of fit, we believe that B_1 imperfections did not lead to first-order approximation errors in measured T_2 values. In addition, the goodness of fit showed that the effect of B_1 inhomogeneity on SNR was negligible for the analyzed tissue.

With 0.62 ± 0.1 (10^{-3} mm^2/s), our ADC values in this study are in good agreement with our previous work at 7 T[32] (0.51-0.66 [10^{-3} mm^2/s]) using fresh hearts from animals of the same breed and comparable weight. ADC values of fresh hearts reported by Mazumder et al[20] (0.52 ± 0.026 [10^{-3} mm^2/s], Yorkshire, 41-50 kg) and Agger et al[18] (0.54 ± 0.026 [10^{-3} mm^2/s], Danish Landrace, 50-60 kg) are slightly lower and ADC values of fixed hearts reported by Wu et al[41] (0.671 ± 0.106 [10^{-3} mm^2/s], minipigs, 45-50 kg) and Pashakhanloo et al[42] (0.633 ± 0.04 [10^{-3} mm^2/s], Yorkshire, 50 ± 18 kg) are slightly higher. Literature results of comparisons between fixed and unfixed heart tissue are sparse. While the ADC in our study decreases after fixation, Agger et al[18] report only a slight increase (11%) and Mazumder et al[20] a strong increase in the ADC (~54%). There are contradictory literature reports on postfixation ADC as well. While Shepherd et al[26] report an increase in ADC, others have shown a decrease postfixation.[13,31,43] These contradictory reports may possibly be the result of varying tissue storage conditions during sample preparation.

In their study on the effects of various fixation methods on heart tissue, Agger et al[18] showed that freezing of heart tissue leads to large increases in the ADC (71%) and that subsequent perfusion fixation will further increase the ADC (88%). Due to limited scanner availability, Mazumder et al[20] stored freshly excised hearts in an ice bath for a prolonged period of time (5-48 h) in order to prevent tissue decomposition prior to scans, while Shepherd el al[26] placed excised rat brains in ice-cold artificial cerebrospinal fluid for 1 h in order to minimize ischemic damage. None of the studies reporting reduced ADC values have used ice, ice baths, or temperatures below 4°C for storage. A dedicated study may help to assess the influence of ice or varying storage temperatures on various tissue types, but this has not been the scope of our study.

There is more consensus in studies regarding the effect of formalin fixation on FA. Comparisons of prefixation and postfixation tissue (heart and nervous tissue) report consistent or decreasing FA following fixation. The results in our study are in good agreement with Agger et al[18] and Mazumder et al,[20] who scanned hearts prefixation and postfixation with a time difference of 24 hours and 12-18 days, respectively. We show that FA decreases with prolonged tissue fixation. This may explain why Agger et al[18] reported consistent FA values, while Mazumder et al[20] reported a decrease in FA.

Our results show that all eigenvalues decrease following fixation. Alterations of the main eigenvector of diffusion are the most pronounced, and the second and third eigenvalues are less affected. Both Agger et al,[18] for heart tissue, and D'Arceuil and de Crespigny,[13] for white matter, showed that the effects on the main eigenvector are most pronounced. In order to improve our understanding of changes in the ADC and FA it is paramount to report changes in the individual eigenvalues. Future studies analyzing diffusion metrics in highly structured tissue, such as the brain or the heart, should therefore report all eigenvalues.

Agger et al[18] demonstrated that immersion fixation using formalin does not affect main fiber orientation and therefore tractography results. This is in agreement with studies by Scollan et al[16] and Helm et al,[44] who compared the main eigenvector orientation in fixed hearts to myofiber orientation in histology. Results obtained in this study support this observation. Even prolonged, continuous tissue fixation had little impact on the helix angle and therefore main eigenvector orientation. Furthermore, the smooth gradient from endocardium to epicardium was consistent in the presence of scan-to-scan slice offsets.

To our knowledge this is the first study analyzing effects of formalin fixation on the secondary eigenvector orientation within cardiac tissue. Recent developments in cardiac DTI, particularly in vivo applications, have shown that the secondary eigenvector angle holds high diagnostic value for myocardial remodeling in cardiac pathologies.[2–4] In this study we demonstrate that continuous tissue fixation using formalin does not affect the average secondary eigenvector orientation. Sheetlets generally run perpendicular to myocytes, which means through-plane in the short axis slice, and thus scan-to-scan slice offsets are more apparent in the visualization of |E2A|.

Kim et al[45] report a consistent main eigenvalue and decreasing secondary and tertiary eigenvalues for increasing diffusion times in refrigerated and thawed heart tissue of the calf. While this is in good agreement with the changes we found in heart tissue postfixation, we also found that diffusion time-induced alterations in fixed and unfixed tissue follow a similar trend, but with a different scale. Longer diffusion times and therefore increased anisotropy have been shown to decrease uncertainty in the determination of the main eigenvector orientation.[46] In this study we have shown that the dependence of FA from diffusion encoding time is reduced following fixation using formalin, indicating that formalin fixation introduces diffusion barriers along the main direction of diffusion.

Reference values, such as SNR in the saline solution and noise in the background, were meant to remove external factors, such as temperature and coil heating, for the assessment of SNR and diffusion metrics. While the background noise was very stable, SNR in the saline solution was affected by destructive B_1 interference. However, considering the combination of the SNR and the ADC reference in saline solution, we believe that the results of this study are unaffected by temperature variation.

In order to minimize tissue decomposition-induced changes in derived metrics of fresh hearts, we set the scanning protocol to 63 minutes, trading higher SNR for limited volume coverage. The diffusion weighting of b = 1000 s/mm^2 was chosen to maintain comparability to other fixation studies on porcine hearts such as Agger et al[18] (b = 1000 s/mm^2) and Mazumder et al[20] (1271 s/mm^2). While additional higher b-values may

have increased the dynamic range for restricted diffusion and enabled analysis based on non-Gaussian models, they also require longer diffusion gradients, leading to longer echo times and a loss in SNR, particularly at 7 T. In this study we show that fixation leads to decreases in T_2 and T_2^*, which are already short at ultrahigh field strengths. An assessment of respective tradeoffs and optimal b-values for ex vivo cDTI of fixed porcine hearts at 7 T may be subject to future studies.

Since we received sets of two hearts per experiment, prefixation scans within one set were performed with a time difference of ~40 minutes between excision and measurement. We found no systematic difference in diffusivity between hearts measured first and second. This is in agreement with prior experiments analyzing sample stability of fresh hearts following excision.[32] However, variations in heart size and times for transport, tissue preparation and sample fixation may have resulted in different tissue temperatures. Thus, prefixation scans in this study may therefore include a temperature bias.

Throughout the study, hearts were repeatedly taken from the fixation container and placed in dedicated plastic containers for measurements. Therefore, slight offsets in slice positioning were present in some repeat scans, despite slice positioning with respect to anatomical markers. In general these offsets were more pronounced for the prefixation scans and rather small for scans of fixed hearts. They may thus be related to tissue changes introduced by the fixation process. While these offsets had little impact on derived structural parameters in the LV of fixed samples, there were distinct differences at intersection points to the right ventricle. Particularly at very basal slices, structural coherence at these points was lower. Further analysis of these changes may be part of future studies, but was outside the scope of this work.

In conclusion, we have demonstrated that continuous immersion fixation of porcine hearts using formalin leads to alterations of relaxation parameters and diffusion metrics, such as eigenvalues, ADC and FA. Thus, tissue fixation durations should be kept in mind when interpreting the impact of diseases on these parameters. In addition, our results highlight the importance of proper method selection and reproducible tissue handling, preparation and storage. In recent years, metrics of microstructure been shown to be precise and specific markers for remodeling in cardiac pathologies.[3–5,19] The preservation of anisotropy and overall microstructure following even long periods of immersion in formalin may enable future studies assessing ventricular remodeling of cardiac microstructure in various cardiac pathologies in more detail.

ACKNOWLEDGEMENTS

The authors thank Mihaela Pali for excellent surgical assistance.

Parts of this work will be used in the doctoral thesis of David Lohr.

FUNDING INFORMATION

This work was supported by the Federal Ministry of Education and Research (grant number, 01EO1504).

ORCID

David Lohr https://orcid.org/0000-0002-6509-3776

REFERENCES

1. Ariga R, Tunnicliffe EM, Manohar SG, et al. Identification of myocardial disarray in patients with hypertrophic cardiomyopathy and ventricular arrhythmias. *J Am Coll Cardiol*. 2019;73(20):2493-2502.
2. Ferreira PF, Kilner PJ, McGill LA, et al. In vivo cardiovascular magnetic resonance diffusion tensor imaging shows evidence of abnormal myocardial laminar orientations and mobility in hypertrophic cardiomyopathy. *J Cardiovasc Magn Reson*. 2014;16(1):87. https://doi.org/10.1186/s12968-014-0087-8
3. Nielles-Vallespin S, Khalique Z, Ferreira PF, et al. Assessment of myocardial microstructural dynamics by in vivo diffusion tensor cardiac magnetic resonance. *J Am Coll Cardiol*. 2017;69(6):661-676.
4. von Deuster C, Sammut E, Asner L, et al. Studying dynamic myofiber aggregate reorientation in dilated cardiomyopathy using in vivo magnetic resonance diffusion tensor imaging. *Circ Cardiovasc Imaging*. 2016;9(10):e005018. https://doi.org/10.1161/CIRCIMAGING.116.005018
5. Mekkaoui C, Jackowski MP, Kostis WJ, et al. Myocardial scar delineation using diffusion tensor magnetic resonance tractography. *J Am Heart Assoc*. 2018;7(3):e007834. https://doi.org/10.1161/JAHA.117.007834
6. Mekkaoui C, Reese TG, Jackowski MP, et al. Diffusion tractography of the entire left ventricle by using free-breathing accelerated simultaneous multisection imaging. *Radiology*. 2017;282(3):850-856.
7. Nguyen C, Fan Z, Sharif B, et al. In vivo three-dimensional high resolution cardiac diffusion-weighted MRI: A motion compensated diffusion-prepared balanced steady-state free precession approach. *Magn Reson Med*. 2014;72(5):1257-1267.
8. Stoeck CT, von Deuster C, Genet M, Atkinson D, Kozerke S. Second order motion compensated spin-echo diffusion tensor imaging of the human heart. *Magn Reson Med*. 2016;75(4):1669-1676.
9. Sosnovik DE, Mekkaoui C, Huang S, et al. Microstructural impact of ischemia and bone marrow-derived cell therapy revealed with diffusion tensor magnetic resonance imaging tractography of the heart in vivo. *Circulation*. 2014;129(17):1731-1741.
10. Landman BA, Farrell JA, Huang H, Prince JL, Mori S. Diffusion tensor imaging at low SNR: nonmonotonic behaviors of tensor contrasts. *Magn Reson Imaging*. 2008;26(6):790-800.

11. Scott AD, Nielles-Vallespin S, Ferreira PF, McGill L-A, Pennell DJ, Firmin DN. The effects of noise in cardiac diffusion tensor imaging and the benefits of averaging complex data. *NMR Biomed*. 2016;29(5):588-599.
12. McClymont D, Teh I, Schneider JE. The impact of signal-to-noise ratio, diffusion-weighted directions and image resolution in cardiac diffusion tensor imaging – insights from the ex-vivo rat heart. *J Cardiovasc Magn Reson*. 2017;19(1):90. https://doi.org/10.1186/s12968-017-0395-x
13. D'Arceuil H, de Crespigny A. The effects of brain tissue decomposition on diffusion tensor imaging and tractography. *Neuroimage*. 2007;36(1):64-68.
14. Eggen MD, Swingen CM, Iaizzo PA. Ex vivo diffusion tensor MRI of human hearts: Relative effects of specimen decomposition. *Magn Reson Med*. 2012;67(6):1703-1709.
15. Hsu EW, Muzikant AL, Matulevicius SA, Penland RC, Henriquez CS. Magnetic resonance myocardial fiber-orientation mapping with direct histological correlation. *Am J Physiol Heart Circ Physiol*. 1998;274(5):H1627-H1634.
16. Scollan DF, Holmes A, Winslow R, Forder J. Histological validation of myocardial microstructure obtained from diffusion tensor magnetic resonance imaging. *Am J Physiol Heart Circ Physiol*. 1998;275(6):H2308-H2318.
17. Sosnovik DE, Wang R, Dai G, et al. Diffusion spectrum MRI tractography reveals the presence of a complex network of residual myofibers in infarcted myocardium. *Circ Cardiovasc Imaging*. 2009;2(3):206-212.
18. Agger P, Lass T, Smerup M, Frandsen J, Pedersen M. Optimal preservation of porcine cardiac tissue prior to diffusion tensor magnetic resonance imaging. *J Anat*. 2015;227(5):695-701.
19. Beyhoff N, Lohr D, Foryst-Ludwig A, et al. Characterization of myocardial microstructure and function in an experimental model of isolated subendocardial damage. *Hypertension*. 2019;74(2):295-304.
20. Mazumder R, Choi S, Clymer BD, White RD, Kolipaka A. Diffusion tensor imaging of healthy and infarcted porcine hearts: study on the impact of formalin fixation. *J Med Imag Rad Sci*. 2016;47(1):74-85.
21. Abdullah OM, Drakos SG, Diakos NA, Wever-Pinzon O, Kfoury AG, Stehlik J. Characterization of diffuse fibrosis in the failing human heart via diffusion tensor imaging and quantitative histological validation. *NMR Biomed*. 2014;27(11):1378-1386.
22. Giannakidis A, Gullberg GT, Pennell DJ, Firmin DN. Value of formalin fixation for the prolonged preservation of rodent myocardial microanatomical organization: evidence by MR diffusion tensor imaging. *Anat Rec*. 2016;299(7):878-887.
23. Dawe RJ, Bennett DA, Schneider JA, Vasireddi SK, Arfanakis K. Postmortem MRI of human brain hemispheres: T2 relaxation times during formaldehyde fixation. *Magn Reson Med*. 2009;61(4):810-818.
24. Nagara H, Inoue T, Koga T, Kitaguchi T, Tateishi J, Goto I. Formalin fixed brains are useful for magnetic resonance imaging (MRI) study. *J Neurol Sci*. 1987;81(1):67-77.
25. Shatil AS, Uddin MN, Matsuda KM, Figley CR. Quantitative ex vivo MRI changes due to progressive formalin fixation in whole human brain specimens: longitudinal characterization of diffusion, relaxometry, and myelin water fraction measurements at 3T. *Front Med*. 2018;5:31. https://doi.org/10.3389/fmed.2018.00031
26. Shepherd TM, Thelwall PE, Stanisz GJ, Blackband SJ. Aldehyde fixative solutions alter the water relaxation and diffusion properties of nervous tissue. *Magn Reson Med*. 2009;62(1):26-34.
27. Thickman DI, Kundel HL, Wolf G. Nuclear magnetic resonance characteristics of fresh and fixed tissue: the effect of elapsed time. *Radiology*. 1983;148(1):183-185.
28. Tovi M, Ericsson A. Measurements of T1 and T2 over time in formalin-fixed human whole-brain specimens. *Acta Radiol*. 1992;33(5):400-404.
29. Yong-Hing CJ, Obenaus A, Stryker R, Tong K, Sarty GE. Magnetic resonance imaging and mathematical modeling of progressive formalin fixation of the human brain. *Magn Reson Med*. 2005;54(2):324-332.
30. Wang C, Song L, Zhang R, Gao F. Impact of fixation, coil, and number of excitations on diffusion tensor imaging of rat brains at 7.0 T. *Eur Radiol Exper*. 2018;2(1):25. https://doi.org/10.1186/s41747-018-0057-2
31. Pattany PM, Puckett WR, Klose KJ, et al. High-resolution diffusion-weighted MR of fresh and fixed cat spinal cords: evaluation of diffusion coefficients and anisotropy. *Am J Neuroradiol*. 1997;18(6):1049-1056.
32. Lohr D, Terekhov M, Weng AM, Schroeder A, Walles H, Schreiber LM. Spin echo based cardiac diffusion imaging at 7T: An ex vivo study of the porcine heart at 7T and 3T. *PLoS ONE*. 2019;14(3):e0213994. https://doi.org/10.1371/journal.pone.0213994
33. Yeh F-C. DSI Studio. http://dsi-studio.labsolver.org. Accessed April 22, 2016.
34. Reeder SB, Wintersperger BJ, Dietrich O, et al. Practical approaches to the evaluation of signal-to-noise ratio performance with parallel imaging: Application with cardiac imaging and a 32-channel cardiac coil. *Magn Reson Med*. 2005;54(3):748-754.
35. Jiang H, van Zijl PC, Kim J, Pearlson GD, Mori S. DtiStudio: resource program for diffusion tensor computation and fiber bundle tracking. *Comput Methods Programs Biomed*. 2006;81(2):106-116.
36. Laule C, Vavasour IM, Kolind SH, et al. Magnetic resonance imaging of myelin. *Neurotherapeutics*. 2007;4(3):460-484.
37. Bottomley PA, Foster TH, Argersinger RE, Pfeifer LM. A review of normal tissue hydrogen NMR relaxation times and relaxation mechanisms from 1–100 MHz: Dependence on tissue type, NMR frequency, temperature, species, excision, and age. *Med Phys*. 1984;11(4):425-448.
38. Shepherd TM, Flint JJ, Thelwall PE, et al. Postmortem interval alters the water relaxation and diffusion properties of rat nervous tissue--implications for MRI studies of human autopsy samples. *Neuroimage*. 2009;44(3):820-826.
39. Schmid P, Lunkenheimer PP, Redmann K, et al. Statistical analysis of the angle of intrusion of porcine ventricular myocytes from epicardium to endocardium using diffusion tensor magnetic resonance imaging. *Anat Rec*. 2007;290(11):1413-1423.
40. Crawford CNC, Barer R. The action of formaldehyde on living cells as studied by phase-contrast microscopy. *Q J Microsc Sci*. 1951;s3–92(20):403-452.
41. Wu EX, Wu Y, NichollsJM, et al. MR diffusion tensor imaging study of postinfarct myocardium structural remodeling in a porcine model. *Magnetic resonance in medicine*. 2007;58(4):687-695.
42. Pashakhanloo F, Herzka DA, Mori S, et al. Submillimeter diffusion tensor imaging and late gadolinium enhancement cardiovascular magnetic resonance of chronic myocardial infarction. *Journal of cardiovascular magnetic resonance : official journal of the Society for Cardiovascular Magnetic Resonance*. 2017;19(1):9.
43. Madi S, Hasan KM, Narayana PA. Diffusion tensor imaging of in vivo and excised rat spinal cord at 7 T with an icosahedral encoding scheme. *Magn Reson Med*. 2005;53(1):118-125.

44. Helm PA, Younes L, Beg MF, Ennis DB, Leclercq C, Faris OP. Evidence of structural remodeling in the dyssynchronous failing heart. *Circ Res*. 2006; 98(1):125-132.
45. Kim S, Chi-Fishman G, Barnett AS, Pierpaoli C. Dependence on diffusion time of apparent diffusion tensor of ex vivo calf tongue and heart. *Magn Reson Med*. 2005;54(6):1387-1396.
46. Jones DK. Determining and visualizing uncertainty in estimates of fiber orientation from diffusion tensor MRI. *Magn Reson Med*. 2003;49(1):7-12.

SUPPORTING INFORMATION

Additional supporting information may be found online in the Supporting Information section at the end of this article.

How to cite this article: Lohr D, Terekhov M, Veit F, Schreiber LM. Longitudinal assessment of tissue properties and cardiac diffusion metrics of the ex vivo porcine heart at 7 T: Impact of continuous tissue fixation using formalin. *NMR in Biomedicine*. 2020;33:e4298. https://doi.org/10.1002/nbm.4298

3.3 Characterization of Myocardial Microstructure and Function in an Experimental Model of Isolated Subendocardial Damage

〉 Published in *Hypertension* – 2019[56]

These citations have been applied in this publication.[34,38,41-43,45-49,53-56,68,69,76,98,101,102,105,106,111,120,123-179]

Experimental data suggests that adverse remodeling in response to cardiovascular risk factors and effects of cardiac disease first surface in the subendocardium, the innermost layer of the myocardium. Diagnostic markers for subendocardial integrity and status may therefore facilitate early detection of adverse remodeling, cardiac damage, and enable risk stratification as well as treatment monitoring in asymptomatic disease states.

In this study we aimed to assess whether subendocardial fibrosis (mouse model) affects the LV myofiber configuration and leads to impaired cardiac function and whether corresponding structural and functional changes are detectable both *in vivo* and *ex vivo*.

Subendocardial damage was induced using isoproterenol injections (n=20), while the corresponding control (n=18) received saline solution. Methods applied included a graded exercise test, echocardiography (speckle-tracking and dobutamine stress), *ex vivo* DTI, gene expression analysis and histology.

Gravimetric measures revealed no significant differences, no signs of cardiac hypertrophy were found, and EF and other parameters of global systolic function remained unchanged. Isoproterenol-treated animals developed pronounced subendocardial fibrosis, accompanied by diastolic dysfunction and significantly increased E/e' ratios. Global peak LS and LSR were markedly reduced. Transmural and subendocardial MD were significantly lower and subepicardial layers exhibited a significant reduction in HA. ANP, ST2, CD68, Galectin-3, and precursors of collagen I and III levels were significantly upregulated in the LV.

In this study we show that subendocardial fibrosis induces myofiber configuration changes predominantly in remote regions and leads to signs of diastolic dysfunction and reduced longitudinal deformation. Corresponding microstructural and functional changes were detectable. Subepicardial HA as well as global peak LS were identified as highly sensitive predictors for the presence of subendocardial fibrosis and thus, as diagnostic measures for early detection of cardiac impairment. Structural changes and respective measurement using DTI will have to be confirmed in patients *in vivo*.

Heart

OPEN

Characterization of Myocardial Microstructure and Function in an Experimental Model of Isolated Subendocardial Damage

Niklas Beyhoff, David Lohr, Anna Foryst-Ludwig, Robert Klopfleisch, Sarah Brix, Jana Grune, Arne Thiele, Lasti Erfinanda, Arata Tabuchi, Wolfgang M. Kuebler, Burkert Pieske, Laura M. Schreiber, Ulrich Kintscher

Abstract—Subendocardial damage is among the first cardiac manifestations of hypertension and is already present in asymptomatic disease states. Accordingly, markers of subendocardial impairment may facilitate early detection of cardiac damages and risk stratification under these conditions. This study aimed to investigate the impact of subendocardial damage on myocardial microstructure and function to elucidate early pathophysiologic processes and to identify corresponding diagnostic measures. Mice (n=38) were injected with isoproterenol to induce isolated subendocardial scarring or saline as corresponding control. Cardiac function and myocardial deformation were determined by high-frequency echocardiography. The cardiac stress response was assessed in a graded exercise test and during dobutamine stress echocardiography. Myocardial microstructure was studied ex vivo by 7 T diffusion tensor magnetic resonance imaging at a spatial resolution of 100×100×100 µm^3. Results were correlated with histology and biomarker expression. Subendocardial fibrosis was accompanied by diastolic dysfunction, impaired longitudinal deformation (global peak longitudinal strain [LS]: −12.5±0.5% versus −15.6±0.5%; P<0.001) and elevated biomarker expression (ANP [atrial natriuretic peptide], Galectin-3, and ST2). Systolic function and cardiac stress response remained preserved. Diffusion tensor magnetic resonance imaging revealed a left-shift in helix angle towards lower values in isoproterenol-treated animals, which was mainly determined by subepicardial myofibers (mean helix angle: 2.2±0.8° versus 5.9±1.0°; P<0.01). Longitudinal strain and subepicardial helix angle were highly predictive for subendocardial fibrosis (sensitivity, 82%–92% and specificity, 89%–90%). The results indicate that circumscribed subendocardial damage alone can cause several hallmarks observed in cardiovascular high-risk patients. Microstructural remodeling under these conditions involves also remote regions, and corresponding changes in longitudinal strain and helix angle might serve as diagnostic markers. **(*Hypertension*. 2019;74:295-304. DOI: 10.1161/HYPERTENSIONAHA.119.12956.)** ● **Online Data Supplement**

Key Words: diffusion tensor magnetic resonance imaging ■ myocardial strain; remodeling ■ speckle tracking ■ subendocardium

The subendocardium is the innermost myocardial layer and is highly vulnerable against injury.[1] Therefore, the subendocardium is often considered the myocardial layer affected first in many cardiac diseases.[1] Experimental data indicate that adverse remodeling in response to multiple cardiovascular risk factors starts in the subendocardium of the left ventricle (LV) before occurring in other myocardial layers.[2–5] Hypertension and concomitant cardiac hypertrophy are accompanied by abnormal coronary autoregulation and consequently reduced perfusion pressure in the subendocardium, which may predispose to subendocardial ischemia.[6,7] Recently, Ishizu et al[2] demonstrated that subendocardial fibrosis is among the first cardiac manifestations of hypertension preceding functional changes. Accordingly, diagnostic markers of subendocardial status may facilitate early detection of cardiac damages and risk stratification already in asymptomatic disease states. Despite accepted clinical surrogates of subendocardial function such as global peak LS,[8] however, multiple confounding factors hamper the

Received March 6, 2019; first decision March 26, 2019; revision accepted May 12, 2019.

From the Charité—Universitätsmedizin Berlin, corporate member of Freie Universität Berlin, Humboldt-Universität zu Berlin, and Berlin Institute of Health, Institute of Pharmacology, Center for Cardiovascular Research, Berlin, Germany (N.B., A.F.-L., S.B., J.G., Arne Thiele, U.K.); DZHK (German Centre for Cardiovascular Research), Partner site Berlin, Germany (N.B., A.F.-L., S.B., J.G., Arne Thiele, L.E., Arata Tabuchi, W.M.K., B.P., U.K.); Chair of Cellular and Molecular Imaging, Comprehensive Heart Failure Center (CHFC), University Hospital Wuerzburg, Germany (D.L., L.M.S.); Department of Veterinary Pathology, College of Veterinary Medicine, Freie Universität Berlin, Germany (R.K.); Charité—Universitätsmedizin Berlin, corporate member of Freie Universität Berlin, Humboldt-Universität zu Berlin, and Berlin Institute of Health, Institute of Physiology, Berlin, Germany (J.G., L.E., Arata Tabuchi, W.M.K.); and Department of Internal Medicine and Cardiology, Campus Virchow Klinikum, Charité—Universitätsmedizin Berlin and Deutsches Herzzentrum Berlin (DHZB), Department of Cardiology, Berlin, Germany (B.P.).

The online-only Data Supplement is available with this article at https://www.ahajournals.org/doi/suppl/10.1161/HYPERTENSIONAHA.119.12956.

Correspondence to Ulrich Kintscher, MD, Institute of Pharmacology, Center for Cardiovascular Research, Charité—Universitaetsmedizin Berlin, Hessische St 3–4, 10115 Berlin, Germany. Email ulrich.kintscher@charite.de

establishment of cause-effect relationships between subendocardial pathologies and diagnostic measures in humans and many animal models.

Several cardiac pathologies have been shown to alter the 3-dimensional arrangement of myofibers in the heart.[9–11] Within the normal LV, the myofibers form 2 counter-directional helices varying continuously in orientation (helix angle [HA]) from subendocardium (right-handed helix, positive HA) to subepicardium (left-handed helix, negative HA).[12] The integrity of this microstructural organization is a critical determinant of the mechanical properties of the LV, and disturbance of myofiber geometry may thus result in impaired cardiac function.[13] Diffusion tensor magnetic resonance imaging (DT-MRI) is a feasible tool to study the cardiac myofiber arrangement and has been applied in a variety of pathological conditions in humans as well as in animal studies.[9,10,14–16] However, there is a lack of data regarding the impact of subendocardial damage on myofiber organization and corresponding functional consequences.

In the present study, we aimed to characterize myocardial microstructure and function in an experimental model providing the opportunity to study isolated subendocardial fibrosis in the absence of major confounders like cardiac hypertrophy or altered loading conditions.[17] By combining comprehensive DT-MRI analyses with several measures available in patients, we sought to provide translational evidence for clinical observations. We hypothesized that subendocardial fibrosis (1) affects the myofiber arrangement in the LV; (2) leads to impaired cardiac function; and (3) is detectable by assessment of corresponding microstructural and functional changes.

Methods

The authors declare that all supporting data are available within the article and in the online-only Data Supplement. All in vivo experiments were approved by local authorities (Landesamt für Gesundheit und Soziales Berlin, Germany) and were conducted in accordance with the German Law on the protection of animals. All animals were kept in a 12 hour light/dark cycle and received standard diet ad libitum.

Study Protocol

Subendocardial damage was induced by subcutaneous injection of isoproterenol as described previously.[17,18] Male 129/Sv mice (6–8 weeks old; Janvier Labs, France) were treated for 4 consecutive days with either isoproterenol (n=20; 25 mg/kg; dissolved in saline) or saline as corresponding control (n=18, matched for weight). During the week after final treatment, exercise capacity was assessed by a graded exercise test protocol. After echocardiographic examination (including speckle-tracking echocardiography and dobutamine stress echocardiography) an additional week later, mice were euthanized, and tissues were harvested for further analyses. Hearts were sent to the MRI site (Comprehensive Heart Failure Center, University Hospital Wuerzburg, Germany) for high-resolution DT-MRI measurements in a 7 T scanner at a spatial resolution of 100×100×100 μm^3. Results were correlated with histology and gene expression analyses.

Detailed Methodology

The online-only Data Supplement contains detailed information on echocardiography, the graded exercise test protocol, tissue processing, DT-MRI measurements, histology, gene expression analyses, and statistics.

Results

One animal died after the third isoproterenol-application by reasons not further investigated; another isoproterenol-treated animal developed signs of myocardial infarction (ventricular aneurysm and impaired ejection fraction) and was, therefore, excluded from study results. All control animals finished the study protocol.

Gravimetric Measures and Cardiac Tissue Analyses

Weight development and final body weights were comparable between both groups (Table). No signs of cardiac hypertrophy or lung congestion were found during necropsy, as evident from indexed heart weights and lung wet/dry weight ratios, respectively (Table).

Isoproterenol-treated animals developed pronounced fibrotic lesions in the subendocardium, whereas subepicardial collagen content was similar in both groups (Figure 1A–1C). The degree of subendocardial fibrosis varied between the different cardiac segments (Figure S1 in the online-only Data Supplement) and was found to be highest at the apex of the LV (Figure 1D). Immunohistochemical analyses revealed the presence of $CD68^+$ macrophages within fibrotic lesions, which showed a comparable distribution pattern accordingly (Figure S2).

ANP (atrial natriuretic peptide) mRNA levels were significantly upregulated in the LV after treatment with isoproterenol (Figure 1E). These animals also showed a higher expression of genes involved in inflammation and extracellular matrix turnover, such as CD68, Galectin-3, and precursors of collagen I and III (Figure 1E). GDF15 (growth/differentiation factor 15) was not induced at this time point (Figure 1E). ST2 (interleukin 1 receptor-like 1) levels were significantly upregulated in isoproterenol-treated animals (Figure 1E).

Diffusion Metrics

DT-MRI parameters were assessed for each myocardial layer (subendocardium/subepicardium) and segment (base/mid/apex), or globally for the transmural myocardium and the whole LV (Figure 2A; Figure S3A). Animals with subendocardial fibrosis displayed significantly lower transmural and subendocardial mean diffusivity (MD; Figure 2B and 2C). Subepicardial MD decreased significantly at apex level only (Figure 2B and 2C). Fractional anisotropy (FA) did not differ between both groups in any layer or segment, although variability of FA values decreased after treatment with isoproterenol (Figure 2D; Figure S3B). All eigenvalues of the diffusion tensor were consistently lowered in the apical subendocardium only (Figure S3C–S3E).

Myofiber Arrangement

Myocardial microstructure was studied by 3-dimensional reconstruction of fiber tracts with respect to layer and segment (Figure 3). Both treatment groups showed the stereotypic arrangement of myofibers forming 2 counter-directional helices as illustrated in Figure 3A and 3B. Animals presenting with subendocardial damage showed a left-shift of HA in the LV towards more negative values (Figure 3C). On segmental level, this left-shift reached statistical significance at the apex region only (Figure S4). Analyses of the HA gradient across the myocardial wall revealed lower HAs in the meso-subepicardium of animals with subendocardial fibrosis (Figure 3D). This effect was present in all myocardial segments (Figure S4). Layer-specific analyses indicated that the observed left-shift was caused by a change of subepicardial HA towards steeper angles, whereas HAs in the subendocardium were comparable in all segments (Figure 3E). The reduction of subepicardial HA was evident in all myocardial segments (Figure 3E).

Cardiac Function

Ejection fraction and other parameters of global systolic function remained unchanged after isoproterenol-treatment (Table). Subendocardial fibrosis was accompanied by signs of diastolic dysfunction (Figure 4A); animals had prolonged isovolumic relaxation times (**$P<0.01$) and tended to have slower late filling rates in the transmitral flow profile ($P=0.07$; Table). Deceleration time of the early diastolic filling rate (E) was longer; however, differences did not reach statistical significance ($P=0.07$; Table). Early diastolic mitral annular velocity (e′) was lower (**$P<0.01$) leading to a reverse

Table. End Point Characteristics

Parameter	Control	Isoproterenol	*P* Value
Physiological data			
BW, g	26.2±0.4	26.7±0.3	0.36
ΔBW, %	+7.8±1.1	+9.1±1.0	0.40
Heart rate, bpm	370±7	347±11	0.10
Necropsy data			
Heart weight, mg	189±13	172±13	0.37
Heart weight/BW, mg/g	7.2±0.5	6.5±0.5	0.31
Heart weight/tibia length, mg/mm	11.7±1.1	10.2±0.8	0.27
Lung weight, wet/dry	4.6±0.3	4.9±0.2	0.44
Parasternal long axis view			
EF, %	47±1	46±1	0.57
FAC, %	32±1	30±1	0.47
EDV, μL	69±3	71±3	0.66
ESV, μL	30±2	34±3	0.38
Stroke volume, μL	30±2	29±1	0.52
Parasternal short axis view			
$EF_{Teichholz}$, %	56±1	53±3	0.44
FS, %	29±0.5	27±2	0.58
Apical 4-chamber view			
E, mm/s	729±17	739±26	0.78
A, mm/s	401±18	334±27	0.07
e′, mm/s	20±2	15±1	<0.01
a′, mm/s	16±2	17±1	0.68
E/A	1.9±0.1	2.4±0.2	0.07
E/e′	38±3	52±4	<0.01
a′/e′	0.8±0.1	1.2±0.1	0.03
IVRT, ms	19.2±0.6	22.2±0.6	<0.01
IVCT, ms	20.8±0.8	20.9±1.3	0.92
DT, ms	23.4±1.5	28.7±2.2	0.07
Tei index	0.70±0.01	0.76±0.02	0.03

Mean±SEM; n=10–12 per group; Student *t* test. ΔBW, change in body weight from baseline to final assessment; A, late diastolic filling rate; a′, late diastolic mitral annular velocity; BW, body weight; DT, deceleration time of early diastolic filling rate; E, early diastolic filling rate; e′, early diastolic mitral annular velocity; EF, ejection fraction; $EF_{Teichholz}$, EF according to Teichholz formula; FAC, fractional area change; FS, fractional shortening; EDV, end-diastolic volume; ESV, end-systolic volume; IVRT, isovolumic relaxation time; and IVCT, isovolumic contraction time. **P*<0.05; ***P*<0.01.

relation of e′ and late diastolic mitral annular velocity (**P*<0.05; Table). E/e′ ratios were significantly (***P*<0.01) increased in animals with subendocardial fibrosis (Table).

Myocardial Deformation

Myocardial strain and strain rate were assessed by speckle-tracking echocardiography in the parasternal long and short axis view (Figure 4B). In comparison to controls, isoproterenol-treated animals displayed markedly reduced global LS values (Figure 4C). Global peak radial and circumferential strain were unchanged (Figure 4C). A similar pattern was observed in strain rate, where global longitudinal strain (LS) rate declined in isoproterenol-treated animals, whereas global radial and circumferential Strain Rate remained unaffected (Figure 4C). Although LS was lowered in all myocardial segments, a significant reduction was observed in the apex of the LV only (Figure 4D).

Stress Tests

Dobutamine injections resulted in similar stress responses and did not unmask any signs of systolic dysfunction (Figure 4E; Table S3). Neither absolute peak stress values nor dobutamine-induced relative changes in echocardiographic parameters differed significantly between the 2 groups (Table S3). Similarly, no differences were observed during the graded exercise test; both groups were able to cope with comparable exercise stress in terms of covered distance and maximum running speed achieved (Figure 4F).

Diagnostic Assessment of Subendocardial Damage

Parameters with an appropriate area under the receiver operating characteristic curve for the detection of subendocardial fibrosis are displayed in Table S4. Transmural and subepicardial HA were superior predictors for subendocardial fibrosis among DT-MRI-derived parameters (Figure 5A; Table S4). Similarly, the ratio of positive to negative HA values allowed to distinguish both treatment groups (Table S4). Transmural and subendocardial MD lacked sufficient specificity, and the area under the receiver operating characteristic curve failed to reach statistical significance (Table S4). Among echocardiographic parameters, global peak LS and E/e′ were highly sensitive predictors for the presence of subendocardial fibrosis (Figure 5B; Table S4). Isovolumic relaxation time and global LS Rate also allowed to distinguish between both groups but had a remarkably lower sensitivity (Figure 5B; Table S4).

Linear regression analyses revealed clustered associations between parameters of longitudinal deformation and different DT-MRI-derived predictors for subendocardial damage (Figure 5C). Parameters of diastolic function occasionally correlated with DT-MRI measures but did not show distinct clustering (Figure 5C). Neither systolic function parameters nor radial or circumferential deformation indices showed any association (Figure 5C).

Discussion

In this experimental study, we showed that subendocardial fibrosis (1) induced changes in fiber orientation predominantly in remote regions; (2) was accompanied by signs of diastolic dysfunction and reduced longitudinal deformation, whereas systolic function and cardiac stress response remained preserved; and (3) was detectable via assessment of corresponding microstructural and functional changes.

Subendocardial Vulnerability

Metabolic demand, coronary blood supply, and compressive forces are transmurally heterogeneous where the subendocardium is at higher risk for injury than the outer layers.[1] As a consequence, several cardiovascular risk factors have been shown to affect preferentially the subendocardium during formation of cardiac organ damage (eg, hypertension,[2] diabetes mellitus,[3] ischemic heart disease,[4] and age[5]). Therefore, diagnostic markers of subendocardial status might facilitate early detection of cardiac damage, disease monitoring, and timely onset of treatment already during asymptomatic states. However, direct evidence for subendocardial pathologies is difficult to obtain in patients, and it often remains unclear whether observed changes in noninvasive surrogates are actually because of subendocardial impairment.[20–24]

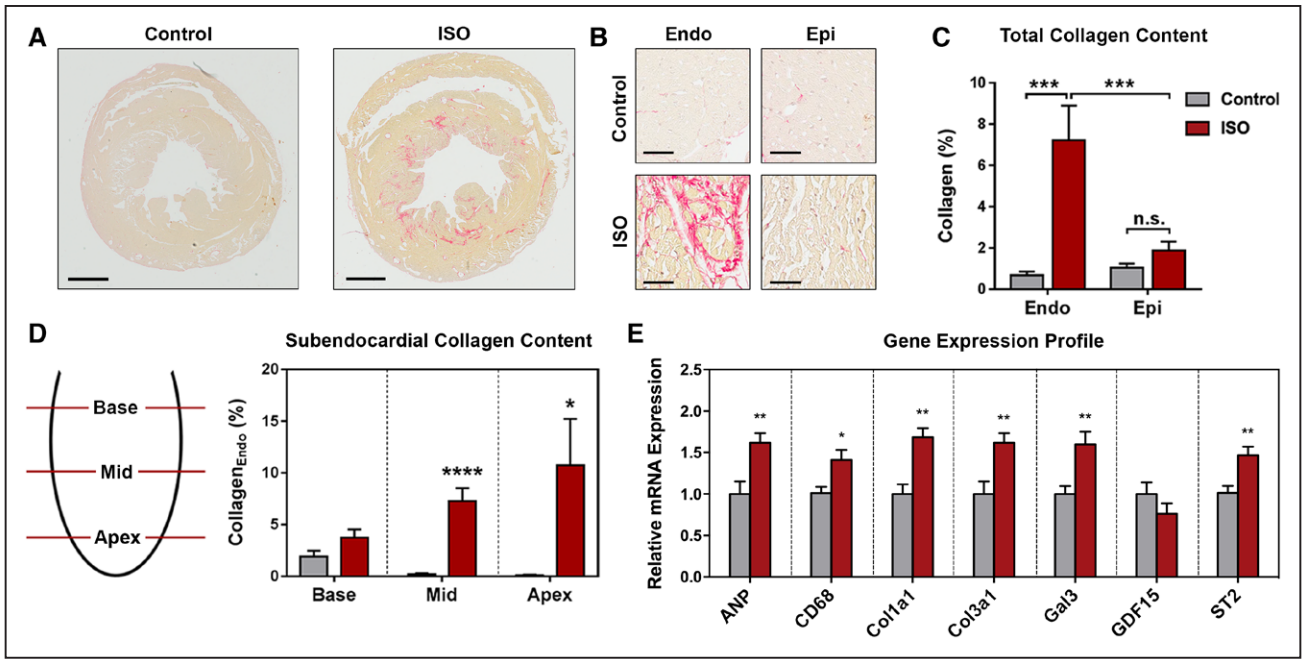

Figure 1. Cardiac tissue analyses. **A**, Representative histology of mid-myocardial cross-sections stained with picrosirius red (scale bar: 1 mm). **B**, Magnified regions within subendocardium and subepicardium (scale bar: 40 μm). **C**, Layer-specific quantification of collagen content (n=10–13 per group; 2-way ANOVA followed by Bonferroni post hoc test). **D**, Segment-specific quantification of subendocardial collagen content (n=10–13 per group; Student *t* test). **E**, Gene expression profile of the left ventricle (n=6 per group; Student *t* test). Collagen$_{Endo}$ indicates subendocardial collagen content; Endo, subendocardium; Epi, subepicardium; ISO, isoproterenol; and n.s., not significant. Mean±SEM; **P*<0.05; ***P*<0.01; ****P*<0.001; and *****P*<0.0001.

Here, we investigated an experimental model of subendocardial fibrosis in the absence of major confounders like cardiac hypertrophy or altered loading conditions,[17,18] which allowed to establish cause-effect relationships under controlled conditions. Application of isoproterenol aggravates the discrepancy between subendocardial oxygen demand and supply leading to ischemic damage in the subendocardium.[25] Accordingly, necrosis, apoptosis, and inflammatory pathways may have contributed to the observed phenotype, as well as differences in calcium signaling, coronary microcirculation, and membrane permeability.[25] The presence of CD68$^+$ cells 2 weeks after final isoproterenol treatment indicates that sustained immune response may also play a role.

Isoproterenol acts via β-adrenergic receptors, whose density is highest at the apex of the LV.[26] Accordingly, damage in this model is predominantly located in apical regions, as shown before.[27]

Microstructural Changes in Response to Subendocardial Damage

Our understanding of structural-functional relationships in the heart is incomplete.[28] DT-MRI is a feasible tool to study the 3-dimensional myofiber arrangement that has been applied in various cardiovascular pathologies in both experimental models[9,15,16,19] and patients.[10,14,29] Despite the growing wealth of cardiac DT-MRI studies, however, there is a lack of data regarding changes that occur during early disease states and investigation of layer-specific alterations.[30] Additionally, the sequential morphological and functional changes during transition from initial subendocardial damage to transmural affection are largely unclear. To our knowledge, this is the first application of DT-MRI to characterize the impact of subendocardial damage on myocardial microstructure.

The effect of fibrosis on MD and FA is controversial.[9,29,31] Subendocardial scarring was accompanied by decreased MD and unaltered FA, which is in accordance with a study by Wu et al[9] that showed decreased subendocardial MD but unchanged transmural FA in the scar tissue after myocardial infarction. Similarly, Strijkers et al[31] reported on reduced MD and increased FA in the infarct region. In contrast, other studies attributed myocardial fibrosis to increased MD and decreased FA.[29,32] This implies that changes in MD might be a promising, yet nonspecific marker for myocardial fibrosis and that future studies are needed to identify morphological correlates for changes in these parameters under different pathological conditions.

In general, MD is considered to decrease with increased cellularity or reduced extracellular space, respectively. Isoproterenol-treatment is known to induce cardiomyocyte hypertrophy and collagen deposition that fills major parts of the extracellular space,[33] both conditions in which free extracellular space is reduced. We, therefore, hypothesize that the observed decline in MD might be due to the relative loss of extracellular space and the consecutive slower diffusion of water molecules in this particular model.

It has been shown that residual myofibers serve as a scaffold for newly developing collagen fiber tracts during scar formation, and that these collagen fibers have the same orientation as surrounding myofibers.[34] FA is considered a measure of directional coherence and orientational integrity. Accordingly, such structured collagen fibers may account for observed unaltered FA in case of no greater disturbance of tissue organization.

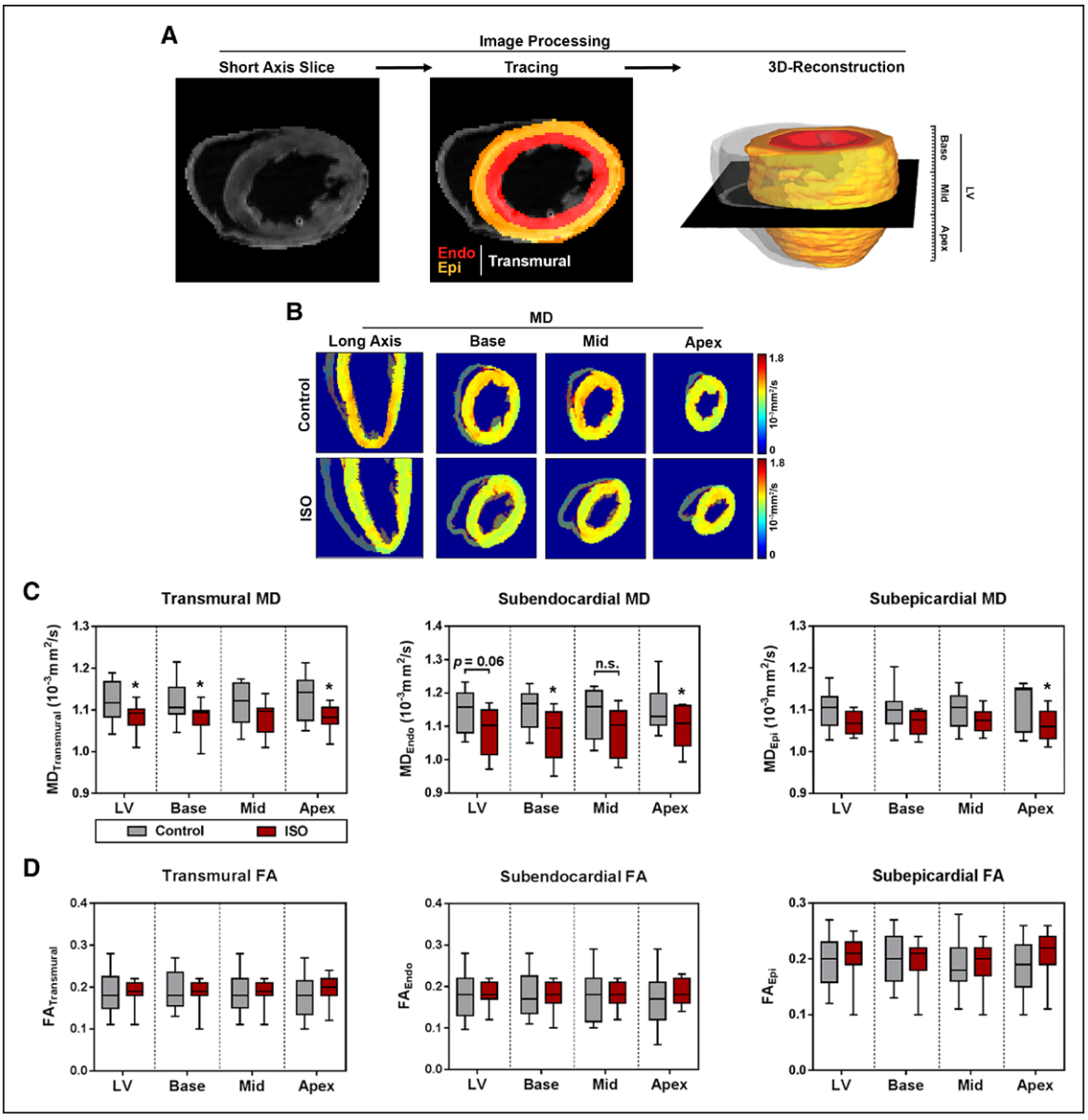

Figure 2. Diffusion tensor magnetic resonance imaging post-processing and diffusion metrics. **A**, Endocardial and epicardial borders were traced manually in multiple short axis slices per heart, and subendocardium (Endo) and subepicardium (Epi) were defined as regions of interest. Subsequently, 3-dimensional volumes were rendered by tomographic reconstruction allowing analyses of both regions for the whole left ventricle (LV) or within myocardial segments (base/mid/apex). **B**, Representative color maps for mean diffusivity (MD) in a reconstructed cardiac long axis and different myocardial short axis segments. **C**, Analysis of MD. **D**, Analysis of fractional anisotropy (FA). Medians and quartiles with minimum and maximum values; n=9–11 per group; Student *t* test. **P*<0.05. ISO indicates isoproterenol.

Notably, no changes in the subendocardial HA were observed despite histological proof of subendocardial fibrotic lesions. Again, formation of collagen fibers running in parallel to residual myofiber tracts[34] may be a likely explanation. In contrast to complete coronary occlusion, scarring in this model occurs next to viable myofiber tracts, and damage is limited to the subendocardium. As a putative mechanism, newly formed collagen fibers may have the same orientation as surrounding myofibers and the ones they replace in response to damage. In the latter case, no greater changes in HA may be detectable.

Subendocardial fibrosis was accompanied by a left shift in HA towards lower values, which is present also in other pathologies.[11,14,16] Interestingly, this left-shift was caused predominantly by subepicardial but not subendocardial myofibers. This suggests that circumscribed subendocardial damage affects also remote regions and induces microstructural remodeling within the entire LV. Similarly, microstructural changes in response to myocardial infarction also involve the remote zone, in which a left shift in HA can be observed.[9] It remains unclear whether this represents adaptive reorientation or passive mechanisms, and further studies are required to clarify the biological relevance of these findings.

Functional Changes in Response to Subendocardial Damage

Isolated subendocardial damage resulted in a phenotype resembling several hallmarks of cardiovascular high-risk patients in the absence of heart failure symptoms or signs. Since

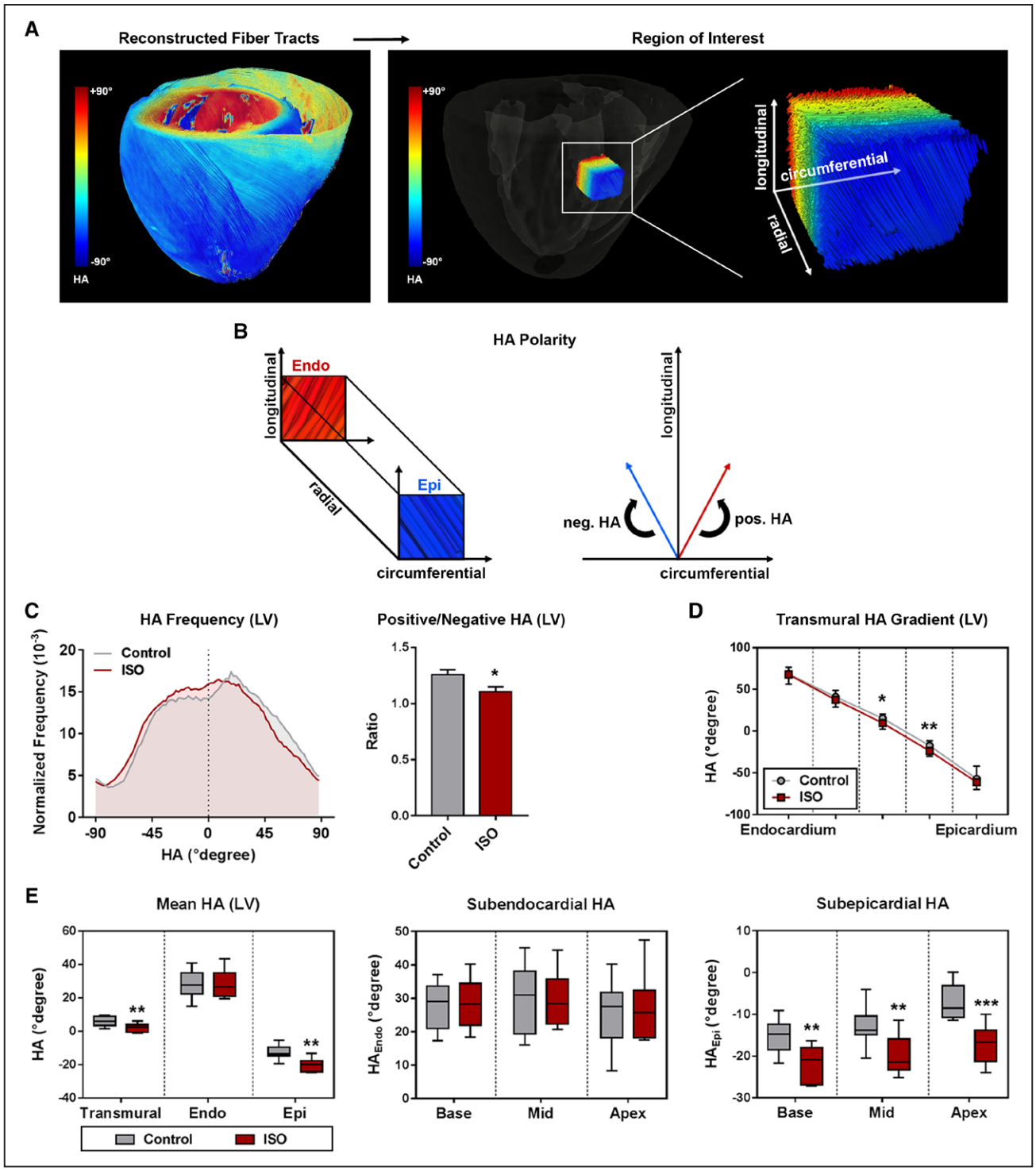

Figure 3. Myofiber geometry. **A**, Representative reconstruction of fiber tracts: helix angle (HA) in the left ventricle (LV) changes continuously from positive values in the subendocardium (right-handed helix), over neutral in the mesocardium, to negative values in the subepicardium (left-handed helix). **B**, Definition of HA-polarity. Mean±SEM (**C**, **D**) or medians and quartiles with minimum and maximum values. **E**, Analysis of HA. Medians and quartiles with minimum and maximum values; n=9–11 per group; Student *t* test. Endo indicates subendocardium; Epi, subepicardium; and ISO, isoproterenol. **P*<0.05 and ***P*<0.01.

impairment of either subendocardium, subepicardium, or transmural myocardium results in distinct phenotypes, it has been proposed to classify heart failure according to the damaged myocardial layer(s).[35,36] Selective subendocardial involvement is usually considered a marker of subclinical disease,[1] which may be accompanied by diastolic dysfunction but preserved ejection fraction together with reduced longitudinal but unaltered radial and circumferential mechanics in patients.[36] The experimental model we used demonstrated a comparable phenotype, which provides evidence for corresponding classification.

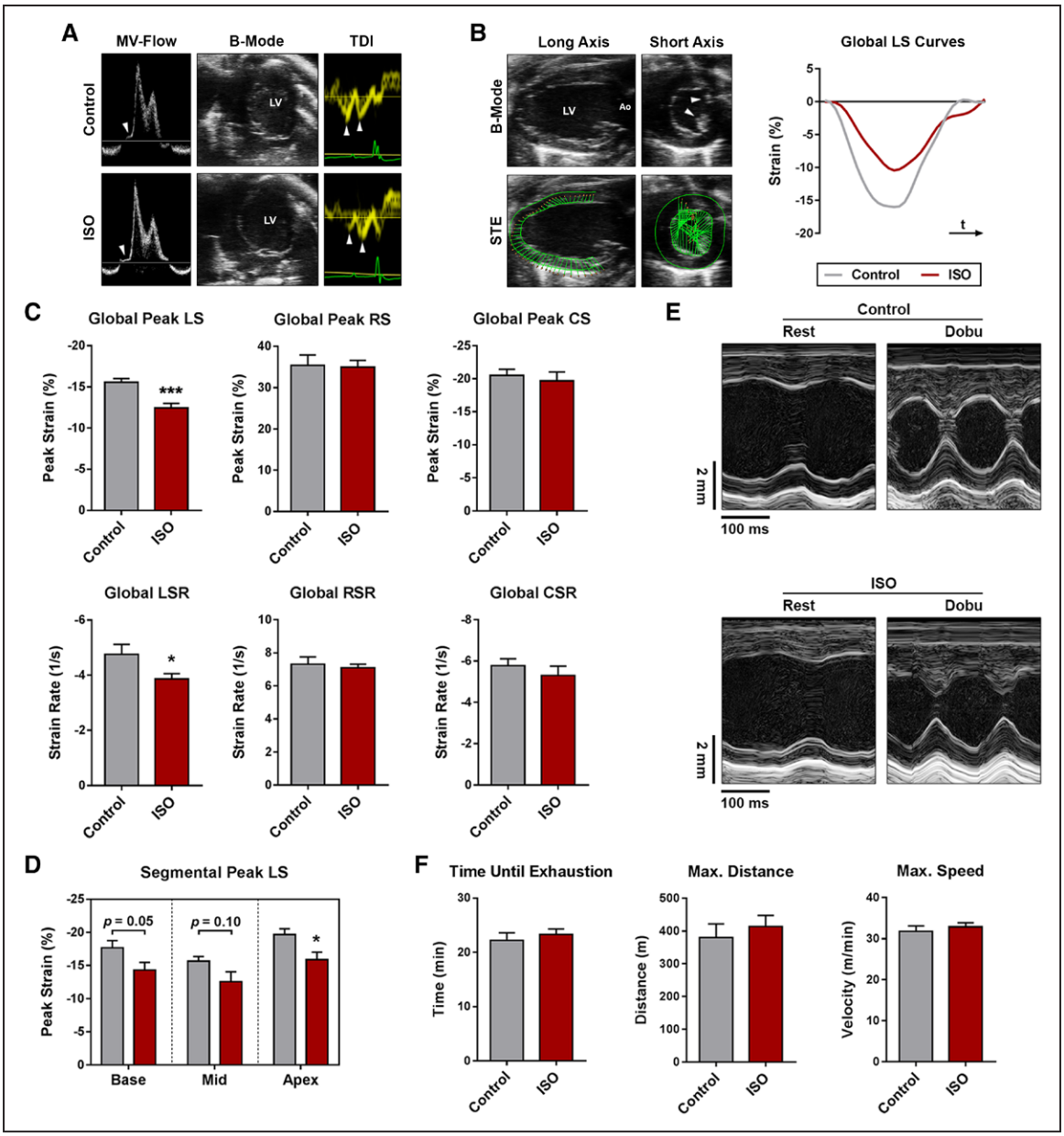

Figure 4. Functional analyses. **A**, Representative transmitral flow patterns (**left**; arrows indicate isovolumic relaxation time), B-mode images of the apical 4 chamber view (**mid**), and tissue Doppler analyses of the septal mitral annulus (**right**; arrows indicate early and late diastolic mitral annular velocities). **B**, Speckle-tracking echocardiography and representative longitudinal strain (LS) curves over one cardiac cycle (arrows indicate papillary muscles). **C**, Global peak strain and global strain rate. **D**, Segmental peak LS. **E**, Representative M-mode images acquired in the parasternal short axis view at rest and during Dobu stress. **F**, Results of the graded exercise test protocol. n=7–12 per group; Student *t* test. Ao indicates aorta; Col1a1, collagen type I, alpha 1 chain; Col3a1, collagen type III, alpha 1 chain; $Collagen_{Endo}$, subendocardial collagen content; CS, circumferential strain; CSR, circumferential strain rate; Dobu, dobutamine; ISO, isoproterenol; LSR, longitudinal strain rate; LV, left ventricle; MV-Flow, transmitral flow pattern; RS, radial strain; RSR, radial strain rate; STE, speckle-tracking echocardiography; and TDI, tissue Doppler imaging. Mean±SEM; **P*<0.05 and ****P*<0.001.

Animals with subendocardial fibrosis showed mild diastolic dysfunction, suggesting that isolated subendocardial fibrosis alone may account for preclinical diastolic dysfunction. As such, subendocardial fibrosis may be of considerable relevance given that preclinical diastolic dysfunction has been shown to be highly prevalent in large population-based studies and that a relevant portion of these subjects shows a progression to congestive heart failure over time.[37,38] Our findings are supported by clinical studies reporting on preclinical diastolic dysfunction in asymptomatic patients with risk factors that are known to affect preferentially the subendocardium.[21,22] However, these studies relied on nonspecific surrogates and did not provide direct evidence for subendocardial pathologies, which warrants further investigations in patients with confirmed subendocardial damage.

Longitudinal, yet not radial or circumferential deformation declined in animals with subendocardial fibrosis. Reduced LS is a common feature of both high-risk patients[21–24] and subjects with overt heart failure. Since longitudinal mechanics of the LV are determined mainly by subendocardial myofibers, impaired LS parameters are well-accepted surrogates of putative subendocardial damage.[1] Reduced LS has been linked

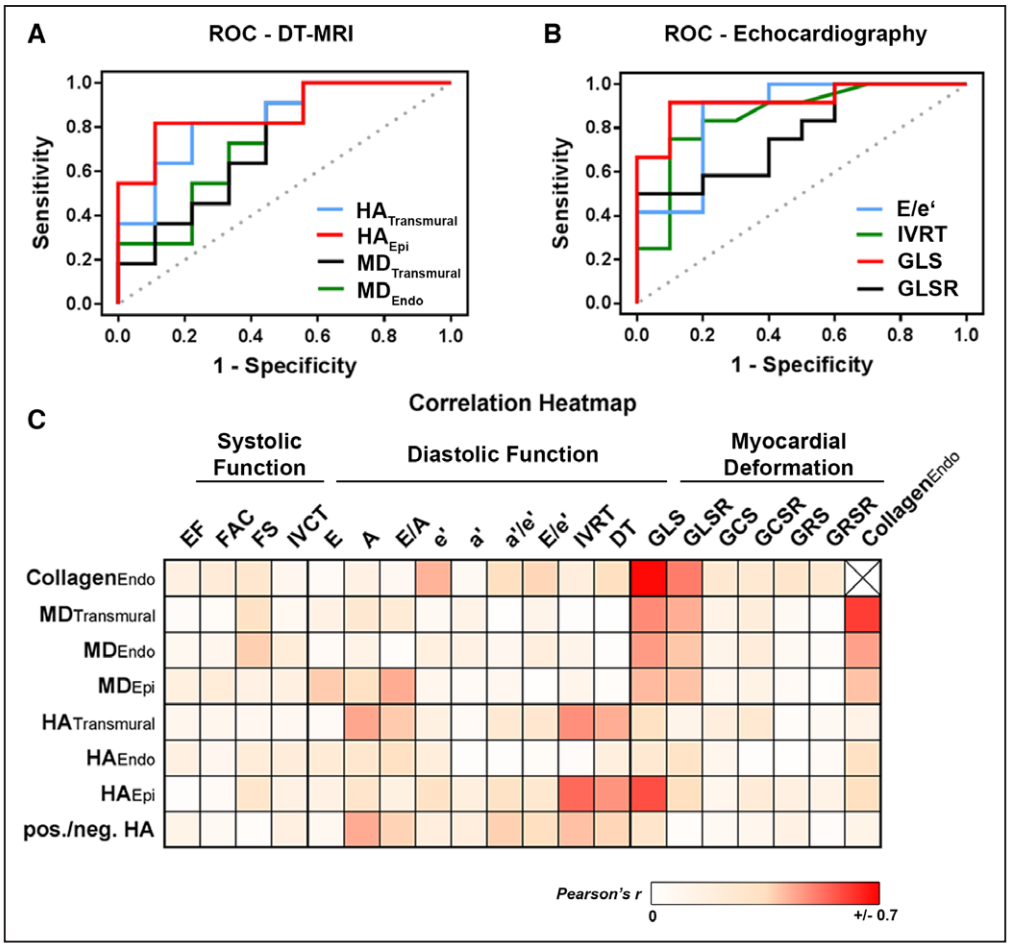

Figure 5. Receiver operating characteristic (ROC) curves and correlation analyses. **A**, ROC curves for diffusion tensor magnetic resonance imaging (DT-MRI)-derived parameters to detect subendocardial fibrosis. **B**, ROC curves for echocardiographic parameters to detect subendocardial fibrosis. **C**, Color-coded correlation coefficients of various parameters (Pearson correlation coefficient *r*). A indicates late diastolic filling rate; a′, late diastolic mitral annular velocity; DT, deceleration time of early diastolic filling rate; E, early diastolic filling rate; e′, early diastolic mitral annular velocity; EF, ejection fraction; FAC, fractional area change; FS, fractional shortening; GCS, global peak circumferential strain; GCRS, global circumferential strain rate; GLS, global peak longitudinal strain; GLSR, global longitudinal strain rate; GRS, global peak radial strain; GRSR, global radial strain rate; HA_{Epi}, subepicardial helix angle; HA_{Endo}, subendocardial helix angle; $HA_{Transmural,}$ transmural helix angle; IVCT, isovolumic contraction time; IVRT, isovolumic relaxation time; MD_{Epi}, subepicardial mean diffusivity; MD_{Endo}, subendocardial mean diffusivity; and $MD_{Transmural}$, transmural mean diffusivity.

to subendocardial fibrosis in preclinical patients due to correlations with circulating biomarkers of increased extracellular matrix turnover.[20,21] Our results confirm that reduced longitudinal deformation indeed closely reflects subendocardial fibrosis, and that global peak LS can serve for diagnostic assessment. This is in accordance with previous studies in this model[18] and in experimental hypertensive heart disease.[2]

Biomarkers play a pivotal role in the clinical diagnosis of heart failure, and several studies demonstrated that circulating markers of cell damage, extracellular matrix turnover, and inflammation are elevated in these patients.[39] We found that several biomarkers associated with heart failure were upregulated in the LV of animals presenting with isolated subendocardial fibrosis. This might be of interest for future studies regarding biomarker assessment in preclinical high-risk patients.

Limitations

The isoproterenol-model is limited with regards to the comparability of the human situation, and technical issues of small animal echocardiography (eg, susceptibility to off-axis imaging, spatial/temporal resolution, and assessment under anesthesia) should be considered. Myocardial deformation analysis by speckle-tracking echocardiography in small animals is limited regarding assessment of left-ventricular torsion. The latter may be assessed by magnetic resonance imaging, which, however, was performed ex vivo in our study, and thus did not allow to study dynamic changes occurring during the cardiac cycle. The model we used is known to develop elevated diastolic pressures,[40] and we observed increased E/e′ ratios as a noninvasive surrogate. However, invasive measurements of hemodynamics were not performed in the present study. We applied an established graded exercise test protocol that was originally developed for another mouse strain,[41] and that has never been evaluated in 129/Sv mice before. Due to technical issues, only systolic function parameters could have been assessed during dobutamine stress. Biomarker expression was determined 2 weeks after final treatment with isoproterenol. Despite this relatively long time period, direct action of isoproterenol on biomarker expression cannot be ruled out. There was no readout for successful cardioplegic arrest, and fixation during different phases of the cardiac cycle may have an impact on DT-MRI analyses. Hearts were scanned after

comparable time intervals of fixation, but absolute values of MD and FA might have been affected by formalin-fixation.[42]

Conclusions

Circumscribed subendocardial damage can account for several hallmarks observed in cardiovascular high-risk patients. Microstructural remodeling in response to subendocardial damage involves also other myocardial layers indicating a newly identified remote process.

Finally, our data provide translational evidence for both established surrogates of subendocardial damage and novel markers of microstructural remodeling that might serve as diagnostic measures for early detection of cardiac impairment. Among these, global peak LS and subepicardial HA were the best predictors of subendocardial damage.

Perspectives

As a future direction, DT-MRI may be used to identify characteristic microstructural changes in various cardiac diseases facilitating diagnostic application. Based on this, DT-MRI might help to further improve our understanding of cardiac pathologies and might ultimately serve as a diagnostic tool in patients. The present work indicates that microstructural changes are present already in early disease stages, and that DT-MRI is capable of assessing them. These findings have to be confirmed in patients by in vivo DT-MRI for translation of our results. The transmural heterogeneity of microstructural changes as observed in our study should be considered in future investigations.

Acknowledgments

We thank Beata Höft for her excellent technical assistance, Moritz Fischer for the help in designing the DT-MRI setup, Franziska Schwarz (scivisto.com) for the graphical abstract, and Andrew D. Scott (Royal Brompton Hospital and Imperial College London) for insightful discussions regarding the DT-MRI data. Parts of this work will be used in the doctoral thesis of David Lohr.

Sources of Funding

This work was supported by the German Centre for Cardiovascular Research (DZHK; BER 5.4 PR) and by the German Ministry of Education and Research (grant numbers 01EO1004 and 01EO1504). Arne Thiele is supported by a research grant of the German cardiac society (DGK).

Disclosures

None.

References

1. Stanton T, Marwick TH. Assessment of subendocardial structure and function. *JACC Cardiovasc Imaging.* 2010;3:867–875. doi: 10.1016/j.jcmg.2010.05.011
2. Ishizu T, Seo Y, Kameda Y, Kawamura R, Kimura T, Shimojo N, Xu D, Murakoshi N, Aonuma K. Left ventricular strain and transmural distribution of structural remodeling in hypertensive heart disease. *Hypertension.* 2014;63:500–506. doi: 10.1161/HYPERTENSIONAHA.113.02149
3. Martinez DA, Guhl DJ, Stanley WC, Vailas AC. Extracellular matrix maturation in the left ventricle of normal and diabetic swine. *Diabetes Res Clin Pract.* 2003;59:1–9.
4. Bache RJ, Schwartz JS. Effect of perfusion pressure distal to a coronary stenosis on transmural myocardial blood flow. *Circulation.* 1982;65:928–935. doi: 10.1161/01.CIR.65.5.928
5. Wanagat J, Wolff MR, Aiken JM. Age-associated changes in function, structure and mitochondrial genetic and enzymatic abnormalities in the Fischer 344 x Brown Norway F(1) hybrid rat heart. *J Mol Cell Cardiol.* 2002;34:17–28. doi: 10.1006/jmcc.2001.1483
6. Harrison DG, Florentine MS, Brooks LA, Cooper SM, Marcus ML. The effect of hypertension and left ventricular hypertrophy on the lower range of coronary autoregulation. *Circulation.* 1988;77:1108–1115. doi: 10.1161/01.CIR.77.5.1108
7. Fujii M, Nuno DW, Lamping KG, Dellsperger KC, Eastham CL, Harrison DG. Effect of hypertension and hypertrophy on coronary microvascular pressure. *Circ Res.* 1992;71:120–126.
8. Mor-Avi V, Lang RM, Badano LP, et al. Current and evolving echocardiographic techniques for the quantitative evaluation of cardiac mechanics: ASE/EAE consensus statement on methodology and indications endorsed by the Japanese Society of Echocardiography. *J Am Soc Echocardiogr.* 2011;24:277–313. doi: 10.1016/j.echo.2011.01.015
9. Wu Y, Zhang LJ, Zou C, Tse HF, Wu EX. Transmural heterogeneity of left ventricular myocardium remodeling in postinfarct porcine model revealed by MR diffusion tensor imaging. *J Magn Reson Imaging.* 2011;34:43–49. doi: 10.1002/jmri.22589
10. Nielles-Vallespin S, Khalique Z, Ferreira PF, et al. Assessment of myocardial microstructural dynamics by *in vivo* diffusion tensor cardiac magnetic resonance. *J Am Coll Cardiol.* 2017;69:661–676. doi: 10.1016/j.jacc.2016.11.051
11. von Deuster C, Sammut E, Asner L, Nordsletten D, Lamata P, Stoeck CT, Kozerke S, Razavi R. Studying dynamic myofiber aggregate reorientation in dilated cardiomyopathy using in vivo magnetic resonance diffusion tensor imaging. *Circ Cardiovasc Imaging*. 2016;9:e005018. doi: 10.1161/CIRCIMAGING.116.005018
12. Streeter DD Jr, Spotnitz HM, Patel DP, Ross J Jr, Sonnenblick EH. Fiber orientation in the canine left ventricle during diastole and systole. *Circ Res.* 1969;24:339–347. doi: 10.1161/01.RES.24.3.339
13. Palit A, Bhudia SK, Arvanitis TN, Turley GA, Williams MA. Computational modelling of left-ventricular diastolic mechanics: effect of fibre orientation and right-ventricle topology. *J Biomech.* 2015;48:604–612. doi: 10.1016/j.jbiomech.2014.12.054
14. Wu MT, Tseng WY, Su MY, Liu CP, Chiou KR, Wedeen VJ, Reese TG, Yang CF. Diffusion tensor magnetic resonance imaging mapping the fiber architecture remodeling in human myocardium after infarction: correlation with viability and wall motion. *Circulation.* 2006;114:1036–1045. doi: 10.1161/CIRCULATIONAHA.105.545863
15. Sosnovik DE, Mekkaoui C, Huang S, Chen HH, Dai G, Stoeck CT, Ngoy S, Guan J, Wang R, Kostis WJ, Jackowski MP, Wedeen VJ, Kozerke S, Liao R. Microstructural impact of ischemia and bone marrow-derived cell therapy revealed with diffusion tensor magnetic resonance imaging tractography of the heart in vivo. *Circulation.* 2014;129:1731–1741. doi: 10.1161/CIRCULATIONAHA.113.005841
16. Wu EX, Wu Y, Nicholls JM, Wang J, Liao S, Zhu S, Lau CP, Tse HF. MR diffusion tensor imaging study of postinfarct myocardium structural remodeling in a porcine model. *Magn Reson Med.* 2007;58:687–695. doi: 10.1002/mrm.21350
17. Samuel CS, Bodaragama H, Chew JY, Widdop RE, Royce SG, Hewitson TD. Serelaxin is a more efficacious antifibrotic than enalapril in an experimental model of heart disease. *Hypertension.* 2014;64:315–322. doi: 10.1161/HYPERTENSIONAHA.114.03594
18. Beyhoff N, Brix S, Betz IR, Klopfleisch R, Foryst-Ludwig A, Krannich A, Stawowy P, Knebel F, Grune J, Kintscher U. Application of speckle-tracking echocardiography in an experimental model of isolated subendocardial damage. *J Am Soc Echocardiogr.* 2017;30:1239.e2–1250.e2. doi: 10.1016/j.echo.2017.08.006
19. Lohr D, Terekhov M, Weng AM, Schroeder A, Walles H, Schreiber LM. Spin echo based cardiac diffusion imaging at 7T: an ex vivo study of the porcine heart at 7T and 3T. *PLoS One.* 2019;14:e0213994. doi: 10.1371/journal.pone.0213994
20. Ikonomidis I, Tzortzis S, Triantafyllidi H, Parissis J, Papadopoulos C, Venetsanou K, Trivilou P, Paraskevaidis I, Lekakis J. Association of impaired left ventricular twisting-untwisting with vascular dysfunction, neurohumoral activation and impaired exercise capacity in hypertensive heart disease. *Eur J Heart Fail.* 2015;17:1240–1251. doi: 10.1002/ejhf.403
21. Kang SJ, Lim HS, Choi BJ, Choi SY, Hwang GS, Yoon MH, Tahk SJ, Shin JH. Longitudinal strain and torsion assessed by two-dimensional speckle tracking correlate with the serum level of tissue inhibitor of matrix metalloproteinase-1, a marker of myocardial fibrosis, in patients with hypertension. *J Am Soc Echocardiogr.* 2008;21:907–911. doi: 10.1016/j.echo.2008.01.015

22. Mizuguchi Y, Oishi Y, Miyoshi H, Iuchi A, Nagase N, Oki T. The functional role of longitudinal, circumferential, and radial myocardial deformation for regulating the early impairment of left ventricular contraction and relaxation in patients with cardiovascular risk factors: a study with two-dimensional strain imaging. *J Am Soc Echocardiogr.* 2008;21:1138–1144. doi: 10.1016/j.echo.2008.07.016
23. Parikh JD, Hollingsworth KG, Wallace D, Blamire AM, MacGowan GA. Normal age-related changes in left ventricular function: role of afterload and subendocardial dysfunction. *Int J Cardiol.* 2016;223:306–312. doi: 10.1016/j.ijcard.2016.07.252
24. Lumens J, Delhaas T, Arts T, Cowan BR, Young AA. Impaired subendocardial contractile myofiber function in asymptomatic aged humans, as detected using MRI. *Am J Physiol Heart Circ Physiol.* 2006;291:H1573–H1579. doi: 10.1152/ajpheart.00074.2006
25. Rona G. Catecholamine cardiotoxicity. *J Mol Cell Cardiol.* 1985;17:291–306. doi: 10.1016/S0022-2828(85)80130-9
26. Mori H, Ishikawa S, Kojima S, Hayashi J, Watanabe Y, Hoffman JI, Okino H. Increased responsiveness of left ventricular apical myocardium to adrenergic stimuli. *Cardiovasc Res.* 1993;27:192–198. doi: 10.1093/cvr/27.2.192
27. Collins P, Billings CG, Barer GR, Daly JJ, Jolly A. Quantitation of isoprenaline-induced changes in the ventricular myocardium. *Cardiovasc Res.* 1975;9:797–806. doi: 10.1093/cvr/9.6.797
28. Buckberg GD, Weisfeldt ML, Ballester M, et al. Left ventricular form and function: scientific priorities and strategic planning for development of new views of disease. *Circulation.* 2004;110:e333–e336. doi: 10.1161/01.CIR.0000143625.56882.5C
29. Abdullah OM, Drakos SG, Diakos NA, Wever-Pinzon O, Kfoury AG, Stehlik J, Selzman CH, Reid BB, Brunisholz K, Verma DR, Myrick C, Sachse FB, Li DY, Hsu EW. Characterization of diffuse fibrosis in the failing human heart via diffusion tensor imaging and quantitative histological validation. *NMR Biomed.* 2014;27:1378–1386. doi: 10.1002/nbm.3200
30. Watson SR, Dormer JD, Fei B. Imaging technologies for cardiac fiber and heart failure: a review. *Heart Fail Rev.* 2018;23:273–289. doi: 10.1007/s10741-018-9684-1
31. Strijkers GJ, Bouts A, Blankesteijn WM, Peeters TH, Vilanova A, van Prooijen MC, Sanders HM, Heijman E, Nicolay K. Diffusion tensor imaging of left ventricular remodeling in response to myocardial infarction in the mouse. *NMR Biomed.* 2009;22:182–190. doi: 10.1002/nbm.1299
32. Pop M, Ghugre NR, Ramanan V, Morikawa L, Stanisz G, Dick AJ, Wright GA. Quantification of fibrosis in infarcted swine hearts by ex vivo late gadolinium-enhancement and diffusion-weighted MRI methods. *Phys Med Biol.* 2013;58:5009–5028. doi: 10.1088/0031-9155/58/15/5009
33. Pick R, Jalil JE, Janicki JS, Weber KT. The fibrillar nature and structure of isoproterenol-induced myocardial fibrosis in the rat. *Am J Pathol.* 1989;134:365–371.
34. Goergen CJ, Chen HH, Sakadžić S, Srinivasan VJ, Sosnovik DE. Microstructural characterization of myocardial infarction with optical coherence tractography and two-photon microscopy. *Physiol Rep.* 2016;4:e12894. doi: 10.14814/phy2.12894
35. Sengupta PP, Narula J. Reclassifying heart failure: predominantly subendocardial, subepicardial, and transmural. *Heart Fail Clin.* 2008;4:379–382. doi: 10.1016/j.hfc.2008.03.013
36. Geyer H, Caracciolo G, Abe H, Wilansky S, Carerj S, Gentile F, Nesser HJ, Khandheria B, Narula J, Sengupta PP. Assessment of myocardial mechanics using speckle tracking echocardiography: fundamentals and clinical applications. *J Am Soc Echocardiogr.* 2010;23:351–369; quiz 453. doi: 10.1016/j.echo.2010.02.015
37. Kane GC, Karon BL, Mahoney DW, Redfield MM, Roger VL, Burnett JC Jr, Jacobsen SJ, Rodeheffer RJ. Progression of left ventricular diastolic dysfunction and risk of heart failure. *JAMA.* 2011;306:856–863. doi: 10.1001/jama.2011.1201
38. Vogel MW, Slusser JP, Hodge DO, Chen HH. The natural history of preclinical diastolic dysfunction: a population-based study. *Circ Heart Fail.* 2012;5:144–151. doi: 10.1161/CIRCHEARTFAILURE.110.959668
39. de Boer RA, Daniels LB, Maisel AS, Januzzi JL Jr. State of the art: newer biomarkers in heart failure. *Eur J Heart Fail.* 2015;17:559–569. doi: 10.1002/ejhf.273
40. Brooks WW, Conrad CH. Isoproterenol-induced myocardial injury and diastolic dysfunction in mice: structural and functional correlates. *Comp Med.* 2009;59:339–343.
41. Petrosino JM, Heiss VJ, Maurya SK, Kalyanasundaram A, Periasamy M, LaFountain RA, Wilson JM, Simonetti OP, Ziouzenkova O. Graded maximal exercise testing to assess mouse cardio-metabolic phenotypes. *PLoS One.* 2016;11:e0148010. doi: 10.1371/journal.pone.0148010
42. Giannakidis A, Gullberg GT, Pennell DJ, Firmin DN. Value of formalin fixation for the prolonged preservation of rodent myocardial microanatomical organization: evidence by MR diffusion tensor imaging. *Anat Rec (Hoboken).* 2016;299:878–887. doi: 10.1002/ar.23359

Novelty and Significance

What Is New?

- First characterization of microstructural changes in response to subendocardial damage by diffusion tensor magnetic resonance imaging.
- Comprehensive assessment of functional consequences of isolated subendocardial damage in the absence of confounding factors.

What Is Relevant?

- Subendocardial damage leads to microstructural reorganization of cardiac fibers predominantly in remote regions.
- Subendocardial damage can account for several observations in cardiovascular high-risk patients, and assessment of corresponding changes may facilitate early detection of cardiac damages.

Summary

Isolated subendocardial damage resulted in a phenotype resembling several hallmarks of cardiovascular high-risk patients, and changes in myofiber arrangement under these conditions were characterized for the first time.

3.4 Myocardial Infarction after High-Dose Catecholamine Application - A Case Report from an Experimental Imaging Study

〉 Published in *frontiers in Cardiovascular Medicine* – 2020[180]

These citations have been applied in this publication.[56,150,152,175,177,181-188]

Survival of MI is likely to result in HF, which represents one of today's major health burdens. Despite this fact, there is still a lack of understanding when it comes to structural and functional alterations of the myocardium as well as structure-function interactions.

This is a case report of an animal that exhibited features of MI following treatment with the catecholamine isoproterenol in an experimental imaging study in mice (chapter 3.3, page 49). In this study we employed a published animal model of isolated subendocardial fibrosis, where mice received subcutaneous injections of 25 mg/kg isoproterenol for four consecutive days. The study protocol also included state-of-the-art imaging modalities: ultra-high frequency echocardiography for the characterization of cardiac function, speckle tracking analysis for the assessment of myocardial strain, and high resolution *ex vivo* DTI for the characterization of myocardial microstructure. Detailed histopathology was performed to validate and evaluate results observed using either imaging modality.

Compared to its littermates, recovery times following the four injections were slightly prolonged. Echocardiography two weeks after treatment with isoproterenol showed wall thinning and prominent apical aneurysm, strongly increased LV volumes, distinct reductions in global systolic function, and akinetic apical segments. Speckle tracking revealed reduced radial strain in corresponding apical segments and more pronounced alteration in longitudinal strain compared to other animals treated with isoproterenol (-4.6 vs. -12.5±1.9%). Histology showed transmural scarring in the apex and confirmed aneurysmatic wall thinning as well as replacement fibrosis. Fiber tracking based on DTI data illustrated that tract reconstruction on a submillimeter scale was possible in some areas of the infarct zone, whereas tract reconstruction failed for increasingly long distances. This observed disarray in orientation and the loss of contractile fiber tracts correlated well with segments exhibiting increased mean diffusivity, impaired cardiac function, and replacement fibrosis.

While the evaluation of cardiac function via non-invasive imaging modalities is a keystone of the diagnosis and follow-up assessment of both MI and HF, underlying structural changes are currently not assessable in clinical routine practice. In this pre-clinical case report we demonstrate that emerging imaging techniques such as speckle tracking and DTI provide valuable insights into pathophysiology and structure-function interactions of heart failure following MI.

frontiers in Cardiovascular Medicine

CASE REPORT
published: 19 November 2020
doi: 10.3389/fcvm.2020.580296

Myocardial Infarction After High-Dose Catecholamine Application—A Case Report From an Experimental Imaging Study

Niklas Beyhoff[1,2,3†], *David Lohr*[4†], *Arne Thiele*[1,2], *Anna Foryst-Ludwig*[1,2], *Robert Klopfleisch*[5], *Laura M. Schreiber*[4] *and Ulrich Kintscher*[1,2*]

[1] Charité - Universitätsmedizin Berlin, Corporate Member of Freie Universität Berlin, Humboldt-Universität zu Berlin, and Berlin Institute of Health, Institute of Pharmacology, Center for Cardiovascular Research, Berlin, Germany, [2] DZHK (German Centre for Cardiovascular Research), Partner Site Berlin, Berlin, Germany, [3] Berlin Institute of Health (BIH), Berlin, Germany, [4] Chair of Molecular and Cellular Imaging, Comprehensive Heart Failure Center, University Hospital Würzburg, Würzburg, Germany, [5] Department of Veterinary Pathology, College of Veterinary Medicine, Freie Universität Berlin, Berlin, Germany

OPEN ACCESS

Edited by:
Sebastian Kelle,
Deutsches Herzzentrum
Berlin, Germany

Reviewed by:
Richard Nethononda,
Chris Hani Baragwanath Hospital,
South Africa
Alessandro Faragli,
Deutsches Herzzentrum
Berlin, Germany

***Correspondence:**
Ulrich Kintscher
ulrich.kintscher@charite.de

[†] These authors have contributed equally to this work

Specialty section:
This article was submitted to Cardiovascular Imaging, a section of the journal Frontiers in Cardiovascular Medicine

Received: 05 July 2020
Accepted: 12 October 2020
Published: 19 November 2020

Citation:
Beyhoff N, Lohr D, Thiele A, Foryst-Ludwig A, Klopfleisch R, Schreiber LM and Kintscher U (2020) Myocardial Infarction After High-Dose Catecholamine Application—A Case Report From an Experimental Imaging Study. Front. Cardiovasc. Med. 7:580296. doi: 10.3389/fcvm.2020.580296

Although heart failure following myocardial infarction (MI) represents a major health burden, underlying microstructural and functional changes remain incompletely understood. Here, we report on a case of unexpected MI after treatment with the catecholamine isoproterenol in an experimental imaging study in mice using different state-of-the-art imaging modalities. The decline in cardiac function was documented by ultrahigh-frequency echocardiography and speckle-tracking analyses. Myocardial microstructure was studied *ex vivo* at a spatial resolution of $100 \times 100 \times 100\ \mu m^3$ using diffusion tensor magnetic resonance imaging (DT-MRI) and histopathologic analyses. Two weeks after ISO treatment, the animal showed an apical aneurysm accompanied by reduced radial strain in corresponding segments and impaired global systolic function. DT-MRI revealed a loss of contractile fiber tracts together with a disarray of remaining fibers as corresponding microstructural correlates. This preclinical case report provides valuable insights into pathophysiology and morphologic–functional relations of heart failure following MI using emerging imaging technologies.

Keywords: myocardial infarction, catecholamines, speckle tracking, diffusion tensor imaging, magnetic resonance imaging, case report, heart failure, echocardiography

INTRODUCTION

Although heart failure following myocardial infarction (MI) represents a major health burden, underlying structural/functional relationships remain incompletely understood (1, 2). While adverse cardiac remodeling after MI is considered to directly affect the mechanical and electrical properties of the heart (3–5), the exact impact of microstructural changes on myocardial function remains unclear. Here, we report on a case of unexpected MI after treatment with the catecholamine isoproterenol (ISO) in an experimental imaging study in mice correlating a comprehensive set of functional parameters with detailed histopathology and diffusion tensor magnetic resonance imaging (DT-MRI).

CASE DESCRIPTION

We conducted an experimental imaging study to characterize myocardial microstructure and function in a murine model of circumscribed subendocardial damage whose results have been published previously (6). Briefly, male 129/Sv mice (6–8 weeks old) received subcutaneous injections of 25 mg/kg ISO or saline as placebo control for four consecutive days according to a standard protocol (**Figure 1A**) (6). The case animal was randomized to the ISO group. During baseline echocardiography prior to treatment, all animals showed comparable parameters of cardiac function and ventricular dimensions. At baseline, the case animal had a left ventricular ejection fraction of 48% without any evidence of regional wall motion abnormalities (**Figure 1B** and **Supplementary Video 1**). First differences became apparent after the first injection, where it required a longer recovery period than its littermates. Recovery time was also slightly prolonged after the second to fourth injection. Typically, ISO does not cause chronic alterations of ventricular dimensions and systolic function in this model (6). However, echocardiography 2 weeks after final injection revealed wall thinning and a pronounced aneurysm of the apex of the left ventricle (LV) resulting in massively increased LV volumes and markedly reduced global systolic function (**Figures 1B–D**). Cardiac enlargement was also evident from indexed heart weight obtained during necropsy (**Figure 1E**). Apical segments were akinetic, whereas the base appeared to contract normally (**Figure 2A** and **Supplementary Video 2**). During speckle-tracking echocardiography, the same segmental differences were observed in reduced apical but preserved basal radial strain of the LV (**Figure 2B**). The ISO-mediated decline in longitudinal deformation indices (7) was substantially more pronounced in this animal (global longitudinal strain: −4.6 vs. −12.5% ± 1.9%; global longitudinal strain rate: −1.8 vs. −3.9 ± 0.7^{-s}).

Histological analyses showed subendocardial fibrosis within basal and midmyocardial sections of the LV (**Figure 3A**). Fibrotic lesions in the apex exceeded the subendocardial layer resulting in transmural scarring and

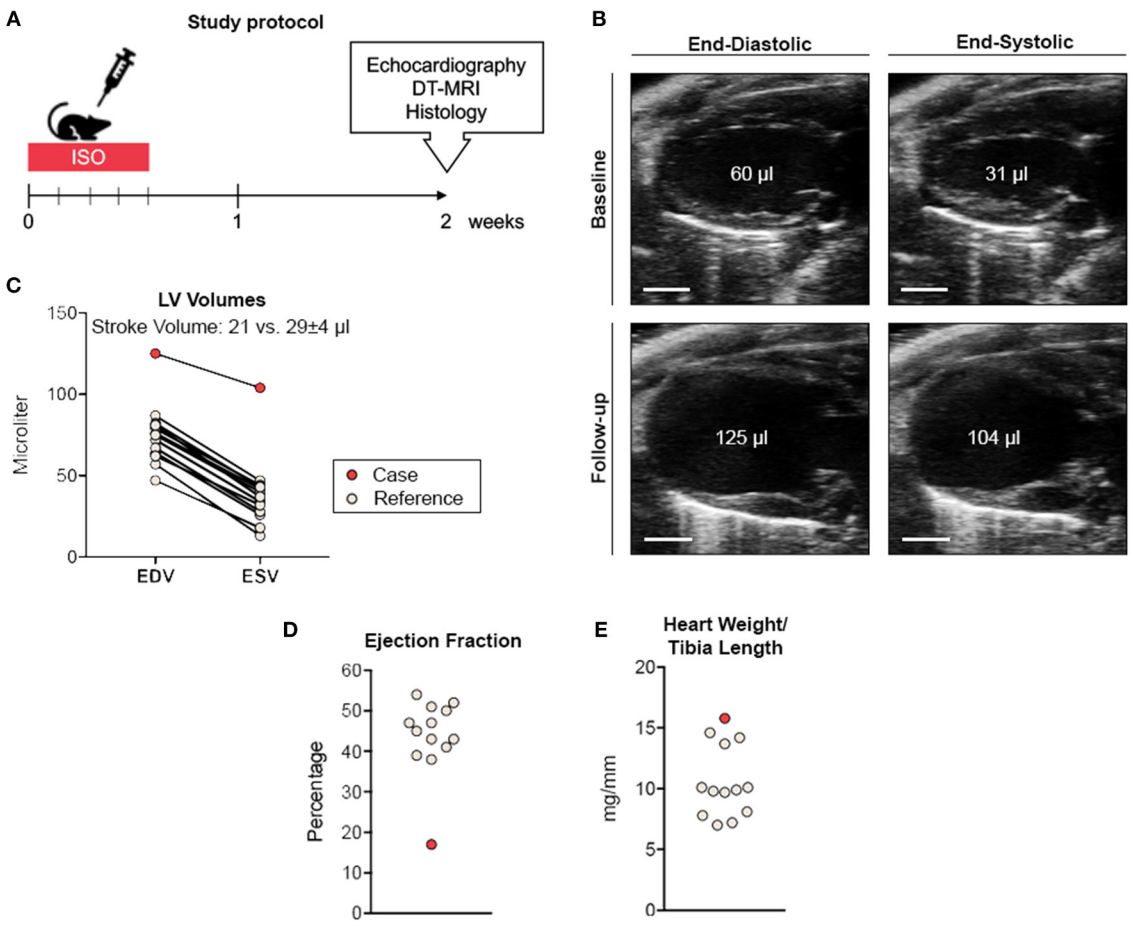

FIGURE 1 | Study protocol and cardiac phenotyping. **(A)** Study protocol. **(B)** Parasternal long-axis view during end-diastole and end-systole before (upper panel) and 2 weeks after ISO treatment (lower panel). Scale bar represents 2 mm. **(C)** Comparative volumetry indicating increased left ventricular volumes accompanied by reduced stroke volume. **(D)** Ejection fraction analysis. **(E)** Normalized heart weights indicating cardiac enlargement. Remaining ISO-treated animals ($n = 12$) served as reference. EDV, end-diastolic volume; ESV, end-systolic volume.

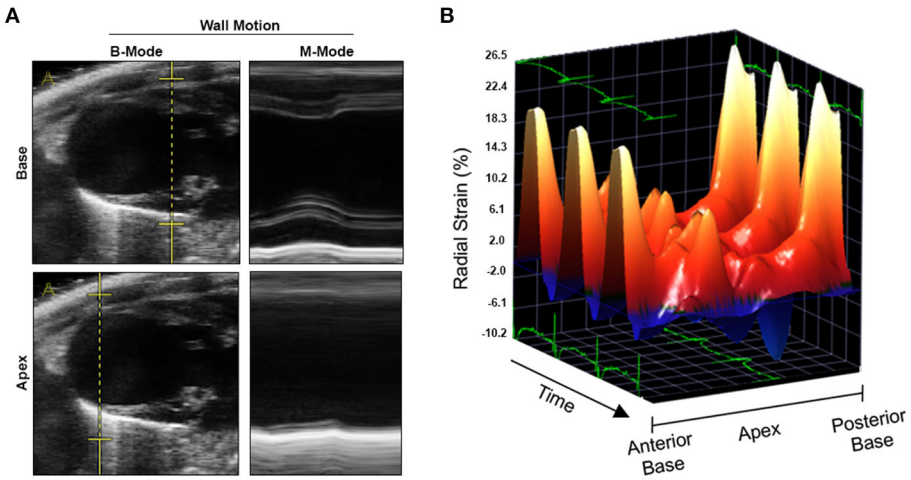

FIGURE 2 | Wall motion analyses by conventional and speckle-tracking echocardiography. **(A)** Reconstructed M-modes at basal (upper panel) and apical level (lower panel) indicating apical akinesia. **(B)** Three-dimensional reconstruction of radial strain during three cardiac cycles. Three-dimensional Cartesian coordinate system mapping radial strain, time/cardiac cycles, and myocardial segments derived from the cardiac long axis (from anterior base over apex to posterior base). Radial strain in midmyocardial and apical segments (both anterior and posterior) was markedly lower as compared to basal segments.

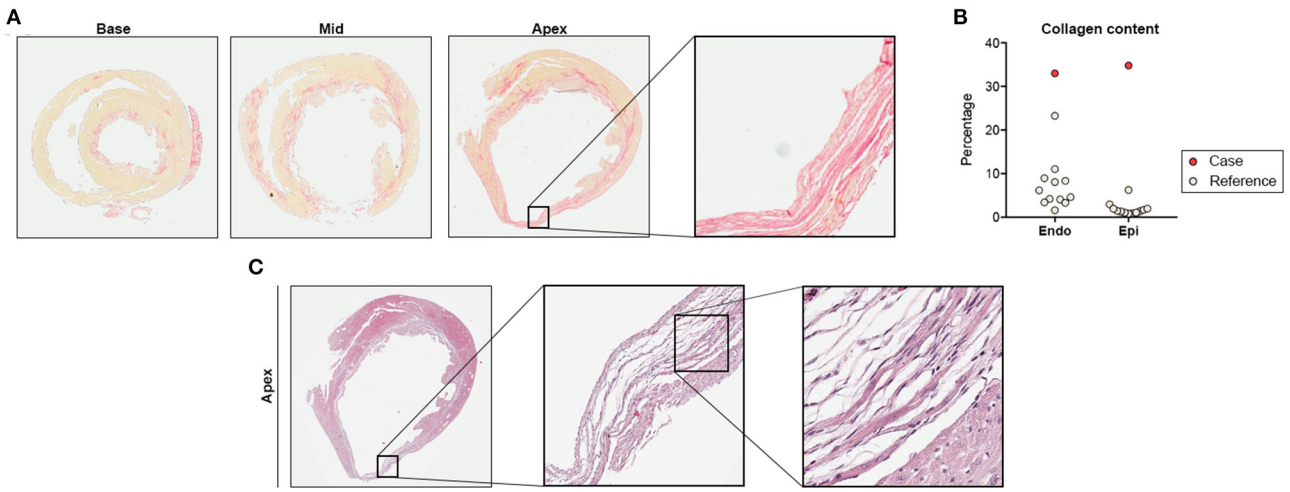

FIGURE 3 | Histological analysis. **(A)** Cardiac cross-sections at basal, midmyocardial, and apical level with exemplary region of interest showing transmural scarring (Picrosirius red staining for detection of collagen fibers). **(B)** Collagen quantification in subendocardium (Endo) and subepicardium (Epi). **(C)** Detailed histology of the apical scar presented in **(A)** indicating replacement fibrosis in response to cardiomyocyte loss (hematoxylin-eosin stain). Remaining ISO-treated animals ($n = 12$) served as reference.

aneurysmatic wall thinning (**Figures 3A,B**). In contrast, the remaining ISO-treated animals showed circumscribed subendocardial collagen accumulation, as expected in this model (**Figure 3B**) (6, 7). Histopathology of the apical scar revealed replacement fibrosis in response to a profound loss of cardiomyocytes (**Figure 3C**).

Myocardial microstructure was studied at a spatial resolution of 100 × 100 × 100 μm^3 using DT-MRI at 7 T. By using an *ex vivo* approach without constraining influences such as motion, strain, and electrocardiogram (ECG) triggering, we aimed for full coverage of the entire LV with the highest possible image resolution and quality. On average, the case showed highly reduced mean diffusivity in the LV when compared to the remaining animals (**Figures 4A,B**). Mean diffusivity was found to be higher in apical (=infarcted) than in basal (=remote) segments (**Figure 4C**). Three-dimensional tractography showed that orientation coherence of myocardial fibers was maintained on a submillimeter scale, while increasing minimal tract lengths revealed increasingly sparse tract reconstruction (**Figures 4D,E**). Compared to the remaining ISO-treated animals, there was a reduced number of voxels with positive helix angle in the midventricular

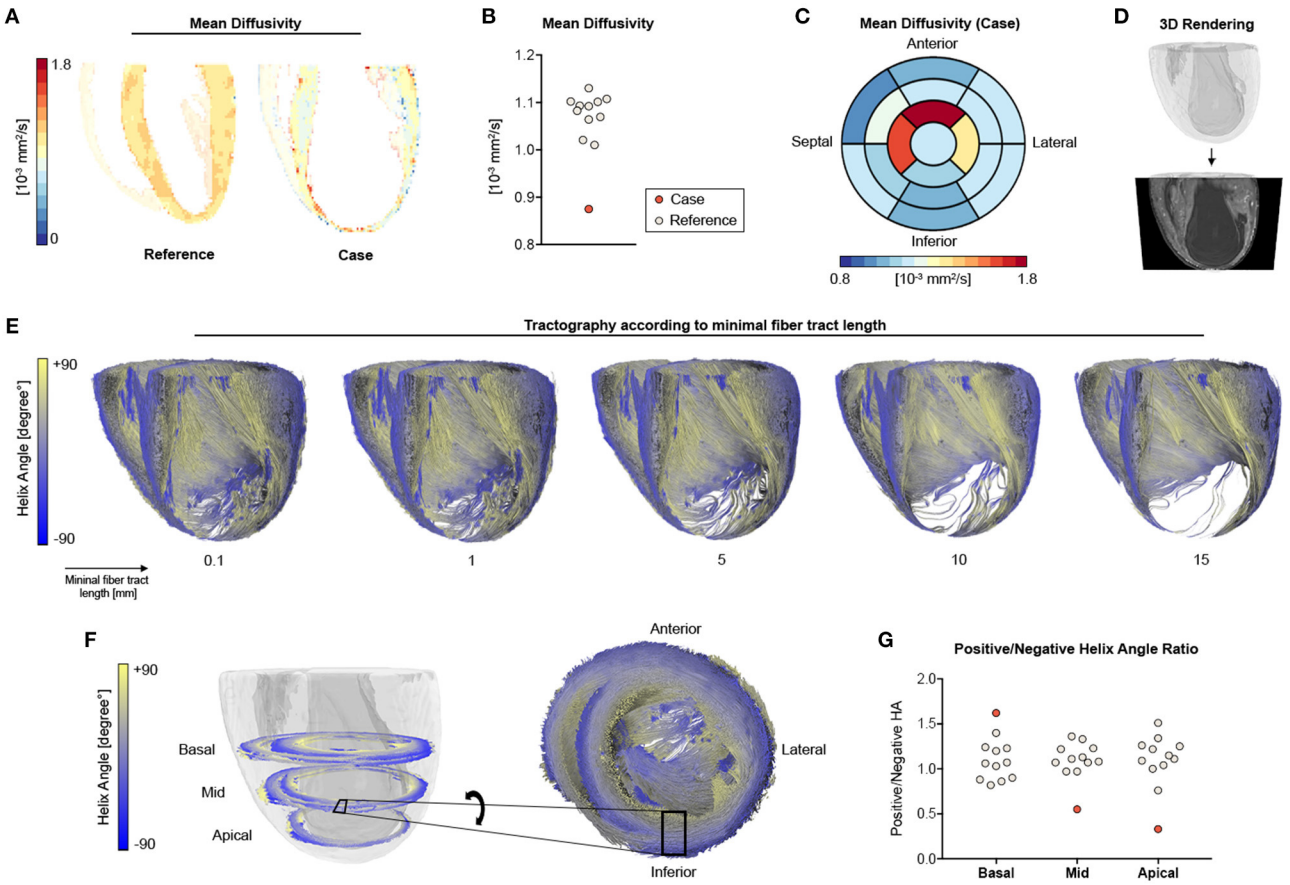

FIGURE 4 | DT-MRI analysis. **(A)** Long-axis mean diffusivity for a representative heart of the ISO group (reference) and the infarcted heart (case). **(B)** Quantitative analyses of mean diffusivity in the left ventricle. **(C)** Bull's-eye plot for mean diffusivity of the infarcted heart. **(D)** Whole-heart volume rendering and respective surface cut for tractography visualization in **(E)** tractography of the main eigenvector using varying minimal fiber bundle lengths (0.1, 1, 5, 10, 15 mm) as termination criteria. **(F)** Helix angle distribution in a basal, midcavity, and apical slab of the infarcted animal with zoomed tractography. **(G)** Ratio of positive to negative voxels in basal, midcavity, and apical segments. Remaining ISO-treated animals ($n = 11$) served as reference.

and apical segments resulting in a lower positive-to-negative helix angle ratio, whereas the proportion of fiber tracts with positive helix angle was higher in basal segments (**Figures 4F,G**).

DISCUSSION

Evaluation of cardiac function by noninvasive imaging tools is a cornerstone in the diagnosis and follow-up evaluation of both MI and heart failure. Yet, the underlying structural basis for cardiac function abnormalities often remains elusive. DT-MRI is an emerging imaging technique that facilitates three-dimensional reconstruction of the cardiac myofiber arrangement on a submillimeter scale [as comprehensively reviewed by Mekkaoui et al. (8)]. In the present report, DT-MRI revealed a pronounced disarray and loss of contractile fiber tract as microstructural correlates of impaired cardiac function in an uncommon case of MI. In accordance with histopathologic analysis, the disturbance of myofiber organization occurred predominantly in exactly those myocardial segments that showed impaired contraction/deformation.

Given that ISO's cardiotoxic effects are believed to be mediated by aggravating the mismatch between myocardial oxygen demand (positive inotropic effect) and supply (reduced coronary flow via positive chronotropic effects and consecutive shortening of the diastolic interval), the used experimental model may be considered as a preclinical correlate of type 2 MI (9). Indeed, there is clinical evidence that β-adrenergic agonists can induce characteristics of MI, although these effects are transient when treated accordingly (10).

Apical ballooning is also a key feature of stress cardiomyopathy (also known as Takotsubo syndrome), a transient acute heart failure syndrome putatively caused by the release of catecholamines in response to sympathetic stimulation (11). Interestingly, application of ISO has been shown to induce several characteristics of stress cardiomyopathy in rats including transient apical akinesia and reversible left ventricular systolic dysfunction (12). In contrast to stress cardiomyopathy, however, the present case showed an irreversible damage pattern with severe replacement fibrosis in response to cardiomyocyte death (apical scarring), a pronounced loss of myofiber tracts, and sustained left ventricular systolic failure. Typically, ISO leads to

circumscribed subendocardial fibrosis in the used mouse model. As the damage exceeded the subendocardium and resulted in transmural affection in the presented case, it appears likely that (1) there was a higher vulnerability against ISO-mediated effects (e.g., greater response of the myocardium to β-adrenergic signaling); (2) ISO provoked unexpected thromboembolic coronary occlusion; and/or (3) ISO was accompanied by additional harmful effects, such as coronary artery dissection. However, our study was designed to characterize morphology and function rather than to elucidate the etiology of this unexpected event, which is why the prespecified study protocol did not include an appropriate assessment of the abovementioned aspects (e.g., lack of ECG recording and troponin assessment after ISO application, specialized tissue preparation for DT-MRI hampering the detection of thrombotic material).

In conclusion, this preclinical case report provides insights into pathophysiological and morphologic–functional relations of heart failure following MI by combining latest functional analysis and cardiac imaging techniques. The advent of clinical DT-MRI may facilitate simultaneous assessment of morphologic and functional changes under these conditions.

DATA AVAILABILITY STATEMENT

All datasets generated for this study are included in the article/**Supplementary Material**.

ETHICS STATEMENT

The animal study was reviewed and approved by Landesamt für Gesundheit und Soziales (LAGeSo), Berlin, Germany.

AUTHOR CONTRIBUTIONS

NB performed data collection and statistical analyses, created the figures, and drafted the manuscript. DL performed data collection/data analysis related to DT-MRI and created individual figure tiles. AT, AF-L, and RK performed data collection. AF-L, LS, and UK conceived and designed the study, critically reviewed, and amended the manuscript. LS and UK acquired funding for the study. All authors have contributed extensively to the manuscript.

FUNDING

This work was supported by the German Centre for Cardiovascular Research (DZHK; BER 5.4 PR) and by the Federal Ministry of Education and Research (grant number: 01EO1504). We acknowledge support from the German Research Foundation (DFG) and the Open Access Publication Fund of Charité—Universitätsmedizin Berlin. NB is participant in the BIH-Charité Junior Clinician Scientist Program funded by the Charité—Universitätsmedizin Berlin and the Berlin Institute of Health. AT was supported by a research grant of the German cardiac society (DGK).

ACKNOWLEDGMENTS

The authors thank Ms. Beata Höft for her excellent technical assistance.

SUPPLEMENTARY MATERIAL

The Supplementary Material for this article can be found online at: https://www.frontiersin.org/articles/10.3389/fcvm.2020.580296/full#supplementary-material

Supplementary Video 1 | Parasternal long-axis view at baseline prior to treatment. B-mode echocardiography showed normal left ventricular ejection fraction in the absence of any regional wall motion abnormalities.

Supplementary Video 2 | Parasternal long-axis view 2 weeks after ISO treatment. B-mode echocardiography revealed reduced global systolic function due to a pronounced apical aneurysm. ECG-gated kilohertz visualization ultrasound imaging for ultrahigh spatiotemporal resolution.

REFERENCES

1. Buckberg GD, Weisfeldt ML, Ballester M, Beyar R, Burkhoff D, Coghlan HC, et al. Left ventricular form and function: scientific priorities and strategic planning for development of new views of disease. *Circulation.* (2004) 110:e333–6. doi: 10.1161/01.CIR.0000143625.56882.5C
2. Watson SR, Dormer JD, Fei B. Imaging technologies for cardiac fiber and heart failure: a review. *Heart Fail Rev.* (2018) 23:273–89. doi: 10.1007/s10741-018-9684-1
3. Strijkers GJ, Bouts A, Blankesteijn WM, Peeters THJM, Vilanova A, Prooijen MC van, et al. Diffusion tensor imaging of left ventricular remodeling in response to myocardial infarction in the mouse. *NMR Biomed.* (2009) 22:182–90. doi: 10.1002/nbm.1299
4. Taccardi B, Macchi E, Lux RL, Ershler PR, Spaggiari S, Baruffi S, et al. Effect of myocardial fiber direction on epicardial potentials. *Circulation.* (1994) 90:3076–90. doi: 10.1161/01.CIR.90.6.3076
5. Kadish A, Shinnar M, Moore EN, Levine JH, Balke CW, Spear JF. Interaction of fiber orientation and direction of impulse propagation with anatomic barriers in anisotropic canine myocardium. *Circulation.* (1988) 78:1478–94. doi: 10.1161/01.CIR.78.6.1478
6. Beyhoff N, Lohr D, Foryst-Ludwig A, Klopfleisch R, Brix S, Grune J, et al. Characterization of myocardial microstructure and function in an experimental model of isolated subendocardial damage. *Hypertension.* (2019) 74:295–304. doi: 10.1161/HYPERTENSIONAHA.119.12956
7. Beyhoff N, Brix S, Betz IR, Klopfleisch R, Foryst-Ludwig A, Krannich A, et al. Application of speckle-tracking echocardiography in an experimental model of isolated subendocardial damage. *J Am Soc Echocardiogr.* (2017) 30:1239–50.e2. doi: 10.1016/j.echo.2017.08.006
8. Mekkaoui C, Reese TG, Jackowski MP, Bhat H, Sosnovik DE. Diffusion MRI in the heart. *NMR Biomed.* (2017) 30:e3426. doi: 10.1002/nbm.3426
9. Thygesen K, Alpert JS, Jaffe AS, Chaitman BR, Bax JJ, Morrow DA, et al. Fourth universal definition of myocardial infarction (2018). *Eur Heart J.* (2019) 40:237–69. doi: 10.1093/eurheartj/ehy462
10. Abraham J, Mudd JO, Kapur N, Klein K, Champion HC, Wittstein IS. Stress cardiomyopathy after intravenous administration of catecholamines and beta-receptor agonists. *J Am Coll Cardiol.* (2009) 53:1320–5. doi: 10.1016/j.jacc.2009.02.020
11. Ghadri J-R, Wittstein IS, Prasad A, Sharkey S, Dote K, Akashi YJ, et al. International expert consensus document on Takotsubo Syndrome (Part I): clinical characteristics, diagnostic criteria, and pathophysiology. *Eur Heart J.* (2018) 39:2032–46. doi: 10.1093/eurheartj/ehy076

12. Sachdeva J, Dai W, Kloner RA. Functional and histological assessment of an experimental model of Takotsubo's cardiomyopathy. *J Am Heart Assoc.* (2014) 3:e000921. doi: 10.1161/JAHA.114.000921

Conflict of Interest: The authors declare that the research was conducted in the absence of any commercial or financial relationships that could be construed as a potential conflict of interest.

3.5 A Novel Mono-surface Antisymmetric 8Tx/16Rx Coil Array for Parallel Transmit Cardiac MRI in Pigs at 7T

〉 Published in *Scientific Reports* – 2020[189]

These citations have been applied in this publication.[190-243]

Despite numerous technical challenges, early studies have demonstrated that CMR at ultrahigh field strengths (7T) may improve SNR and enable novel insights into cardiac pathology. B_1-non-uniformity, and thus difficulties regarding power deposition, and SAR-safety are induced by the shorter wavelength in tissue at ultrahigh field strength, an issue that is increasingly addressed with dedicated RF hardware.

In this study we aimed to design, simulate, construct, and test an 8Tx/16Rx mono-surface coil that enables homogeneous and efficient RF excitation using parallel transmit technology as well as rapid parallel imaging acceleration.

The coil was designed for ultrahigh field CMR in large animals with weights of 40-80 kg. Measurements using a pig body phantom (≤-10dB) and a 46 kg pig cadaver (≤-11 dB) demonstrated accepted decoupling. Capacitor values determined through bench-top measurements were in good agreement with initial CSD simulations. Relative standard deviation (RSD) of the flip angle within the heart region (ex vivo) was 0.19 using hardware phases, which improved to 0.16 using static pTx shimming. For comparison, RSD was 0.35 using a human array prototype. EM simulations showed that pTx shimming increased transmit efficiency by ≥3. Simultaneously, the L-shaped distribution of elements enabled high parallel imaging acceleration factors (R=2-6) with small noise amplification (g_{R4}=1.03, g_{R4}=1.05, g_{R4}=1.09, g_{R6}=1.26) in another *ex vivo* measurement (68 kg). *In vivo* measurements in a 60 kg pig confirmed great transmit and receive properties, enabling artifact-free acceleration to R=4, without the presence of destructive interference.

In conclusion, we designed, simulated, constructed and tested a mono-surface antisymmetric array design that enabled homogenous and efficient RF excitation as well as rapid parallel imaging acceleration, an essential aspect to CMR. We demonstrate that dedicated hardware that properly utilizes the potential of parallel transmit technology enables large animal studies at 7T with high image quality and SNR, offering access to new discoveries and information on cardiac pathology. The developed design can easily be adapted as multi-channel coil arrays for different ultrahigh field MR applications such as cardiac, brain, spine or abdominal imaging.

SCIENTIFIC REPORTS
nature research

OPEN

A Novel Mono-surface Antisymmetric 8Tx/16Rx Coil Array for Parallel Transmit Cardiac MRI in Pigs at 7T

Ibrahim A. Elabyad*, Maxim Terekhov, David Lohr, Maria R. Stefanescu, Steffen Baltes & Laura M. Schreiber

A novel mono-surface antisymmetric 16-element transmit/receive (Tx/Rx) coil array was designed, simulated, constructed, and tested for cardiac magnetic resonance imaging (cMRI) in pigs at 7T. The cardiac array comprised of a mono-surface 16-loops with two central elements arranged anti-symmetrically and flanked by seven elements on either side. The array was configured for parallel transmit (pTx) mode to have an eight channel transmit and 16-channel receive (8Tx/16Rx) coil array. Electromagnetic (EM) simulations, bench-top measurements, phantom, and MRI experiments with two pig cadavers (68 and 46 kg) were performed. Finally, the coil was used in pilot *in-vivo* measurements with a 60 kg pig. Flip angle (FA), geometry factor (g-factor), signal-to-noise ratio (SNR) maps, and high-resolution cardiac images were acquired with an in-plane resolution of 0.6 mm × 0.6 mm (*in-vivo*) and 0.3 mm × 0.3 mm (*ex-vivo*). The mean g-factor over the heart was 1.26 (R = 6). Static phase B_1^+ shimming in a pig body phantom with the optimal phase vectors makes possible to improve the B_1^+ homogeneity by factor > 2 and transmit efficiency by factor > 3 compared to zero phases (before RF shimming). Parallel imaging performed in the *in-vivo* measurements demonstrated well preserved diagnostic quality of the resulting images at acceleration factors up to R = 6. The described hardware design can be adapted for arrays optimized for animals and humans with a larger number of elements (32–64) while maintaining good decoupling for various MRI applications at UHF (e.g., cardiac, head, and spine).

With the development of ultrahigh field (UHF) strength ($B_0 \geq 7$ T) magnetic resonance imaging (MRI) scanners, a significant improvement in the SNR, and hence in spatial and temporal resolutions can be achieved compared to conventional lower field strength (e.g., $B_0 \leq 3$ T) MRI scanners[1,2]. Because of the radiofrequency (RF) wavelength-lowering effects of the B_1^+ field at 7 T ($\lambda_{eff} \approx 12$ cm, i.e., in the order of a human thorax), the design of an optimized RF coil array at 7 T is becoming more challenging. This is because of standing waves creating constructive and destructive interferences of the transmitted B_1^+ field magnitude and hence strong intensity artifacts occurring in the acquired MR images[3–6]. For brain imaging at 7 T, different coil array designs and technologies have been introduced to solve the issues of B_1^+ field inhomogeneity such as microstrip transmission line (MTL) resonators[7–12], inverted (MTL) resonators[13], stepped impedance resonators[14–19], and by utilizing a high-impedance surface as the RF-shield to improve the efficiency and penetration of the B_1^+ field[20,21].

Despite the numerous technical challenges related to B_0 and B_1^+ field inhomogeneities, the application of UHF scanners for cardiovascular research holds significant promise[22,23]. Another hardware challenge is the necessity to increase the number of elements of the array at 7 T (typical 16–32) to allow for parallel imaging and RF-shimming while keeping all resonant coil elements well decoupled. At 7 T, most of the commercial human cardiac coil arrays are designed as local Tx/Rx arrays. Different coil arrays and design concepts have been introduced for cMRI in humans at UHF including, MTL resonators[24,25], conventional multichannel local Tx/Rx loop arrays[26–32], dipole antenna arrays[33–39], combined dipoles and loop arrays[40,41] and dielectric resonant antenna arrays[42].

The existing commercial cardiac coil arrays for humans at 7 T comprise two independent anterior and posterior arrays. The anterior array is the most efficient, because it is fixed near to the heart region and its element

Chair of Cellular and Molecular Imaging, Comprehensive Heart Failure Center (CHFC), University Hospital Wuerzburg, D-97078, Wuerzburg, Germany. *email: Elabyad_I@ukw.de

dimensions are optimized to have good penetration and transmit efficiency (Tx_{eff}) of the B_1^+ field up to 10 cm depth within the thorax. The posterior array is used in order to improve the penetration of the B_1^+ field within the heart from the back side of the thorax. However, the contribution of the B_1^+ field from the posterior array is low compared to the anterior array due to its large distance to the heart. Recent studies[43,44] presented two 8Tx/16Rx coil arrays comprising two independent anterior−posterior (A–P) parts optimized for moderate weight pigs (<50 kg). The distance from the center of the pig heart to the posterior array for the 46 kg pig was about 16 cm and, thus, the posterior array contributed only about 10% of the total B_1^+ field, despite the optimized sizes of the array elements.

The magnitude and phase of the signal for each individual transmit coil element can be optimized to provide a uniform combined B_1^+ field distribution in the selected region-of-interest (ROI). This process is referred to as RF-shimming or B_1^+ shimming[45–50]. Using eight independent RF power amplifiers (RFPAs) in pTX mode allows driving the individual 8Tx channels of the array dynamically (i.e. to vary the magnitude/phase of each channel or the RF-pulse waveforms), which enables shaping of 2D and 3D excitation profiles based on a wide-range of optimization criteria[51,52]. Another major issue is that the limited RF power given from the RFPA is distributed to both array parts. Approximately half of the RF power contributes to only 10% of the total B_1^+ field under the assumption that the power is divided equally to both arrays. This makes the standard vendor-integrated pTx B_1^+ shimming algorithm, which is usually developed for the cylindrical Tx/Rx head coils (e.g., birdcage) inefficient for cardiac arrays, comprising two independent anterior and posterior arrays. The vendor-integrated pTx B_1^+ shimming algorithm targeted to achieve an optimal combination of B_1^+ field homogeneity and mean value, tries to compensate the low penetration from the posterior array, and thus provides high amplitudes to most of its channels, resulting in low amplitudes for some of the channels of the anterior array.

One of the major challenges associated in cMRI is gating the acquisition to compensate the heart motion and that of surrounding tissues such as the lung. Standard cMRI protocols actively implement the parallel acquisition techniques (PAT), which allows for reducing total acquisition time (TA), leading, however, to an SNR penalty proportional to the square root of the phase encoding lines reduction factor and g-factor of the array. Therefore, characterization of the noise amplification (g-factor) is an important aspect when testing RF coil arrays for cMRI at 7 T. The rationale of proposed mono-surface antisymmetric array design for 7 T cMRI in pigs is to reduce the coupling among the elements and to provide optimal receive properties for efficient parallel acquisition, while simultaneously minimizing the mutual correlation of the transmitted B_1^+ fields generated by individual elements and, hence, to improve RF-shimming capabilities. This mono-surface array design combines the properties of both volume resonator and surface coils in the most appropriate way and provides a well-balanced of combination of both B_1^+ and B_1^- fields.

In this paper, we report a novel 8Tx/16Rx pTx cardiac coil array composed of 16-loop elements allocated on the mono-surface of one printed circuit board (PCB) and fixed on half-elliptical housing. The housing dimensions were designed to fit with pigs of body weights ranging from 40 to 80 kg. Final tuning and matching of the mono-surface array were done using a 46 kg pig cadaver. The testing and validation of the array's transmitting and receiving properties was done using two cadaver pigs (68 and 46 kg) in weights. Finally, the cardiac array was used in the *in-vivo* scans using a 60 kg pig. The mean g-factor within the heart region of 1.26 was shown with an acceleration factor of R = 6. Static phase B_1^+ shimming in a pig body phantom with the optimal phase vectors shows the potential to improve the B_1^+ homogeneity characterized via relative-standard-deviation (RSD) by factor > 2 and transmit efficiency (Tx_{eff}) by factor > 3 compared to zero-phases (without RF-shimming). To investigate the potential benefit of the mono-surface array in pTx B_1^+ shimming and parallel imaging, phantom and cadaver pig MR-measurements were additionally performed and compared to an 8Tx/16Rx pTx human cardiac array prototype. After B_1^+ shimming using the vendor pTx algorithm, the mono-surface array has demonstrated improvement in B_1^+ homogeneity coefficient by factor > 4 in a 20 cm spherical phantom and by about 43% in a pig body phantom compared to before shimming with hardware (HW) phases.

Results

Array characterization. *S-matrix measurements.* Simulated and measured S-matrices for the mono-surface array loaded with the pig body phantom are shown in Table 1. Simulated and measured S-matrices for the mono-surface array loaded with a 20 cm diameter spherical phantom are shown in Supplementary Table S1. For the spherical phantom, the worst-case transmission coefficient S_{ij} was below −8 dB due to reduced loading of the side elements (e.g., 14 and 16). For the pig body phantom, the worst-case transmission coefficient S_{ij} was below −10 dB between elements 14 and 16. The S-matrix was measured when the array was loaded with a cadaver of 46 kg pig (cadaver #2) [see Supplementary Table S2]. With loading of the *ex-vivo* pig, reflection coefficients S_{ii} were below −15 dB for all 16 elements. The worst-case transmission coefficient S_{ij} was below −11 dB between elements 1 and 6 and between elements 2 and 5.

Quality factor measurements. Since the mono-surface array has different element dimensions, bending, and loading conditions due to the heterogeneity of the pig thorax, the quality factors (Q) will be different. Both unloaded (Q_{un}) and loaded (Q_{lo}) quality factors were measured from matched S_{ii} reflection coefficients for all 16 loops. For all 16-elements, Q_{lo} were measured when the array loaded with a 46 kg pig cadaver. The measured Q_{lo}/Q_{un} ratio for all elements was in the range of 0.50 to 0.75.

Phantom MRI measurements. *Spherical phantom.* Figure 1 illustrates the simulated and measured central coronal B_1^+ field distributions within a 20 cm diameter spherical phantom for eight individual Tx-channels (T_{x1}, T_{x2}, T_{x3}, T_{x4}, T_{x5}, T_{x6}, T_{x7}, and T_{x8}). The combined B_1^+ fields per channel were normalized to their maxima. Good agreement between the CST simulations and the experimentally measured FA maps was achieved for most

El.#	1	2	3	4	5	6	7	8	9	10	11	12	13	14	15	16	El.#
	−13	−16	−20	−15	−20	−15	−28	−26	−23	−20	−35	−29	−23	−25	−27	−36	1
		−14	−14	−22	−14	−23	−20	−28	−17	−23	−33	−36	−21	−23	−30	−24	2
1	**−16**		**−21**	−22	−16	−30	−12	−29	−24	−28	−19	−44	−23	−27	−30	−30	3
2	*−17*	**−16**		**−21**	−30	−16	−38	−11	−28	−12	−48	−17	−30	−27	−38	−28	4
3	*−21*	*−12*	**−18**		**−24**	−20	−15	−27	−11	−27	−20	−27	−19	−27	−28	−30	5
4	*−12*	*−21*	*−27*	**−18**		**−20**	−24	−18	−24	−13	−29	−24	−27	−20	−34	−19	6
5	*−18*	*−14*	*−15*	*−28*	**−15**		**−15**	−32	−16	−45	−12	−34	−17	−37	−17	−38	7
6	*−14*	*−19*	*−28*	*−15*	*−22*	**−15**		**−14**	−34	−12	−34	−11	−34	−13	−48	−14	8
7	*−25*	*−35*	*−12*	*−36*	*−15*	*−27*	**−21**		**−24**	−27	−20	−35	−11	−30	−12	−42	9
8	*−35*	*−25*	*−36*	*−12*	*−27*	*−15*	*−26*	**−21**		**−24**	−35	−19	−38	−13	−50	−12	10
9	*−18*	*−17*	*−13*	*−25*	*−13*	*−22*	*−19*	*−24*	**−28**		**−15**	−42	−10	−35	−22	−42	11
10	*−17*	*−18*	*−25*	*−13*	*−22*	*−13*	*−24*	*−18*	*−20*	**−28**		**−16**	−37	−10	−37	−14	12
11	*−24*	*−26*	*−22*	*−36*	*−25*	*−29*	*−10*	*−33*	*−18*	*−32*	**−21**		**−16**	−33	−11	−37	13
12	*−26*	*−24*	*−36*	*−22*	*−29*	*−25*	*−33*	*−10*	*−32*	*−19*	*−42*	**−20**		**−27**	−44	−10	14
13	*−22*	*−21*	*−23*	*−32*	*−31*	*−29*	*−12*	*−27*	*−10*	*−27*	*−10*	*−37*	**−15**		**−13**	−41	15
14	*−21*	*−22*	*−32*	*−23*	*−30*	*−31*	*−27*	*−12*	*−26*	*−10*	*−37*	*−10*	*−32*	**−15**		**−13**	16
15	*−36*	*−56*	*−22*	*−36*	*−24*	*−47*	*−16*	*−42*	*−10*	*−35*	*−23*	*−41*	*−10*	*−39*	**−15**		
16	*−57*	*−36*	*−36*	*−22*	*−47*	*−24*	*−41*	*−16*	*−35*	*−10*	*−41*	*−23*	*−39*	*−10*	*−45*	**−15**	
	1	2	3	4	5	6	7	8	9	10	11	12	13	14	15	16	

Table 1. Simulated (italic) and measured S-Matrix in dB for the mono-surface array loaded with the pig body phantom with $\varepsilon_r = 59.3$ and $\sigma = 0.79$ S/m.

of the channels (T_{x1}, T_{x2}, T_{x3}, T_{x6}, T_{x7}, and T_{x8}). The B_1^+ field patterns show good similarity between simulations and measurements and match well even within the locations of destructive interferences. However, some differences between simulated and measured FA maps are observed for the Tx-channels (T_{x4} and T_{x5}) [see Fig. 1(d,h,i,m)].

Pig body phantom. Figure 2 demonstrates the simulated B_1^+ field distribution in the central transversal cross-section and the measured in corresponding position FA maps within the pig body phantom. Good agreement between the simulated B_1^+ field distributions and the experimentally measured FA maps was achieved for all 8Tx channels.

Validation of B_1^+ shimming (combined FA maps). Figure 3 demonstrates the results of the simulated combined B_1^+ field distribution and the experimentally measured FA maps in transversal, coronal, and sagittal central slices within the pig body phantom before optimization (with zero-phases), HW phases, and after B_1^+ shimming (with two optimized phase vectors PV1 and PV2). It can be seen in the EM simulation results that the implementation of the HW phases led to an enhancement in Tx_{eff} by factor > 3 (from 2.2 to 6.9 $\mu T/\sqrt{kW}$), without any additional RF-shimming compared to zero-phases. This proves that the initially optimized HW phases were close to optimal regarding maximization of the transmit efficiency. With PV1, the RSD was decreased by factor > 3 (from 0.35 to 0.10) and Tx_{eff} was increased by factor > 3 (from 2.2 to 6.7 $\mu T/\sqrt{kW}$) compared to zero-phases. With PV2, the RSD was decreased by factor > 2 (from 0.35 to 0.15) and the Tx_{eff} was increased by factor > 3.4 (from 2.2 to 7.5 $\mu T/\sqrt{kW}$) compared to zero-phases. With HW phases and even with prior pTx shimming, the mean FA was increased by 80% (from 10° to 18°) compared to zero-phases [see Fig. 3(f)]. The RSD computed in the selected ROI of the measured FA map was improved by factor > 3 (from 0.32 to 0.10) compared to zero-phases. It is interesting to see that with PV2, the RSD was improved by factor > 6 and factor > 2 compared to zero-phases and HW phases, respectively [see Fig. 3(h)]. The enhancement in the B_1^+ field penetration for PV2 compared to zero-phases, HW phases and PV1 is particularly clear in the simulated and measured central coronal [see Fig. 3(i–p)] and sagittal [see Fig. 3(q–y)] slices.

Good agreement between the simulated combined transversal B_1^+ field distributions and the measured FA maps was achieved for zero-phases, HW phases and PV2. However, there were some discrepancies between the CST simulation results and the experimentally measured FA maps for PV1. The potential sources of observed discrepancies are: (i) light asymmetry of the pig phantom prototype compared to the ideal simulation model [see Fig. 4(c,e)] and (ii) shift in phantom position with respect to the coil in comparison to simulated position.

Figure 5 shows the simulated improvement of the SNR achieved by static B_1^+ field shimming of the selected phase vector PV2 obtained using our in-house developed phase optimization method. An increase in mean SNR (a.u.) was observed in the whole volume of the pig body phantom from 36 before shimming with zero-phases to 83 after shimming with PV2 (i.e., factor 2.3), in median value of SNR within phantom from 14 before shimming to 25 after shimming with PV2 (i.e., factor 1.7), and in volume within SNR is 83 iso-surface (i.e., "SNR above mean for optimized case"): by a factor of 1.7 and an absolute volume increase of 1362 cm^3.

B_1^+ shimming using the pTx system. *Combined FA maps.* Figure 6(a–d) illustrates the measured combined central transversal FA maps in the 20 cm diameter spherical phantom and the pig body phantom acquired

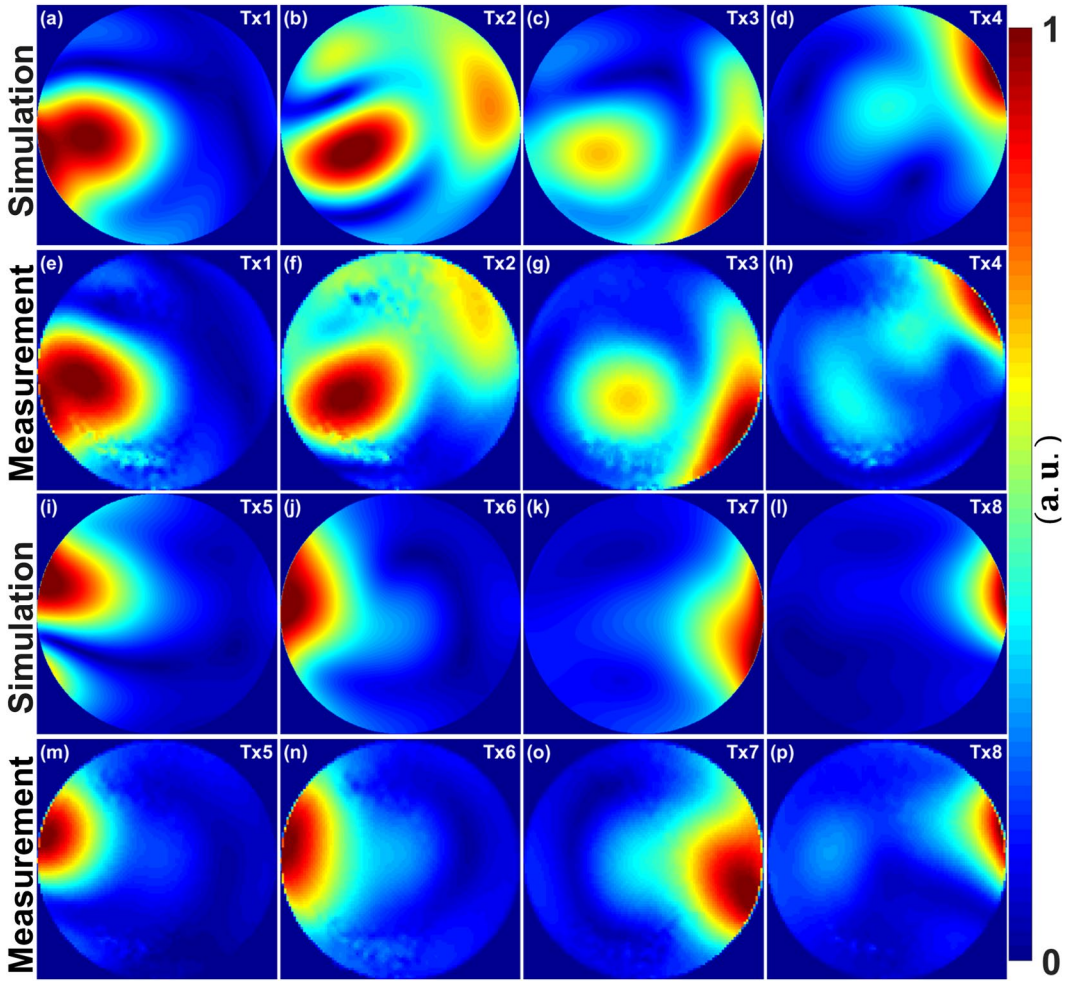

Figure 1. Simulated normalized central coronal B_1^+ field distributions and measured FA maps for the individual 8Tx channels (T_{x1}–T_{x8}) of the mono-surface array within a spherical phantom of 20 cm in diameter. Simulation (**a**–**d**) & (**i**–**l**). Measurement (**e**–**h**) & (**m**–**p**). All images were seen from F–H direction as shown in the array setup of Fig. 4 (**h**).

using the mono-surface array without shimming and after on-scanner static B_1^+ shimming with both amplitude/phases using the vendor integrated pTx shimming algorithm. It is important to notice that the found amplitudes for the pig body phantom were approximately equal for all 8Tx-channels [see Supplementary Table S3], which means that static B_1^+ shimming was performed with the maximum amplitude efficiency. For the spherical phantom [see Fig. 6(a,b)], the on-scanner B_1^+ shimming improved the FA homogeneity coefficient by factor > 4 (the RSD was decreased from 0.33 to 0.08) in the selected 3D ROI ($10 \times 10 \times 1.0\,cm^3$) compared to before shimming with HW phases. For the pig body phantom, the RSD has improved from 0.10 before pTx shimming to 0.07 after pTx shimming. This corresponds to a 43% improvement in the FA homogeneity coefficient compared to before shimming with HW phases. The vendor integrated static B_1^+ shimming in combination with the mono-surface array allows for shaping a relatively homogeneous profile of the FA in the area of the heart within the pig body phantom [see Fig. 6(c,d)].

g-factor maps. Figure 6(e–h) demonstrates the measured g-factor maps acquired using the mono-surface array with acceleration factors of R = 2, 3, 4, and 6 after a vendor integrated on-scanner pTx B_1^+ shimming. For accelerations defined in the left−right (L−R) direction, the g-factor in the region corresponding to the position of the pig's heart increases gradually with acceleration factors. The mean values of g-factor for accelerations from R = 2 to 6 changes from 1.03 to 1.40, respectively, being very moderate values for a typical cardiac array. That way, an acceleration up to R = 6 is possible in L−R direction whereas for classical double-surface arrays with individual anterior and posterior parts, the acceleration regime is practically not feasible with R > 3.

MRI measurements with pig cadavers. *Cadaver #1 (68 kg).* Figure 7(a–c) illustrate the combined FA maps in short axis (SA) views within the whole thorax of pig cadaver #1 (68 kg) acquired using the mono-surface array without shimming and after on-scanner pTx B_1^+ shimming compared to the human array prototype. The coil showed good homogeneity in the FA map with a computed FA mean value of 14° before pTx shimming. After

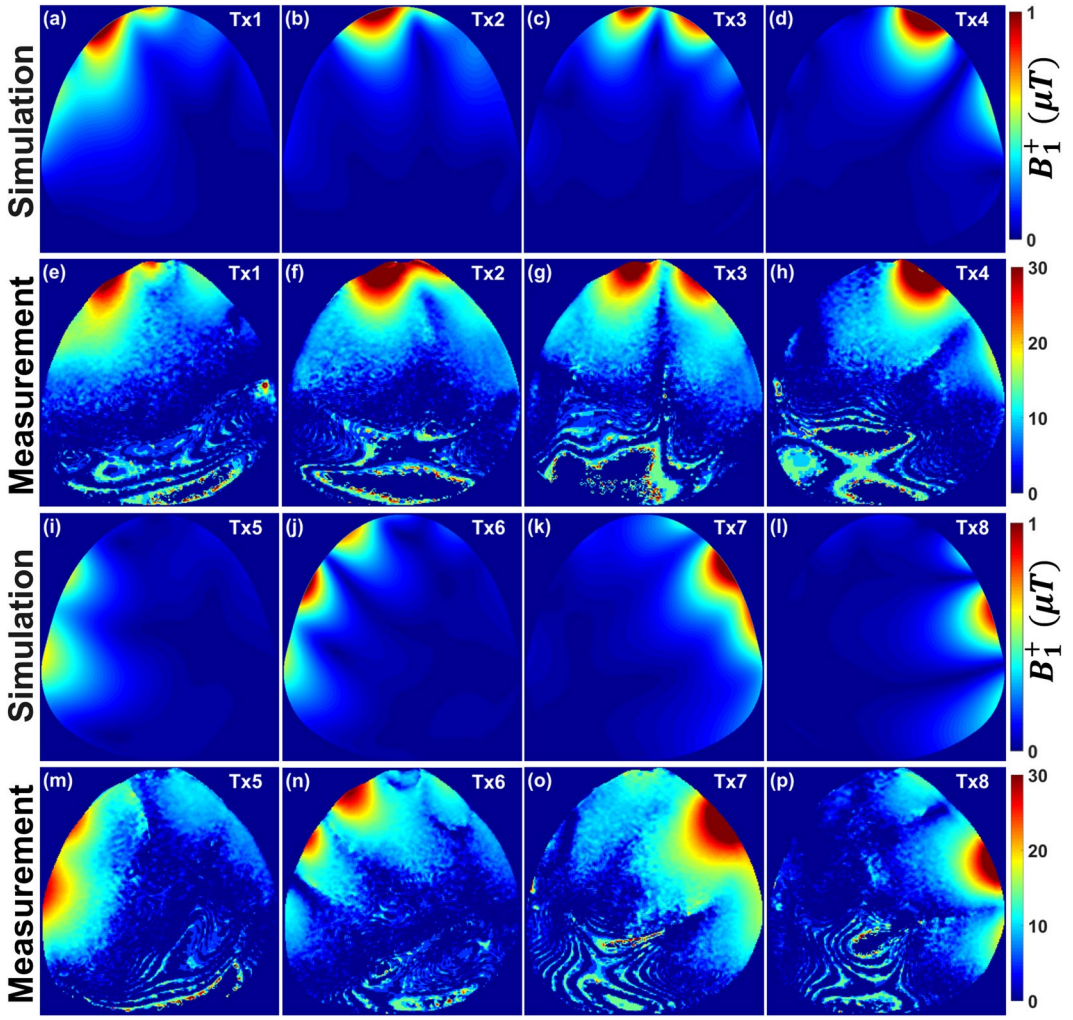

Figure 2. Simulated central transversal B_1^+ field distribution in μT and measured FA maps in degrees for the individual 8Tx channels (T_{x1}–T_{x8}) of the mono-surface array within the pig body phantom. Simulation (**a**–**d**) & (**i**–**l**). Measurement (**e**–**h**) & (**m**–**p**). All images were seen from F–H direction as shown in the array setup of Fig. 4 (**h**).

the vendor's B_1^+ shimming, the mean FA was increased by about 21%. With the pig cadaver #1, the vendor static B_1^+ shimming has improved the RSD from 0.19 to 0.16. For the recently published[44] antisymmetric anterior coil array comprising of 8-elements combined with a rectilinear 8-elements posterior array and optimized for smaller pigs (<50 kg), the RSD was computed as 0.46 within the pig heart. This result shows that static B_1^+ shimming using pTX RFPA combined with the mono-surface array significantly improved the B_1^+ field homogeneity coefficient (factor > 2.8) compared to an 8Tx/16Rx pig cardiac array comprising two independent A−P parts. The RSD in the pig cadaver #1 using the mono-surface array was improved by factor > 2 (from 0.35 to 0.16) compared to the human array prototype [see Fig. 7(b,c)].

Figure 7(d) shows the noise correlation matrix acquired using the mono-surface array loaded with the pig cadaver of 46 kg. Despite the complexity of the mono-surface array, the maximum noise correlation was 0.4. Figure 7(e,f) depicts coronal views demonstrating a relatively homogeneous B_1^+ field excitation acquired using the mono-surface array, while destructive B_1^+ artefacts are clearly visible for the human array prototype.

Figure 8 demonstrates the parallel imaging performance of the mono-surface array compared to the human cardiac array prototype. G-factor maps were acquired for acceleration factors of R = 2, 3, 4, and 6 in a pig cadaver #1 (68 kg). For both coils, the acceleration was set in the L−R direction. For the mono-surface array, the mean of the g-factor in the heart ROI was evaluated as: 1.03, 1.05, 1.09, and 1.26 for R = 2, 3, 4 and 6, respectively. It is important to notice that the dedicated mono-surface array provides improved parallel imaging capabilities with up to 50% lower g-factor for the high acceleration rates (R = 6) compared to human array prototype.

Cadaver #2 (46 kg). Figure 9 shows SA [see Fig. 9(a)] and long axis (LA) [see Fig. 9(b)] views acquired using R = 2, 3 and 4 in a pig cadaver #2 (46 kg). Images in the second row show SNR maps for the respective anatomical images. Placement of the four LV ROIs and the respective SNR in dependence of the acceleration factor are displayed in

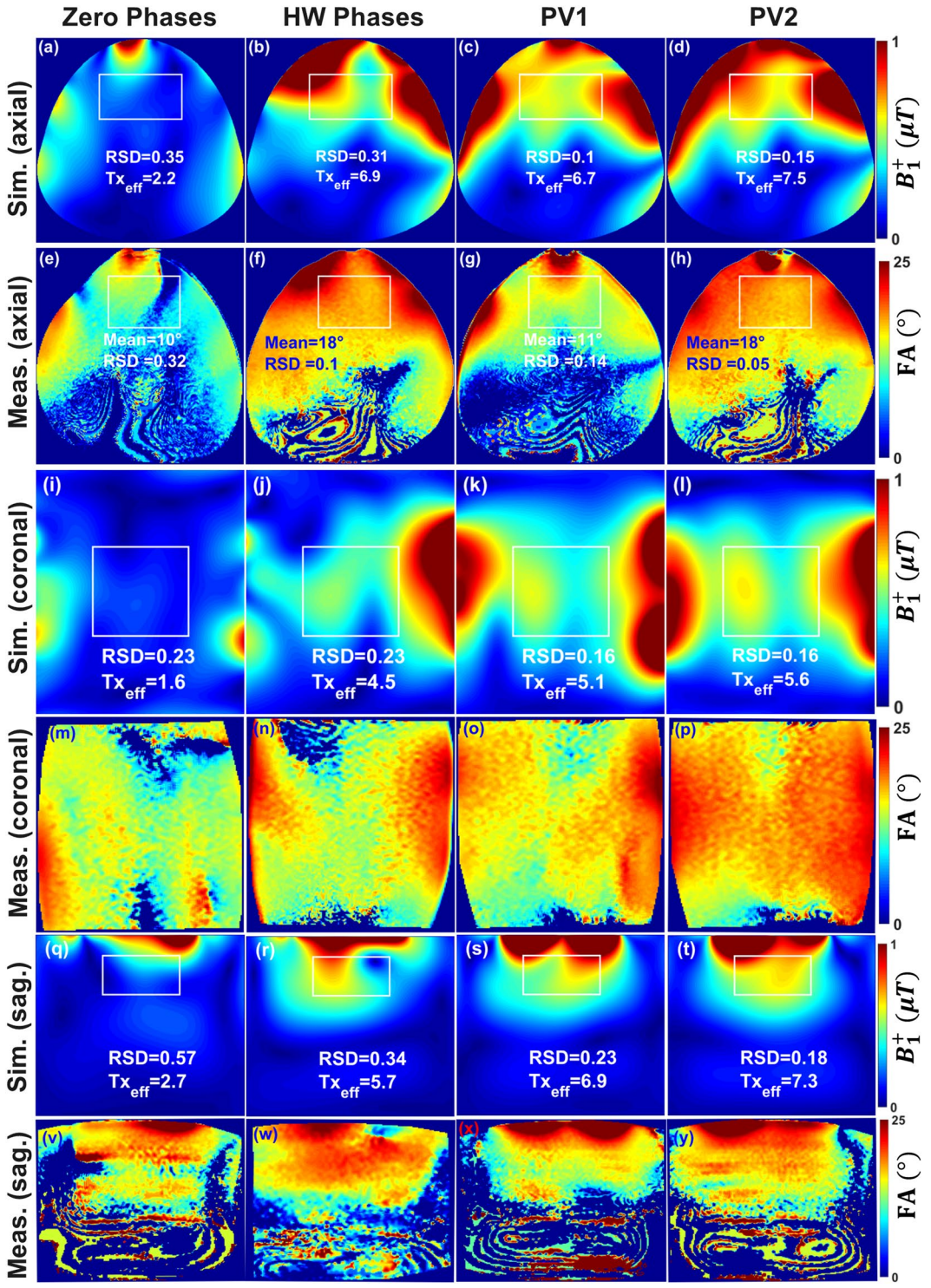

Figure 3. Simulated combined B_1^+ field distribution and measured FA maps in axial (**a**–**h**), coronal (**i**–**p**) and sagittal (**q**–**y**) central slices within the pig body phantom with zero-phases, HW phases and after static phase B_1^+ shimming with PV1 and with PV2.

Fig. 9(c). Mean SNR values in the ROIs range from 64–79, 48–61, 33–41 (SA view) and 62–101, 50–81, 34–58 (LA view) for acceleration factors R = 2, 3, 4, respectively. For the SA view this corresponds to a drop of about 23% and 48% for R = 3 and R = 4. Respective drops for the LA view are about 20% and 44% for R = 3 and R = 4.

***In-vivo* MRI measurements with pig (60 kg).** Figure 10 shows *in-vivo* single frames of the GRE CINE images of the pig heart acquired with parallel imaging acceleration factors R = 2, 3, 4 and 6. The number of phase encoding steps (NPE), TA, and number of heart beats (HB) used for acquisition are shown in the corresponding

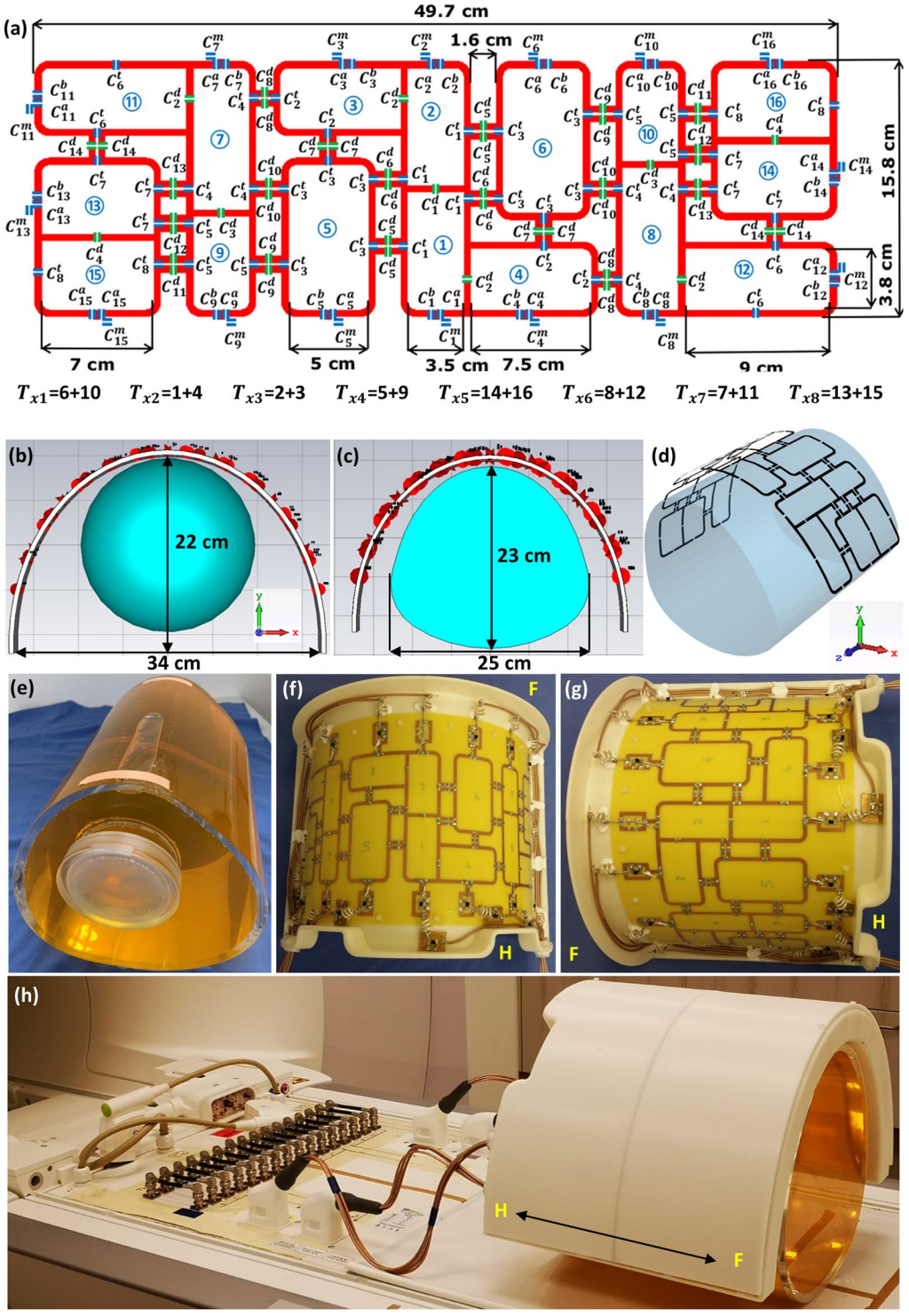

Figure 4. Schematic of the mono-surface array with element dimensions, capacitor variables, and channel numbers (T_{x1}–T_{x8}) (**a**), RF coil simulation model loaded with a 20 cm diameter spherical phantom (**b**) and a pig body phantom (**c**,**d**). (**e**) Prototype of the in-house developed pig body phantom. Prototype of the mono-surface array shown from the head−foot (**H**–**F**) direction (**f**) and side view (**g**). (**h**) The mono-surface array setup loaded with a pig body phantom and connected to the interface via four ODU plugs and to the 7 T scanner.

images. For the large number of PE-lines at R = 2 a significant blurring of the heart wall is observed. This is due to the large amount of HB required during acquisition and, which often results in poor consistency of the acquired image k-spaces due to intrinsic variation of the both heart rhythm and motion. This effect is removed by higher acceleration (less PE-steps), where, a lower amount of HB is needed. With the acceleration factors R = 2, 3, 4 and 6, visualization shows clear sharp contours for the myocardium wall.

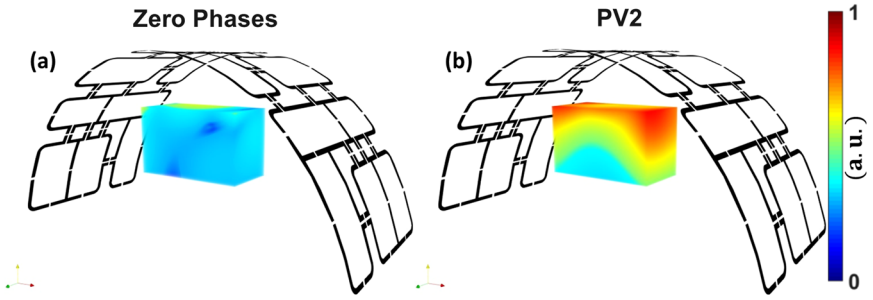

Figure 5. Simulated 3D SNR improvement achieved by the static B_1^+ shimming with PV2 compared to zero-phases.

Figure 11 show *in-vivo* multiple heart phases acquired with GRE CINE at acceleration factor R = 3 (every second reconstructed heart phase is shown).

Discussion

In this study we designed, simulated, built, and tested a mono-surface 8Tx/16Rx pTx coil array for cMRI in pigs at 7 T. The mono-surface array was driven in pTx mode on a 7 T scanner. The mono-surface array shows a significant improvement in the B_1^+ field homogeneity after RF-shimming, which proves the high efficiency of the developed array design for using with the pTx-capable MR-system in large animal cardiac studies at UHF.

The PCB was fixed on one half-elliptical housing, which was designed to fit pigs ranging from 40–80 kg [see Fig. 4(f–h)]. The mono-surface array enabled efficient B_1^+ shimming capabilities and showed better control of the B_1^+ field distribution for all individual 8Tx channels in a spherical phantom [see Fig. 1] and in a pig body phantom [see Fig. 2]. However, both simulated and measured B_1^+ field distribution per channel within a 20 cm diameter spherical phantom shows some stronger overlaps between the channels T_{x2} (combined elements 1 & 4), T_{x3} (combined elements 2 & 3) and T_{x4} (combined elements 5 & 9) [see Fig. 1(b,c,d,f,g,h)]. This overlap of the B_1^+ profiles in the central coronal plane at about 10 cm depth from the coil surface has many reasons. First, the spherical phantom was selected to test the worst-case scenario for loading conditions, where the side elements are not loaded properly (e.g., T_{x5} for combined elements 14 & 16, and T_{x6} for combined elements 8 & 12) and similarly for the antisymmetric channels T_{x7} and T_{x8}. For example, based on bench-top S-parameter measurements for the individual 16 elements, the channels T_{x7} (combined elements 7 & 11) and T_{x8} (combined elements 13 & 15) present poor decoupling (e.g., $S_{13,15} = -8$ dB and $S_{14,16} = -9$ dB) [see Supplementary Table S1]. Second, there is ± 10° error in the measured relative HW phase per element, which was measured at distance of about 10 cm from the element surface. The measured relative HW phases were used to compute the required RF cable phase shifters, which were used to implement the optimal phase vectors PV1 and PV2 [see Table 2]. However, the mono-surface array demonstrated accepted decoupling when loaded with the pig body phantom ($S_{13,15} = -11$ dB and $S_{14,16} = -10$ dB) [see Table 1] and with a 46 kg pig cadaver ($S_{13,15} = -16$ dB and $S_{14,16} = -12$ dB) [see Supplementary Table S2].

The capacitor values optimized on bench-top measurements were in good agreement with those capacitor values initially optimized in CST-DS (pig body phantom as load) [see Table 3]. For some elements, there are discrepancies between the optimized capacitor values in CST-DS simulations and on bench-top measurements, which mainly arises at the feeding ports of the splitting tuning and matching capacitors (e.g., C_{14}^m, C_{14}^a and C_{14}^b for element 14). This is because the discrete implemented PS circuits were added to adjust the HW phases, and they were not modeled in the CST simulations since they were considered to be ideal 50 Ω circuits. However, in the real coil prototype, the additional discrete PSs might change the input impedance at the coil feeding ports, which cause some discrepancies among capacitors optimized using simulations and bench-top measurements.

The developed 8Tx/16Rx cardiac array demonstrated high efficiency in both Tx and Rx properties for cMRI at 7 T. Due to the good decoupling and low correlation between the B_1^+ fields generated by all individual 16 elements it enables efficient capabilities for static phase B_1^+ shimming using phases control [see Fig. 3] and pTx RFPA based B_1^+ shimming with both amplitudes/phases in phantom [see Fig. 6] and pig cadaver [see Fig. 7] providing improved homogeneity and penetration of the B_1^+ field. A comparison between an antisymmetric coil array and a standard rectilinear symmetric coil array has previously been made[44]. The main issue of the standard rectilinear coil array design is the coupling between the diagonal elements. The coupling between neighboring and diagonal elements can be minimized by the optimal distribution of the coil elements of the array. The basic idea of the mono-surface array design is to move some elements from the longitudinal distribution in the *z*-axis in a standard rectilinear design[44] to the transversal direction in the *x*-axis [see Fig. 4(a)]. Then, the central four elements (e.g., elements 1–4) together form two antisymmetric L-shaped channel pairs driven by independent two RFPA. This will facilitate the decoupling of the central four elements by using a common conductor and a shared decoupling capacitor[30,31,43,44,53] (SDC) (i.e., between elements 1 & 2, elements 2 & 3, and elements 1 & 4). Additionally, this gives more degrees of freedom to distribute the surrounding two elements 5 and 6 via the selection of five different decoupling locations using capacitive decoupling mechanism (C_5^d, C_6^d, C_7^d, C_9^d, and C_{10}^d) in conjunction with a gap of 1.5 cm from each side of the array. The dimensions of the antisymmetric elements were selected to create a balance between the optimal dimensions of the individual 16-loops and the total external dimensions of the array

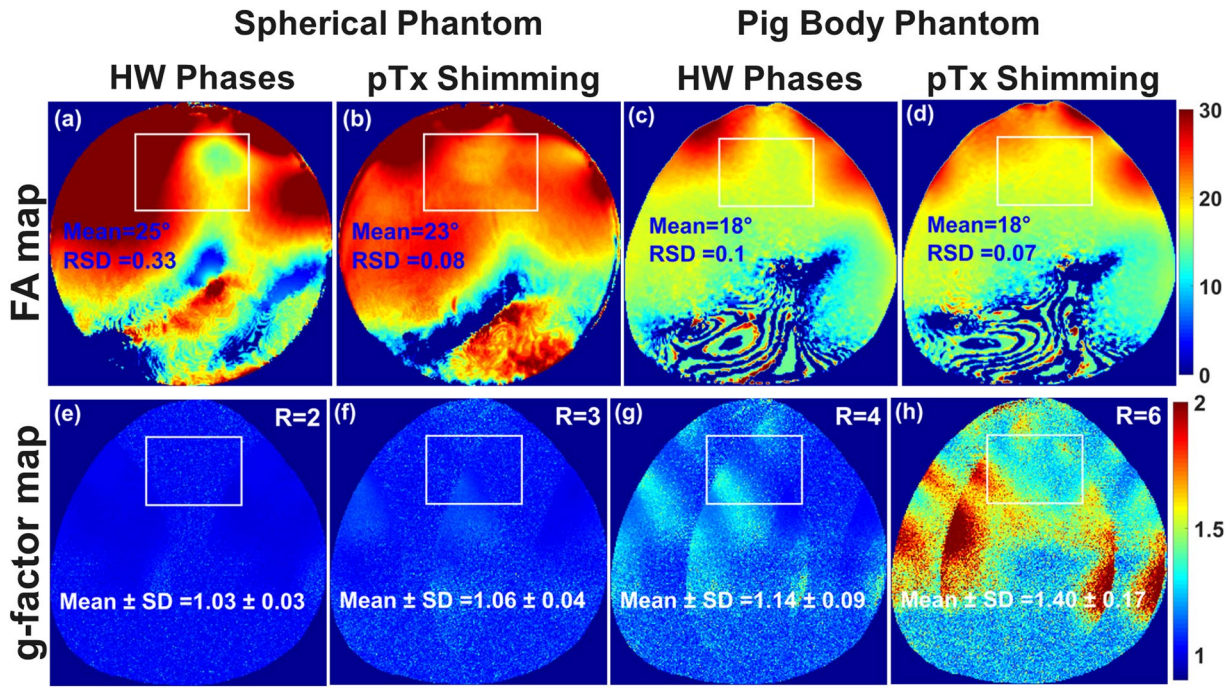

Figure 6. Measured central transversal FA maps in degrees acquired using the mono-surface array within a spherical phantom of 20 cm in diameter (**a**,**b**) and within a pig body phantom (**c**,**d**) before on-scanner static B_1^+ shimming using the vendor shimming algorithm. (**e**–**h**) Measured g-factor maps within the pig body phantom with acceleration in the L−R direction for R = 2, 3, 4, and 6, respectively. The mean ± SD of the g-factor values were computed in the selected ROI.

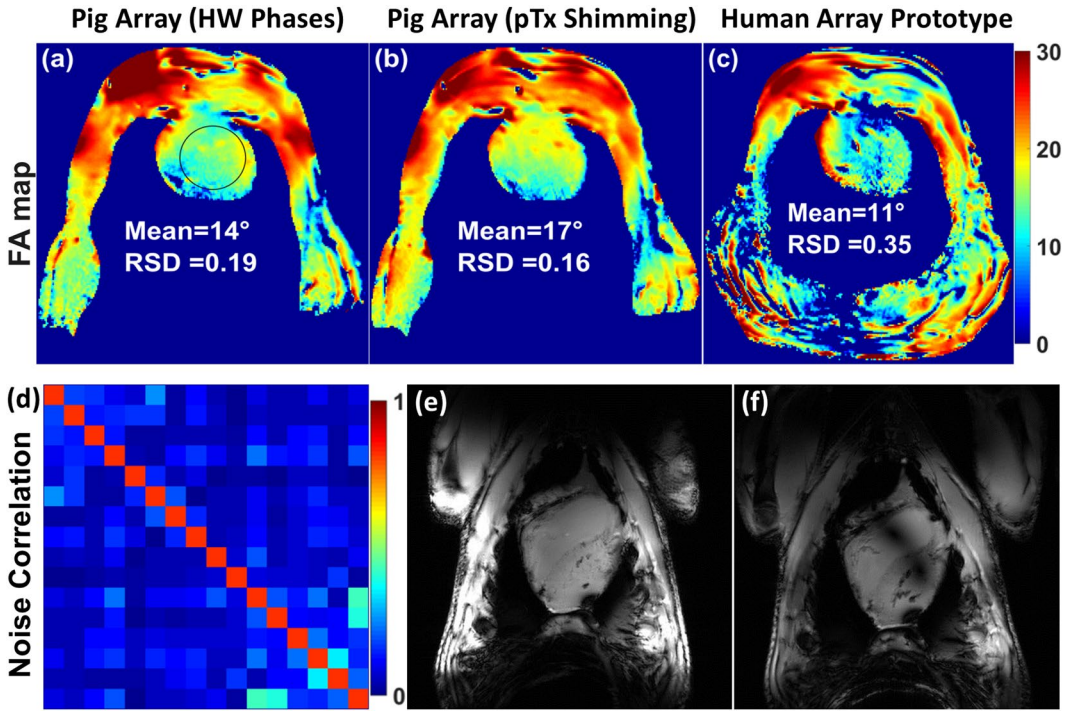

Figure 7. Measured FA maps in transversal view acquired using the mono-surface array within a cadaver pig #1 (68 kg) without on-scanner shimming (with HW phases) (**a**), and after on-scanner static B_1^+ shimming using the vendor shimming algorithm (**b**). (**c**) Transversal FA map acquired from the same animal using an 8Tx/16Rx human cardiac array prototype. (**d**) Measured noise correlation matrix from the mono-surface array loaded with a pig cadaver. (**e**,**f**) Coronal views demonstrate relatively homogeneous B_1^+ field excitation using the dedicated mono-surface array (**e**) while the coronal images acquired using the human cardiac array prototype shows clearly visible destructive B_1^+ artefacts (**f**).

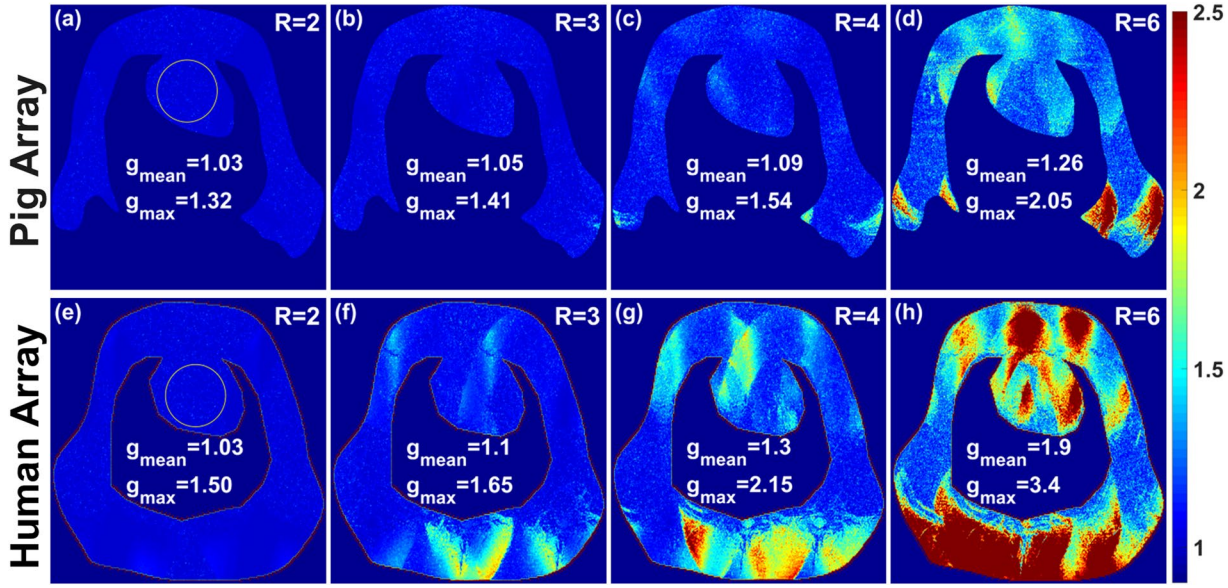

Figure 8. Measured g-factor maps of R = 2, 3, 4, and 6 within a cadaver pig #1 (68 kg) with acceleration in the L−R direction were acquired using the mono-surface array (**a**–**d**) compared to an 8Tx/16Rx human cardiac array prototype (**e**–**h**). The mean and maximum of the g-factors were evaluated in the ROI of the heart. The mono-surface array geometry and housing shaping provide clearly observed benefit for the parallel imaging acceleration providing up to 50% lower g-factor for the high acceleration rates (R = 6) compared to the human cardiac array prototype.

to fit perfectly with the half-elliptical housing. Additionally, instead of extending the other loop elements in the longitudinal *z*-axis like in the standard rectilinear array design, eight elements (3, 4, 11, 12, 13, 14, 15 and 16) were extended in the transversal *x*-axis. These elements results in a stronger penetration of the B_1^+ field within the pig heart after bending.

The phase vector optimization results reveal the significant advantage of the mono-surface array in terms of static phase B_1^+ shimming optimization potential. The new mono-surface array design provides additional degrees of freedom for B_1^+ shimming (e.g., the L-shaped element distribution, loop sizes and geometries, and the antisymmetric 16 elements allocation on the half-elliptical housing). Even without RFPA-based static B_1^+ shimming, the developed coil array with the optimized HW phases showed homogeneous FA map distribution (RSD of 0.19) without noticeable destructive interferences within the heart region [see Fig. 7(a)]. After on-scanner RFPA-based static pTx B_1^+ shimming with the RSD of the measured FA within the heart region of pig cadaver #1 is 0.16 [see Fig. 7(b)]. This result shows that the mono-surface array after on-scanner RFPA-based static pTx B_1^+ shimming has a significant improvement in the B_1^+ field homogeneity becoming by factor of 2.8 higher compared to a pTx cardiac array of similar design with two independent A−P parts (RSD = 0.46)[44].

Due to the difficultly to find in literature a dedicated multichannel pTx coil array for pigs at 7 T, we compared our new array design to some published human arrays. The measured mean g-factors that we report in this work using the dedicated coil array in a pig cadaver #1 with acceleration factors of R = 4 (1.09) [see Fig. 8(a–d)] is lower than the mean g-factors mentioned in the literature (1.58, 2.33, and 1.2) using 8-channel[30], 16-channel[31] and 32-channel[26] Tx/Rx loop human coil arrays, respectively. The mean g-factor obtained from the mono-surface array with acceleration factors of R = 6 is 1.26, which is about 58% lower than the measured mean g-factor mentioned in the literature[26] (g_{mean} = 2) with 32-channel Tx/Rx human coil array. High resolutions (0.3 mm × 0.3 mm) cardiac images were acquired using the mono-surface array in a pig cadaver #2 [see Fig. 9]. The mono-surface array provides relatively small intensity variation across the region of the heart. In comparison to the smaller designs with two independent arrays[43,44], the mono-surface array reveals practically negligible noise amplification over R = 2, 3, and 4. The posterior wall in a SA view remains clearly visible for acceleration factors R = 2, 3, and 4, indicating that the coil is capable for high quality volumetric cMRI acquisitions in *in-vivo* use.

The demonstrated *in-vivo* results confirm that the optimized phase vector (PV2) provides homogeneous B_1^+ excitation of the heart region without visible destructive interference and sufficiently good coverage of the posterior rear wall [see Fig. 10]. The noise level (σ_N) computed as standard deviation in marked ROIs increases with decreasing number of PE-lines. An average tissue-to-blood contrast of eight is observed on both LA and SA views. The mono-surface array has high parallel imaging capability, enabling high spatial resolution cMRI. The antisymmetric design allows for efficient usage of the acceleration with phase-encoding direction angulated according to the standard anatomical views of the heart. A low acceleration factor (R = 2) resulted in blurring of the *in-vivo* images due to the relatively large amount of PE-lines and thus, HB used for CINE reconstruction. This was, however, efficiently handled by increasing the acceleration and correspondingly decrease the number of PE-lines needed for the reconstruction. By this way, errors originated from losing k-space coherence were effectively prevented. No visible artefacts of GRAPPA reconstruction are observed in the *in-vivo* scans despite the

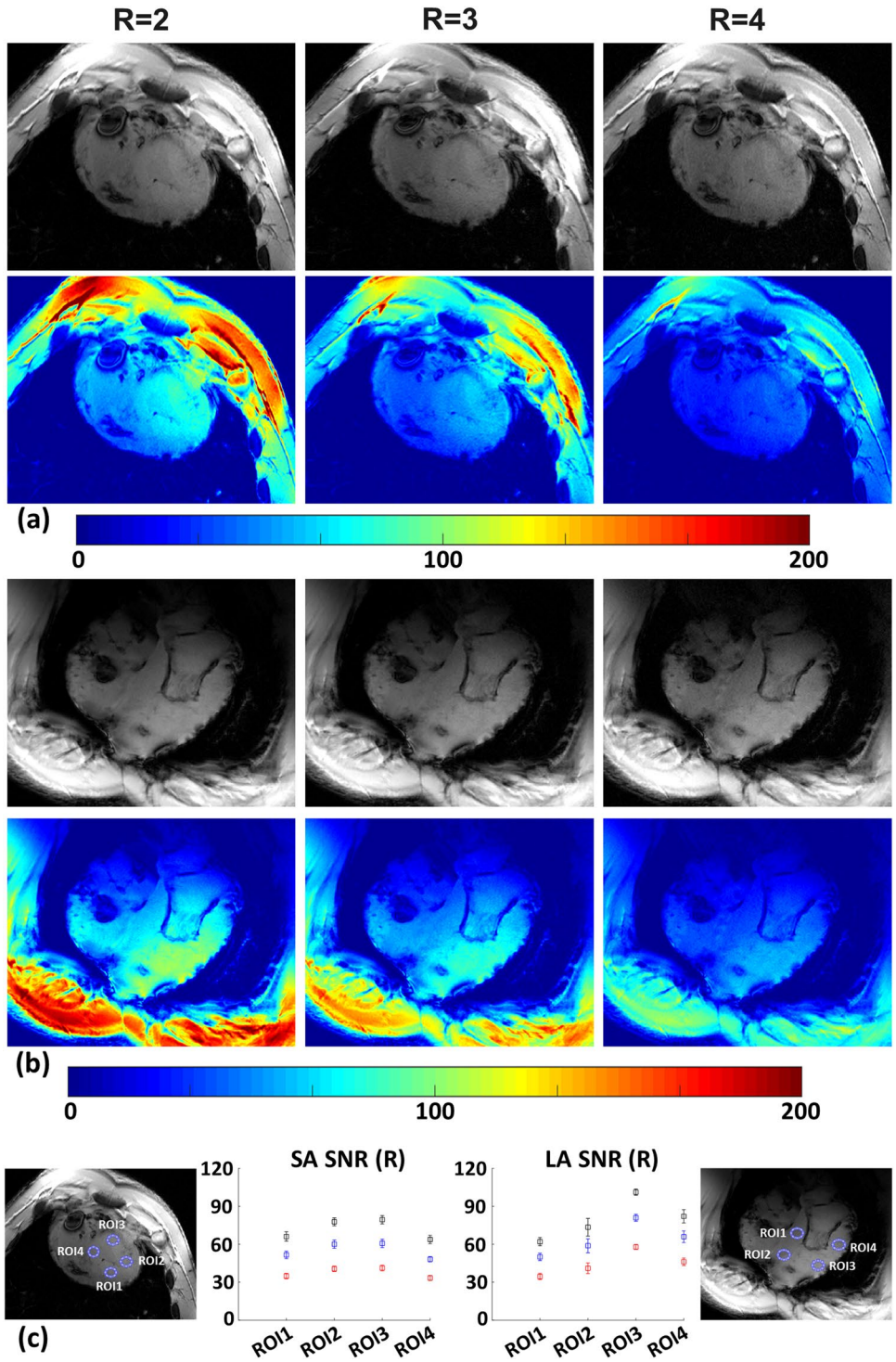

Figure 9. Impact of parallel imaging acceleration on SNR in anatomical images within a cadaver pig #2 (46 kg). (**a**) Anatomical SA and corresponding SNR maps for varying acceleration factors R = 2, 3 and 4 (left to right). (**b**) Respective LA views analogous to (**a**). (**c**) SNR plots of mean ± single standard deviation in four myocardial ROIs for SA and LA views in dependence of the acceleration factor. Black: R = 2, Blue: R = 3, and Red: R = 4.

significant reduction of total PE-steps. Both LA and SA anatomical views provided high spatial (0.6 mm in-plane) and sufficient temporal resolution while keeping fair diagnostic quality SNR [see Fig. 11]. The *in-vivo* measurements using the mono-surface array confirmed high potential of the antisymmetric design in terms of both transmit and receive properties. Both LA and SA views could be visualized with high spatial resolution if a drastically reduced number of phase encoding steps (and number of heart cycles) was used for the reconstruction of 30 cardiac phases. The spatial resolution of 0.6 mm achieved *in-vivo* is essentially superior to that used under typical clinical cMRI conditions at 3 T (1–1.5 mm in-plane spatial resolution).

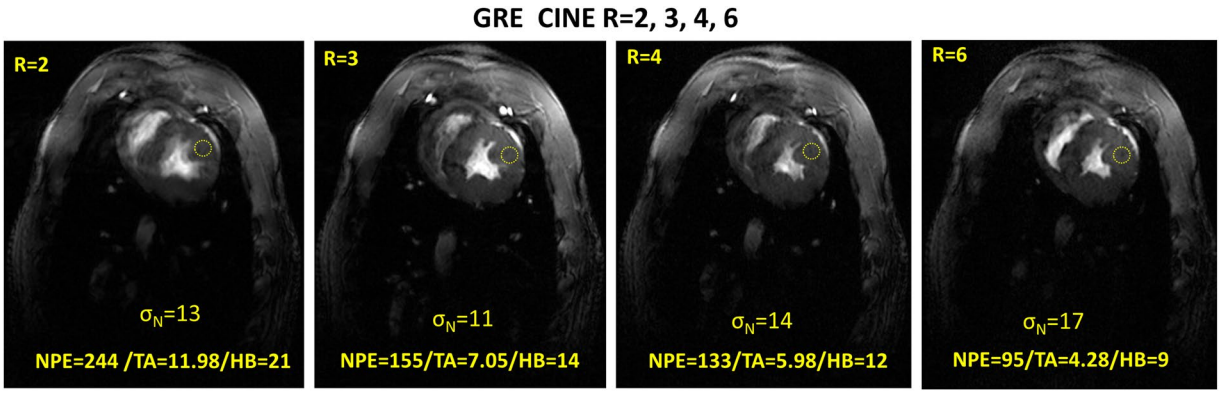

Figure 10. Single frames of the GRE CINE images of the pig heart acquired in a 60 kg pig *in-vivo* with parallel imaging acceleration factors R = 2, 3, 4, and 6. Spatial resolution 0.6 mm × 0.6 mm × 6 mm, FA = 35°, retrospective reconstruction 30 phases, frame at trigger delay = 270 ms. For the large number of PE-lines significant blurring of the heart is observed due to relatively large number of HB needed for acquisition and probably poor consistency of the acquired k-space. This effect is removed by higher acceleration (less PE-steps) and, thus, less amount of HB needed. With R = 3 and 4 the myocardium wall has clear sharp contours.

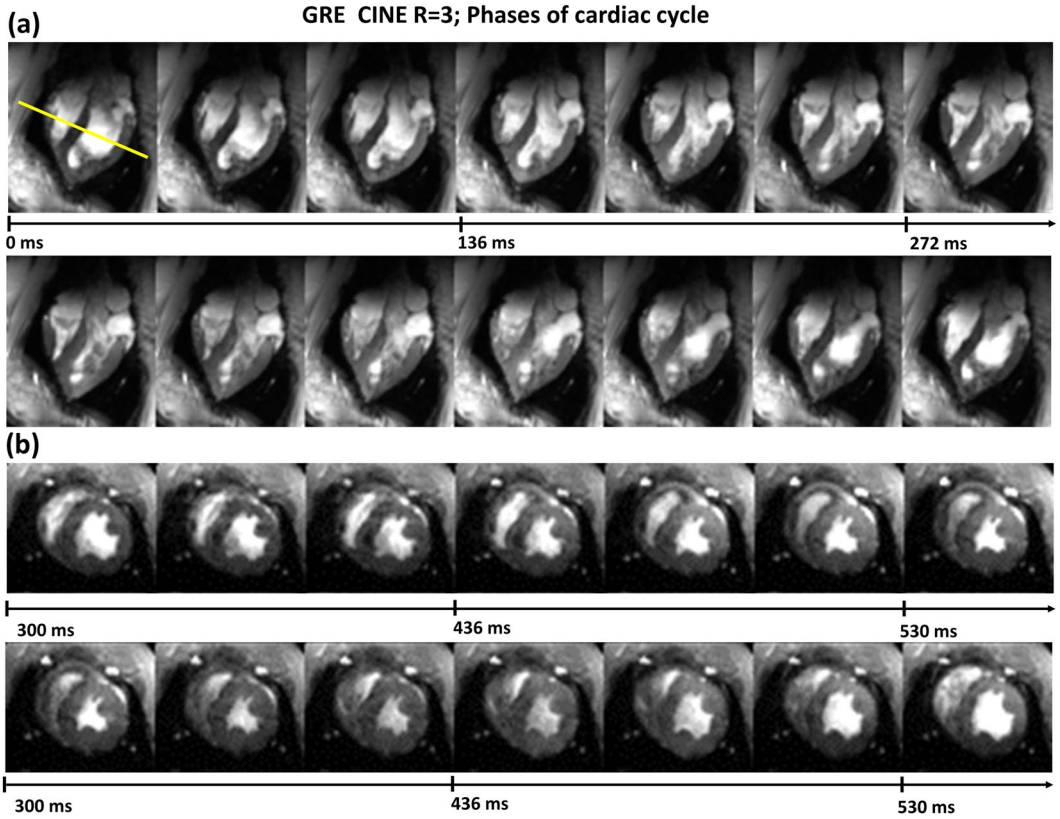

Figure 11. Multiple heart phases acquired in a 60 kg pig *in-vivo* with GRE CINE at acceleration factor R = 3. LA view (**a**) and SA view (**b**) are shown. High spatial resolution of 0.6 mm in-plane is demonstrated while keeping fair diagnostic quality SNR. This is essentially superior to the typical clinical cMRI at 3 T which usually is obtained at in-plane spatial resolutions of 1–1.5 mm.

The mono-surface antisymmetric array design, hardware electronics, RF shimming simulations described in this paper can be easily adapted for multichannel coil arrays optimized for different MR applications (e.g., cardiac, head, and spine) at UHF. The number of loop elements can be easily increased to 32 or even 64, while maintaining good decoupling among all elements.

pTx Channel #	Element#	HW Phases[°]	PV1[°]	PV2[°]	Cable PSs for PV1 [°]	Cable PSs for PV2 [°]
T_{x1}	6	−98	−25	59	45	90 + 22.5
	10	−91	4.0	48	22.5	90 + 45
T_{x2}	1	−30	81	114	0	90 + 22.5
	4	15	12	11	90 + 22.5	180 + 90
T_{x3}	2	−66	19	91	22.5	90 + 22.5
	3	−113	−246	148	180 + 45 + 22.5	0
T_{x4}	5	13	110	181	22.5	90
	9	70	−214	−71	45	45
T_{x5}	14	87	−111	−4.0	180 + 90 + 45	0
	16	82	−169	−77	0	45 + 22.5
T_{x6}	8	136	−47	3.0	180 + 90 + 22.5	45
	12	164	−106	−72	22.5	90 + 45
T_{x7}	7	68	−188	−139	0	90 + 22.5
	11	98	−96	247	180 + 90 + 45	90 + 22.5
T_{x8}	13	140	−164	−67	45	90 + 22.5
	15	164	−82	−35	0	90

Table 2. Measured relative HW phases for the mono-surface array loaded with the pig body phantom, relative optimized phases (PV1 and PV2), and the required coaxial cable PSs required to validate the optimal vectors PV1 and PV2. The coaxial cable PSs were computed after subtracting the HW phases from PV1 and PV2, subtraction the results from the maximum positive phase value and finally rounding the resulted phase nearest to 22.5°.

Methods

Array design. The antisymmetric coil array was composed of a mono-surface with 16-elements which were arranged so that the central two elements were arranged anti-symmetrically and flanked by seven elements on either side. Figure 4(a) shows the schematic of the dedicated mono-surface antisymmetric array for pigs. The 14 loop elements were distributed around the central two loop elements 1 and 2 in an antisymmetric arrangement to reduce element coupling due to less overall proximity of neighboring elements[44]. In addition, this method aims to minimize the overlapping of the B_1^+ profiles from each individual Tx channel in the heart region of the pig. The dimensions of the central loops 1 and 2 were selected as 3.50 cm × 7.35 cm as described in[43,44]. The decoupling between the central two elements 1 and 2 is accomplished using a common conductor and a SDC[30,31,43,44,53] of C_1^d. The size of the antisymmetric L-shaped elements 3 and 4 was 3.80 cm × 7.50 cm. The antisymmetric L-shaped elements 3 and 4 were decoupled from the loop elements 2 and 1 using a SDC of C_2^d. The elements 1, 2, 3 and 4 formed a pair of antisymmetric L-shaped channels (T_{x2} and T_{x3}) to reduce coupling between the neighboring elements 5 and 6. The size of the elements 5 and 6 was selected as 5.0 cm × 9.0 cm. Both loop elements have the larger dimensions in the array in order to make a balance between the dimensions of all surrounding loops in the array. This results in five different locations for capacitive decoupling with the surrounding elements (1, 2, 3, 7 and 9) with a gap of 1.5 cm. The elements 1, 2, and 3 were decoupled from the neighboring elements 5 and 6 using capacitive decoupling mechanism of two equal capacitors of C_5^d, C_6^d and C_7^d in addition to two gaps of 1.60 cm and 1.1 cm, respectively. The elements 7 and 9 and the antisymmetric identical elements 8 and 10 were decoupled using a SDC of C_3^d. Both antisymmetric L-shaped loop elements 11 and 12 were decoupled with elements 7 and 8 using a SDC of C_2^d. The elements 13 and 15 and the antisymmetric identical elements 14 and 16 were decoupled using a SDC of C_4^d. The total external dimension of the array is 15.8 cm × 49.7 cm.

EM simulations. EM simulations were performed using CST Microwave Studio (CST-MWS) (Computer Simulation Technology AG Darmstadt, Germany). Figure 4(b–d) illustrates the RF-simulation models of the dedicated cardiac coil array as simulated in CST-MWS. In this paper, the mono-surface array was simulated with two different phantom loads (a 20 cm diameter spherical phantom and a pig body phantom [see Fig. 4(b,c)]. Both phantoms have the same electrical properties with $\varepsilon_r = 59.3$ and $\sigma = 0.79$ S/m. All feeding ports, tuning, matching, and decoupling capacitors were modeled as 50 Ω discrete face ports for RF circuit co-simulations to obtain the initial values of capacitors using CST-DS[54]. The array has a copper (Cu) track width of 4 mm and a thickness of 35 μm etched on a 0.3 mm FR4 ($\varepsilon_r = 4.24$ and $\tan\delta = 0.014$ at 297.2 MHz) PCB (Q-print Electronic GmbH, Heddesheim, Germany). The PCB was bent and fixed around the half-elliptical housing ($x_{diamter} = 34$ cm and $y_{rad} = 22$ cm and 5 mm thickness) made from ABS ($\varepsilon_r = 2.8$ and $\tan\delta = 0.0095$ at 297.2 MHz) [see Fig. 4(b)]. For matching, tuning, and decoupling, fixed chip nonmagnetic capacitors (Voltronics Corp., Denville, NJ, USA) were used. The total number of mesh cells was 40.195 and 43.332 million for the spherical and pig phantoms, respectively. Individual 16-AC simulation tasks corresponding to the 16-elements of the array were evaluated at 297.2 MHz for each load. The 3D-data of the H-field for each resonance element was exported to MATLAB (MathWorks, Natick, MA, USA) for post-processing.

The two circularly polarized components of the magnetic field with opposite directions of rotation, which represent the transmit field (B_1^+) and the receive field (B_1^-) are given by: $B_1^+ = (B_x + iB_y)/2$ and $B_1^- = (B_x - iB_y)^*/2$, respectively, where B_x and B_y are the complex transversal components of the magnetic field in the x and y directions,

Capacitor	Bench	Simulation	Capacitor	Bench	Simulation
C_1^d	12.7	12.7	C_{14}^m	10.0	6.20
C_2^d	12.7	12.7	C_{15}^m	8.20	6.20
C_3^d	13.3	13.3	C_{16}^m	8.20	6.20
C_4^d	7.20	7.20	C_1^a	10.0	8.20
C_5^d	10.0	10.0	$\boldsymbol{C_2^a}$	10.0	8.20
C_6^d	0.50	0.50	C_3^a	6.20	6.20
C_7^d	1.00	1.00	C_4^a	6.20	6.20
C_8^d	1.00	1.00	C_5^a	4.70	2.10
C_9^d	10.0	10.0	C_6^a	4.70	2.10
C_{10}^d	1.00	1.00	C_7^a	6.20	6.20
C_{11}^d	1.00	1.00	C_8^a	8.20	6.20
C_{12}^d	1.00	1.00	C_9^a	10.0	8.20
C_{13}^d	1.00	1.00	C_{10}^a	8.20	8.20
C_{14}^d	2.10	2.10	C_{11}^a	6.20	6.20
C_1^t	7.20	7.20	C_{12}^a	8.20	6.20
C_2^t	6.20	6.20	C_{13}^a	8.20	8.20
C_3^t	8.20	8.20	C_{14}^a	10.5	8.20
C_4^t	10.0	10.0	C_{15}^a	10.0	10.0
C_5^t	12.1	12.1	C_{16}^a	10.0	10.0
C_6^t	4.70	4.70	C_1^b	11.6	10.0
C_7^t	10.0	10.0	C_2^b	11.0	10.0
C_8^t	6.70	6.70	C_3^b	9.20	8.20
C_1^m	6.20	6.20	C_4^b	10.9	8.20
C_2^m	6.20	6.20	C_5^b	6.70	6.20
C_3^m	6.20	6.20	C_6^b	4.70	6.20
C_4^m	4.70	6.20	C_7^b	6.20	7.80
C_5^m	10.0	12.0	C_8^b	8.20	7.80
C_6^m	8.20	12.0	C_9^b	8.20	9.00
C_7^m	10.0	10.0	C_{10}^b	9.20	9.00
C_8^m	10.0	10.0	C_{11}^b	8.20	7.40
C_9^m	10.0	10.0	C_{12}^b	6.20	7.40
C_{10}^m	10.0	10.0	C_{13}^b	13.3	10.0
C_{11}^m	10.0	4.70	C_{14}^b	8.20	10.0
C_{12}^m	10.0	4.70	C_{15}^b	12.7	10.0
C_{13}^m	10.0	6.20	C_{16}^b	10.0	10.0

Table 3. Optimized capacitor values of the mono-surface array in pF obtained using CST RF-circuit co-simulation loaded with the dedicated pig body phantom and final optimized capacitor obtained using bench-top measurements loaded with the pig cadaver of 46 kg.

i is the imaginary unit, and the asterisk indicates the complex conjugate. The RSD $= \mathrm{SD}(B_1^+)/\overline{B_1^+}$, and $\mathrm{Tx_{eff}} = \overline{B_1^+}/\sqrt{P_{in}}$ in $\mu\mathrm{T}/\sqrt{\mathrm{kW}}$, were evaluated in the selected ROI, where SD is the standard deviation, $\overline{B_1^+}$ is the mean value of the B_1^+ field, and P_{in} is the stimulated input power in (kW). The mono-surface array was fed with the same total input stimulated power ($P_{in} = 8$ W) and all coil elements were fed with equal amplitudes.

The simulated 3D-SNR map within the pig body phantom [see Fig. 5(q,r)] was computed using magnitudes of the combined B_1^+ field and B_1^- fields of individual 16-elements, with a low FA (<10°) approximation:

$$\mathrm{SNR} \propto \sqrt{\sum_{k=1}^{N}(B_1^+ \cdot B_{1,k}^{-*})^2} \tag{1}$$

where the combined B_1^+ was given by

$$B_1^+ = \sum_{k=1}^{N} b_{1,k}^+(\varphi_k) \tag{2}$$

where $b_{1k}^+ = |b_{1k}^+|e^{i\varphi_k}$ is the complex B_1^+ field for each coil element (N = 1–16) and i is the imaginary unit.

Static phase B_1^+ shimming. To achieve the best possible image quality with the proposed mono-surface array for *in-vivo* MRI studies, comprehensive B_1^+ field optimizations of static phase B_1^+ shimming within a pig body phantom was performed. Static phase B_1^+ shimming was carried out within the pig body phantom using two optimization cost functions within a 3D ROI of $12 \times 10 \times 1.0\,\mathrm{cm}^3$ resulting in two optimal phase vectors (PV1 and PV2). The first optimal phase vector (PV1) was found using the optimization of the cost function F_{c1} of Eq. (3) for maximum B_1^+ field homogeneity. The second optimal phase vector (PV2) was found using weighted combination of both B_1^+ field homogeneity and transmit efficiency using the cost functions F_{c3} of Eq. (5). The optimization cost functions were given by

$$F_{c1} = \frac{\overline{B_1^+}}{\mathrm{RSD}[\max(B_1^+) - (\overline{B_1^+})]} \cdot \mathrm{TXE} \tag{3}$$

$$F_{c2} = \frac{\min(B_1^+)}{\mathrm{RSD}} \cdot \mathrm{TXE} \tag{4}$$

$$F_{c3} = \mathrm{w}F_{c1} + \sqrt{(1 - \mathrm{w}^2)}F_{c2} \text{ where } \mathrm{w} = 0.8 \tag{5}$$

$$\text{where TXE} = \frac{|\sum_{\mathrm{k}=1}^{\mathrm{N}} b_{1,\mathrm{k}}(\{\varphi_\mathrm{k}\})|}{\sum_{\mathrm{k}=1}^{\mathrm{N}} |b_{1,\mathrm{k}}(\{\varphi_\mathrm{k}\})|} \tag{6}$$

$$\{\varphi_\mathrm{k}\} = \mathrm{argmax}[F_{c(1,3)}(\{\varphi_\mathrm{k}\})] \tag{7}$$

Channel pairing for the 8Tx/16Rx pTx system. The pTx system provides 16 kW Tx power output for eight individual feeding lines (8Tx RFPA channels). Each of these lines is then split equally by a 1:2 wilkinson power splitter, both outputs of the power divider fed two elements of the array. Therefore, each of the 8Tx channels was driven by a 2 kW/channel. To form an 8Tx/16Rx coil array, each two neighbouring loops were combined in one Tx channel [see Fig. 4(a)]. For example, the antisymmetric L-shaped Tx channel (T_{x2}) which have a common conductor and a SDC was formed by the combination of the two L-shaped elements 1 and 4. Likewise, the Tx channel (T_{x3}) was formed by the combination of the two L-shaped elements 2 and 3. The same applies to the other antisymmetric L-shaped Tx channel (T_{x6} and T_{x7}), which was formed by the combination of the two elements 8 & 12 and the elements 7 & 11, respectively. The same applies to the other antisymmetric rectangular channels (T_{x5} and T_{x8}) were formed by the combination of the two elements 14 & 16 and the elements 13 & 15, respectively. The 2Tx channels (T_{x1} and T_{x4}) were formed by the combination of the two elements 6 & 10 and the elements 5 & 9, respectively. The array was connected to a Tx/Rx switch and 16-preamplifier interface (Rapid Biomedical GmbH, Rimpar, Germany) via four plugs (ODU GmbH & Co. KG, Mühldorf a. Inn, Germany) [see Fig. 4(h)]. Each plug was connected to four loop elements of the array via four 50 Ω coaxial cables K-02252-D-60 (Huber + Suhner, Herisau, Switzerland). The Tx/Rx interface was connected to the pTX system via two compatible Siemens Rx plugs and one Tx pTx plug (ODU GmbH & Co. KG, Mühldorf a. Inn, Germany). PTx B_1^+-shimming for varying both amplitudes/phases for the 8Tx/16Rx mono-surface array was performed using software provided by the vendor of the MRI system in the pTx mode. The 8Tx/16Rx mono-surface array was compared to an 8Tx/16Rx pTx transceiver human cardiac array prototype (Rapid Biomedical GmbH, Rimpar, Germany). The 8Tx/16Rx human cardiac array prototype consists of two sections, each comprising 8 loop elements with one central element, surrounded by seven elements, forming a circular shape coil arrangement[55]. Figure 4(f–h) shows the prototype of the dedicated 8Tx/16Rx mono-surface pig array loaded with the pig body phantom connected to the interface and the 7 T MRI system.

Array characterization. *S-matrix measurements.* After obtaining the initial capacitor values from RF-circuit co-simulations using CST-DS, the final values of matching, tuning and decoupling capacitors were optimized on bench-top measurements using the cadaver of 46 kg pig as the load. The S-matrix was measured using an E5080A 4-port Vector Network Analyzer (VNA) (Keysight Technologies, Santa Rosa, CA, USA). For each resonant element, one solenoid cable trap was designed to remove the unbalanced surface current and cable resonance on the coaxial cables.

Relative HW phases. The implemented HW phases were obtained using an in-house developed MATLAB algorithm as described in[50]. To adjust the phase shift between the 16 loops, individual low pass π-network discrete phase shifter (PS) circuits were designed. The PS consists of two equal capacitors and one nonmagnetic and high quality factor inductor (Coilcraft, Inc., Silver Lake Road, Cary, IL). All PS circuits were inserted between cable traps and loops. The measured relative HW phases in the pig body phantom are shown in Table 2. To validate the optimal vectors PV1 and PV2, the phases are adjusted by coaxial cables and connected via BNC connectors to the interface as shown in Fig. 4(h). The coaxial RF cable phases were computed account of HW phases and with rounding the resulted phase to the nearest k·22.5°, where k is integer number [see Table 2].

MRI measurements. All MR measurements were performed on a 7 T whole-body MAGNETOM Terra scanner (Siemens Healthineers, Erlangen, Germany) equipped with 8-channel RFPA (2 kW/channel) in pTx

mode. All animals used in this work were German Landrace pigs obtained from Heinrichs Tierzucht GmbH, Heinsberg, Germany.

The two pig cadavers for coil optimization and testing were provided for MR-measurements immediately after usage in the approved project 55.2 DMS 2532–2–664 (Regierung Unterfranken, Germany). Euthanasia was performed with an intravenous application of 150-mg/kg pentobarbital under isoflurane anesthesia with fentanyl analgesia. The final and optimized version of the array was used for the *in-vivo* scans in agreement with the aims of the project named above. All experiments were performed in accordance with relevant guidelines and regulations.

Phantom MRI measurements. Phantom MR-experiments were performed using a 20 cm diameter spherical phantom and a pig body phantom (internal dimensions: maximum height in y-axis = 23 cm, maximum width in x-axis = 25 cm, length in z-axis = 30 cm, and with 1.0 cm thickness) to validate the B_1^+ field simulations [see Fig. 4(c–e)]. We selected the spherical phantom to test the worst-case scenario for loading conditions with side elements not loaded properly by the sphere. The pig body phantom was designed in-house and constructed from Plexiglas (Kunststoff Acryl Design GmbH, Essen, Germany). The composition of the phantom contents was: water (12.56 kg), PVP (5.96 kg), and salt NaCl (172 g), which results in volume of about 16 L and the electrical properties are $\varepsilon_r \cong 58$ and $\sigma \cong 0.77$ S/m. The measurements of the B_1^+ spatial distribution in both phantoms and pig cadaver experiments were performed using the saturated double flip angle method (SDAM) based on a GRE sequence. The GRE-SDAM measurement parameters were: TE/TR = 1.8/4000 ms, pixel resolution 2 × 2 mm, slice thickness = 4 mm for the transversal and for coronal views. The images for FA-map reconstruction were acquired in two successive measurements with doubling voltage of the excitation RF-pulse. The actual FA maps were reconstructed using an in-house developed MATLAB script.

MRI measurements with pig cadavers. Performing measurements in a fresh pig cadaver allows consistent conditions for high-resolution scans using varying acceleration factors, while avoiding cardiac and respiratory motion. In particularly, the FA-maps can be acquired using ground-truth SDAM methods which are not feasible *in-vivo*, since the long repetition times needed to exclude effects of T_1 weighting, result in long acquisition times. The total measurement time was about two hours covering the preparatory pulse sequences, anatomical GRE sequence, FA maps, SNR maps, noise correlation, and the g-factor maps. The pig cadavers were placed head first in dorsal recumbence inside the scanner. The position of the heart was estimated to fit approximately in the center of the coil. The sequence parameters for characterization of SNR and parallel imaging capability of the array in cadaver experiments were based on the standard GRE CINE protocol. The sequence parameters were: TR/TE = 69.52/4.07, FA = 45°, pixel size = 0.3 mm × 0.3 mm, number of averages = 8, FOV = 320 × 320 mm and a slice thickness of 6 mm. The analysis of SNR was carried out on SA and LA images. Varying parallel acceleration factors from R = 2–6 resulted in TEs/TRs of 4.7/69.52 ms, 4.7/78.21 ms, and 4.7/78.75 ms. Parallel imaging methodology used for accelerating MR image acquisitions was Generalized Auto-Calibrating Partially Parallel Acquisition (GRAPPA). The SNR in the images was calculated as the signal intensity in a given voxel divided by the image noise. The noise was determined as the standard deviation within a ROI placed in air. A correction factor was applied according to[56]. In addition, the SNR in myocardial tissue in dependence of the acceleration factors was assessed within four ROIs placed in the left ventricle for both SA and LA views. The GRE-SDAM measurement parameters for both cadaver pig measurements were: TE/TR = 1.8/4000 ms, pixel resolution 2 × 2 mm, slice thickness 6 mm, and number of slices = 6. The g-factor characterizations for both cadaver pig measurements were done using vendor-provide protocol and reconstruction pipeline ("coilutil"). The measurements sequence was GRE with TR = 3.9/TE = 10 ms FA = 15°, number of averages = 10, slice thickness = 6 mm, spatial resolution in-plane 0.5 × 0.5 mm. For comparison the FA-maps and g-factor measurements were done with the 68 kg cadaver using 8TX/16RX human cardiac array prototype.

In-vivo MR measurements. The pig for an *in-vivo* measurement was anesthetized using isoflurane with additional fentanyl analgesia and artificially ventilated using an MR-compatible ventilator (Draeger, Germany). Ventilation parameters, heart rate, sPO2 and rectal temperature were monitored through whole session. The heart rhythm monitoring was performed using ECG (vendor integrated) and acoustic triggering system (ACT, MRI.Tools, Berlin, Germany) connected to the external triggering input. Outside of the scanner bore the ECG and ACT system show very close heart rate and duration of RR-interval (as measured by scanner system). Inside the bore the ECG signal was significantly distorted by magneto-hydrodynamic-effect and, thus, ACT system was used for the triggering of CINE acquisition. The measurement parameters of the GRE CINE pulse sequence were: TR/TE = 44/2.9 ms, FA = 35°, pixel resolution in-plane 0.6 mm × 0.6 mm, slice thickness 6 mm; 30 heart beating phases was retrospectively reconstructed using 21, 14, 12, and 9 RR-cycles acquired with parallel imaging GRAPPA acceleration factors R = 2, 3, 4, and 6, respectively. The *in-vivo* measurement was performed using the optimal phase vector PV2.

Received: 25 July 2019; Accepted: 30 January 2020;
Published online: 20 February 2020

References

1. Yacoub, E. *et al.* Imaging brain function in humans at 7 tesla. *Magn. Reson. Med.*, **4**, 588–594, (April 2001).
2. Vaughan, J. T *et al.* 7T versus 4T: RF power, homogeneity, and signal-to-noise comparison in head images. *Magn. Reson. Med.*, **24**, 1, 24–30, (July 2001).
3. Ibrahim, T. S., Lee, R., Abduljalil, A. M., Baertlein, B. A. & Robitaille, P.-M. L., Dielectric resonances and B1 field inhomogeneity in UHFMRI: computational analysis and experimental findings. *Mag. Reson. Imag.*, **19**, 2, 219–226, (Feb. 2001).
4. Yang, Q. X. *et al.* Analysis of wave behavior in lossy dielectric samples at high field. *Magn. Reson. Med.*, **47**, 5, 982–989, (May 2002).
5. Van de Moortele, P. F. *et al.* B1 destructive interferences and spatial phase patterns at 7T with a head transceiver array coil. *Magn. Reson. Med.*, **54**, 6, 1503–1518, (Dec. 2005).

6. Ibrahim, T. S. *et al*. Design and performance issues of RF coils utilized in ultra high field MRI: Experimental and numerical evaluations. *IEEE Trans. Biomed. Eng*., **52**, 7, 1278–1284, (Jul. 2005).
7. Zhang, X. *et al*. Microstrip RF surface coil design for extremely high field MRI and spectroscopy. *Magn. Reson. Med*., **46**, 3, 443–450, (Sep. 2001).
8. Vaughan, J. T. *et al*. High-frequency volume coils for clinical NMR imaging and spectroscopy. *Magn. Reson. Med*., **32**, 2, 206–218, (Aug. 1994).
9. Zhang, X. L. *et al*. A microstrip transmission line volume coil for human head MR imaging at 4T. *J. Magn. Reson*., **161**, 2, 242–251, (Apr. 2003).
10. Zhang, X. *et al*. Higher-order harmonic transmission-line RF coil design for MR applications. *Magn. Reson. Med*., **53**, 5, 1234–1239, (May 2005).
11. Wu, B. *et al*. Multi-channel microstrip transceiver arrays using harmonics for high field MR imaging in humans. *IEEE Trans. Med. Imag*., **31**, 2, 183–191, (Feb. 2012).
12. Wu, B. *et al*. Shielded microstrip array for 7T human MR imaging. *IEEE Trans. Med. Imag*., **29**, 1, 179–184, (Jan. 2010).
13. Zhang, X. *et al*. An inverted-microstrip resonator for human head proton MR imaging at 7 tesla. *IEEE Trans. Biomed. Eng*., **52**, 3, 495–504, (Mar. 2005).
14. Akgun, C. E. *et al*. Novel multi-channel transmission line coil for high field magnetic resonance imaging. *In IEEE MTT-S Int. Microw. Symp. Dig.*, Boston, MA, USA, Jun, 1425–1428. (2009).
15. Akgun, C. E. *et al*. Alternating impedance multi-channel transmission line resonators for high field magnetic resonance imaging. *In IEEE MTT-S Int. Microw. Symp. Dig.*, May, 756–759 (2010).
16. Sohn, S.-M., DelaBarre, L., Vaughan, J. T. & Gopinath, A. RF multichannel head coil design with improved B1+ Fields uniformity for high field MRI systems. *In IEEE MTT-S Int. Microw. Symp. Dig.*, Jun., 1–3 (2012).
17. Elabyad, I. A. & Omar, A. An investigation of alternating impedance microstrip transceiver coil arrays for MRI at 7T. *In IEEE MTT-S Int. Microw. Symp. Dig.*, Baltimore, MD, USA, Jun., 1–4 (2011).
18. Sohn, S.-M., DelaBarre, L., Gopinath, A. & Vaughan, J. T. RF head coil design with improved RF magnetic near-fields uniformity for magnetic resonance imaging (MRI) systems. *IEEE Trans. Microw. Theory Techn*., **62**, 8, 1784–1789, (Aug. 2014).
19. Akgun, C. E. *et al*. Stepped impedance resonators for high-field magnetic resonance imaging. *IEEE Trans. Biomed. Eng*., **61**, 2, 327–333, (Feb. 2014).
20. Chen, Z., Solbach, K., Erni, D., & Rennings, A. Improving Efficiency and Signal-to-Noise-Ratio of a Surface Coil by a High-Impedance-Surface RF Shield for 7-T Magnetic Resonance Imaging. *IEEE Trans. Microw. Theory Techn*., **65**, 3, 988–997, (March 2017).
21. Chen, Z., Solbach, K., Erni, D. & Rennings, A. Electromagnetic field analysis of a dipole coil element with surface impedance characterized shielding plate for 7-T MRI. *IEEE Trans. Microw. Theory Techn*., **64**, 3, 972–981, (March 2016).
22. Niendorf, T. *et al*. W(h)ither human cardiac and body magnetic resonance at ultrahigh fields? technical advances, practical considerations, applications, and clinical opportunities. *NMR in biomedicine*, **29**, 9, 1173–1197, (Sep. 2016).
23. Niendorf, T. *et al*. High field cardiac magnetic resonance imaging: a case for ultrahigh field cardiac magnetic resonance. *Circ Cardiovasc Imaging*, **10**, 6, e005460, (June. 2017).
24. Snyder, C. J. *et al*. Initial results of cardiac imaging at 7 Tesla. *Magn. Reson. Med*., **61**, 3, 517–524, (Mar. 2009).
25. Vaughan, J. T. *et al*. Whole-body imaging at 7T: preliminary results. *Magn. Reson. Med*., **61**, 1, 244–248, (Jan 2009).
26. Graessl, A. *et al*. Modular 32-channel transceiver coil array for cardiac MRI at 7.0T. *Magn. Reson. Med*., **72**, 1, 276–290, (Jul. 2014).
27. Dieringer, M. A. *et al*. Design and application of a four-channel transmit/receive surface coil for functional cardiac imaging at 7T. *J. Magn Reson Imag*., **33**, 3, 736–741, (Mar. 2011).
28. Winter, L. *et al*. Comparison of three multichannel transmit/receive radiofrequency coil configurations for anatomic and functional cardiac MRI at 7.0T: implications for clinical imaging. *Eur. Radiol*., **22**, 10, 2211–2220, (Oct. 2012).
29. Niendorf, T. *et al*. Progress and promises of human cardiac magnetic resonance at ultrahigh fields: a physics perspective. *J. Magn Reson*., **229**, 202–222, (April 2013).
30. Gräßl, A. *et al*. Design, evaluation and application of an eight channel transmit/receive coil array for cardiac MRI at 7.0T. *Eur. J. Radiol*., **82**, 5, 752–759, (May 2013).
31. Thalhammer, C. *et al*. Two-dimensional sixteen channel transmit/receive coil array for cardiac MRI at 7.0T: design, evaluation, and application. *J. Magn Reson Imag*., **36**, 4, 847–857, (Oct. 2012).
32. Versluis, M. J., Tsekos, N., Smith, N. B. & Webb, A. G. Simple RF design for human functional and morphological cardiac imaging at 7 tesla. *J. Magn Reson*, **200**, 1, 161–166, (Sep. 2009).
33. Raaijmakers, A. J. E. *et al*. Design of a radiative surface coil array element at 7T: the single-side adapted dipole antenna. *Magn. Reson. Med*., **66**, 5, 1488–1497, (Nov. 2011).
34. Raaijmakers, A. J. *et al*. The fractionated dipole antenna: a new antenna for body imaging at 7 Tesla. *Magn. Reson. Med*., **75**, 3, 1366–1374, (Mar. 2016).
35. Duan, Q. *et al*. A 7T spine array based on electric dipole transmitters. *Magn. Reson. Med*., **74**, 4, 1189–1197, (Oct. 2015).
36. Oezerdem, C. *et al*. 16-channel bow tie antenna transceiver array for cardiac MR at 7.0 tesla. *Magn. Reson. Med*., **75**, 6, 2553–2565, (June 2016).
37. Raaijmakers, A. J. E., Luijten, P. R. & van Den Berg, C. A. Dipole antennas for ultrahigh-field body imaging: a comparison with loop coils. *NMR in Biomedicine*, **29**, 9, 1122–1130, (Sep. 2016).
38. Ertürk, M. A. *et al*. Toward imaging the body at 10.5 tesla. *Magn. Reson. Med*., **77**, 1, 434–443, (Jan 2017).
39. Ipek, O. *et al*. Characterization of transceive surface element designs for 7 tesla magnetic resonance imaging of the prostate: radiative antenna and microstrip. *Phys Med. Biol*., **57**, 2, 343–355, (Dec. 2011).
40. Ertürk, M. A., Raaijmakers, A. J., Adriany, G., Uğurbil, K. & Metzger, G. J. A 16-channel combined loop-dipole transceiver array for 7T esla body MRI. *Magn. Reson. Med*., **77**, 2, 884–894, (Feb. 2017).
41. Steensma, B. R. *et al*. An 8-channel Tx/Rx dipole array combined with 16 Rx loops for high-resolution functional cardiac imaging at 7T. *Magn Reson Mater Phy*, **31**, 1, 7–18, (Feb. 2018).
42. Aussenhofer, S. A. & Webb, A. G., An eight-channel transmit/receive array of TE01 mode high permittivity ceramic resonators for human imaging at 7T. *J. Magn Reson*, **243**, no., 122–129, (June 2014).
43. Elabyad, I. A. *et al*. Design and evaluation of a novel symmetric multichannel transmit/receive coil array for cardiac MRI in pigs at 7T. *IEEE Trans. Microw. Theory Techn*., **67**, 9, 3928–3945, (Sep. 2019).
44. Elabyad, I. A. *et al*. Design of a Novel Antisymmetric Coil Array for Parallel Transmit Cardiac MRI in Pigs at 7T. *J. Magn. Reson*., **305**, 195–208, (Aug. 2019).
45. Xin, S. X. *et al*. Fetus MRI at 7T: shimming strategy and SAR safety implications. *IEEE Trans. Microw. Theory Techn*., **61**, 5, 2146–2152, (May 2013).
46. Ibrahim, T. S. Ultrahigh-field MRI whole-slice and localized RF field excitations using the same RF transmit array. *IEEE Trans. Med. Imag*., **25**, 10, 1341–1347, (Oct. 2006).
47. Mao, W., Smith, M. B. & Collins, C. M. Exploring the limits of RF shimming for high field MRI of the human head. *Magn. Reson. Med*., **56**, 4, 918–922, (Oct. 2006).
48. Collins, C. M., Liu, W., Swift, B. J. & Smith, M. B. Combination of optimized transmit arrays and some receive array reconstruction methods can yield homogeneous images at very high frequencies. *Magn. Reson. Med*., **54**, 6, 1327–32, (Dec. 2005).

49. Yoo, H., Gopinath, A. & Vaughan, J. T. A method to localize RF field in high-field magnetic resonance imaging systems. *IEEE Trans. Biomed. Eng.*, **59**, 12, 3365–3371, (Dec. 2012).
50. Elabyad, I. A., Herrmann, T., Bruns, C., Bernarding, J. & Erni, D. RF shimming and improved SAR safety for MRI at 7T with combined eight-element stepped impedance resonators and traveling-wave antenna. *IEEE Trans. Microw. Theory Techn.*, **66**, 1, 540–555, (Jan. 2018).
51. Krikken, E. *et al*. Homogeneous B1 (+) for bilateral breast imaging at 7T using a five dipole transmit array merged with a high density receive loop array. *NMR in biomedicine*, **32**, no.2, e4039, (Feb. 2019).
52. Schmitter, S. *et al*. Cardiac imaging at 7 Tesla: Single- and two-spoke radiofrequency pulse design with 16-channel parallel excitation. *Magn. Reson. Med.*, **70**, 5, 1210-1219, (Nov. 2013).
53. Perrier, A. L. *et al*. Design of a two-channel NMR coil using an impedance transformation approach. *IEEE Sensors Journal*, **12**, 6, 1801–1808, (June 2012).
54. Kozlov, M. & Turner, R. Fast MRI coil analysis based on 3-D electromagnetic and RF circuit co-simulation. *J. Magn Reson*, **200**, 1, 147–152, (Sep. 2009).
55. Terekhov, M. *et al*. Customized B1+-Shaping using multi-Channel transceiver array prototype for 7 T cardiac MRI with central elements symmetry. *Proc 28th Intl. Soc. Mag. Reson. Med*. Sydney, Australia (2020).
56. Dietrich, O., Raya, J. G., Reeder, S. B., Reiser, M. F. & Schoenberg, S. O. Measurement of signal-to-noise ratios in MR images: influence of multichannel coils, parallel imaging, and reconstruction filters. *J. Magn Reson Imag.* **26**(2), 375–385 (2007).

Acknowledgements

This project is funded by the German Ministry of Education and Research (BMBF) with grant # 01EO1004 & 01EO1504. We would like to thank Michael Hock, Markus Ankenbrand, Oleg Poznansky, Denis Kokorin, Steven Nguyen, Maya Bille, Verena Burkard, and Kerstin Körner for their help during the *ex-vivo* and *in-vivo* pig MRI experiments. We would like to thank Dr. Mohammed Hankir for proofreading an earlier version of this manuscript. This publication was supported by the Open Access Publication Fund of the University of Wuerzburg.

Author contributions

The design, simulation, construction, and testing of the novel mono-surface array was carried out by I. Elabyad. Manuscript was written by I. Elabyad. Pictures were made by I. Elabyad, M. Terekhov, and D. Lohr. Phantom MRI measurements and static phase RF-shimming were conducted by I. Elabyad and M. Terekhov. Cadaver MRI experiments were conducted by D. Lohr and M. R. Stefanescu and M. Terekhov. *In-vivo* pig MRI experiments was performed by D. Lohr and M. Terekhov. Anesthesia and euthanasia of pigs was performed by S. Baltes. L.M. Schreiber analyzed and discussed the results. All the authors analyzed and discussed the results. All the authors reviewed and contributed to the manuscript.

Competing interests

The authors declare no competing interests.

Additional information

Supplementary information is available for this paper at https://doi.org/10.1038/s41598-020-59949-6.

Correspondence and requests for materials should be addressed to I.A.E.

Reprints and permissions information is available at www.nature.com/reprints.

Publisher's note Springer Nature remains neutral with regard to jurisdictional claims in published maps and institutional affiliations.

3.6 A Deep Learning Based Cardiac Cine Segmentation Framework – Transfer Learning Application to 7T Ultrahigh-Field MRI

〉 Published in *medRxiv* – 2020[70]

These citations[13,45,72,74,244-280] have been applied in this publication.

In order to facilitate discussion, reproducibility and reuse we made all required code openly available.

Code and Models:

github.com/chfc-cmi/cmr-seg-tl
doi.org/10.5281/zenodo.3876351

Artificial neural networks have become state of the art for image segmentation and are increasingly applied to the assessment of cardiac function based on MRI. Limited availability of annotated data due to data access, privacy issues, missing data harmonization, and data protection is one of the biggest obstacles to routine applications of neural networks in clinical routine.

Primary aim of this study was to provide annotated, clinical data for cardiac cine segmentation as well as DL models, guidelines and easily accessible tools, enabling researchers and clinicians to apply DL based segmentation models in their respective research. Furthermore, we aimed to assess how much and which data is required to enable transfer learning on 7T cine data.

We applied a publicly available segmentation model to create RV, LV, and blood pool labels for a publicly available data set. Data with accurate ($\Delta<15\%$ compared to publicly available ESV and EDV) labels was used to train a neural network for LV segmentation, assessing influences of architectures, loss functions, and input data. The resulting network was used for transfer learning to the segmentation task on 7T cine data of healthy volunteers (n=22, 7874 images). Data requirements for transfer learning were assessed using structured and random subsets of input data for model training.

Accurate labels were gained for 763 examinations (238350 images). Our initial model achieved $DICE_{LV}=0.835$ and $DICE_{MY}=0.670$ on 7T cardiac cine images. Transfer learning using 7T cine data and ImageNet weight initialization significantly improved model performance ($DICE_{LV}=0.900$ and $DICE_{MY}=0.791$). Using structured and random subsets we found that training could be reduced by 90%, with no negative impact on segmentation performance ($DICE_{LV}=0.908$, $DICE_{MY}=0.805$). Key to maintaining model performance were end-systolic and end-diastolic images.

Access to our labeled data, segmentation models, and all respective code will facilitate further application and research. We demonstrate that this data and methodology enable transfer learning approaches, such as 7T cine segmentation. Furthermore, we show that not all data has the same value with respect to supervised learning. In addition, this study demonstrates that we need to evaluate how existing models can be applied to individual research questions and how we decide on the adaptations required to successfully do so.

Deep Learning Based Cardiac Cine Segmentation – Transfer Learning Application to 7T Ultrahigh-Field MRI

[1]Markus Johannes Ankenbrand[*ᵀ], [1]David Lohr [ᵀ], [1,2]Wiebke Schlötelburg,

[1,3]Theresa Reiter, [2]Tobias Wech, [1]Laura Maria Schreiber

[1]Chair of Cellular and Molecular Imaging, Comprehensive Heart Failure Center (CHFC), University Hospital Wuerzburg, Wuerzburg, Germany
[2]Department of Radiology, University Hospital Wuerzburg, Wuerzburg, Germany
[3]Department of Internal Medicine I, University Hospital Wuerzburg, Wuerzburg, Germany

[ᵀ] Equal Contribution

*Correspondence
Dr. Markus J. Ankenbrand
Chair of Cellular and Molecular Imaging
Comprehensive Heart Failure Center (CHFC)
University Hospital Wuerzburg
Am Schwarzenberg 15
97078 Wuerzburg
Germany
E-Mail: Ankenbrand_M@ukw.de

Word count: 4727

Parts of this work will be used in the doctoral thesis of David Lohr

Parts of this work have been accepted at the ISMRM 2020.

Abstract

Background Artificial neural networks show promising performance in automatic segmentation of cardiac MRI. However, training requires large amounts of annotated data and generalization to different vendors, field strengths, sequence parameters, and pathologies is limited. Transfer learning addresses this challenge, but specific recommendations regarding type and amount of data required is lacking. In this study we assess data requirements for transfer learning to experimental cardiac MRI at 7T where the segmentation task can be challenging. In addition, we provide guidelines, tools, and annotated data to enable transfer learning approaches by other researchers and clinicians.

Methods A publicly available segmentation model was used to annotate a publicly available data set. This labelled data set was subsequently used to train a neural network for segmentation of left ventricle and myocardium in cardiac cine MRI. The network is used as starting point for transfer learning to 7T cine data of healthy volunteers (n=22; 7873 images). Structured and random data subsets of different sizes were used to systematically assess data requirements for successful transfer learning.

Results Inconsistencies in the publically available data set were corrected, labels created, and a neural network trained. On 7T cardiac cine images the initial model achieved $DICE_{LV}$=0.835 and $DICE_{MY}$=0.670. Transfer learning using 7T cine data and ImageNet weight initialization improved model performance to $DICE_{LV}$=0.900 and $DICE_{MY}$=0.791. Using only end-systolic and end-diastolic images reduced training data by 90%, with no negative impact on segmentation performance ($DICE_{LV}$=0.908, $DICE_{MY}$=0.805).

Conclusions This work demonstrates and quantifies the benefits of transfer learning for cardiac cine image segmentation. We provide practical guidelines for researchers planning transfer learning projects in cardiac MRI and make data, models and code publicly available.

Key words: Deep learning, neural networks, cardiac magnetic resonance, ultrahigh-field, 7T, cardiac function, segmentation, transfer learning

Background

Image segmentation, which is of great interest in cardiac magnetic resonance imaging is applied to partition acquired images into functionally meaningful regions, allowing the extraction of quantitative static measures such as myocardial mass, left ventricle (LV) volume, right ventricle (RV) volume, and wall thickness, as well as dynamic measures such as wall motion and the ejection fraction (EF). Cardiac cine MRI is the accepted gold standard for this assessment of cardiac function[1] and anatomy and is therefore of paramount clinical importance[2,3]. Proper segmentation of such data sets is a tedious and time-consuming process that has increasingly been tackled using various deep learning approaches[4-7].

Artificial neural networks have been shown to outperform other methods on several high profile image analysis benchmarks and, thus, so-called deep learning models have become state-of-the-art for a wide variety of computer vision tasks. Multiple factors like the wide application area of deep learning, available compute power, and increasing investments as well as user-friendly open source software have enabled a rapid development of the field of artificial intelligence. This led to ever increasing applications in medical imaging such as MRI[8] where tasks nowadays range from data acquisition and image reconstruction[9-11], image restoration[12,13], to image registration[14,15], segmentation[16-19] as well as classification[20,21] and outcome prediction[22,23].

There is consensus in the field that the limited availability of labelled or annotated data due to data access, privacy issues, missing data harmonization, and data protection is one of the main obstacles for future clinical applications of deep neural networks[17,19,24]. While some resources like the UK Biobank[25] already exist to address this issue, the high quality standards and the amount of work required to organize and maintain such a resource makes data access expensive. In addition, such data may already exceed the quality that is available in clinical routine cardiac MRI. This leads to neural networks, which perform very well for a very specific task within a confined data space, where training and testing data share the same distribution. However, these networks usually lack generalization capabilities. While methods such as data augmentation, transfer learning, weakly-, self-supervised, and unsupervised learning have been applied to overcome the issue of small datasets in research, it is unclear how much data is really required in order to create a well-generalizing network or to apply transfer learning.

In this work, we aim to enable researchers and clinicians in cardiology to apply deep learning-based segmentation models in their respective research by providing guidelines and easily accessible tools as well as annotated data for transfer learning. We create labels for a public

data set, the Data Science Bowl Cardiac Challenge Data[26] (further referred to as Kaggle data set) which, at this point, does not have segmentation labels. We further create a base network for LV segmentation using these labels and evaluate its performance on 7T human cine data. In addition, we assess if transfer learning improves model performance for the 7T segmentation task and analyze how much and which data is required. The framework provided in this study in combination with access to scripts and the data used, will enable researchers to reproduce our results and apply deep learning based segmentation in their respective field.

Methods

The Kaggle Data Set

As mentioned above, cardiac MRI is the gold standard for the assessment of cardiac function, a key indicator of cardiac disease. The 2015 Data Science Bowl challenged participants to create an algorithm for automatic assessment of end-systolic and end-diastolic volumes (ESV and EDV) and thus, ejection fraction, based on cardiac cine MRI. The data set consists of a training, a validation, and a test set and once the challenge has ended, all sets and their corresponding volume information (end-systolic and end-diastolic) was made available for research and academic pursuits, leading to a total of 1140 "annotated" cardiac MRI examinations of normal and abnormal cardiac function. Images are in DICOM format resolving up to 30 phases of the cardiac cycle. While we will focus on short axis images in this study, the Kaggle data set also contains alternative views. Examinations were done on 1.5 T and 3.0 T systems (Siemens Magnetom Aera and Skyra, Siemens Healthineers, Erlangen, Germany) with applications of both FLASH and TrueFISP sequences. An overview of the complete data set and its variation in patient data and sequence parameters is given in Table 1.

Data Curation

The complete data set is a compilation of real, clinical data from several sites and as such, subject to inconsistencies within individual examinations. Those can be a combination of:

- missing time points
- inconsistent slice spacing
- inconsistent image dimension
- repeat measurements (identical slice location)
- scaled images
- image rotations

Prior to the application of the published segmentation network of Bai et al.[4] we performed data curation, correcting inconsistencies in all but 8 examinations. More detailed information and curated data can be found in the online repository (https://github.com/chfc-cmi/cmr-seg-tl, https://doi.org/10.5281/zenodo.3876351).

Creating Labels

Once the data was corrected for inconsistencies we ran the Python based segmentation model of Bai et al. for the complete data set, generating RV, LV, and blood pool labels as well as LV ESV and EDV volumes. ESV and EDV values were then compared to the ground truth values provided by Kaggle in order to determine the accuracy of the network prediction. Based on this comparison we created confidence sets where the predicted values were in the range of ±5% (p5), ±10% (p10), and ±15% (p15) of the true value. Respectively, these sets contained 175, 520, and 763 examinations and 54540, 162480, and 238350 images. All scores (label versus ground truth) for ESV and EDV values are listed in the online repository.

Hardware

In order to deal with the extensive computation demands we used a custom workstation and a high performance cluster, both with graphical processing units. Details are given in the online repository.

Framework - Deep neural network

All implementations were realized using Pytorch[27] and fastai[28] V1. Training of neural networks (U-Net[29] architectures with varying backbones: Restnet34[30], ResNet50[31], and VGG16[32]) was performed using fastai's implementation of the *one cycle* policy[33] with adjusted learning rates (lr) and the confidence sets p5, p10, and p15.

Parameter Search

During the parameter search, we evaluated the influence of different training parameters on the efficacy of the trained model. Training speeds of the varying models and their architectures is given in the online repository. Training with a weight-decay of 0.02 and a batch-size of 32 was done for 30 epochs with frozen weights ($lr = 1e^{-4}$) and another 30 epochs with unfrozen weights ($lr = 1e^{-5}$). Details regarding frozen and unfrozen weights are provided in the online repository. The smallest training set (p5) was used initially, image size was 256x256, and moderate data

augmentation transforms (s1: flip [none], rotation [20°], lighting [0.4], zoom [1.2], padding [zeros]) were applied.

In order to avoid an extensive parameter grid search, we assessed parameter dependent performance changes in incremental steps. After each step, we determined the best-performing model using EF predictions and introduced subsequent parameter variations on this respective model.

In the first step we evaluated the influence of the architecture (VGG16, ResNet34, ResNet50) compared to the fully convolutional Network by Bai et al[4]. trained on UKBB data (further referred to as UKBB model). Due to memory limitations, we had to reduce the batch size for training of the VGG16 and the ResNet50 models.

In the second step, we assessed variations in the loss function such as cross-entropy (default), generalized DICE[34], and focal loss. In the third and last step we evaluated the influence of the number of training images using the confidence sets p5, p10, and p15.

We assessed the influence of training data resolution, training a model with lower input resolution (128x128, r34_CE_p5_128). Details are provided in the online repository.

Data Augmentation

Since transfer learning applications assessed in this study are based on 7T data we expect somewhat different image contrast and artefacts compared to conventional, clinical datasets. In addition, we intended to account for the heterogeneous training data, which led to the following set of augmentations for the initial networks (s1: flip [none], rotation [20°], lighting [0.4], zoom [1.2], padding [zeros]). Further, we aimed to introduce some robustness to forms of data variations, such as 90°-rotations and flips (left-right) using more extensive data augmentation (s2: flip [Left-Right], rotation [90°], lighting [0.4], zoom [1.2], padding [zeros]). In order to test the efficacy of these transforms we trained a new model (r34_CE_p5_s2) and compared EF predictions on a dataset including rotated and flipped images retained during the data curation process.

Transfer Learning

All assessments regarding transfer learning to 7T data are done using model: r34_CE_p5_s2. As initial point of comparison we used the UKBB model to create labels for 7T data, in order to assess generalization capability of a model, which was trained on a very homogeneous data set (UKBB).

Following approval of the local ethics committee (7/17-SC), n=22 (14 female, 8 male) were examined using a 7T whole body MRI system (Siemens MAGNETOM Terra, Erlangen, Germany) and a 1TX/16RX thorax coil (MRI Tools, Berlin, Germany)[35]. Written informed consent was obtained prior to all measurements. Patient age was 22-53 years, body weight 52-95 kg, and height: 151-185cm. For triggering, both the integrated ECG and an external acoustic triggering system (MRI Tools, Berlin, Germany) were used in order to synchronize measurements with the heartbeat, choosing whichever method provided a more stable trigger signal during the examination. Images were obtained during initial sequence implementation and optimization for 7T cardiac MRI using a cardiovascular (CV) GRE cine-sequence and protocol parameters therefore vary to some degree. The parameters were: TE = 3.57ms, FOV = 340 mm x 320 mm, interpolated voxel size = 0.66 x 0.66 x 6 mm, GRAPPA acceleration factors: R = 2 and R = 3. Depending on the heart rate 6-11 segments and 20-35 cardiac phases were measured using retrospective gating. Short axis CINE stacks for volumetric evaluation varied in the number of slices (14-17) and multiple breath-holds (~13s) were necessary to acquire the whole stack. Images were assigned into training, validation and test sets (14, 5, 3 subjects and 5076, 1842, 955 images, respectively). All images were manually segmented by an expert radiologist (TR). Three data sets of the test set were additionally segmented by an expert cardiologist (WS), in order to obtain an estimate of interobserver-variability.

Starting Point for Model Training - 7T Human

To assess the efficacy of transfer learning for LV segmentation based on clinical 1.5T and 3T data and experimental (human) 7T data, we compare models with varying degrees of training and transfer learning. Using a U-Net architecture with a ResNet34 backbone (r34_CE_p5_s2), we generated the following three models:

1) initialization with random weights (R)
2) initialization with ImageNet-weights – transfer learning 1 (TL)
3) Model 2, pre-trained on Kaggle data - transfer learning 2 (TL^2)

All models were used to generate predictions for the 7T test set.

Model performance was always evaluated using the Soerensen-DICE[36] coefficient between predictions and respective ground truth labels.

Data Requirements for Model Training - 7T Human

To assess how much and what data is required for convergence of a model we trained all models (R, TL, TL^2) with subsets of the training data. These subsets were created in two ways:

1) Complete subject data (all slices and all phases) from either 14, 7, 3, 1 subjects (5076, 2626, 1001, 306 images, respectively); Partial subject data (only end-systolic and end-diastolic images) from all subjects (448 images)

2) Shuffle all images once, create a list of images (1-5076), and generate subsets corresponding to the respective image numbers from subset 1, always starting the count with image #1

When training with subsets, the model is exposed to a smaller number of images in every epoch. We therefore increased the number of epochs for the subsets to correct for this effect.

Results

Framework - Deep neural network

Parameter Search

Results of the parameter search are illustrated in Figure 1, showing the absolute distance between the EF predictions based on model segmentation and ground truth data provided by Kaggle. Overall, the impact of parameter variation on model performance was small (3.64-4.06% mean distance to ground truth EF).

In a first approach to interpret these results, we compared varying architectures, such as ResNet34, ResNet50, and VGG16 with the UKBB model (Figure 1A). All models led to lower mean and median distance values compared to the UKBB model (table 2). The lowest median distance values were found using a ResNet50 (2.79%), while the lowest mean distance values were found using a ResNet34 (3.64%). Differences in the absolute distance between the models (r34, r50) were rather small (Δ0.08%), however. Considering computational demand, we selected the ResNet34.

In the next step of the parameter search we evaluated model performance using varying loss functions, namely cross-entropy, generalized DICE, and focal loss (Figure 1B). Using the generalized DICE score led to the highest mean (3.93%) and median (3.07%) distance values. Median distance values were similar for cross-entropy and focal loss (2.87% vs 2.86%), while the mean distance value was lowest using cross-entropy (3.64%).

We thus selected cross-entropy for the next step of the parameter search, where we evaluated model performance using varying confidence sets: 5%, 10%, 15% (Figure 1C). Using the various confidence sets only slightly affected median distance values (2.87%, 2.89%, 2.91%). Based on EF predictions the model: r34_CE_p5_s1 performed best achieving a mean distance value of 3.64%.

Data Augmentation

Figure 2shows the performance of our models on the image set containing rotated images, plus the performance of an additional model where data augmentation allowed left-right flips, as well as rotations of up to 90°. Median and mean absolute distance values were lowest (3.06%, 4.08%) using the model with extended data augmentation (r34_CE_p5_s2).

Transfer Learning

Exemplary cine images from the Kaggle and the 7T cine data set as well as respective data augmentation are shown in Figure 3A and 3B. While the Kaggle data set includes images with varying field of views and resolution, the 7T data is consistent.

Figure 4 presents the inter-observer variability as difference of LV volume within each image in ml for all slices and phases of the 7T human cine test set (n=3). The slice count starts with 0 at the most apical slice and moves towards the most basal slice with increasing slice number. Overall expert 2 achieved $DICE_{LV} = 0.94$ and $DICE_{MY} = 0.81$ and deviations in LV volume of individual images were lower than ±5 ml in all but one image (set 3, slice 12, phase 4). Compared to expert 1, who labelled our training data, and expert 2 the AI model achieved $DICE_{LV} = 0.90$, $DICE_{MY} = 0.79$ as well as $DICE_{LV} = 0.91$, $DICE_{MY} = 0.81$. Deviations in LV volume of individual images were smaller than 5 ml in >95% of the cases. Exemplary predictions of the AI and deviations to expert 1 are shown in Figure 5. All apical slices labelled by the AI were in excellent agreement with that of our experts. The largest deviations between AI and both experts was found for the very basal slice where myocardial tissue moves in and out of plane throughout the cardiac cycle.

Starting Point for Model Training

Results of model training using varying degrees of transfer learning are displayed in Figure 6. Plotted are the DICE scores for the left ventricle and the myocardium in dependence of the number of images seen during training, showing performance and overall convergence for the

three models analyzed. All curves have been smoothed to increase interpretability. Respective plots of the raw data are shown in the online repository.

Starting with the full data set, there are clear differences in starting points (DICE after first epoch), convergence speed, and peak performance (highest performance reached) for the three models.

R: Random weight initialization followed by training using 7T data led to the:

- lowest starting points with $DICE_{LV}$ ~ 0.57 and $DICE_{MY}$ ~ 0.25
- lowest convergence speed, reaching plateau values after 100.000 images
- lowest peak performance with $DICE_{LV}$ ~ 0.89 and $DICE_{MY}$ ~0.77

TL: ImageNet weight initialization followed by training using 7T data led to the:

- starting points of $DICE_{LV}$ ~ 0.77 and $DICE_{MY}$ ~ 0.51
- higher convergence speed, reaching plateau values after 50.000-60.000 images
- higher peak performance with $DICE_{LV:}$ 0.91 and $DICE_{MY}$: 0.79

TL^2: ImageNet weight initialization, pre-trained (Kaggle data), re-trained 7T data led to the:

- highest starting points with $DICE_{LV}$ ~ 0.90 and $DICE_{MY}$ ~ 0.78
- higher convergence speed, reaching plateau values after 40.000-50.000 images
- higher peak performance with $DICE_{LV:}$ 0.92 and $DICE_{MY}$: 0.81

Data Requirements for Model Training

Results of model training using varying degrees of transfer learning and a smaller amount of training data are displayed in Figure 6 as well. The full training data set consists of 14 volunteers, while the subsets consist of 7, 3, and 1 volunteer. For the most part, curves follow the trend described for the full data set, while each reduction in volunteers led to lower starting points. Peak performances remain similar with a reduction to 7 volunteers, but drop using subset n3, in particular for models R and TL. Only for a very small number of training images (n1) peak performances are higher for model R ($DICE_{LV}$: 0.86; $DICE_{MY}$: 0.72) compared to TL ($DICE_{LV}$: 0.83; $DICE_{MY}$: 0.70).

For small subsets, such as n3 and n1, starting points as well as peak performances of all models is higher using the random selection of training images instead of all images from a set (3/1) of volunteers. The same trend is shown for the set n7 using models R and TL.

Using only end-systolic and end-diastolic images led to similar convergence speed and peak performance regarding DICE scores compared to the full data set ($R_{LV,MY}$: 0.90, 0.77; $TL_{LV,MY}$: 0.90, 0.78; $TL^2_{LV,MY}$: 0.92, 0.81 versus $R_{LV,MY}$: 0.89, 0.77; $TL_{LV,MY}$: 0.91, 0.79; $TL^2_{LV,MY}$:

0.92, 0.81). In addition, the selection of end-systolic and end-diastolic images led to increased DICE-scores as starting points, fast convergence, and higher peak performance for all models, when compared to the same number of randomly selected images.

Discussion

In this study, we successfully used a specialized, publicly available model[4] to produce labels for a public data set of clinical 1.5 and 3T cardiac cine MRI, enabling access to more annotated data. Based on these labels we created a basic AI model, other researchers can use for their individual segmentation tasks. In addition, we applied transfer learning to segmentation of 7T human cine data, demonstrating that models based on these labels and a moderate amount of new domain data enable state-of-the-art segmentation results.

One of the obstacles to get started in deep learning based segmentation is the large amount of annotated data required to train an initial model. In this study we circumvent this problem by using the public Kaggle data set, to which we provide labels. The quality of these labels was evaluated using the volume information (end-systolic and end-diastolic volumes) included in the original Kaggle data set. Therefore, careful data curation had to be applied to avoid data inconsistencies (slice spacing, changes in image dimensions and image resolution, as well as missing slices) within individual patients. In addition, we found that label quality was connected to image orientation and image resolution. Scores (mean distance between labels and Kaggle "ground truth"), data curation scripts, as well as labels are provided in the online repository, enabling future use in other studies. We want to point out that label quality and accuracy was assessed via comparison to volume information only, with rare exceptions of visual confirmation. Thresholds of 5%, 10%, and 15% (deviation to the "ground truth") for the subsets used in this study were chosen arbitrarily. With 54540, 162480, and 239350 images respectively, we assumed these three sets to provide the reasonable compromise between label accuracy and label quantity needed to assess data requirements in this specific transfer learning application.

Based on the now annotated data we trained initial segmentation models with varying architectures (ResNet34, ResNet50, VGG16), varying loss functions (cross-entropy, generalized DICE, focal loss), varying training sets (p5, p10, p15). The final model we selected was a ResNet34, using cross-entropy as a loss function, and the p5 set for training with an image resolution of 256x256. While we selected this model based on performance (mean distance to

ground truth EF), overall impacts of parameter variations (3.64-4.06% mean distance to ground truth EF) were rather small. Similar to the use in this study, researchers or clinicians can use this model as a starting point for their respective transfer learning applications.

Considering the performance of this model on 7T human cine data ($DICE_{LV}$: 0.84, $DICE_{MY}$: 0.67), generalization capability appears limited. This is also true for the UKBB model (7T human cine, $DICE_{LV}$: 0.67, $DICE_{MY}$: 0.52). As the authors[4] point out, the UKBB model was "trained on a single data set, the UK Biobank dataset, which is a relatively homogenous dataset" and might therefore "not generalize well to other vendor or sequence datasets". With respect to the performance on 7T data this just means that, compared to the UKBB dataset, the Kaggle data set contains image patterns and characteristics more similar to the 7T data we acquired. In addition, it emphasizes why improvements in generalization[37-39] are needed and why we applied an additional step of transfer learning to 7T data.

Due to differences in training data our initial models based on UKBB labels outperformed the UKBB model on the Kaggle data. While the UKBB model was trained on the homogeneous UKBB data, our models were trained on the heterogeneous Kaggle data itself. In addition, we applied data augmentation with respect to rotations and contrast and used only Kaggle data with the most accurate (top 15%) labels.

While multiple studies[4,5,26,40] have demonstrated great image segmentation results for one specific dataset, these models have not been tested on other datasets or initially lack generalization capability. In this study, we show that transfer learning leads to improved model performance. DICE scores achieved on 7T human cine data prior to and after transfer learning were $DICE_{LV}$: 0.84, $DICE_{MY}$: 0.67 and $DICE_{LV}$: 0.92, $DICE_{MY}$: 0.81, respectively. This was comparable to human inter-observer variability ($DICE_{LV}$: 0.94 and $DICE_{MY}$: 0.81) and is within the range of state-of-the-art results, despite the relatively small set of training data[19]. In addition, inter-observer-variability in EDV (3.5%) and ESV (10.5%) between our model and the expert radiologist are in good agreement with literature reports (EDV: 2.5-5.3%, ESV: 6.8-13.9%)[41] based on SSFP CMR imaging.

Typically, segmentation of the left ventricle is done to evaluate ejection fraction, a clinically used parameter. In this study we show that the model based volume prediction on the test set is very accurate for apical, mid-cavity and basal slices, with the exception of the most basal slice, where myocardial tissue moves in and out of plane throughout the cardiac cycle. Since we do not have a "ground-truth" segmentation for the Kaggle data and no information on labelling protocols, we do not know if there is any consistency in the definition of basal slices or the inclusion or exclusion of papillary muscle.

While transfer learning allows models to adapt to similar tasks and new datasets, containing new characteristics and patterns, this step also requires new labels. This aspect is often a limitation, since labelled medical data is difficult to acquire, particularly in areas that require domain-specific knowledge. In addition, the manual labelling process for high quality segmentations itself is often tedious and labor intensive. In this study we show that transfer learning applications (ImageNet weights to Kaggle data to 7T data) for cardiac cine segmentation of human 7T data can provide state-of-the-art results when training with labelled data from 7-14 volunteers (2626 – 5076 images), reaching $DICE_{LV}$: 0.92 and $DICE_{MY}$: 0.81 as well as accurate EF values. Having labels for three volunteers (1001 images) leads to decent results ($DICE_{LV}$: 0.91 and $DICE_{MY}$: 0.80). We consider labels for only one volunteer to be insufficient ($DICE_{LV}$: 0.88 and $DICE_{MY}$: 0.77).

For small training datasets ($n \leq 1001$) we show that a random selection of images from multiple volunteers leads to better performance compared to the selection of all images from a smaller number of volunteers (n=3 or n=1, figure 6). Generalization capabilities of a model increase with the amount of variation provided in the training data and thus using data from a multitude of patients or volunteers, where morphology and therefore image content and contrast differ, may be more beneficial than providing the same number of more coherent images from a small number of volunteers. Furthermore we demonstrate that the number of required images can drastically be reduced (from 5076 to 448 images), using labelled data from specific heart phases, end-diastolic and end-systolic, instead of all images. This may be possible, because knowing the two extreme states of contraction the model can deal more easily with intermediate states. Considering that n=448 images (roughly two cardiac EF examinations) enable close to state-of-the-art results for cardiac cine segmentation, data requirements for transfer learning applications in closely related tasks are low. In addition, labels for end-diastolic and end-systolic images are created in routine clinical cardiac examinations and thus easily accessible.

In summary, how much and which kind of data should be included in the transfer learning process should be carefully considered prior to labelling new data. In particular, the notion to provide data patient by patient may result in higher data requirements than necessary. There are various other routine cardiac MR examinations such as T_2, T_1, LGE, and even T_2^* that require segmentation[38,39,42]. Transfer learning applications to image segmentation of such varying contrasts may benefit from the amount of annotated data and the framework provided in this study.

With respect to future use of this annotated data we recommend researchers take the following steps:

1) use the pre-trained model we provide (r34_CE_p5_s2)
2) re-train with training data from the new domain and tune hyper parameters using validation data from the new domain
3) evaluate model performance on a test set from the new domain

In this study, we used only the 5-15% of the most accurate kaggle labels to create our base models. Thus, researchers attempting to train their own base network using the labelled Kaggle data should always assess label quality.

The experimental 7T data used in this study is not comparable to clinical cardiac MRI in patients. Future performances on clinical data should be evaluated against the Kaggle dataset.

There are some limitations connected to the use of the Kaggle dataset. While there are variations in measurement parameters, such as resolution, FOV, matrix size, TE, TR, bandwidth, and slice thickness, most examinations (~90%) were done at 1.5T. In addition, all data was acquired using Siemens whole body MRI systems. Models trained using this dataset might thus not generalize well to other vendor datasets, requiring transfer learning as demonstrated in this study.

Since no disease-related information is provided in the Kaggle dataset, we have no knowledge which and how many pathological patterns are currently represented in the dataset. In this study we demonstrate that transfer learning to 7T data of healthy human volunteers enables DICE scores of $DICE_{LV}$: 0.92 and $DICE_{MY}$: 0.81. A clinical application would require a performance assessment or transfer learning for specific cardiac pathologies, both beyond the scope of this cardiology-related methodological work.

Furthermore, the accuracy of the labels we created was assessed based on comparison to provided volume information only and visual confirmation of the contours may be biased, because we do not know if the provided volume information is based on consistent definitions of basal slices or the inclusion or exclusion of papillary muscle. This should be considered when creating models based on this dataset. In general, there is a need for a standard benchmark dataset, where labels are based on standardized protocols and images are representations of diverse clinical phenotypes (diseases, vendors, field strengths, sequences, protocols).

Conclusions

In this study, we provide access to annotated cardiac cine MRI data, and AI models, which can be used as a starting point for transfer learning applications. Using such a base model, we demonstrate that transfer learning from clinical 1.5 and 3T cine data to 7T cine data is feasible with moderate data requirements, enabling future applications to other cardiac MRI examinations such as T_2, T_1, LGE, and even T_2^*. Furthermore, we show that not all data has the same value with respect to transfer learning approaches and that careful selection of the training data may drastically reduce data requirements.

Declarations

Ethics approval and consent to participate

Ethics approval of the local ethics committee at the University Hospital Würzburg has been granted under reference number 7/17-SC.

Consent for publication

All human volunteers gave their consent for publication using our institutional consent form.

Availability of data and materials

The datasets supporting the conclusions of this article are available in the zenodo repository, https://doi.org/10.5281/zenodo.3876350 and source code is available in GitHub and zenodo https://github.com/chfc-cmi/cmr-seg-tl, https://doi.org/10.5281/zenodo.3894647. The raw 7T images are not publicly available due to data privacy regulations.

Competing interests

The Department of TW (Department of Diagnostic and Interventional Radiology, University Hospital, Wuerzburg, Germany) revceives a research grant from Siemens Healthcare GmbH.

Funding

This work was supported by the German Ministry of Education and Research (grant number, 01EO1504). The funding body took no role in the design of the study, collection, analysis, and interpretation of data and in writing the manuscript.

Authors' contributions

DL, MJA, LMS & TW designed the study. MJA, DL & TW developed the computational methods. DL, WS and TR collected the data. MJA and DL analyzed and interpreted the data. DL wrote the initial draft of the manuscript. All authors read and approved the final manuscript.

Acknowledgements

We thank Andreas Hotho for insightful discussions.

List of abbreviations

LV	left ventricle
RV	right ventricle
EF	ejection fraction
ESV	end-systolic volume
EDV	end-diastolic volume
lr	learning rate
UKBB	UK Biobank

References

1. Moon JC, Lorenz CH, Francis JM, Smith GC, Pennell DJ. Breath-hold FLASH and FISP cardiovascular MR imaging: left ventricular volume differences and reproducibility. *Radiology.* Jun 2002;223(3):789-797.

2. Curtis JP, Sokol SI, Wang Y, et al. The association of left ventricular ejection fraction, mortality, and cause of death in stable outpatients with heart failure. *J Am Coll Cardiol.* Aug 20 2003;42(4):736-742.

3. Karamitsos TD, Francis JM, Myerson S, Selvanayagam JB, Neubauer S. The role of cardiovascular magnetic resonance imaging in heart failure. *J Am Coll Cardiol.* Oct 6 2009;54(15):1407-1424.

4. Bai W, Sinclair M, Tarroni G, et al. Automated cardiovascular magnetic resonance image analysis with fully convolutional networks. *Journal of cardiovascular magnetic resonance : official journal of the Society for Cardiovascular Magnetic Resonance.* Sep 14 2018;20(1):65.

5. Baumgartner CF, Koch LM, Pollefeys M, Konukoglu E. An Exploration of 2D and 3D Deep Learning Techniques for Cardiac MR Image Segmentation. *arXiv e-prints.* 2017. https://ui.adsabs.harvard.edu/abs/2017arXiv170904496B. Accessed September 01, 2017.

6. Jang Y, Hong Y, ha S, Kim S, Chang H-J. Automatic Segmentation of LV and RV in Cardiac MRI. 2018:161-169.

7. Tran PV. A Fully Convolutional Neural Network for Cardiac Segmentation in Short-Axis MRI. *arXiv e-prints.* 2016. https://ui.adsabs.harvard.edu/abs/2016arXiv160400494T. Accessed April 01, 2016.

8. Liu J, Pan Y, Li M, et al. Applications of deep learning to MRI images: A survey. *Big Data Mining and Analytics.* 2018;1(1):1-18.

9. Chen F, Taviani V, Malkiel I, et al. Variable-Density Single-Shot Fast Spin-Echo MRI with Deep Learning Reconstruction by Using Variational Networks. *Radiology.* Nov 2018;289(2):366-373.

10. Schlemper J, Caballero J, Hajnal JV, Price AN, Rueckert D. A Deep Cascade of Convolutional Neural Networks for Dynamic MR Image Reconstruction. *IEEE transactions on medical imaging.* Feb 2018;37(2):491-503.

11. Zhu B, Liu JZ, Cauley SF, Rosen BR, Rosen MS. Image reconstruction by domain-transform manifold learning. *Nature.* 2018/03/01 2018;555(7697):487-492.

12. Benou A, Veksler R, Friedman A, Riklin Raviv T. Ensemble of expert deep neural networks for spatio-temporal denoising of contrast-enhanced MRI sequences. *Med Image Anal.* Dec 2017;42:145-159.

13. Bermudez C, Plassard AJ, Davis TL, Newton AT, Resnick SM, Landman BA. Learning Implicit Brain MRI Manifolds with Deep Learning. *Proceedings of SPIE--the International Society for Optical Engineering.* Mar 2018;10574.

14. de Vos BD, Berendsen FF, Viergever MA, Sokooti H, Staring M, Isgum I. A Deep Learning Framework for Unsupervised Affine and Deformable Image Registration. *arXiv e-prints.* 2018. https://ui.adsabs.harvard.edu/abs/2018arXiv180906130D. Accessed September 01, 2018.

15. Wu G, Kim M, Wang Q, Munsell BC, Shen D. Scalable High-Performance Image Registration Framework by Unsupervised Deep Feature Representations Learning. *IEEE transactions on bio-medical engineering.* Jul 2016;63(7):1505-1516.

16. Akkus Z, Galimzianova A, Hoogi A, Rubin DL, Erickson BJ. Deep Learning for Brain MRI Segmentation: State of the Art and Future Directions. *Journal of Digital Imaging.* 2017/08/01 2017;30(4):449-459.

17. Hesamian MH, Jia W, He X, Kennedy P. Deep Learning Techniques for Medical Image Segmentation: Achievements and Challenges. *Journal of Digital Imaging.* 2019/08/01 2019;32(4):582-596.

18. Ruijsink B, Puyol-Antón E, Oksuz I, et al. Fully Automated, Quality-Controlled Cardiac Analysis From CMR: Validation and Large-Scale Application to Characterize Cardiac Function. *JACC: Cardiovascular Imaging.* 2019/07/17/ 2019.

19. Chen C, Qin C, Qiu H, et al. Deep learning for cardiac image segmentation: A review. *arXiv e-prints.* 2019. https://ui.adsabs.harvard.edu/abs/2019arXiv191103723C. Accessed November 01, 2019.

20. Liu F, Shen C. Learning Deep Convolutional Features for MRI Based Alzheimer's Disease Classification. *arXiv e-prints.* 2014. https://ui.adsabs.harvard.edu/abs/2014arXiv1404.3366L. Accessed April 01, 2014.

21. Pinaya WHL, Gadelha A, Doyle OM, et al. Using deep belief network modelling to characterize differences in brain morphometry in schizophrenia. *Scientific Reports.* 2016/12/12 2016;6(1):38897.

22. Bello GA, Dawes TJW, Duan J, et al. Deep-learning cardiac motion analysis for human survival prediction. *Nature Machine Intelligence.* 2019/02/01 2019;1(2):95-104.

23. Dawes TJW, de Marvao A, Shi W, et al. Machine Learning of Three-dimensional Right Ventricular Motion Enables Outcome Prediction in Pulmonary Hypertension: A Cardiac MR Imaging Study. *Radiology.* May 2017;283(2):381-390.

24. Lundervold AS, Lundervold A. An overview of deep learning in medical imaging focusing on MRI. *Zeitschrift für Medizinische Physik.* 2019/05/01/ 2019;29(2):102-127.

25. Sudlow C, Gallacher J, Allen N, et al. UK Biobank: An Open Access Resource for Identifying the Causes of a Wide Range of Complex Diseases of Middle and Old Age. *PLOS Medicine.* 2015;12(3):e1001779.

26. Data Science Bowl Cardiac Challenge Data 2016. https://www.kaggle.com/c/second-annual-data-science-bowl/data. Accessed 29th of July 2019.

27. Paszke A, Gross S, Massa F, et al. PyTorch: An Imperative Style, High-Performance Deep Learning Library. *arXiv e-prints.* 2019:arXiv:1912.01703. https://ui.adsabs.harvard.edu/abs/2019arXiv191201703P. Accessed December 01, 2019.

28. Howard J, Gugger S. Fastai: A Layered API for Deep Learning. *Information.* 2020;11(2):108.

29. Ronneberger O, Fischer P, Brox T. U-Net: Convolutional Networks for Biomedical Image Segmentation. *arXiv e-prints.* 2015:arXiv:1505.04597. https://ui.adsabs.harvard.edu/abs/2015arXiv150504597R. Accessed May 01, 2015.

30. He K, Zhang X, Ren S, Sun J. Deep Residual Learning for Image Recognition. *arXiv e-prints.* 2015:arXiv:1512.03385. https://ui.adsabs.harvard.edu/abs/2015arXiv151203385H. Accessed December 01, 2015.

31. Abbasi-Sureshjani S, Amirrajab S, Lorenz C, Weese J, Pluim J, Breeuwer M. 4D Semantic Cardiac Magnetic Resonance Image Synthesis on XCAT Anatomical Model. *arXiv e-prints.* 2020. https://ui.adsabs.harvard.edu/abs/2020arXiv200207089A. Accessed February 01, 2020.

32. Simonyan K, Zisserman A. Very Deep Convolutional Networks for Large-Scale Image Recognition. *arXiv e-prints.* 2014:arXiv:1409.1556. https://ui.adsabs.harvard.edu/abs/2014arXiv1409.1556S. Accessed September 01, 2014.

33. Smith LN. A disciplined approach to neural network hyper-parameters: Part 1 -- learning rate, batch size, momentum, and weight decay. *arXiv e-prints.* 2018:arXiv:1803.09820. https://ui.adsabs.harvard.edu/abs/2018arXiv180309820S. Accessed March 01, 2018.

34. Sudre CH, Li W, Vercauteren T, Ourselin S, Jorge Cardoso M. Generalised Dice Overlap as a Deep Learning Loss Function for Highly Unbalanced Segmentations. 2017; Cham.

35. Lohr D, Terekhov M, Kosmala A, Stefanescu MR, Hock M, Schreiber LM. Cardiac MRI with the Siemens Terra 7T System: Initial Experience and Optimization of Default Protocols. Paper presented at: Proc. of the 26th Annual Meeting of ISMRM; April, 2018; Paris, France.

36. Zijdenbos AP, Dawant BM, Margolin RA, Palmer AC. Morphometric analysis of white matter lesions in MR images: method and validation. *IEEE transactions on medical imaging.* 1994;13(4):716-724.

37. Feng X, Yang J, Laine AF, Angelini ED. Discriminative Localization in CNNs for Weakly-Supervised Segmentation of Pulmonary Nodules. *arXiv e-prints.* 2017:arXiv:1707.01086. https://ui.adsabs.harvard.edu/abs/2017arXiv170701086F. Accessed July 01, 2017.

38. Chen J, Li H, Zhang J, Menze B. Adversarial Convolutional Networks with Weak Domain-Transfer for Multi-Sequence Cardiac MR Images Segmentation. *arXiv e-prints.* 2019. https://ui.adsabs.harvard.edu/abs/2019arXiv190809298C. Accessed August 01, 2019.

39. Wang J, Huang H, Chen C, Ma W, Huang Y, Ding X. Multi-sequence Cardiac MR Segmentation with Adversarial Domain Adaptation Network. *arXiv e-prints.* 2019. https://ui.adsabs.harvard.edu/abs/2019arXiv191012514W. Accessed October 01, 2019.

40. Tran PV. A Fully Convolutional Neural Network for Cardiac Segmentation in Short-Axis MRI. *arXiv e-prints.* 2016:arXiv:1604.00494. https://ui.adsabs.harvard.edu/abs/2016arXiv160400494T. Accessed April 01, 2016.

41. Luijnenburg SE, Robbers-Visser D, Moelker A, Vliegen HW, Mulder BJM, Helbing WA. Intra-observer and interobserver variability of biventricular function, volumes and mass in patients with congenital heart disease measured by CMR imaging. *Int J Cardiovasc Imaging.* 2010;26(1):57-64.

42. Vesal S, Ravikumar N, Maier A. Automated Multi-sequence Cardiac MRI Segmentation Using Supervised Domain Adaptation. *arXiv e-prints.* 2019. https://ui.adsabs.harvard.edu/abs/2019arXiv190807726V. Accessed August 01, 2019.

Table 1: Data Composition and measurement parameters of the Kaggle data

Metric	Count
Male	670
Female	470
Age: 0-17 [years]	202
Age: 18 – 30 [years]	173
Age: 31-50 [years]	298
Age: 51+ [years]	467
Max Age [years]	88
Min Age [years]	0.04
1.5 T	1025
3.0 T	115

Metric	Range
Echo Time [ms]	1.04 - 1.54
Repetition Time [ms]	14 - 54.72
Bandwidth [Hz/Pixel]	915 - 1235
Slice Thickness [mm]	5 - 8
Matrix Size	120-608 x 160-736
Resolution [mm]	0.59 - 1.95
Phases	112 - 416

Table 2: Summary statistics of absolute deviation of predicted and true EF in % for the parameter search. Sorted from lowest to highest mean value. Models are named by architecture (ResNet34: r34, ResNet50: r50, VGG16: v16), loss function (cross entropy: CE, focal, DICE), confidence set (p5, p10, p15), and data augmentation (s1, s2).

Model	Mean	Sd	Median	Iqr
r34_CE_p5_ s1	3.64	3.38	2.87	3.72
r50_CE_p5_s1	3.71	3.73	2.79	3.70
r34_CE_p15_s1	3.73	3.38	2.91	3.72
r34_focal_p5_s1	3.75	3.90	2.86	3.80
r34_CE_p10_s1	3.77	4.44	2.89	3.76
r34_DICE_p5_s1	3.93	3.43	3.07	3.91
v16_CE_p5_s1	4.06	4.94	3.02	3.87
UKBB	5.42	8.83	3.72	4.34

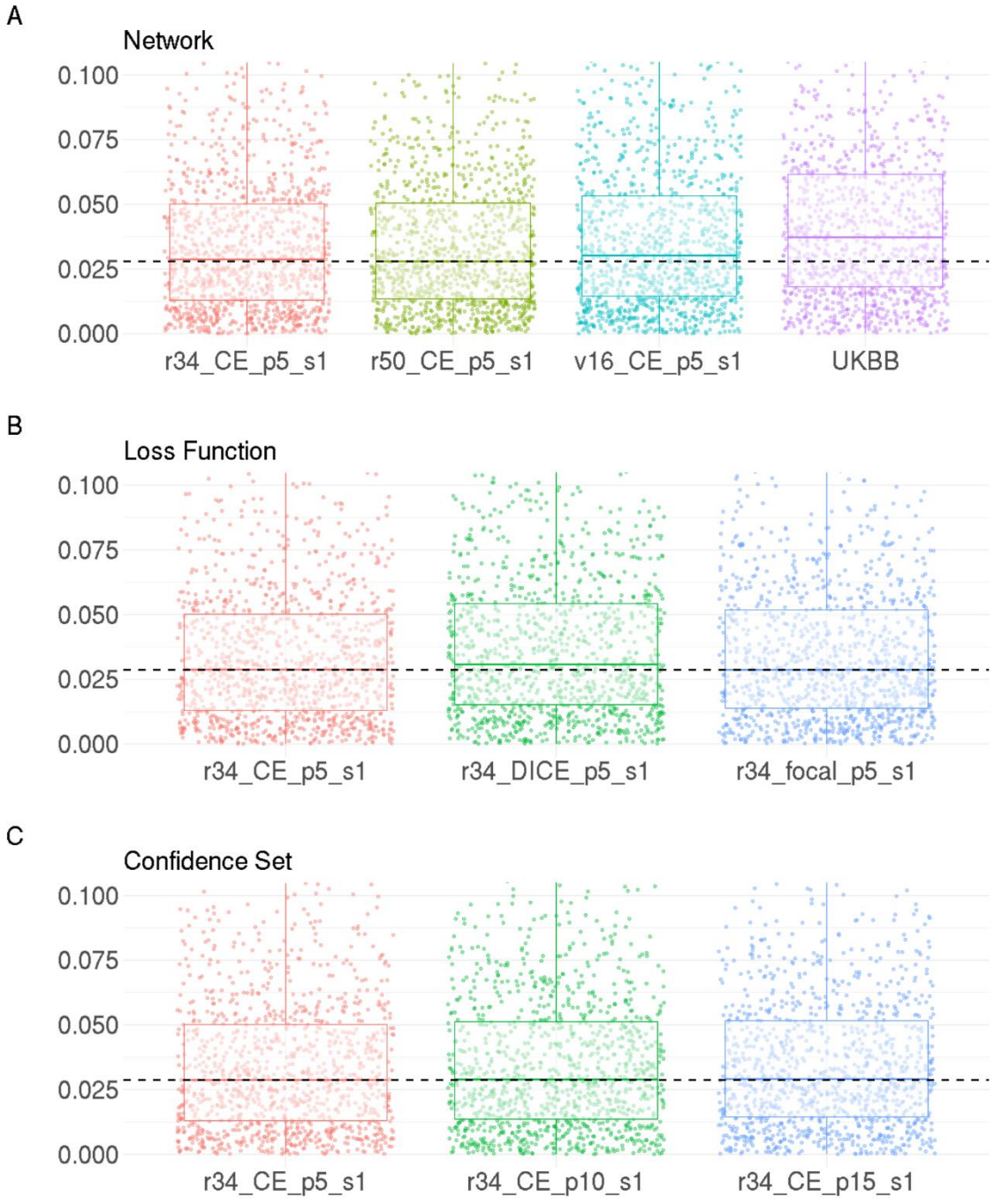

Figure 1: Model evaluation during incremental parameter search. Plots show the absolute distance between the EF prediction based on model segmentation and ground truth data provided by Kaggle. The range of the y-axis is restricted for better comparability, dashed lines indicates lowest median. Model performance with **A:** Architectures (r34: ResNet34, r50: ResNet50, VGG16: v16, UKBB). **B:** Loss functions (Cross-entropy: CE, DICE, focal loss). **C:** Confidence sets (p5: 5%, p10: 10%, p15: 15%).

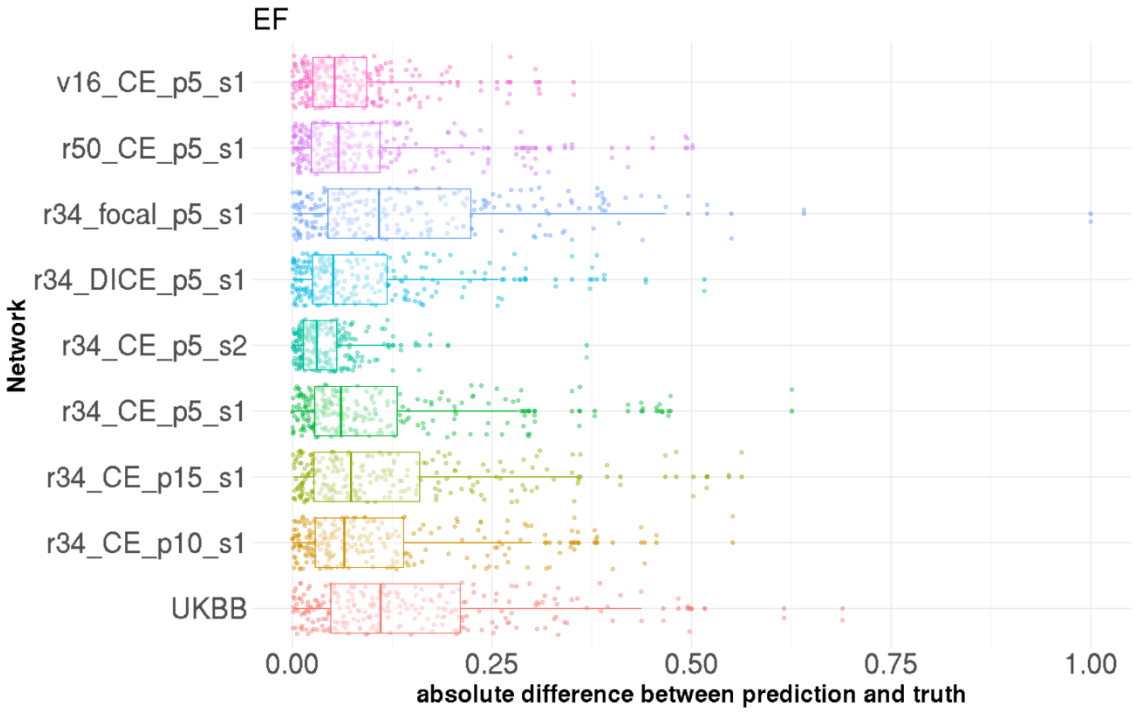

Figure 2: Model evaluation based on data including rotated images. Plots show the absolute distance between the EF predictions based on model segmentation and ground truth data provided by Kaggle for all models of the parameter search, plus one model trained with extended data augmentation (s2). Models are named by architecture (ResNet34: r34, ResNet50: r50, VGG16: v16), loss function (cross entropy: CE, focal, DICE), confidence set (p5, p10, p15), and data augmentation (s1: standard data augmentation, s2: extended data augmentation, enabling LR-flips and rotations up to 90°).

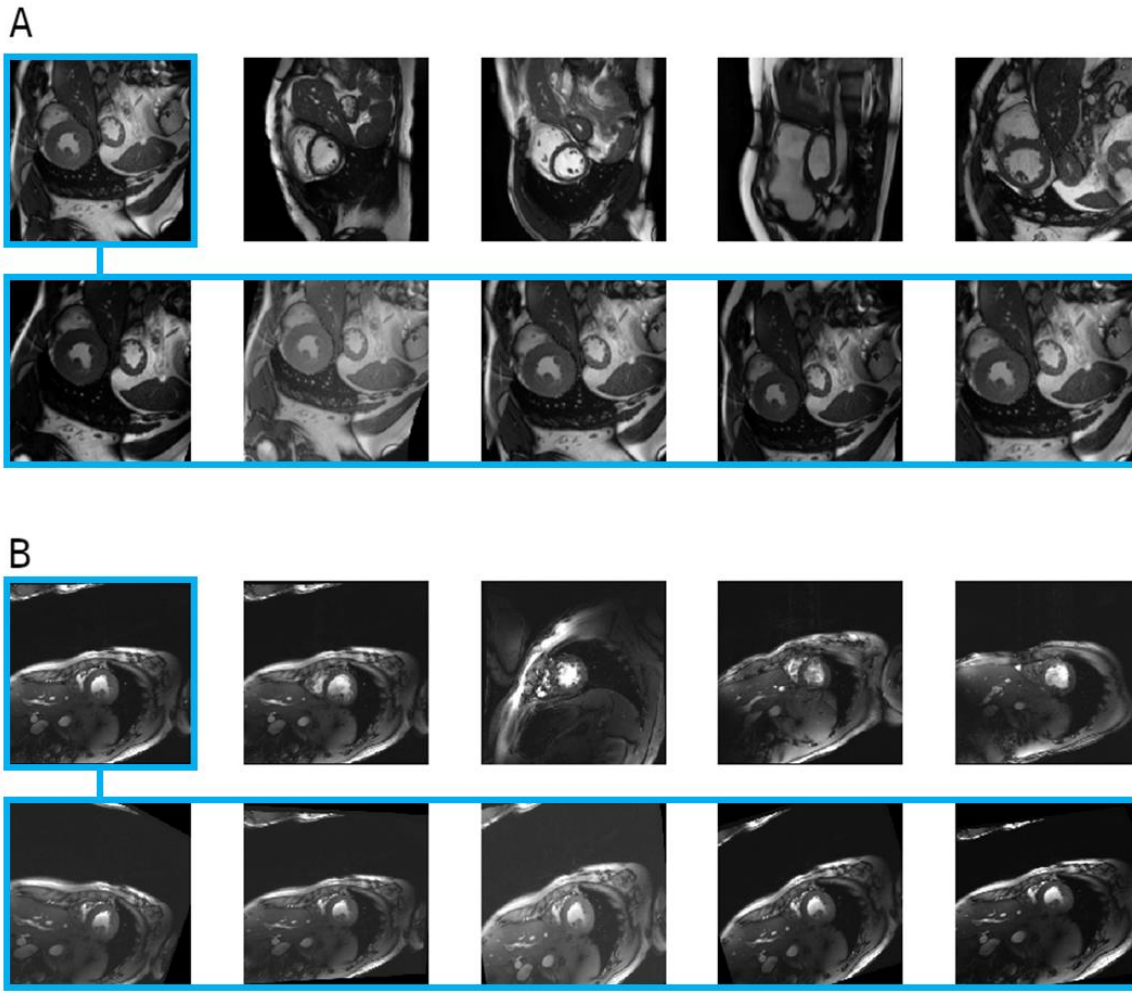

Figure 3: Exemplary cine images and respective data augmentation. Random selection of five images (top) with five data augmentation examples (bottom) for the first image of the random selection. A: Kaggle data. B: 7T human cine data.

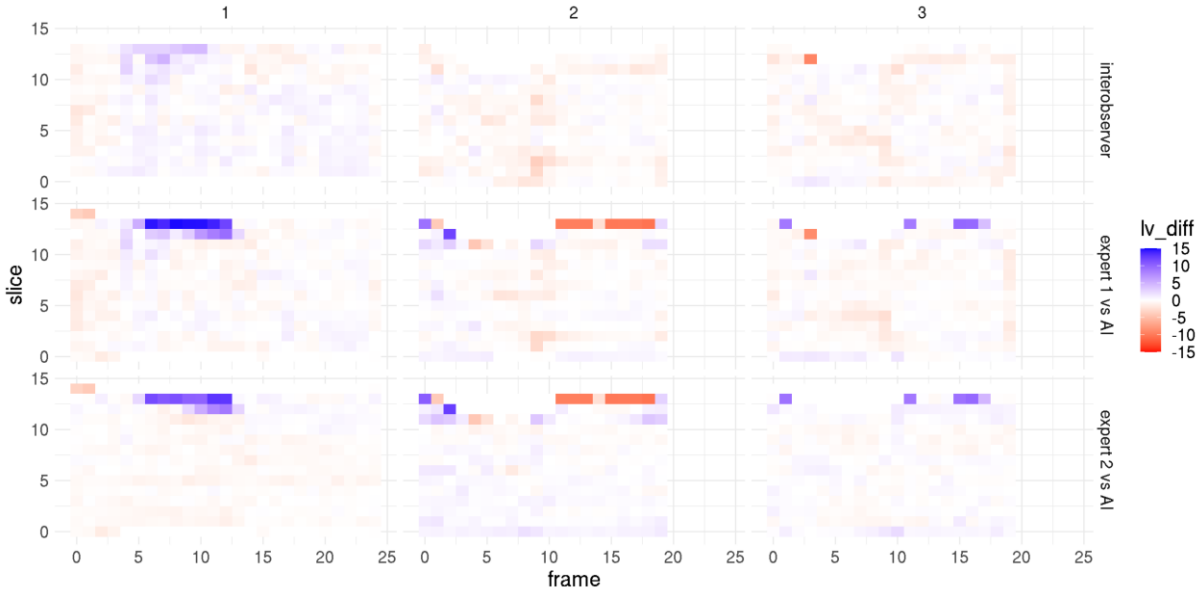

Figure 4: Inter-observer variability. Difference in LV volume in [ml] for all slices and phases of the 7T cine images of the test set. The slice count starts with 0 at the most apical slice and moves towards the most basal slice with increasing slice number. Top: Inter-observer variability of the two experts. Middle: Inter-observer variability expert 1 (labelled training data as well) versus AI. Bottom: Inter-observer variability expert 2 versus AI.

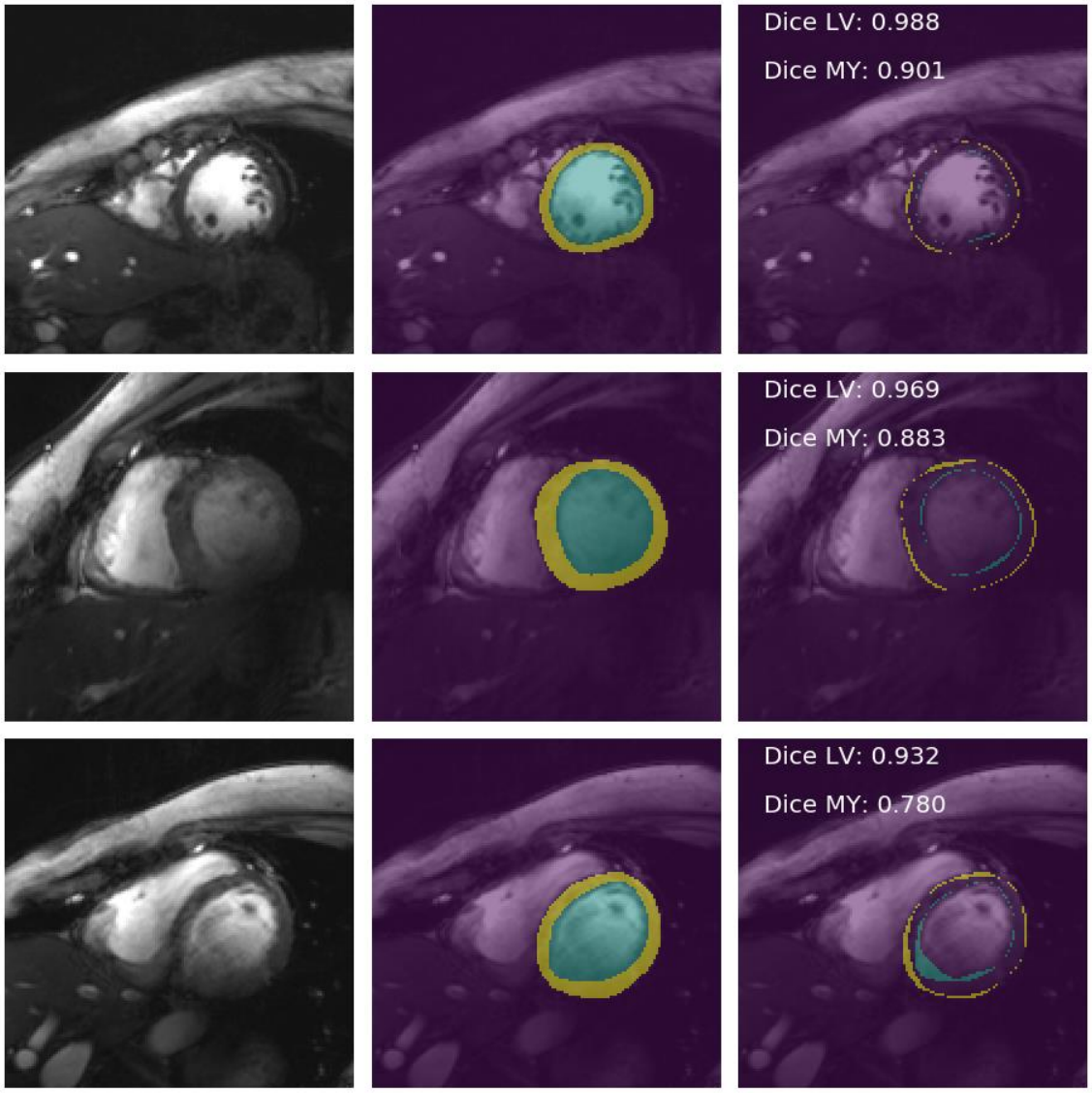

Figure 5: Predictions of TL^2 on the 7T human test set. Examples of mid-cavity segmentation results with high (top), intermediate (middle) and low (bottom) DICE scores. Images (left), with predicted classes (middle, background: purple, LV: blue, MY: yellow) and differences to the ground truth (right, LV-error: blue, MY-error: yellow).

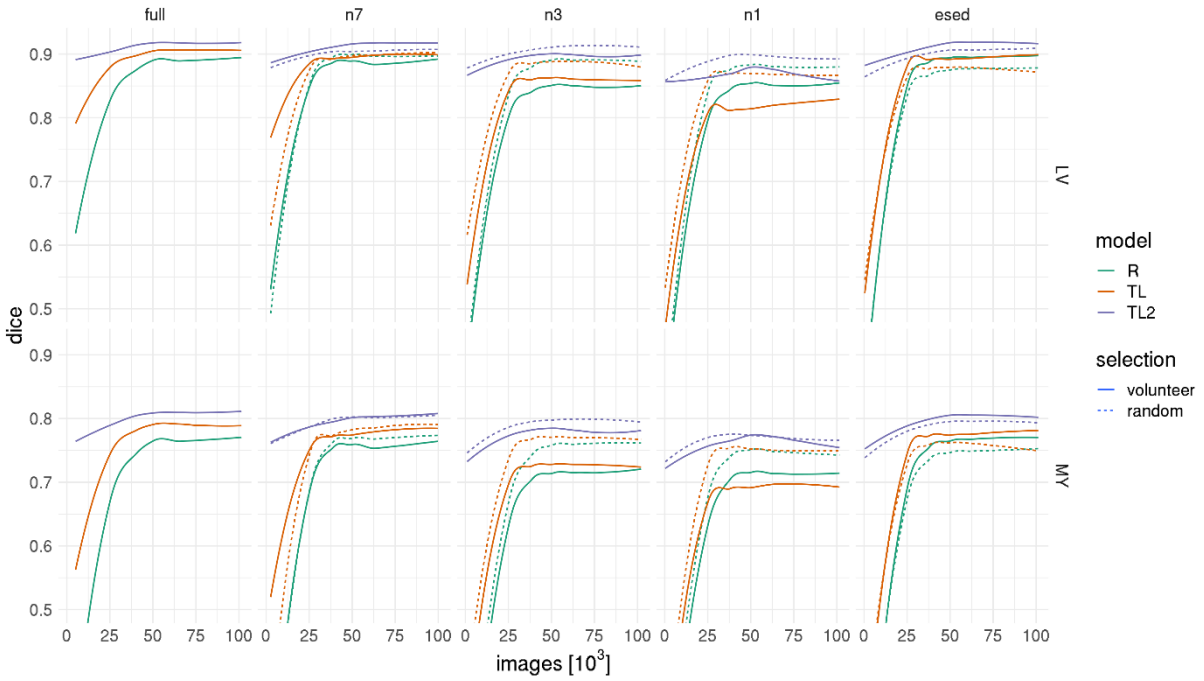

Figure 6: Training evaluation based on the validation set. DICE scores of the left ventricle and the myocardium in 7T human cardiac cine images normalized for the number of images seen. Varying degrees of transfer learning (R: ResNet34 initialized with random weights and trained using 7T cine images, TL: ResNet34 initialized with ImageNet weights and trained using 7T cine images, TL^2: ResNet34 initialized with ImageNet weights, pre-trained on the 1.5T and 3T Kaggle cine images and re-trained on 7T cine images) are shown for the two subsets 1 (line): subset of whole volunteers (full=14, 7, 3, 1), 2 (dotted line): subset of random images with image numbers corresponding to first subset. In addition, there is one model ("esed") trained using only end-systolic and end-diastolic images from all volunteers and a corresponding model trained with a number of random images equivalent to the "esed"-set.

3.7 Exploring ensemble applications for multi-sequence myocardial pathology segmentation

〉 Published in *Lecture Notes in Computer Science* 2020[75]

The final authenticated publication is available online at
https://doi.org/10.1007/978-3-030-65651-5_6

〉 Retained author rights (consent to publish) are attached in the appendix

These citations[64,65,70-72,281-292] have been applied in this publication.

As indicated on page 7, this paper was published as part of the challenge for myocardial pathology segmentation (MyoPS 2020[63]), which was hosted in conjunction with the conferences STACOM and MICCAI.

In order to facilitate discussion, reproducibility and reuse we made all required code openly available.

Code:

github.com/chfc-cmi/miccai2020-myops
doi.org/10.5281/zenodo.3982324

Models:

doi.org/10.5281/zenodo.3985837

Next to automatic segmentation for the MR based assessment of cardiac function, DL is increasingly applied to segment pathologic alterations such as scar and edema. These segmentations enable determination of myocardial salvage and viability, which is essential in the diagnosis and treatment management for patients with MI.

Primary aim of this study was the development of a DL model for myocardial pathology segmentation, such as scar and edema, based on multi-sequence data. Furthermore, we aimed to determine whether models based on multi-sequence data or individual sequences (LGE for scar tissue) performed better.

Only data provided in the context of the MyoPS 2020 challenge was used. All images were co-registered with the same image resolution by the organizers. Data contained cine, LGE, and T_2-weighted images for a total of 45 patients and respective labels for LV blood pool, RV blood pool, LV healthy myocardium, LV myocardial edema, and LV myocardial scar. After an initial assessment of data preprocessing (contrast enhancement, cropping, and resizing), we trained and evaluated multi-channel-multi-class models versus pathology specific models using various loss functions. Data augmentation (rotation, brightness, contrast, artifacts, noise) was applied to improve model training. Well performing models were combined into a bagging ensemble approach.

For pre-processing only cropping improved model performance. During model training, cross entropy based model training yielded the highest performance for non-pathologic classes ($Dice_{RV}$: 0.783, $Dice_{LV}$: 0.855, $Dice_{My}$: 0.696). Highest mean performance on both pathology classes ($Dice_{scar+edema:}$ 0.345) was achieved using a multi-channel-multi-class model (class weights: 0.35). Two model submissions were allowed and evaluation of Dice scores on the test set was performed by the organizers. Our multi-channel-multi-class model with class weights of 0.35 achieved $Dice_{scar}$: 0.593±0.232 and $Dice_{scar+edema}$: 0.611±0.111 and the bagging ensemble approach $Dice_{scar}$: 0.620±0.240 and $Dice_{scar+edema}$: 0.665±0.137.

In this study we demonstrate that multi-sequence input data enables model performances similar to pathology specific input data and that a bagging ensemble can drastically improve multi-sequence-multi-class segmentation. Both submitted models achieved higher Dice scores than were reported for inter-observer variability ($Dice_{scar}$: 0.524±0.158).

Exploring ensemble applications for multi-sequence myocardial pathology segmentation

Markus J. Ankenbrand[1[0000-0002-6620-807X]] David Lohr[1[0000-0002-6509-3776]] and Laura M. Schreiber[1[0000-0002-8827-1838]]

[1] Chair of Cellular and Molecular Imaging, Comprehensive Heart Failure Center, University Hospital Würzburg, Am Schwarzenberg 15, 97078 Würzburg, Germany
Ankenbrand_M@ukw.de

Abstract. We tested different loss functions and hyper-parameters using a 2D U-Net architecture (resnet34 backbone) with five-fold cross-validation on the training data. Pathology specific sequence data (e.g. LGE for scar and T_2 for edema) was used as a sole input for training and in combination with all sequences. We wanted to address the question whether for limited training data it is beneficial to incorporate prior knowledge by predicting classes with their appropriate sequence or if a neural network is able to infer these relationships from a multi-sequence dataset. In addition, we aimed to create a model zoo, combining predictions from models with high performance on individual classes. Images were cropped to the central 256x256 region as this contained the region of interest in all cases. To improve robustness and learn more general features extensive data augmentation was used, including both MR artifacts (motion, noise) and standard image transformations (zoom, rotation, brightness, contrast). Variations of training data, loss functions and hyper-parameters led to 21 models trained. The multi-sequence model was trained using all image sequences input via color channels producing pixel-level segmentation for all six classes (background, left ventricle, right ventricle, myocardium, edema, and scar). Cross-entropy as a loss function performed best (metric: dice) for non-pathologic tissue, while pathology weighted focal-loss (0.35 for both scar and edema) had best mean performance on scar and edema.

These results indicate that the employed neural networks are capable of learning multi-sequence segmentation end-to-end. Combining different outputs from a model zoo further improved segmentation performance.

Keywords: Deep Learning, U-Net, Ensemble, Segmentation, Cardiac MRI

1 Introduction

1.1 Background

Cardiac magnetic resonance (CMR) imaging applies methods to investigate cardiac function and pathologies non-invasively. Different measurement sequences are used to produce images with different contrast, enabling diagnosis of varying pathologic tissue

alterations. It is common practice to segment the left ventricle and the myocardium to assess clinically relevant parameters like ejection fraction, stroke volume and myocardial mass as well as wall motion. Scar volume, as a result of acute myocardial infarction, has significant prognostic value for outcome prediction and treatment, thus, increasing the importance of accurate pathology segmentation. In clinical practice, such segmentations are commonly done semi-automatically. Fully automatic segmentation algorithms have been proposed using different methods, including artificial neural networks [1, 2]. However, these networks are usually trained on a single sequence and a subset of tissue/pathology classes. For the prediction of multiple pathologic tissue alterations in parallel, it might be beneficial to train segmentation networks, which combine information from multiple sequences.

1.2 Related work

Neural networks, particularly convolutional neural networks and U-Nets [3] have been used for segmentation of cardiac magnetic resonance images [1, 4]. Beside healthy tissue also pathological classes like left ventricular scar [5] or left atrial scar have been addressed [6, 7]. However, the simultaneous use of multiple sequences and multiple classes presents a new set of challenges.

2 Experiments

In the MyoPS 2020 challenge, three different sequences (bSSFP, LGE, SPAIR) were measured for each of 45 patients, providing ground truth segmentation for left ventricular (LV) blood pool, right ventricular (RV) blood pool, LV myocardium (MY), edema, and scar for 25 patients. All data was provided aligned (MvMM method [8, 9]) in a common space with identical spatial resolution by the organizers. The aim of the challenge was to create an algorithm for pixel-wise segmentation of the pathology classes edema and scar. In this study, we employed variations of individual neural networks as well as a model ensemble, combining models with high performance on individual morphologic classes.
The experiments and parameter search were done in Google Colab GPU instances. For the final training and prediction, we used our local HPC i. 8x Intel(R) Xeon(R) CPU E5-2630 v3 @ 2.40GHz ii. 512 GB of memory iii. 1x NVIDIA Tesla K80 with 12 GB of memory.

3 Methods

3.1 Software

We built our model using open source software including python 3.7.7, pytorch 1.5.1 [10], fastai2 0.0.17 [11], torchio 0.15.5 [12], MONAI 0.2.0, nibabel 3.2.1 [13] as well as their dependencies. Our model and code is openly available on GitHub and zenodo

(https://github.com/iimog/miccai2020-myops and https://doi.org/10.5281/zenodo.3982324).

3.2 Processing pipeline and architecture

We converted all images from nifti to png format saving each slice as one image with sequences combined as color channels. Additionally, each sequence was saved independently as a grey-scale image. We tried normalization of the LGE and T_2 images using contrast limited adaptive histogram equalization (CLAHE) [14]. In this step, in addition to the original images, transformed images with simulated MR artifacts (motion and noise) were produced using torchio [12]. These images were used to train U-Nets [3] with a resnet34 [15] backbone (initialized using ImageNet [16] weights) with further augmentations (rotation, brightness, contrast) with fastai2 [4, 11]. Performance of different hyper-parameter settings were evaluated using dice scores from five-fold cross-validation. The same split was used for all experiments and every data set was part of the validation set at least once.

3.3 Hyper-parameter search

Preliminary experiments. In preliminary experiments the effect of contrast enhancements using CLAHE as well as cropping vs resizing to 256x256 pixels were tested.

Systematic experiments. For the general multi-channel/multi-class networks, different losses were tested. Cross-entropy loss (ce) was compared to differently weighted focal loss [17]. We experimented with some classes receiving higher weights (values used are indicated in parentheses), while the other classes received balanced weights:

- all classes with equal weights (balanced)
- myocardium (0.2, 0.3), edema (0.2, 0.3) and scar (0.2, 0.3), label: multi_pathoMyo
- edema (0.2, 0.35, 0.49) and scar (0.2, 0.35, 0.49), label: multi_patho
- edema (0.2, 0.4, 0.6, 0.8, 0.99), label: multi_edema
- scar (0.2, 0.4, 0.6, 0.8, 0.99), label: multi_scar

Additionally, pathology specific networks (t2_edemaOnly, lge_scarOnly) were trained on their corresponding sequence only (edema with T_2 and scar with LGE) using two different weightings of the focal loss (0.5 and 0.8). In total 21 networks were trained this way for 30 epochs (10 epochs frozen, 20 epochs unfrozen) and a base learning rate of 10^{-3}.

Targeted experiments. The best performing networks from the systematic experiments were selected based on mean dice score over all cross validations. For LV, RV and myocardium only the network with the highest dice score was selected. For the pathology classes first the network with highest mean dice over both classes was selected, then for each class the two remaining networks with highest individual dice

scores in the respective class were selected. This way a total of six networks were selected. These networks were trained for 60 epochs (20 frozen, 40 unfrozen) in order to assess benefits of prolonged training duration.

Final training. For the evaluation on the test set, the six networks from the targeted experiments were trained from scratch using all 25 data sets for training and no validation set. Training was done for 60 epochs (20 frozen, 40 unfrozen), since average performance was increased with prolonged training duration.

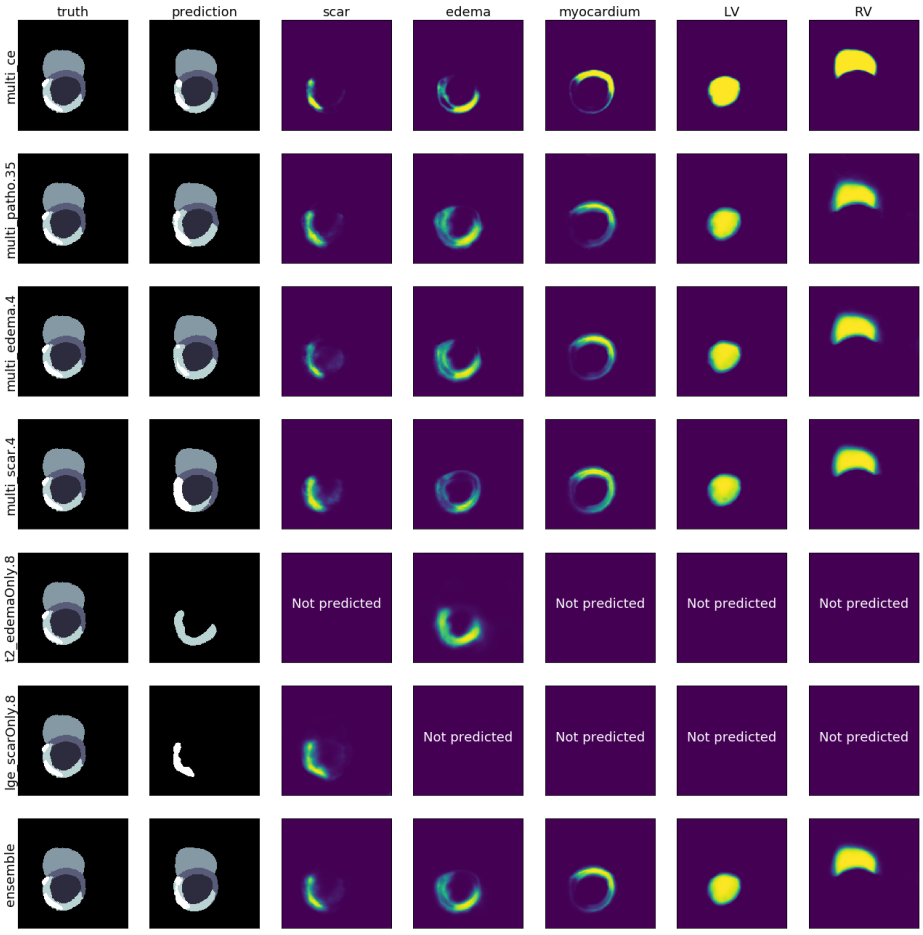

Fig. 1. Probability maps for all classes and derived prediction (second column) for the six networks and the ensemble, compared to the ground truth (first column) for a single slice of the training data. The result of the ensemble method (bottom row) is the mean over the probability maps of the six separate networks above.

3.4 Ensemble method

The networks were trained with different foci, which led to different strengths and weaknesses. Therefore, we combined predictions from the different networks in a bagging approach. This combination included predictions from all six networks from the final training. Class probabilities were averaged over all networks, taking into account that the specialized networks only returned predictions for their respective pathology class. The final prediction for each pixel was the argmax of these averages (
Fig. 1).

4 Results

4.1 Cross-validation results on training set

Preliminary experiments indicated that not using CLAHE and cropping to 256x256 pixels yields better results than normalization or resizing. Thus, only cropping was used in the systematic experiments. In the systematic experiments, the network with cross-entropy loss reached the best results for LV, RV and myocardium segmentation with mean values of $dice_{LV}$=0.855, $dice_{RV}$=0.783 and $dice_{MY}$=0.696. The best mean performance on both pathology classes: mean($dice_{edema}$, $dice_{scar}$)=0.345 was achieved using the multi-channel network (multi_patho) with weights of 0.35 for both pathology classes. Of the remaining networks the highest dice on scar was reached by the multi-channel network (multi_scar, weight: 0.4) and by the specialized LGE network (lge_scarOnly, weight 0.8) (**Fig. 2**), while the specialized T_2 network (t2_edemaOnly, weight: 0.8) and the multi-channel network (multi_edema, weight: 0.4) reached the highest dice scores for edema (**Fig. 2**). Longer training improved dice scores for almost all classes and networks (**Fig. 3**, **Table 1**).

4.2 Performance on test set

Evaluation results on the test set were provided by the challenge organizers for two models, the multi_patho.35 network and the ensemble method. The ensemble reached better performance with mean ± standard deviation of $dice_{scar}$=0.620±0.240 and $dice_{edema+scar}$=0.665±0.137 compared to $dice_{scar}$=0.593±0.232 and $dice_{edema+scar}$=0.611±0.111 for the single network. For all but one patient dice scores for scar were greater than 0 indicating at least some overlap between truth and prediction.

Table 1. Mean performance of the targeted experiment networks over the five-fold cross-validation after 60 epochs of training. Highest dice for each class in bold.

Network	$dice_{LV}$	$dice_{MY}$	$dice_{RV}$	$dice_{edema}$	$dice_{scar}$	mean dice edema, scar
multi_patho.35	0.829	0.649	0.773	0.246	0.441	**0.343**
multi_scar.4	0.850	0.690	0.779	0.202	**0.479**	0.341

6

multi_ce	**0.853**	**0.695**	**0.787**	0.227	0.438	0.333
multi_edema.4	0.843	0.664	0.781	0.261	0.400	0.330
lge_scarOnly.8	-	-	-	-	0.467	-
t2_edemaOnly.8	-	-	-	**0.276**	-	-

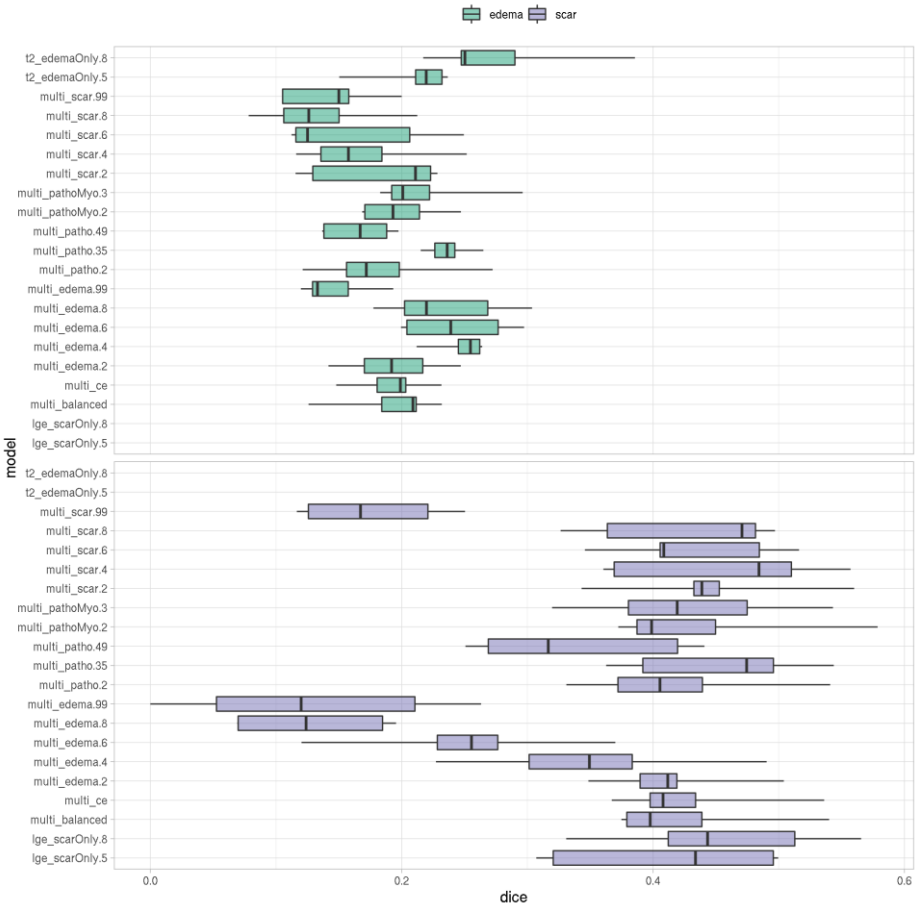

Fig. 2. Dice score for edema (top panel) and scar (bottom panel) over the five cross-validation folds of each of the 21 networks from the systematic parameter search. Naming of models: input channels (multi, lge, t2), focused classes (scar, edema, patho: scar+edema, pathoMyo: scar+edema+MY, ce for cross-entropy and balanced have identical weight for all classes) and weight for those classes as suffix.

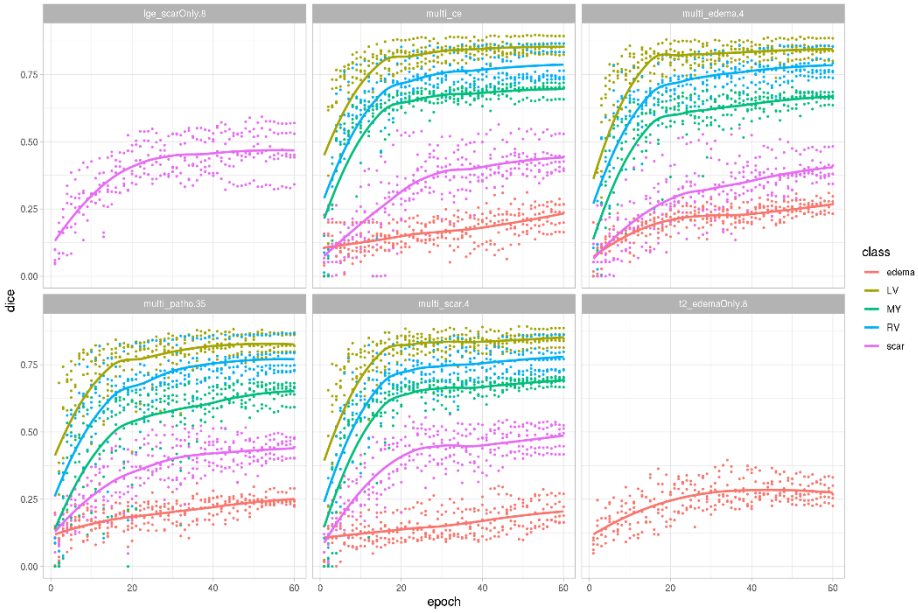

Fig. 3. Dice scores throughout training of the six networks from the targeted experiments. Data for all five cross-validation folds is shown with loess-smoothed lines for each class. The first 20 epochs were trained with frozen weights, the remaining 40 with unfrozen weights.

5 Discussion

It is possible to train neural networks both on separate sequences and on multiple sequences with good performance. For scar the reported dice score is higher than that achieved by individual observers reported as 0.524±0.158 [9]. Segmentation quality can be further improved by training a model zoo with focus on different classes and combining their predictions using a bagging ensemble method. We showed that it is even possible to combine predictions from networks that were trained on different input data (channels) with a different set of output channels using averaging. While these results are promising, further experiments are needed to optimize the hyper-parameters for this challenging task. Additionally more and diverse training data is needed to train an algorithm with good performance and to reliably estimate its performance on unseen data.

8

Acknowledgements

This work was supported by the German Ministry of Education and Research (grant number, 01EO1504). The funding body took no role in the design of the study, collection, analysis, and interpretation of data and in writing the manuscript.

References

1. Bai, W., Sinclair, M., Tarroni, G., Oktay, O., Rajchl, M., Vaillant, G., Lee, A.M., Aung, N., Lukaschuk, E., Sanghvi, M.M., Zemrak, F., Fung, K., Paiva, J.M., Carapella, V., Kim, Y.J., Suzuki, H., Kainz, B., Matthews, P.M., Petersen, S.E., Piechnik, S.K., Neubauer, S., Glocker, B., Rueckert, D.: Automated cardiovascular magnetic resonance image analysis with fully convolutional networks. Journal of Cardiovascular Magnetic Resonance 20, (2018)
2. Baumgartner, C.F., Koch, L.M., Pollefeys, M., Konukoglu, E.: An Exploration of 2D and 3D Deep Learning Techniques for Cardiac MR Image Segmentation. pp. 111-119. Springer International Publishing, Cham (Year)
3. Ronneberger, O., Fischer, P., Brox, T.: U-Net: Convolutional Networks for Biomedical Image Segmentation. pp. 234-241. Springer International Publishing, Cham (Year)
4. Ankenbrand, M.J., Lohr, D., Schlötelburg, W., Reiter, T., Wech, T., Schreiber, L.M.: A Deep Learning Based Cardiac Cine Segmentation Framework for Clinicians - Transfer Learning Application to 7T. medRxiv 2020.2006.2015.20131656 (2020)
5. Zabihollahy, F., White, J.A., Ukwatta, E.: Convolutional neural network-based approach for segmentation of left ventricle myocardial scar from 3D late gadolinium enhancement MR images. Med Phys 46, 1740-1751 (2019)
6. Li, L., Weng, X., Schnabel, J.A., Zhuang, X.J.A.: Joint Left Atrial Segmentation and Scar Quantification Based on a DNN with Spatial Encoding and Shape Attention. abs/2006.13011, (2020)
7. Li, L., Wu, F., Yang, G., Xu, L., Wong, T., Mohiaddin, R., Firmin, D., Keegan, J., Zhuang, X.: Atrial scar quantification via multi-scale CNN in the graph-cuts framework. Med Image Anal 60, 101595 (2020)
8. Zhuang, X.: Multivariate Mixture Model for Cardiac Segmentation from Multi-Sequence MRI. pp. 581-588. Springer International Publishing, (Year)
9. Zhuang, X.: Multivariate Mixture Model for Myocardial Segmentation Combining Multi-Source Images. IEEE Transactions on Pattern Analysis and Machine Intelligence 41, 2933-2946 (2019)
10.Paszke, A., Gross, S., Massa, F., Lerer, A., Bradbury, J., Chanan, G., Killeen, T., Lin, Z., Gimelshein, N., Antiga, L., Desmaison, A., Kopf, A., Yang, E., DeVito, Z., Raison, M., Tejani, A., Chilamkurthy, S., Steiner, B., Fang, L., Bai, J., Chintala, S.: PyTorch: An Imperative Style, High-Performance Deep Learning Library. 8024--8035 (2019)
11.Howard, J., Gugger, S.: fastai: A Layered API for Deep Learning. Information 11, 108 (2020)
12.Pérez-García, F., Sparks, R., Ourselin, S.: TorchIO: a Python library for efficient loading, preprocessing, augmentation and patch-based sampling of medical images in deep learning. arXiv:2003.04696 [cs, eess, stat] (2020)

13.Brett, M., Markiewicz, C.J., Hanke, M., Côté, M.-A., Cipollini, B., McCarthy, P., Jarecka, D., Cheng, C.P., Halchenko, Y.O., Cottaar, M., Ghosh, S., Larson, E., Wassermann, D., Gerhard, S., Lee, G.R., Wang, H.-T., Kastman, E., Kaczmarzyk, J., Guidotti, R., Duek, O., Rokem, A., Madison, C., Morency, F.C., Moloney, B., Goncalves, M., Markello, R., Riddell, C., Burns, C., Millman, J., Gramfort, A., Leppäkangas, J., Sólon, A., van den Bosch, J.J.F., Vincent, R.D., Braun, H., Subramaniam, K., Gorgolewski, K.J., Raamana, P.R., Nichols, B.N., Baker, E.M., Hayashi, S., Pinsard, B., Haselgrove, C., Hymers, M., Esteban, O., Koudoro, S., Oosterhof, N.N., Amirbekian, B., Nimmo-Smith, I., Nguyen, L., Reddigari, S., St-Jean, S., Panfilov, E., Garyfallidis, E., Varoquaux, G., Legarreta, J.H., Hahn, K.S., Hinds, O.P., Fauber, B., Poline, J.-B., Stutters, J., Jordan, K., Cieslak, M., Moreno, M.E., Haenel, V., Schwartz, Y., Baratz, Z., Darwin, B.C., Thirion, B., Papadopoulos Orfanos, D., Pérez-García, F., Solovey, I., Gonzalez, I., Palasubramaniam, J., Lecher, J., Leinweber, K., Raktivan, K., Fischer, P., Gervais, P., Gadde, S., Ballinger, T., Roos, T., Reddam, V.R., freec84: nibabel. vol. 10.5281/zenodo.591597. Zenodo (2020)
14.Pizer, S.M., Amburn, E.P., Austin, J.D., Cromartie, R., Geselowitz, A., Greer, T., Terhaarromeny, B., Zimmerman, J.B., Zuiderveld, K.: Adaptive Histogram Equalization and Its Variations. Comput Vision Graph 39, 355-368 (1987)
15.He, K., Zhang, X., Ren, S., Sun, J.: Deep Residual Learning for Image Recognition. In: 2016 IEEE Conference on Computer Vision and Pattern Recognition (CVPR), pp. 770-778. (Year)
16.Russakovsky, O., Deng, J., Su, H., Krause, J., Satheesh, S., Ma, S., Huang, Z., Karpathy, A., Khosla, A., Bernstein, M., Berg, A.C., Fei-Fei, L.: ImageNet Large Scale Visual Recognition Challenge. International Journal of Computer Vision 115, 211-252 (2015)
17.Lin, T.-Y., Goyal, P., Girshick, R., He, K., Dollár, P.: Focal Loss for Dense Object Detection. arXiv:1708.02002 [cs] (2017)

4 DISCUSSION

"Functional and structural characterization of the myocardium" is a very generic thesis topic that could be addressed in many different ways. While the main aim of this thesis involved ultrahigh field cardiac MRI and DTI to do so, there are numerous other methodologies and aspects to consider. Some of them, such as echocardiography, standard clinical CMR, histology, gene expression analysis, and necropsy were applied in publications of this thesis, providing context to our understanding of microstructural and functional changes in cardiac pathology.

As indicated in the introduction, the publications of this thesis can be sorted into three categories:

1. *ex vivo* cardiac DTI at 7T
2. hardware development for translational cardiac MRI at 7T
3. deep learning based segmentation for cardiac MRI data

There are two things these categories have in common. First, they are based on the same diagnostic methodology, namely MRI, and second, they all refer to technologies (ultrahigh field MRI, cardiac DTI, and AI) that are likely to have a strong impact on clinical CMR within the next 10 years. All publications of this thesis also contribute to the more holistic aim of this thesis, because developed methods may be applied for the assessment of microstructural and functional changes in CVDs, improving our understanding thereof.

Within the following chapter, I will discuss individual contributions of the publications to their respective field as well as to this thesis. This includes considerations beyond the already published discourse. In chapters 4.2 and 4.3 published results will be linked to aims of this thesis and thus discussed in the context of CMR for the assessment of myocardial structure and function as well as deep learning in medical imaging.

4.1 Publications of this Thesis

Spin echo based cardiac diffusion imaging at 7T: An ex vivo study of the porcine heart at 7T and 3T

Over the years *ex vivo* DTI studies of cardiac microstructure at ultrahigh field strengths have been performed using hearts of rodents, while measurements in porcine,[101,105,120] canine,[53,90,130] and even goat[293] hearts have been limited to field strengths ≤4.7T. Due to similarities in organ size, coronary anatomy, immunology and physiology compared to humans, porcine animal models are attractive for pre-clinical protocols and translational research of CVDs and their diagnosis and treatment.[294,295]

Measurements *ex vivo* provide a controlled environment with ideal conditions for the acquisition of high fidelity data. This study[76] is the first to utilize the latest 7T MRI technology for ultrahigh field DTI of excised large animal hearts, confirming that a commercial setup using a 1Tx/32Tx head coil leads to increased SNR in diffusion acquisitions (Δ52% compared to 3T without parallel imaging). While theoretically the gain in SNR is proportional to the square of B_0, our values fit well to literature reports, where SNR gains do not reach theoretical expectations. Studies comparing SNR at 7T and 4T showed that practically, the SNR gain is highly dependent on localization (head coil). While the SNR gain in the center of the brain was approximately 100%, SNR was only about 40% higher in the periphery of the brain.[296,297] Decreased T_2* values at ultrahigh field strength add to signal loss, particularly for scans without parallel imaging acceleration and thus, long echo times and readouts. In our study we found these scans to be strongly affected by susceptibility effects, causing deformation of the reconstructed diffusion tensor. For the coil we used, parallel imaging acceleration of R=3 was optimal regarding the trade-off between SNR loss as acceleration penalty and susceptibility effects for longer echo trains. Based on these scans (R≥3) we demonstrated that the change in field strength does not affect derived diffusion metrics, which is an important finding with respect to future ultrahigh field examinations. Dedicated multi-channel arrays with 64[109,298] or more channels may further improve SNR at 7T. Studies analyzing potential SNR at ultrahigh field strength suggest that synergistic combinations of a higher number of receive channels and parallel imaging acceleration enable access to SNR gains closer to theoretical expectations,[104,299-301] while simultaneously addressing increased susceptibility effects and decreased T_2* values. Based on hardware and software developments scans at 7T are likely to improve SNR in other sequence modalities besides DTI, pushing currently existing limitations of spatial resolution.

In 2017, approximately 15% of the sites equipped with a 7T MRI system have explored CMR applications.[302] With the number of 7T systems steadily increasing, the number of translational studies using these systems is likely to increase as well. For all these studies this work offers valuable information on general feasibility and proper setup for *ex vivo* DTI at ultrahigh field strengths.

With respect to this thesis, this study resulted in a DTI data processing pipeline applicable to all following DTI studies and respective publications as well as a setup for high resolution *ex vivo* DTI of excised large animal hearts. Using this setup at 7T, we assessed the impact of continuous formalin fixation on excised large animal hearts and evaluated a custom stimulated echo sequence implemented for *in vivo* DTI acquisitions.

Longitudinal assessment of tissue properties and cardiac diffusion metrics of the ex vivo porcine heart at 7 T: Impact of continuous tissue fixation using formalin

Most *ex vivo* DTI studies are performed on fixed tissue specimen, where rapid chemical fixation (often formalin) is applied to prevent autolytic effects after organ harvest. Compared to brain tissue T_2 and T_2* are lower in the heart and even shorter at ultrahigh field strengths. This study on the effects of continuous tissue fixation using formalin is the first to provide information on changes in T_2 and T_2* and their impact on SNR in diffusion MRI at ultrahigh field strength. T_2 and T_2* in the LV drop significantly following fixation, leading to a loss in SNR of b_0 images, which directly influences data fidelity of derived diffusion metrics.[102,111] Since *ex vivo* scans are set up to achieve high fidelity, high resolution data, fixation induced effects should be considered when designing a study protocol, particularly at ultrahigh field strengths. These considerations should include the question, whether tissue fixation due to limited scan times or storage demands is really required. A way to address the SNR loss due to decreasing T_2* values and subsequent k-space filter effects is dedicated RF hardware. As mentioned above, combinations of high parallel imaging factors and a large number of receive channels appear to be beneficial for ultrahigh field MRI.[299-301]

Observed changes in diffusivity following fixation are in good agreement with prior literature reports.[123,126] The longitudinal study setup improves our understanding of already published observations and enables more meaningful and accurate comparisons between such studies and newly generated data, which increases the value of quantitative measures with respect to the impact of diseases. Despite observed changes in diffusivity results of this work support the observation that formalin based tissue fixation does not affect cardiomyocyte orientation.[54,123,130] In addition, I provide initial evidence that this observation is true for average sheetlet orientation as well. This metric, or rather the change in sheetlet orientation between systole and diastole, has become of particular interest for the assessment of dynamic microstructural changes during contraction in patients with CVDs.[38,41,43]

Measurements *in vivo* are based on two different sequence types, spin echo and stimulated echo acquisitions. The stimulated echo approach encodes diffusion over two consecutive heart beats, assuming that the position of the heart is consistent in the same heart phase of each heartbeat.[303] This process enables very long diffusion times. While differences in diffusion metrics derived from these sequences have been analyzed and discussed for measurements *in vivo*,[51,116] there

is no data on sequence related differences for *ex vivo* measurements. Literature results comparing these two sequence types *in vivo* suggest that the expected loss in SNR using a stimulated echo approach decreases with increasing field strength.[51,116] This is likely due to increasing longitudinal relaxation times, shortened transverse relaxation times, and increased susceptibility effects at ultrahigh field strength. In *ex vivo* measurements the stimulated echo approach (mixing time: 100ms) still results in a SNR loss (on average 25-31% in fixed hearts) at 7T. However, long diffusion times and the resulting increase in fractional anisotropy have been shown to decrease uncertainty in the determination of the main eigenvector orientation.[131] Future studies at ultrahigh field strength may therefore rely on a stimulated echo approach. Results of this thesis allow comparison of diffusion metrics derived from both sequences.

Characterization of Myocardial Microstructure and Function in an Experimental Model of Isolated Subendocardial Damage

Our understanding of structure-function interactions in the heart is incomplete, particularly when it comes to disease.[152] Therefore more diverse and interdisciplinary studies creating data, which connects structural and functional alterations, are becoming increasingly important to improve our knowledge of cause-effect relationships in CVDs.[38,43,45]

This is the first study assessing the impact of subendocardial damage on myocardial microstructure and function, where data is generated using a mouse model of isolated subendocardial fibrosis in which major confounders like hypertrophy and altered loading conditions[150,172] are absent.

Adverse remodeling in response to cardiovascular risk factors is considered to start in the endocardium[46-48] and subendocardial integrity could thus function as a diagnostic marker for early detection of cardiac damages and facilitate risk stratification. Our study provides translational evidence that global peak longitudinal strain and subepicardial HA are markers of microstructural remodeling and may serve as diagnostic measures for early detection of cardiac impairment.

In order to achieve the setup for reproducible, high resolution *ex vivo* DTI of mouse hearts required for this study, we custom designed, and 3D-printed a small sledge, which allowed accurate specimen placement within the cryoprobe, while DSI Studio's support of Bruker 2dseq files enabled direct application of the developed DTI processing pipeline. Method development in this study in combination with the functional assessment performed by collaboration partners enabled the assessment of myocardial structure-function interactions.

Using diffusion tensor imaging we demonstrate that subendocardial damage and fibrosis lead to lower transmural and subendocardial mean diffusivity and significantly lower HA in subepicardial layers. Similar, remodeling with a shift towards lower values has previously been reported in other pathologies.[43,120,178] In this study the left shift was predominantly found in remote zones (subepicardial layers), which is comparable to observations made post MI.[179] Functional assessment using echocardiography revealed that animals with isolated

subendocardial fibrosis exhibited mild diastolic dysfunction, which has been shown to be highly prevalent in large population studies, where these particular subjects progressed to congestive heart failure over time.[160,176] Our study suggests that subendocardial fibrosis may account for preclinical diastolic dysfunction, an observation which is supported by reports of preclinical diastolic dysfunction in asymptomatic patients suffering from risk factors linked to effects on the subendocardium.[161,163] Since myofiber bundles run longitudinally they are thought to determine longitudinal mechanics, which is why impaired LS parameters are considered as well accepted surrogates of subendocardial damage.[159,161,174] This study confirms that reduced longitudinal deformation is indeed linked to subendocardial fibrosis and that global peak LS can be used to assess this. The observed phenotype of diastolic dysfunction with preserved ejection fraction in combination with reduced longitudinal but unaltered radial and circumferential deformation is comparable to that of selective subendocardial involvement, which is considered as a marker for subclinical disease.[174]

In conclusion, subendocardial damage appears to be connected to several hallmarks observed in cardiovascular high-risk patients. We demonstrate that metrics derived from echocardiography and cardiac DTI can be highly sensitive surrogates for microstructural remodeling in response to such subendocardial damage, which may facilitate early detection of cardiac impairment. Validation of our translational evidence in patients with confirmed subendocardial damage may enable future clinical application.

Myocardial Infarction after High-Dose Catecholamine Application - A Case Report from an Experimental Imaging Study

Survival of MI is often followed by heart failure and the already mentioned, grim prospect of ~50% 5-year mortality following initial diagnosis.[2] While adverse remodeling after MI is known to affect mechanical and electrical properties,[45,175,183,186] we have very limited understanding of the underlying microstructural and functional alterations.[152,177] This case report features unexpected MI after treatment with the catecholamine isoproterenol, where the application was meant to induce subendocardial fibrosis as described in Beyhoff et al.[56] This case is of particular interest, because it could be considered as a pre-clinical model of Type 2 MI.[187] The respective animal was part of our experimental imaging study (Hypertension - 2019) and thus, a comprehensive set of functional parameters, detailed histopathology, and high resolution DTI data were available.

The ratio of voxels showing positive and negative HA was found to quantify myocardial disarray quite well. While results of Beyhoff et al[56] support this observation, future applications of this metric in DTI assessments of CVDs will be required to assess and validate applicability in various CVDs. To date, *in vivo* DTI is available only to a select few research sites. Moving towards future clinical applications of DTI, derived metrics need to be linked to unique and, most importantly, actionable readouts. With respect to longitudinal deformation during contraction, this ratio may be such a readout. In addition to rather simple

interpretation, its determination is straightforward and requires only minor data processing and negligible compute power.

In this study we link pronounced loss of myofiber tracts to replacement fibrosis and apical scarring as well as left-ventricular systolic failure. We demonstrate that a simultaneous assessment of functional and structural changes improves our understanding of morphology-function interactions and enables validation and discovery of clinically useful surrogates for disease detection and possibly severity classification.

A Novel Mono-surface Antisymmetric 8Tx/16Rx Coil Array for Parallel Transmit Cardiac MRI in Pigs at 7T

As previously mentioned, heart size, coronary anatomy, immunology and physiology in pigs are highly similar to that of humans. Porcine animal models are therefore attractive for pre-clinical protocols and translational research of CVDs with respect to diagnosis and treatment.[38,120,179,294,295] Early studies have already demonstrated that CMR at 7T can lead to higher SNR,[57-61] but to date there are no studies exploiting the potential of ultrahigh field strength for translational studies in large animals.

In this study we aimed to design, simulate, construct, and test an 8Tx/16Rx mono-surface coil that enables homogeneous and efficient RF excitation using parallel transmit technology as well as rapid parallel imaging acceleration for CMR in large animals at 7T.

We demonstrate that EM simulations for the developed coil fit well to MR measurements in phantoms. Due to cardiac motion and required breath holds CMR applications benefit greatly from fast image acquisition, which is typically achieved using parallel imaging acceleration. Historically, multi-channel arrays have been designed to enable high acceleration factors with minimal noise amplification. At 7T however, we want to make use of multiple transmit channels as well as multiple receive channels. Coil design and element configurations may become a compromise between optimal performance regarding transmit and receive. The L-shaped distribution of elements in our design enabled high parallel imaging acceleration factors (R=2-6) with small noise amplification (g_{R2}=1.03, g_{R3}=1.05, g_{R4}=1.09, g_{R6}=1.26) in an *ex vivo* measurement (pig, 68 kg). Compared to literature reports of g_{R4}=1.2-2.33 using a 32-channel[199] and a 16-channel[219] loop array in humans, our coil exhibits negligible noise amplification for R=2-4. Furthermore, pTx shimming increased transmit efficiency by ≥3 and reduced RSD in the flip angle, demonstrating that the coil design offers additional degrees of freedom and thus, effective and flexible B_1-shimming. This is of paramount importance for longitudinal translational studies, where changes of body shape and size due to animal aging lead to different conditions with respect B_1-non-uniformity at ultrahigh field strength.

Vendor supplied patient safety systems have originally been developed in clinical systems, where SAR deposition and tissue heating are easy to manage due to lower field strengths and single transmit excitation. With the advent of parallel

transmit technology and B_1-shimming in ultrahigh field MRI, new methods and guidelines need to be established.[194,304-306] This is of particular importance, since cardiac CMR techniques such as LGE, T_2, and perfusion imaging are demanding with respect to RF excitation. Thus, B_1-non-uniformity and SAR-safety may limit application in humans. Clinically, in addition to cardiac function, these techniques enable the assessment of myocardial fibrosis, scar visualization, establishment of HF etiology,[8,11] and the characterization of myocardial tissue in various CVDs.[8,9,11,12]

Preliminary data shows that the dedicated hardware we developed can leverage the potential of ultrahigh field strengths and enables standard cardiac CMR techniques such as LGE and perfusion imaging in large animals. Initial work has been done to demonstrate that this coil design is scalable. This enables not only longitudinal, translational, large animal studies, but also the transfer to other ultrahigh field applications like spine or abdominal imaging.

Deep Learning Based Cardiac Cine Segmentation Framework – Transfer Learning Application to 7T Ultrahigh-Field MRI

Deep learning is a rapidly developing field that is increasingly applied in cardiac image segmentation, particularly for the assessment of cardiac function based on MRI. Many reviews on AI and AI based image segmentation have identified the limited availability of annotated data as one of the biggest obstacles to routine applications of neural networks in clinical routine.[245,250,258,262,264] Reasons for this are difficulties regarding data access, data privacy, missing data harmonization, and data protection.

In this study we generate cardiac cine segmentation annotations for a publicly available data set[307] of clinical 1.5T and 3.0T images. In total, we labeled short axis slices for 1,140 cardiac MRI examinations of normal and abnormal cardiac function. Following data curation (correction for slice spacing, changes in image dimensions and image resolution, as well as missing slices, etc.), MR examinations with the top 5%, 10%, and 15% label accuracy contained 54540, 162480, and 239350 images, respectively. Label accuracy was determined indirectly, comparing ESV and EDV derived from predicted labels to ground truth values provided by Kaggle. With respect to MRI data this is the biggest data set currently openly available. Other public data sets contain 30-200 examinations and have typically been published in the context of MICCAI (International Conference on Medical Image Computing and Computer-assisted Intervention).[308-315] While there is a clear need for high fidelity data and resources with respective annotations, the high amount of work required to organize and maintain such data bases inevitably makes access expensive. In addition, we have to ask ourselves, if such high fidelity data is realistically comparable to routine clinical cardiac MRI or if such data is only suitable to answer research questions.

We employ a publicly available model[74] for label generation and demonstrate that training of DL segmentation models using the newly annotated dataset enables state-of-the-art results and even transfer learning approaches, such as 7T cardiac cine segmentation. During the labelling process we noticed that

segmentation was working particularly well for certain patients and failed for others. Concerning applications of DL models this is a dilemma that will continue to come up: is this model suitable for my data and if not, can I adapt my data in a certain way to improve model compatibility? In our case the model by Bai et al[74] was trained on data from the UK Biobank, which is a relatively homogeneous data set, where all images are acquired using the same sequence and the same scanner type. Increasing the similarity between the Kaggle data and UK Biobank data thus resulted in increased model performance for label generation. In general, it is useful to understand why a model makes a certain prediction and it is arguably part of human nature that we want to understand, why a certain decision was made. This notion is probably even stronger when the information we are presented is meant to be used for diagnostic purposes and treatment decisions. Explainability and interpretability of neural networks is therefore an active field of research. In order to deal with model compatibility and model-data-interactions we developed misas (model interpretation through sensitivity analysis for segmentation), a software tool that enables sensitivity analysis for segmentation models.[316] Misas provides intuitive local interpretations, transforming an input image in a defined manner and analyzing the impact of this transformation on the resulting model performance. This process allows users to gain information on model-data interactions, concretely, if a model is suitable for a certain dataset, if data needs to be adapted prior to input, how robust a model is to diverse input data, or if and to what degree potential perturbations, such as image artifacts affect model performance. To the best of our knowledge, misas is the first tool of its kind and the open source Python library Ankenbrand et al.[316] provide therefore enables the scientific community to apply sensitivity analysis to their own data and models. While developed based on cardiac image segmentation tasks, misas is applicable to basically every image segmentation task.

The curated and now labeled dataset allowed training of a basic cardiac MRI segmentation model, which we used for a transfer learning approach to 7T cine data. We assess how much and which data is required to enable this transfer learning application. As initially pointed out, labeled data is limited and often difficult to acquire, particularly in areas that require domain specific knowledge. In addition, the generation of new labels is a time-consuming and tedious process, which means that the lower the amount of labeled data required for transfer learning, the better. Our study demonstrates that end-diastolic and end-systolic images appear to be more valuable with regard to model performance than images from other or even random heart phases. Compared to full CMR examinations from 14 volunteers, using end-diastolic and end-systolic images only, allowed reduction of training images from 5076 to 448, which corresponds to Δ91%. This has major implications. Firstly, state-of-the-art segmentation results comparable to inter-observer variability can be achieved with moderate data requirements. Secondly, the notion to label patient by patient may result in higher data requirements than necessary. Thirdly, we can profit from clinical segmentations, where labeling end-diastolic and end-systolic data is common practice for the evaluation of cardiac function.

Our demonstration of transfer learning to 7T data suggests that data and models provided as part of this study will enable segmentation models for other cardiac MR examinations, such as T_2, T_1, LGE, and T_2*, and even DTI. Further analysis with respect to data requirements to enable these transfer learning applications may be subject to future studies.

In order to facilitate reproducibility and further application in research by others all labeled data, segmentation models, and respective code was published using the code and data repositories GitHub and Zenodo. As pointed out initially, AI is a rapidly developing field, where it is paramount that potential end users such as clinicians get access to functioning and well documented code. If contact to such tools remains limited for clinicians, it is unlikely that applications will gain a foothold in a clinical setting.

Exploring ensemble applications for multi-sequence myocardial pathology segmentation

Next to the assessment of cardiac function, CMR allows imaging of the acute injury and ischemic regions post MI, providing pathological and morphological information of the myocardium. Similar to the segmentation for the assessment of cardiac function, DL is used to segment such pathologic alterations (scar and edema). Clinically, two different sequences are used and segmentations are done separately for each sequence.

We participated in the myocardial pathology segmentation (MyoPS 2020) challenge, where the aim was to combine multi-sequence CMR data to classify myocardial pathology, infarcted and edema regions to be precise. All our approaches were based on DL, demonstrating that individual sequences lead to good segmentation results for their target, for example LGE for scar tissue. More interestingly, we demonstrate that multi-sequence-multi-class models enable results comparable to the dedicated sequences and that combining multiple models in a so-called “model ensemble” combines the strengths of individual models in multi-sequence-multi-class segmentation. In addition, the model ensemble provided consistent segmentation for non-pathological regions such as healthy myocardium, LV and RV. With $DICE_{scar}$: 0.59±0.23 and $Dice_{scar+edema}$: 0.61±0.11 for a multi-sequence-multi-class model and $Dice_{scar}$: 0.62±0.24, $Dice_{scar+edema}$: 0.67±0.14 for the ensemble approach, we reached markedly improved segmentation results compared to reported inter-observer variability of manual scar segmentation ($Dice_{scar}$: 0.52±0.16).

While these results already demonstrate that AI outperforms capabilities of human operators regarding pathology segmentation, AI will likely become even better in the future. With only 45 cases of patient data (training set: 25, test set: 20), the amount of labeled data was very small and a larger sample may already have led to significantly improved model performance. New methods are developed to circumvent the bottle-neck that is limited access to annotated data. Self-supervised learning aims to generate labels from the data automatically,[317] unsupervised learning aims to learn representations without paired labeled data,[318] and

unsupervised domain adaption aims to optimize model performance on previously unseen datasets without additional labelling costs.[319-322]

In this challenge all images were co-registered and the model performance was solely judged on pathology segmentation. While this is already an important application with respect to outcome prediction[24-27] and myocardial salvage,[28,29] other CMR metrics such as wall motion or ejection fraction are not considered. Looking towards future clinical applications of AI with respect to multi-sequence-multi-class segmentation, clinicians are likely to expect a more comprehensive approach, where all relevant CMR metrics can be derived at the same time.

Our study is the first application of ensemble methods for cardiac multi-sequence-multi-class segmentation. Model ensembles, also called "model zoos" are becoming more common for segmentation tasks. Therefore, our biggest contribution to the field is that we demonstrate how public tools and libraries, such as PyTorch[266] and fastai,[72] enable high performance segmentation models and even multi-sequence-multi-class segmentation models with moderate requirements to additional programming. Particularly, fastai, which is designed around the main goals "to be approachable and rapidly productive, while also being deeply hackable and configurable [⋯]"[72,323] has accelerated how we develop and build our models. Our study demonstrates how to apply these public DL tools to cardiac image segmentation, in this case pathology segmentation. Aiming to increase interdisciplinary discussion, to facilitate reproducibility and further model applications, we made all models and code publicly available using the repositories GitHub and Zenodo. We thus contribute to make DL more accessible, a process that will drive future research and application.

4.2 Cardiovascular Magnetic Resonance – Assessment of Myocardial Structure and Function

While sequence design, data analysis, and hardware developments in recent years have significantly improved cardiac DTI, the method for *in vivo* imaging remains accessible to only a small number of researchers and physician scientists. No vendor has developed and offered a cardiac DTI product sequence and there is a plethora of challenges still to address, before DTI will be applied in clinical routine examinations.

However, initial work has already been done to address some of these challenges, for example harmonization of DTI metrics with respect to different sequences used. All pulse sequences currently applied for *in vivo* cardiac DTI can be classified as either a stimulated echo acquisition mode[324] with monopolar diffusion gradients or a spin echo with motion-compensated diffusion gradients.[87] Varying sequences and protocol parameters from site to site limit reproducibility and comparison of diffusion metrics. While there are individual studies analyzing intra-scanner variation[52] or coefficients across two time points,[103] there is not enough data to validate accuracy and reproducibility of DTI metrics. Therefore, Teh et al started a multi-center phantom study, aiming to establish accuracy, precision and reproducibility of product pulsed gradient spin echo sequences.[325] Participating sites were sent a custom built phantom with seven tubes of Polyvinylpyrrolidone and detailed measurement instructions. Values for average MD (mean ± standard deviation across scanners) and FA in the reference tube at scans 1 and 2 were 1.149 ± 0.032 and 1.159 ± 0.049 [10^{-3} mm^2/s] and 0.035 ± 0.0013 and 0.030 ± 0.0015, respectively. Overall, results of this study demonstrated good baseline inter- and intra-site reproducibility and the measurement protocol was extended by custom cardiac DTI sequences of the individual sites. We provide 3T data for the product pulsed gradient spin echo sequence and a custom stimulated echo sequence (Lohr et al.[122]) that was implemented as part of this thesis. We thus contribute to validate the accuracy, precision, and reproducibility of state-of-the-art custom sequences for *in vivo* cardiac DTI. This study is a milestone towards protocol harmonization and the establishment of clinical cardiac DTI.

While DTI has been shown to provide novel information on structure-function[38,41,43] and structure-conductivity interactions,[42,45] our understanding of myocardial remodeling in response to cardiac injury or CVDs in general, remains limited. In order to become clinically relevant, DTI metrics need to be linked to unique and, most importantly, actionable readouts. Obviously, measurements of these metrics or rather markers have to be done *in vivo* eventually, but translational *ex vivo* studies are usually preferred for proof of concept studies, because they provide high fidelity data that was measured in an optimized and controlled setting. DTI results of this thesis contribute to the field in this specific area, demonstrating feasibility of 7T *ex vivo* scans of large animal hearts as well as fixation induced alterations in derived diffusion metrics and tissue properties of such hearts.

Furthermore, we show that cardiac DTI provides highly sensitive surrogates for microstructural remodeling in response to subendocardial damage and how these changes relate to echocardiography measurements. We also directly link pronounced loss of contractile myofiber tracts, replacement fibrosis, and LV systolic failure.

All these results contribute to improve the value of *ex vivo* DTI of the heart, which will remain a valuable tool for studies aiming for high data fidelity. Furthermore, we provide insights how structural changes relate to clinically assessable functional changes and how cardiac DTI may provide unique readouts such as our newly introduced metric: the ratio between voxels showing positive HA and voxels showing negative HA. Coming back to the ESC guidelines of acute and chronic heart failure, such readouts may significantly improve diagnosis, establishment of etiology, treatment monitoring, and validation of novel drugs.

As highlighted in the introduction, 7T cardiac MRI is currently a research modality that is developing towards clinical applications. This means that RF hardware, clinically applicable sequences, and SAR-safety, in particular in parallel transmit applications, are still subject to research and validation. In this thesis we implemented and performed CMR using a new generation 7T system and a commercial RF coil. With respect to clinically applicable sequences for functional cardiac MRI at ultrahigh field strengths, we expanded vendor sequences towards accurate cardiac planning and the assessment of cardiac function based on cine sequence acquisitions.[70,263] Image segmentation is a key process of the assessment of quantitative morphological and functional metrics. In order to provide automatic image segmentation for functional 7T data that is robust to contrast variations, we created deep learning models based on clinical data, which we then successfully optimized towards our 7T acquisitions. This transfer to 7T data was already feasible based on a very limited number of images, demonstrating that images acquired at 7T are highly similar to clinical data, containing all relevant features for segmentation and the assessment of cardiac function.

4.3 Deep learning in Medical Imaging

Deep learning technology is applied in almost any newly released digital device in use today and the rapidly developing field is continuing to generate new ideas and concepts, leading to ever better and deeper models. Similarly, applications in healthcare and MRI are increasing, leading to DL solutions for every step of the image generation pipeline.[262,264]

In this thesis we apply deep learning based segmentation that enables both functional and structural characterization of the myocardium based on clinically used MRI sequences. The functional assessment is enabled through automatic segmentation of cine data and the structural assessment through detection and segmentation of scar tissue and edema. With respect to cine data acquired at ultrahigh field strength we demonstrate that transfer learning approaches are able to cope with field strength and sequence induced alterations in contrast compared

to clinical examinations. While we solely focused on cardiac image segmentation, the following thoughts and concepts apply to DL in medical imaging in general.

Deep learning for image segmentation has long been shown to outperform manual operators for various tasks, leading to models for morphology of the ventricles,[17,18] the atria,[19,20] the aorta,[21] the whole heart,[22,23] and even pathology,[252,276,277] such as scar and edema. However, scarcity of labels, data privacy, and low interpretability limit clinical applications, where DL could greatly reduce the workload for clinicians and improve consistency in data analysis. Publications of this thesis aimed to address these limitations, creating newly annotated data, making all data and respective code openly accessible, and using models and architectures that are commonly known, available to everyone, and have been demonstrated to perform well for a large variety of segmentation tasks. In addition to applications in ultrahigh field CMR, we intended to facilitate easy understanding, re-use, reproducibility, and interpretability and thus, discussions around AI in a clinical setting. Due to limited data access, real clinical publications on DL applications are scarce and feasibility of models is discussed in relation to the few, rather small data sets currently available.[308-315] While a future DL model may possibly enable great segmentation results independent of sequence, vendor, field strengths, measurement protocol, patient or even pathology, very stable and well performing task-specific models already do exist. In order to enable clinical application, computer scientists, basic researchers and clinician scientists will have to cooperate, because there are two very basic requirements. Firstly, labeling protocols should be harmonized. This means that there needs to be a clinical consensus on proper segmentation, in particular with respect to the inclusion of basal slices or papillary muscle. Secondly, a benchmark dataset based on this consensus, which is large enough to contain substantial data diversity that reflects the spectrum of clinical CMR needs to be established. The CheXpert benchmark dataset,[326] which consists of 224.316 chest radiographs of 65.240 patients is a good example for such a benchmark dataset. The more than 150 entries to the leaderboard demonstrate that such datasets facilitate discussion and comparable improvements towards clinical establishment of DL applications.

Due to the rapid developments in the field of AI, novel models, concepts, and architectures are usually published on pre-print servers first, while established journals struggle to keep up with respective peer-reviewed publications. With the advent of AI, software in general, but also in medical imaging, has become crucially important. In order to maintain high quality standards, even within preprint publications, transparency and reproducibility through availability of code and data are key, especially for DL, where interpretability is already limited by the black box that is DL.[327,328]

Availability, applicability and reproducibility are essential features of research that prevent redundant work and can be built on.[329,330] In medical imaging, even healthcare in general, this enables the translation from research to clinical applications. However, proper testing and documentation of code takes time and, similar to other fields,[331] the current system in healthcare research does provide

little to no incentives to put in the work. Despite that, we provide all models and code for our AI publications under an open source license using the platform GitHub. This platform provides mechanisms for quality control, usage and collaborations and all projects are developed and continuously tested using a defined and clean environment. It is intuitive to assume that target users of software should be involved in its development and that open source projects empower bioinformatics communities.[332] With the public availability on GitHub, our contributions to the field are shared in a sustainable and productive way for re-use and future research.

5 FUTURE WORK

While results of this thesis emphasize the value of translational *ex vivo* studies, we aimed to establish cardiac DTI in volunteers and patients *in vivo* at both 3T and 7T. Measurements using the stimulated echo sequence demonstrate sequence functionality and comparability of derived diffusion metrics in *ex vivo* and phantom acquisitions.[76,122,325] Due to diffusion encoding over consecutive heart beats, the stimulated echo sequence is highly susceptible to trigger accuracy. Initial scans in large animals *in vivo* at 7T have shown that proper gating based on an acoustic trigger is possible and that B_0 inhomogeneity can be managed. Further measurements in large animals, volunteers, and patients are required to improve the sequence and establish optimal routine protocols, in particular at 7T.

With optimized sequences for accurate cardiac planning and cine imaging we have implemented the gold standard for the measurement of mass and cardiac function via EF on a new generation 7T system. However, other clinical routine applications will require implementation in order to make 7T CMR a viable alternative to clinical 1.5T and 3.0T systems. We therefore continue to develop dedicated, parallel transmit hardware that enables SAR-safe, homogeneous and efficient RF excitation. This is of paramount importance, because next to clinically used CMR acquisitions such as LGE and T_2-weighted images, this hardware also enables us to leverage SNR gains associated with ultrahigh field strength.[57-61]

In this thesis DL is applied for rapid automatic segmentation of cardiac MRI examinations, including short axis cine, LGE, and T_2-weighted images. Future work aims to integrate developed models into clinically used software. This can be a tedious venture, because it requires vendors to provide access to contour files and proper system integration. However, assuming an experienced physician will need approximately 10 seconds to segment a cine short axis image, AI models can accelerate this process a hundredfold. Translation towards clinical applications is therefore connected to a significant gain of time, a valuable resource in healthcare. In addition to clinical applications such model integration will also accelerate data evaluation in pre-clinical studies, allowing rapid and consistent segmentation of MR examinations in mice, rats, or pigs. We based our DL models on a UNet architecture. Theoretically, this architecture enables many other DL applications such as image restoration and even super-resolution techniques. Future work may evaluate these applications in both clinical and pre-clinical cardiac MRI, particularly at 7T.

6 CONCLUSION

The three fields of ultrahigh field MRI, cardiac DTI, and AI are likely to have a strong impact on future clinical CMR. Results obtained in this thesis establish the functional characterization of the myocardium *in vivo* using the latest generation 7T system as well as the structural characterization of the myocardium of large and small animal hearts *ex vivo*. Furthermore, developed methods were applied in pre-clinical studies, improving our understanding of structure-function interactions in cases of subendocardial damage, fibrosis and MI. Developed AI for segmentation of clinical cardiac MRI achieved state-of-the-art results and feasibility of its transfer to ultrahigh field applications was demonstrated. For all deep learning applications we employed open source software tools and made all data and code accessible, and thus, reproducible, and reusable. In conclusion, all results, developed methods, and tools addressed main goals of this thesis, enabling future research in ultrahigh field CMR and related deep learning applications. Furthermore, results of this thesis contribute to diagnostic methods that facilitate early detection, and risk stratification with respect to CVDs. In the long run these findings may contribute to meaningful and accessible ways of prevention in clinical routine applications.

7 APPENDIX

A INDIVIDUAL AUTHOR CONTRIBUTIONS

This chapter lists individual author contributions for each publication (chapter 3, page 11) included in this thesis in detail. The initial table displays contributions to parts of the respective study and experiments and the following table displays contributions to figures and tables (if present) of the same publication. Responsibility decreases from left to right. The label S indicates figures and tables which are part of the supplemental material.

The statement (chapter “Confirmation”) confirms that legal second publication rights for all manuscripts were obtained, where necessary. Details regarding the publication licenses can be found in the respective paper sections in chapter 3.

Author contributions for PLOSONE – 2019

Complete reference:

Lohr D, Terekhov M, Weng AM, Schroeder A, Walles H, et al. Spin echo based cardiac diffusion imaging at 7T: An ex vivo study of the porcine heart at 7T and 3T. *PLOS ONE*. 2019;14(3):e0213994.

DOI: 10.1371/journal.pone.0213994

Table 1: Author contributions to: PLOSONE - 2019

Participated in	**Author Initials**			
Study Design	**DL**	MT	LMS	
Methods Development	**DL**	MT	AS	
Data Collection	**DL**			
Data Analysis and Interpretation	**DL**	MT	LMS	
Manuscript Writing				AMW
Introduction	**DL**	MT	LMS	
Materials & Methods	**DL**	MT	LMS	
Discussion	**DL**	MT	LMS	
First Draft	**DL**			

Explanations: Resources and supervision by HW, supervision and writing: review & editing by AMW.

Table 2: Figures and tables of: PLOSONE - 2019

Figure / Table	**Author Initials**	
Figure 1	**DL**	
Figure 2	**DL**	LMS
Figure 3	**DL**	LMS
Figure 4	**DL**	LMS
Figure 5	**DL**	
Figure 6	**DL**	
Figure 7	**DL**	LMS
Figure 8	**DL**	LMS
Table 1	**DL**	

Explanations: Figures and tables in supplemental material by **DL**.

Author contributions for NMR in Biomedicine – 2020

Complete reference:

Lohr D, Terekhov M, Veit F, Schreiber LM. Longitudinal assessment of tissue properties and cardiac diffusion metrics of the ex vivo porcine heart at 7 T: Impact of continuous tissue fixation using formalin. NMR in biomedicine. 2020;33(7):e4298.
DOI: 10.1002/nbm.4298

Table 3: Author contributions to: NMR in Biomedicine - 2020

Participated in	**Author Initials**		
Study Design	**DL**	LMS	
Methods Development	**DL**	MT	FV
Data Collection	**DL**		
Data Analysis and Interpretation	**DL**	MT	LMS
Manuscript Writing			
Introduction	**DL**	MT	LMS
Materials & Methods	**DL**	MT	LMS
Discussion	**DL**	MT	LMS
First Draft	**DL**		

Explanations: Methodology and Resources by FV.

Table 4: Figures and tables of: NMR in Biomedicine - 2020

Figure / Table	**Author Initials**	
Figure 1	**DL**	
Figure 2	**DL**	LMS
Figure 3	**DL**	LMS
Figure 4	**DL**	LMS
Figure 5	**DL**	LMS
Figure 6	**DL**	LMS
Figure 7	**DL**	
Table 1	**DL**	

Explanations: Figures and tables in supplemental material by **DL**.

Author contributions for Hypertension - 2019

Complete reference:

Beyhoff N, **Lohr D**, Foryst-Ludwig A, Klopfleisch R, Brix S, et al. Characterization of Myocardial Microstructure and Function in an Experimental Model of Isolated Subendocardial Damage. Hypertension. 2019;74(2):295-304.
DOI: 10.1161/HYPERTENSIONAHA.119.12956

Table 5: Author contributions to: Hypertension - 2019

Participated in	**Author Initials**			
Study Design Methods Development	LMS/UK/ NB/**DL**	AFL/WMK	FV	
Data Collection		**DL**	RK, JG	SB/ATi/ LE/ATa
Data Analysis and Interpretation	NB/**DL**/ LMS/UK	MT	LMS	SB/ATi/ LE/ATa
Manuscript Writing	NB **DL**	UK/LMS	AFL/WMK/BP	RK
Introduction Materials & Methods Discussion				
First Draft	NB			

Table 6: Figures and tables of: Hypertension - 2019

Figure / Table	**Author Initials**	
Figure 1A-C	NB	RK
Figure 1D	NB	
Figure 1E	SB	NB
Figure 2A	NB	**DL**
Figure 2B	**DL**	NB
Figure 2C	NB	**DL**
Figure 2D	NB	**DL**
Figure 3A	**DL**	NB
Figure 3B	**DL**	NB
Figure 3C	NB	**DL**
Figure 3D	**DL**	NB
Figure 3E	NB	**DL**

Figure / Table	Author Initials		
Figure 4	NB		
Figure 5	NB		
Figure S1	NB	RK	
Figure S2	NB	JG	RK
Figure S3A	**DL**	NB	
Figure S3B	**DL**	NB	
Figure S3C	NB	**DL**	
Figure S3D	NB	**DL**	
Figure S3E	**DL**	NB	
Figure S3F	NB	**DL**	
Figure S3G	NB	**DL**	
Figure S3H	NB	**DL**	
Figure S3I	**DL**	NB	
Figure S3J	NB	**DL**	
Figure S3K	NB	**DL**	
Figure S3L	NB	**DL**	
Figure S3M	**DL**	NB	
Figure S3N	NB	**DL**	
Figure S3O	NB	**DL**	
Figure S3P	NB	**DL**	
Figure S4A	**DL**	NB	
Figure S4B	NB	**DL**	
Figure S4C	**DL**	NB	
Figure S4D	**DL**	NB	
Figure S4E	NB	**DL**	
Figure S4F	**DL**	NB	
Figure S4G	**DL**	NB	
Figure S4H	NB	**DL**	
Figure S4I	**DL**	NB	
Table 1	NB	AFL	LE, AT
Table S1	NB	AFL	
Table S2	SB	AFL	NB
Table S3	NB	AFL	
Table S4	NB		

Author contributions for Frontiers in Cardiovascular Medicine - 2020

Complete reference:

Beyhoff N*, **Lohr D***, Thiele A, Foryst-Ludwig A, Klopfleisch R, et al. Myocardial Infarction after High-Dose Catecholamine Application - A Case Report from an Experimental Imaging Study. *Frontiers in Cardiovascular Medicine.* 2020;7(247)
DOI: 10.3389/fcvm.2020.580296

Table 7: Author contributions to: Frontiers - 2020

Participated in	**Author Initials**			
Study Design Methods Development	UK/LMS NB/**DL**	AFL		
Data Collection	NB/**DL**	AFL	RK/AT	
Data Analysis and Interpretation	NB/**DL**	UK	LMS	
Manuscript Writing	NB	**DL**	UK	LMS
Introduction				
Materials & Methods				
Discussion				
First Draft	NB			

Explanations: * equal contribution

Table 8: Figures and tables of: Frontiers - 2020

Figure / Table	**Author Initials**	
Figure 1A	NB	
Figure 1B	NB	
Figure 1C	NB	
Figure 1D	NB	
Figure 1E	NB	
Figure 2A	NB	AT
Figure 2B	NB	AT
Figure 3A	NB	RK
Figure 3B	NB	
Figure 3C	NB	
Figure 4A	**DL**	NB
Figure 4B	NB	**DL**
Figure 4C	**DL**	NB
Figure 4D	**DL**	NB
Figure 4E	**DL**	NB
Figure 4F	**DL**	NB
Figure 4G	NB	**DL**

Author contributions for Scientific Reports – 2020

Complete reference:

Elabyad IA, Terekhov M, **Lohr D**, Stefanescu MR, Baltes S, et al. A Novel Mono-surface Antisymmetric 8Tx/16Rx Coil Array for Parallel Transmit Cardiac MRI in Pigs at 7T. *Scientific Reports*. 2020;10(1):3117.
DOI: 10.1038/s41598-020-59949-6

Table 9: Author contributions to: Scientific Reports – 2020

Participated in	**Author Initials**		
Study Design Methods Development	IE		
Data Collection	IT/MT/**DL**	SB	
Data Analysis and Interpretation	IE/MT	**DL**	
Manuscript Writing	IE/MT/**DL**	MRS	LMS/SB
Introduction			
Materials & Methods		SB	
Discussion			
First Draft	IE		

Explanations: Study supervision was done by LMS. The *ex vivo* measurements were done by **DL**, MT and MRS. *In vivo* measurements were performed by **DL** and MT. Animal preparation and animal handling for *ex vivo* and *in vivo* measurements was done by SB, who wrote respective sections in the Materials & Methods section and provided information regarding study approval.

Table 10: Figures and tables of: Scientific Reports – 2020

Figure / Table	**Author Initials**	
Figure 1	IE	MT
Figure 2	IE	MT
Figure 3	IE	MT
Figure 4	IE	
Figure 5	MT	
Figure 6	IE	MT
Figure 7	MT	IE
Figure 8	MT	
Figure 9	**DL**	
Figure 10	MT	**DL**
Figure 11	MT	**DL**
Table 1	IE	
Table 2	IE	
Table 3	IE	

Explanation: Tables in supplemental material by IE

Author contributions for medRxiv – 2020

Complete Reference:

Ankenbrand MJ*, **Lohr D***, Schlötelburg W, Reiter T, Wech T, et al. Deep Learning Based Cardiac Cine Segmentation - Transfer Learning Application to 7T Ultrahigh-Field MRI. *medRxiv*.2020.

DOI: 10.1101/2020.06.15.20131656

Table 11: Author contributions to: medRxiv – 2020

Participated in	**Author Initials**			
Study Design	**DL**&MJA	MT	TW/WS/TR	
Methods Development	MJA	MT	TW	
Data Collection	**DL,** WS	TR	MJA/TW	
Data Analysis and Interpretation	MJA&**DL**			
Manuscript Writing				All others
Introduction	**DL**	MJA	LMS	
Materials & Methods	**DL**	MJA	LMS	
Discussion	**DL**	MJA	LMS	
First Draft	**DL**	MJA		

Explanations: * equal contribution, writing – review & editing by all others. Creation of the online repository by MJA.

Status: Submitted to MRM, currently under revision.

Table 12: Figures and tables of: medRxiv – 2020

Figure / Table	**Author Initials**	
Figure 1	MJA	**DL**
Figure 2	MJA	**DL**
Figure 3	**DL**	MJA
Figure 4	MJA	**DL**
Figure 5	**DL**	MJA
Figure 6	MJA	**DL**
Table 1	**DL**	MJA
Table 2	MJA	**DL**

Explanations: * equal contribution.

Author contributions for LNCS – 2020

Complete reference:

A Ankenbrand M**, Lohr D**, Schreiber LM. Exploring Ensemble Applications for Multi-sequence Myocardial Pathology Segmentation. In: Zhuang X et al. (eds) Myocardial Pathology Segmentation Combining Multi-Sequence Cardiac Magnetic Resonance Images. MyoPS 2020. Lecture Notes in Computer Science, vol 12554. Springer, Cham.

DOI: 10.1007/978-3-030-65651-5_6

Table 13: Author contributions to: LNCS – 2020

Participated in	**Author Initials**		
Study Design	MJA&**DL**	LMS	
Methods Development	MJA	**DL**	
Data Collection	**MJA**	**DL**	LMS
Data Analysis and Interpretation	MJA&**DL**		
Manuscript Writing			
Introduction	**DL**	MJA	LMS
Materials & Methods	MJA	**DL**	LMS
Discussion	MJA	**DL**	LMS
First Draft	MJA	**DL**	

Explanations: Creation of the online repository by MJA.

Status: accepted.

Table 14: Figures and tables of: LNCS – 2020

Figure / Table	**Author Initials**	
Figure 1	**DL**	MJA
Figure 2	MJA	**DL**
Figure 3	MJA	**DL**
Table 1	MJA	**DL**

Confirmation

The doctoral researcher confirms that she/he has obtained permission from both the publishers and the co-authors for legal second publication.
The doctoral researcher and the primary supervisor confirm the correctness of the above mentioned assessment.

David Lohr

Doctoral Researcher's Name	Date, Place	Signature

Prof. Dr. Laura M. Schreiber

Primary Supervisor's Name	Date, Place	Signature

B Consent to Publish

C Curriculum Vitae

BIBLIOGRAPHY

1. https://www.who.int/news-room/fact-sheets/detail/cardiovascular-diseases-(cvds). Accessed October 3, 2020.

2. Mamas MA, Sperrin M, Watson MC, Coutts A, Wilde K, et al. Do patients have worse outcomes in heart failure than in cancer? A primary care-based cohort study with 10-year follow-up in Scotland. *Eur J Heart Fail.* Sep 2017;19(9):1095-1104. DOI: 10.1002/ejhf.822

3. Ceia F, Fonseca C, Mota T, Morais H, Matias F, et al. Prevalence of chronic heart failure in Southwestern Europe: the EPICA study. *Eur J Heart Fail.* Aug 2002;4(4):531-539. DOI: 10.1016/s1388-9842(02)00034-x

4. Mosterd A, Hoes AW. Clinical epidemiology of heart failure. *Heart (British Cardiac Society).* 2007;93(9):1137-1146. DOI: 10.1136/hrt.2003.025270

5. Setoguchi S, Stevenson LW, Schneeweiss S. Repeated hospitalizations predict mortality in the community population with heart failure. *American heart journal.* Aug 2007;154(2):260-266. DOI: 10.1016/j.ahj.2007.01.041

6. Störk S, Hense HW, Zentgraf C, Uebelacker I, Jahns R, et al. Pharmacotherapy according to treatment guidelines is associated with lower mortality in a community-based sample of patients with chronic heart failure A prospective cohort study. *European Journal of Heart Failure.* 2008;10(12):1236-1245. DOI: 10.1016/j.ejheart.2008.09.008

7. Ponikowski P, Voors AA, Anker SD, Bueno H, Cleland JGF, et al. 2016 ESC Guidelines for the diagnosis and treatment of acute and chronic heart failure: The Task Force for the diagnosis and treatment of acute and chronic heart failure of the European Society of Cardiology (ESC)Developed with the special contribution of the Heart Failure Association (HFA) of the ESC. *European Heart Journal.* 2016;37(27):2129-2200. DOI: 10.1093/eurheartj/ehw128

8. Gonzalez JA, Kramer CM. Role of Imaging Techniques for Diagnosis, Prognosis and Management of Heart Failure Patients: Cardiac Magnetic Resonance. *Current heart failure reports.* Aug 2015;12(4):276-283. DOI: 10.1007/s11897-015-0261-9

9. Kilner PJ, Geva T, Kaemmerer H, Trindade PT, Schwitter J, Webb GD. Recommendations for cardiovascular magnetic resonance in adults with congenital heart disease from the respective working groups of the European Society of Cardiology. *Eur Heart J.* Apr 2010;31(7):794-805. DOI: 10.1093/eurheartj/ehp586

10. Hundley WG, Bluemke DA, Finn JP, Flamm SD, Fogel MA, et al. ACCF/ACR/AHA/NASCI/SCMR 2010 Expert Consensus Document on Cardiovascular Magnetic Resonance. *Circulation.* 2010;121(22):2462-2508. DOI: 10.1161/CIR.0b013e3181d44a8f

11. Moon JC, Messroghli DR, Kellman P, Piechnik SK, Robson MD, et al. Myocardial T1 mapping and extracellular volume quantification: a Society for Cardiovascular Magnetic Resonance (SCMR) and CMR Working Group of the European Society of Cardiology consensus statement. *Journal of Cardiovascular Magnetic Resonance.* 2013;15(1):92. DOI: 10.1186/1532-429X-15-92

12. Yoshida A, Ishibashi-Ueda H, Yamada N, Kanzaki H, Hasegawa T, et al. Direct comparison of the diagnostic capability of cardiac magnetic resonance and endomyocardial biopsy in patients with heart failure. *Eur J Heart Fail.* Feb 2013;15(2):166-175. DOI: 10.1093/eurjhf/hfs206

13. Luijnenburg SE, Robbers-Visser D, Moelker A, Vliegen HW, Mulder BJM, Helbing WA. Intra-observer and interobserver variability of biventricular function, volumes and mass in patients with congenital heart disease measured by CMR imaging. *Int J Cardiovasc Imaging.* 2010;26(1):57-64. DOI: 10.1007/s10554-009-9501-y

14. Mooij CF, de Wit CJ, Graham DA, Powell AJ, Geva T. Reproducibility of MRI measurements of right ventricular size and function in patients with normal and dilated ventricles. *Journal of Magnetic Resonance Imaging.* 2008;28(1):67-73. DOI: 10.1002/jmri.21407

15. Plein S, Bloomer TN, Ridgway JP, Jones TR, Bainbridge GJ, Sivananthan MU. Steady-state free precession magnetic resonance imaging of the heart: comparison with segmented k-space gradient-echo imaging. *Journal of Magnetic Resonance Imaging.* 2001;14(3):230-236. DOI: 10.1002/jmri.1178

16. Robbers-Visser D, Boersma E, Helbing WA. Normal biventricular function, volumes, and mass in children aged 8 to 17 years. *Journal of Magnetic Resonance Imaging.* Mar 2009;29(3):552-559. DOI: 10.1002/jmri.21662

17. Isensee F, Jaeger PF, Full PM, Wolf I, Engelhardt S, Maier-Hein KH. Automatic Cardiac Disease Assessment on cine-MRI via Time-Series Segmentation and Domain Specific Features. 2018; Cham.

18. Li C, Tong Q, Liao X, Si W, Chen S, et al. APCP-NET: Aggregated Parallel Cross-Scale Pyramid Network for CMR Segmentation. Paper presented at: 2019 IEEE 16th International Symposium on Biomedical Imaging (ISBI 2019); 8-11 April 2019, 2019.

19. Xia Q, Yao Y, Hu Z, Hao A. Automatic 3D Atrial Segmentation from GE-MRIs Using Volumetric Fully Convolutional Networks. 2019; Cham.

20. Xiong Z, Fedorov VV, Fu X, Cheng E, Macleod R, Zhao J. Fully Automatic Left Atrium Segmentation From Late Gadolinium Enhanced Magnetic Resonance Imaging Using a Dual Fully Convolutional Neural Network. *IEEE transactions on medical imaging.* 2019;38(2):515-524. DOI: 10.1109/TMI.2018.2866845

21. Bai W, Suzuki H, Qin C, Tarroni G, Oktay O, et al. Recurrent Neural Networks for Aortic Image Sequence Segmentation with Sparse Annotations. 2018; Cham.

22. Li J, Zhang R, Shi L, Wang D. Automatic Whole-Heart Segmentation in Congenital Heart Disease Using Deeply-Supervised 3D FCN. 2017; Cham.

23. Yu L, Cheng J-Z, Dou Q, Yang X, Chen H, et al. Automatic 3D Cardiovascular MR Segmentation with Densely-Connected Volumetric ConvNets. 2017; Cham.

24. Lehrke S, Lossnitzer D, Schöb M, Steen H, Merten C, et al. Use of cardiovascular magnetic resonance for risk stratification in chronic heart failure: prognostic value of late gadolinium enhancement in patients with non-ischaemic dilated cardiomyopathy. *Heart.* 2011;97(9):727-732. DOI: 10.1136/hrt.2010.205542

25. Assomull RG, Prasad SK, Lyne J, Smith G, Burman ED, et al. Cardiovascular Magnetic Resonance, Fibrosis, and Prognosis in Dilated Cardiomyopathy. *Journal of the American College of Cardiology.* 2006;48(10):1977-1985. DOI: 10.1016/j.jacc.2006.07.049

26. Kim RJ, Wu E, Rafael A, Chen E-L, Parker MA, et al. The Use of Contrast-Enhanced Magnetic Resonance Imaging to Identify Reversible Myocardial Dysfunction. *New England Journal of Medicine.* 2000;343(20):1445-1453. DOI: 10.1056/nejm200011163432003

27. Selvanayagam JB, Kardos A, Francis JM, Wiesmann F, Petersen SE, et al. Value of Delayed-Enhancement Cardiovascular Magnetic Resonance Imaging in Predicting

Myocardial Viability After Surgical Revascularization. *Circulation.* 2004;110(12):1535-1541. DOI: 10.1161/01.CIR.0000142045.22628.74

28. Pennell D. Myocardial Salvage. *Circulation.* 2006;113(15):1821-1823. DOI: 10.1161/CIRCULATIONAHA.105.618942

29. Lønborg J, Vejlstrup N, Mathiasen AB, Thomsen C, Jensen JS, Engstrøm T. Myocardial area at risk and salvage measured by T2-weighted cardiovascular magnetic resonance: Reproducibility and comparison of two T2-weighted protocols. *Journal of Cardiovascular Magnetic Resonance.* 2011;13(1):50. DOI: 10.1186/1532-429X-13-50

30. Cleveland GG, Chang DC, Hazlewood CF, Rorschach HE. Nuclear magnetic resonance measurement of skeletal muscle: anisotrophy of the diffusion coefficient of the intracellular water. *Biophys J.* 1976;16(9):1043-1053. DOI: 10.1016/S0006-3495(76)85754-2

31. Garrido L, Wedeen VJ, Kwong KK, Spencer UM, Kantor HL. Anisotropy of water diffusion in the myocardium of the rat. *Circ Res.* May 1994;74(5):789-793. DOI: 10.1161/01.res.74.5.789

32. Crank J. *The Mathematics of Diffusion.* Oxford: Oxford University Press; 1975.

33. Streeter DD, Bassett DL. An engineering analysis of myocardial fiber orientation in pig's left ventricle in systole. *The Anatomical Record.* 1966;155(4):503-511. DOI: 10.1002/ar.1091550403

34. Streeter DD, Spotnitz HM, Patel DP, Ross J, Sonnenblick EH. Fiber orientation in the canine left ventricle during diastole and systole. *Circ Res.* 1969;24. DOI: 10.1161/01.res.24.3.339

35. Sosnovik DE, Wang R, Dai G, Reese TG, Wedeen VJ. Diffusion MR tractography of the heart. *Journal of Cardiovascular Magnetic Resonance.* 2009;11:47. DOI: 10.1186/1532-429X-11-47

36. Smerup M, Nielsen E, Agger P, Frandsen J, Vestergaard-Poulsen P, et al. The Three-Dimensional Arrangement of the Myocytes Aggregated Together Within the Mammalian Ventricular Myocardium. *The Anatomical Record.* 2009;292(1):1-11. DOI: 10.1002/ar.20798

37. Hales PW, Schneider JE, Burton RAB, Wright BJ, Bollensdorff C, Kohl P. Histo-anatomical structure of the living isolated rat heart in two contraction states assessed by diffusion tensor MRI. *Progress in Biophysics and Molecular Biology.* 2012;110(2):319-330. DOI: 10.1016/j.pbiomolbio.2012.07.014

38. Nielles-Vallespin S, Khalique Z, Ferreira PF, de Silva R, Scott AD, et al. Assessment of Myocardial Microstructural Dynamics by In Vivo Diffusion Tensor Cardiac Magnetic Resonance. *Journal of the American College of Cardiology.* 2017;69(6):661-676. DOI: 10.1016/j.jacc.2016.11.051

39. Spotnitz HM, Spotnitz WD, Cottrell TS, Spiro D, Sonnenblick EH. Cellular basis for volume related wall thickness changes in the rat left ventricle. *J Mol Cell Cardiol.* 1974;6. DOI: 10.1016/0022-2828(74)90074-1

40. Harrington KB, Rodriguez F, Cheng A, Langer F, Ashikaga H, et al. Direct measurement of transmural laminar architecture in the anterolateral wall of the ovine left ventricle: new implications for wall thickening mechanics. *American Journal of Physiology-Heart and Circulatory Physiology.* 2005;288(3):H1324-H1330. DOI: 10.1152/ajpheart.00813.2004

41. Ferreira PF, Kilner PJ, McGill LA, Nielles-Vallespin S, Scott AD, et al. In vivo cardiovascular magnetic resonance diffusion tensor imaging shows evidence of

abnormal myocardial laminar orientations and mobility in hypertrophic cardiomyopathy. *Journal of Cardiovascular Magnetic Resonance.* 2014;16:87. DOI: 10.1186/s12968-014-0087-8

42. Ariga R, Tunnicliffe EM, Manohar SG, Mahmod M, Raman B, et al. Identification of Myocardial Disarray in Patients With Hypertrophic Cardiomyopathy and Ventricular Arrhythmias. *Journal of the American College of Cardiology.* 2019;73(20):2493-2502. DOI: 10.1016/j.jacc.2019.02.065

43. von Deuster C, Sammut E, Asner L, Nordsletten D, Lamata P, et al. Studying Dynamic Myofiber Aggregate Reorientation in Dilated Cardiomyopathy Using In Vivo Magnetic Resonance Diffusion Tensor Imaging. *Circulation. Cardiovascular imaging.* 2016;9(10):e005018-e005018. DOI: 10.1161/CIRCIMAGING.116.005018

44. Mekkaoui C, Huang S, Chen HH, Dai G, Reese TG, et al. Fiber architecture in remodeled myocardium revealed with a quantitative diffusion CMR tractography framework and histological validation. *Journal of Cardiovascular Magnetic Resonance.* 2012;14(1).

45. Mekkaoui C, Jackowski MP, Kostis WJ, Stoeck CT, Thiagalingam A, et al. Myocardial Scar Delineation Using Diffusion Tensor Magnetic Resonance Tractography. *J Am Heart Assoc.* 2018;7(3):e007834. DOI: 10.1161/JAHA.117.007834

46. Ishizu T, Seo Y, Kameda Y, Kawamura R, Kimura T, et al. Left Ventricular Strain and Transmural Distribution of Structural Remodeling in Hypertensive Heart Disease. *Hypertension.* 2014;63(3):500-506. DOI: 10.1161/HYPERTENSIONAHA.113.02149

47. Martinez DA, Guhl DJ, Stanley WC, Vailas AC. Extracellular matrix maturation in the left ventricle of normal and diabetic swine. *Diabetes Research and Clinical Practice.* 2003;59(1):1-9. DOI: 10.1016/S0168-8227(02)00178-X

48. Wanagat J, Wolff MR, Aiken JM. Age-associated Changes in Function, Structure and Mitochondrial Genetic and Enzymatic Abnormalities in the Fischer 344×Brown Norway F1Hybrid Rat Heart. *Journal of Molecular and Cellular Cardiology.* 2002/01/01/ 2002;34(1):17-28. DOI: 10.1006/jmcc.2001.1483

49. Mekkaoui C, Reese TG, Jackowski MP, Cauley SF, Setsompop K, et al. Diffusion Tractography of the Entire Left Ventricle by Using Free-breathing Accelerated Simultaneous Multisection Imaging. *Radiology.* 2017;282(3):850-856. DOI: 10.1148/radiol.2016152613

50. Nielles-Vallespin S, Mekkaoui C, Gatehouse PD, Reese TG, Keegan J, et al. In vivo diffusion tensor MRI of the human heart: reproducibility of breath-hold and navigator-based approaches. *Magnetic resonance in medicine.* Aug 2013;70(2):454-465. DOI: 10.1002/mrm.24488

51. Scott AD, Nielles-Vallespin S, Ferreira PF, Khalique Z, Gatehouse PD, et al. An in-vivo comparison of stimulated-echo and motion compensated spin-echo sequences for 3 T diffusion tensor cardiovascular magnetic resonance at multiple cardiac phases. *Journal of Cardiovascular Magnetic Resonance.* 2018;20:1. DOI: 10.1186/s12968-017-0425-8

52. Tunnicliffe EM, Scott AD, Ferreira P, Ariga R, McGill LA, Nielles-Vallespin S. Intercentre reproducibility of cardiac apparent diffusion coefficient and fractional anisotropy in healthy volunteers. *Journal of Cardiovascular Magnetic Resonance.* 2014;16. DOI: 10.1186/1532-429x-16-31

53. Hsu EW, Muzikant AL, Matulevicius SA, Penland RC, Henriquez CS. Magnetic resonance myocardial fiber-orientation mapping with direct histological correlation. *American Journal of Physiology - Heart and Circulatory Physiology.* 1998;274(5):H1627-H1634.

54. Scollan DF, Holmes A, Winslow R, Forder J. Histological validation of myocardial microstructure obtained from diffusion tensor magnetic resonance imaging. *American Journal of Physiology - Heart and Circulatory Physiology.* 1998;275(6):H2308-H2318.

55. Abdullah OM, Drakos SG, Diakos NA, Wever-Pinzon O, Kfoury AG, Stehlik J. Characterization of diffuse fibrosis in the failing human heart via diffusion tensor imaging and quantitative histological validation. *NMR in biomedicine.* 2014;27. DOI: 10.1002/nbm.3200

56. Beyhoff N, Lohr D, Foryst-Ludwig A, Klopfleisch R, Brix S, et al. Characterization of Myocardial Microstructure and Function in an Experimental Model of Isolated Subendocardial Damage. *Hypertension.* 2019;74(2):295-304. DOI: 10.1161/HYPERTENSIONAHA.119.12956

57. Elderen SGCv, Versluis MJ, Westenberg JJM, Agarwal H, Smith NB, et al. Right Coronary MR Angiography at 7 T: A Direct Quantitative and Qualitative Comparison with 3 T in Young Healthy Volunteers. *Radiology.* 2010;257(1):254-259. DOI: 10.1148/radiol.100615

58. Hess AT, Bissell MM, Ntusi NAB, Lewis AJM, Tunnicliffe EM, et al. Aortic 4D flow: Quantification of signal-to-noise ratio as a function of field strength and contrast enhancement for 1.5T, 3T, and 7T. *Magnetic resonance in medicine.* 2015;73(5):1864-1871. DOI: 10.1002/mrm.25317

59. Koning W, de Rotte AAJ, Bluemink JJ, van der Velden TA, Luijten PR, et al. MRI of the carotid artery at 7 Tesla: Quantitative comparison with 3 Tesla. *Journal of Magnetic Resonance Imaging.* 2015;41(3):773-780. DOI: 10.1002/jmri.24601

60. Rodgers CT, Clarke WT, Snyder C, Vaughan JT, Neubauer S, Robson MD. Human cardiac 31P magnetic resonance spectroscopy at 7 tesla. *Magnetic resonance in medicine.* 2014;72(2):304-315. DOI: 10.1002/mrm.24922

61. von Knobelsdorff-Brenkenhoff F, Frauenrath T, Prothmann M, Dieringer MA, Hezel F, et al. Cardiac chamber quantification using magnetic resonance imaging at 7 Tesla—a pilot study. *European Radiology.* 2010;20(12):2844-2852. DOI: 10.1007/s00330-010-1888-2

62. Data Science Bowl Cardiac Challenge Data 2016. https://www.kaggle.com/c/second-annual-data-science-bowl/data. Accessed 29th of July 2019.

63. MyoPS 2020: Myocardial pathology segmentation combining multi-sequence CMR. http://www.sdspeople.fudan.edu.cn/zhuangxiahai/0/MyoPS20/index.html. Accessed June 20, 2020.

64. Zhuang X. Multivariate mixture model for cardiac segmentation from multi-sequence MRI. *International Conference on Medical Image Computing and Computer-Assisted Intervention.* 2016:pp.581-588.

65. Zhuang X. Multivariate Mixture Model for Myocardial Segmentation Combining Multi-Source Images. *IEEE Transactions on Pattern Analysis and Machine Intelligence.* 2019;41(12):2933-2946. DOI: 10.1109/TPAMI.2018.2869576

66. https://de.mathworks.com/. Accessed November 10, 2020.

67. Manjon JV, Coupe P, Concha L, Buades A, Collins DL, Robles M. Diffusion Weighted Image Denoising Using Overcomplete Local PCA. *PloS one.* 2013;8(9). DOI: 10.1371/journal.pone.0073021.g001

68. Jiang H, van Zijl PC, Kim J, Pearlson GD, Mori S. DtiStudio: resource program for diffusion tensor computation and fiber bundle tracking. *Computer methods and programs in biomedicine.* Feb 2006;81(2):106-116. DOI: 10.1016/j.cmpb.2005.08.004

69. Yeh F-C. DSI Studio. http://dsi-studio.labsolver.org. Accessed April 22, 2016.

70. Ankenbrand MJ, Lohr D, Schlötelburg W, Reiter T, Wech T, Schreiber LM. Deep Learning Based Cardiac Cine Segmentation – Transfer Learning Application to 7T Ultrahigh-Field MRI. *medRxiv.* 2020. DOI: 10.1101/2020.06.15.20131656

71. Paszke A, Gross S, Massa F, Lerer A, Bradbury J, et al. PyTorch: An Imperative Style, High-Performance Deep Learning Library. 2019:8024--8035.

72. Howard J, Gugger S. Fastai: A Layered API for Deep Learning. *Information.* 2020;11(2):108.

73. Harris CR, Millman KJ, van der Walt SJ, Gommers R, Virtanen P, et al. Array programming with NumPy. *Nature.* 2020;585(7825):357-362. DOI: 10.1038/s41586-020-2649-2

74. Bai W, Sinclair M, Tarroni G, Oktay O, Rajchl M, et al. Automated cardiovascular magnetic resonance image analysis with fully convolutional networks. *Journal of Cardiovascular Magnetic Resonance.* Sep 2018;20(1):65. DOI: 10.1186/s12968-018-0471-x

75. Ankenbrand M, Lohr D, Schreiber LM. Exploring Ensemble Applications for Multi-sequence Myocardial Pathology Segmentation. In: Zhuang X et al. (eds) Myocardial Pathology Segmentation Combining Multi-Sequence Cardiac Magnetic Resonance Images: First Challenge, MyoPS 2020, Held in Conjunction with MICCAI 2020, Lima. Lecture Notes in Computer Science, vol 12554. Springer International Publishing. 2021. DOI: 10.1007/978-3-030-65651-5

76. Lohr D, Terekhov M, Weng AM, Schroeder A, Walles H, Schreiber LM. Spin echo based cardiac diffusion imaging at 7T: An ex vivo study of the porcine heart at 7T and 3T. *PloS one.* 2019;14(3):e0213994. DOI: 10.1371/journal.pone.0213994

77. Bastin ME, Armitage PA, Marshall I. A theoretical study of the effect of experimental noise on the measurement of anisotropy in diffusion imaging. *Magnetic resonance imaging.* Sep 1998;16(7):773-785.

78. Breuer FA, Kannengiesser SAR, Blaimer M, Seiberlich N, Jakob PM, Griswold MA. General formulation for quantitative G-factor calculation in GRAPPA reconstructions. *Magnetic resonance in medicine.* 2009;62(3):739-746. DOI: 10.1002/mrm.22066

79. Cerqueira MD, Weissman NJ, Dilsizian V, Jacobs AK, Kaul S, Laskey WK. Standardized myocardial segmentation and nomenclature for tomographic imaging of the heart. A statement for healthcare professionals from the cardiac imaging committee of the council on clinical cardiology of the american heart association. *Circulation.* 2002;105. DOI: 10.1161/hc0402.102975

80. Chang EY, Du J, Bae WC, Statum S, Chung CB. Effects of achilles tendon immersion in saline and perfluorochemicals on T2 and T2*. *Journal of Magnetic Resonance Imaging.* 2014;40(2):496-500. DOI: 10.1002/jmri.24360

81. Choi S, Cunningham DT, Aguila F, Corrigan JD, Bogner J, et al. DTI at 7 and 3 T: systematic comparison of SNR and its influence on quantitative metrics. *Magnetic resonance imaging.* 2011;29(6):739-751. DOI: 10.1016/j.mri.2011.02.009

82. Deoni SC, Rutt BK, Peters TM. Rapid combined T1 and T2 mapping using gradient recalled acquisition in the steady state. *Magnetic resonance in medicine.* Mar 2003;49(3):515-526. DOI: 10.1002/mrm.10407

83. Dibb R, Liu C. Joint eigenvector estimation from mutually anisotropic tensors improves susceptibility tensor imaging of the brain, kidney, and heart. *Magnetic resonance in medicine.* 2017;77(6):2331-2346. DOI: 10.1002/mrm.26321

84. Dou J, Reese TG, Tseng WY, Wedeen VJ. Cardiac diffusion MRI without motion effects. *Magnetic resonance in medicine.* Jul 2002;48(1):105-114. DOI: 10.1002/mrm.10188

85. Ennis DB, Kindlman G, Rodriguez I, Helm PA, McVeigh ER. Visualization of Tensor Fields Using Superquadric Glyphs. *Magnetic resonance in medicine.* 2005;53(1):169-176.

86. Gahm JK, Kindlmann G, Ennis DB. The effects of noise over the complete space of diffusion tensor shape. *Medical Image Analysis.* 2014;18(1):197-210. DOI: 10.1016/j.media.2013.10.009

87. Gamper U, Boesiger P, Kozerke S. Diffusion imaging of the in vivo heart using spin echoes–considerations on bulk motion sensitivity. *Magnetic resonance in medicine.* 2007;57(2):331-337. DOI: 10.1002/mrm.21127

88. Greenbaum RA, Ho SY, GIbson DG, Becker AE, Anderson RH. Left ventricular fibre architecture in man. *Br Heart J.* 1981;45. DOI: 10.1136/hrt.45.3.248

89. Hales PW, Burton RAB, Bollensdorff C, Mason F, Bishop M, et al. Progressive changes in T1, T2 and left-ventricular histo-architecture in the fixed and embedded rat heart. *NMR in biomedicine.* 2011;24(7):836-843. DOI: 10.1002/nbm.1629

90. Helm P, Beg MF, Miller MI, Winslow RL. Measuring and mapping cardiac fiber and laminar architecture using diffusion tensor MR imaging. *Ann N Y Acad Sci.* 2005;1047. DOI: 10.1196/annals.1341.026

91. Helm PA, Tseng HJ, Younes L, McVeigh ER, Winslow RL. Ex vivo 3D diffusion tensor imaging and quantification of cardiac laminar structure. *Magnetic resonance in medicine.* 2005;54. DOI: 10.1002/mrm.20622

92. Juchem C, Rudrapatna SU, Nixon TW, de Graaf RA. Dynamic Multi-Coil Technique (DYNAMITE) Shimming for Echo-Planar Imaging of the Human Brain at 7 Tesla. *NeuroImage.* 2015;105:462-472. DOI: 10.1016/j.neuroimage.2014.11.011

93. Kanai A, Salama G. Optical Mapping Reveals That Repolarization Spreads Anisotropically and Is Guided by Fiber Orientation in Guinea Pig Hearts. *Circulation Research.* 1995;77(4):784-802. DOI: 10.1161/01.res.77.4.784

94. Köhler S, Hiller K-H, Griswold M, Bauer WR, Haase A, Jakob PM. NMR-microscopy with TrueFISP at 11.75T. *Journal of magnetic resonance.* 2003;161(2):252-257. DOI: 10.1016/S1090-7807(03)00013-2

95. Köhler S, Hiller K-H, Waller C, Bauer WR, Haase A, Jakob PM. Investigation of the microstructure of the isolated rat heart: A comparison between T*2- and diffusion-weighted MRI. *Magnetic resonance in medicine.* 2003;50(6):1144-1150. DOI: 10.1002/mrm.10636

96. Köhler S, Hiller K-H, Waller C, Jakob PM, Bauer WR, Haase A. Visualization of myocardial microstructure using high-resolution T imaging at high magnetic field. *Magnetic resonance in medicine.* 2003;49(2):371-375. DOI: 10.1002/mrm.10346

97. Kung GL, Nguyen TC, Itoh A, Skare S, Ingels NB, Miller DC. The presence of two local myocardial sheet populations confirmed by diffusion tensor MRI and histological validation. *Journal of Cardiovascular Magnetic Resonance.* 2011;34. DOI: 10.1002/jmri.22725

98. Landman BA, Farrell JA, Huang H, Prince JL, Mori S. Diffusion tensor imaging at low SNR: nonmonotonic behaviors of tensor contrasts. *Magnetic resonance imaging.* Jul 2008;26(6):790-800. DOI: 10.1016/j.mri.2008.01.034

99. LeGrice IJ, Smaill BH, Chai LZ, Edgar SG, Gavin JB, Hunter PJ. Laminar structure of the heart: ventricular myocyte arrangement and connective tissue architecture in the dog. *Am J Physiol.* 1995;269.

100. Lelovas PP, Kostomitsopoulos NG, Xanthos TT. A comparative anatomic and physiologic overview of the porcine heart. *Journal of the American Association for Laboratory Animal Science : JAALAS.* 2014;53(5):432-438.

101. Mazumder R, Choi S, Clymer BD, White RD, Kolipaka A. Diffusion Tensor Imaging of Healthy and Infarcted Porcine Hearts: Study on the Impact of Formalin Fixation. *Journal of medical imaging and radiation sciences.* 2016;47(1):74-85. DOI: 10.1016/j.jmir.2015.10.007

102. McClymont D, Teh I, Schneider JE. The impact of signal-to-noise ratio, diffusion-weighted directions and image resolution in cardiac diffusion tensor imaging – insights from the ex-vivo rat heart. *Journal of Cardiovascular Magnetic Resonance.* November 20 2017;19(1):90. DOI: 10.1186/s12968-017-0395-x

103. McGill LA, Ismail TF, Nielles-Vallespin S, Ferreira PF, Scott AD, et al. Reproducibility of in-vivo diffusion tensor cardiovascualar magnetic resonance in hypertrophic cardiomyopathy. *Journal of Cardiovascular Magnetic Resonance.* 2012;14.

104. Ohliger MA, Grant AK, Sodickson DK. Ultimate intrinsic signal-to-noise ratio for parallel MRI: electromagnetic field considerations. *Magnetic resonance in medicine.* Nov 2003;50(5):1018-1030. DOI: 10.1002/mrm.10597

105. Pashakhanloo F, Herzka DA, Mori S, Zviman M, Halperin H, et al. Submillimeter diffusion tensor imaging and late gadolinium enhancement cardiovascular magnetic resonance of chronic myocardial infarction. *Journal of cardiovascular magnetic resonance.* Jan 11 2017;19(1):9. DOI: 10.1186/s12968-016-0317-3

106. Reeder SB, Wintersperger BJ, Dietrich O, Lanz T, Greiser A, et al. Practical approaches to the evaluation of signal-to-noise ratio performance with parallel imaging: Application with cardiac imaging and a 32-channel cardiac coil. *Magnetic resonance in medicine.* 2005;54(3):748-754. DOI: 10.1002/mrm.20636

107. Robson PM, Grant AK, Madhuranthakam AJ, Lattanzi R, Sodickson DK, McKenzie CA. Comprehensive quantification of signal-to-noise ratio and g-factor for image-based and k-space-based parallel imaging reconstructions. *Magnetic resonance in medicine.* Oct 2008;60(4):895-907. DOI: 10.1002/mrm.21728

108. Schmid P, Jaermann T, Boesiger P, Niederer PF, Lunkenheimer PP, et al. Ventricular myocardial architecture as visualised in postmortem swine hearts using magnetic resonance diffusion tensor imaging. *European Journal of Cardio-Thoracic Surgery.* 2005;27(3):468-472. DOI: 10.1016/j.ejcts.2004.11.036

109. Schuppert M, Kreitner K-F, Fischer S, Wein S, Keil B, et al. Determination of the optimal number of coil elements: A semi-theoretical approach *In Proceedings of the 23rd Annual Meeting of ISMRM, Toronto, Ontario, Canada, 2015. p. 1779.*

110. Scott AD, Ferreira PFADC, Nielles-Vallespin S, Gatehouse P, McGill L-A, et al. Optimal diffusion weighting for in vivo cardiac diffusion tensor imaging. *Magnetic resonance in medicine.* 2015;74(2):420-430. DOI: 10.1002/mrm.25418

111. Scott AD, Nielles-Vallespin S, Ferreira PF, McGill L-A, Pennell DJ, Firmin DN. The effects of noise in cardiac diffusion tensor imaging and the benefits of averaging complex data. *NMR in biomedicine.* 2016;29(5):588-599. DOI: 10.1002/nbm.3500

112. Skare S, Hedehus M, Moseley ME, Li T-Q. Condition Number as a Measure of Noise Performance of Diffusion Tensor Data Acquisition Schemes with MRI. *Journal of magnetic resonance.* 2000;147(2):340-352. DOI: 10.1006/jmre.2000.2209

113. Terekhov M, Lohr D, Schreiber LM. Myocardium tissue DTI with stimulated echo at large susceptibility induced B0 gradients: examination of the shimming strategies efficiency and errors. . *In Proceedings of the 25th Annual Meeting of ISMRM, Honolulu, Hawaii, USA, 2017. p. 1841.*

114. Tseng WY, Wedeen VJ, Reese TG, Smith RN, Halpern EF. Diffusion tensor MRI of myocardial fibers and sheets: correspondence with visible cut-face texture. *Journal of Magnetic Resonance Imaging.* 2003;17. DOI: 10.1002/jmri.10223

115. Tseng W-YI, Reese TG, Weisskoff RM, Wedeen VJ. Cardiac diffusion tensor MRI in vivo without strain correction. *Magnetic resonance in medicine.* 1999;42(2):393-403. DOI: 10.1002/(SICI)1522-2594(199908)42:2<393::AID-MRM22>3.0.CO;2-F

116. von Deuster C, Stoeck CT, Genet M, Atkinson D, Kozerke S. Spin echo versus stimulated echo diffusion tensor imaging of the in vivo human heart. *Magnetic resonance in medicine.* 2016;76(3):862-872. DOI: 10.1002/mrm.25998

117. Vu AT, Auerbach E, Lenglet C, Moeller S, Sotiropoulos SN, et al. High resolution whole brain diffusion imaging at 7 T for the Human Connectome Project. *NeuroImage.* 2015;122:318-331. DOI: 10.1016/j.neuroimage.2015.08.004

118. Waldman LK, Nosan D, Villarreal F, Covell JW. Relation between transmural deformation and local myofiber direction in canine left ventricle. *Circ Res.* 1988;63. DOI: 10.1161/01.res.63.3.550

119. Watson BR, Hsu EW. Effects of Formalin Fixation on Diffusion Tensor Imaging of Myocardial Tissues. *In Proceedings of the 20th Annual Meeting of ISMRM, Melborune, Victoria, Australia, 2012. p. 1114.*

120. Wu EX, Wu Y, Nicholls JM, Wang J, Liao S, et al. MR diffusion tensor imaging study of postinfarct myocardium structural remodeling in a porcine model. *Magnetic resonance in medicine.* 2007;58(4):687-695. DOI: 10.1002/mrm.21350

121. Yeh F-C, Verstynen TD, Wang Y, Fernández-Miranda JC, Tseng W-YI. Deterministic Diffusion Fiber Tracking Improved by Quantitative Anisotropy. *PloS one.* 2013;8(11):e80713. DOI: 10.1371/journal.pone.0080713

122. Lohr D, Terekhov M, Veit F, Schreiber LM. Longitudinal assessment of tissue properties and cardiac diffusion metrics of the ex vivo porcine heart at 7 T: Impact of continuous tissue fixation using formalin. *NMR in biomedicine.* 2020;33(7):e4298. DOI: 10.1002/nbm.4298

123. Agger P, Lass T, Smerup M, Frandsen J, Pedersen M. Optimal preservation of porcine cardiac tissue prior to diffusion tensor magnetic resonance imaging. *Journal of Anatomy.* 2015;227(5):695-701. DOI: 10.1111/joa.12377

124. Bottomley PA, Foster TH, Argersinger RE, Pfeifer LM. A review of normal tissue hydrogen NMR relaxation times and relaxation mechanisms from 1–100 MHz: Dependence on tissue type, NMR frequency, temperature, species, excision, and age. *Medical Physics.* 1984;11(4):425-448. DOI: 10.1118/1.595535

125. Carawford CNC, Barer R. The Action of Formaldehyde on Living Cells as Studied by Phase-contrast Microscopy. *Quarterly Journal of Microscopical Science.* 1951;s3-92(20):403-452.

126. D'Arceuil H, de Crespigny A. The effects of brain tissue decomposition on diffusion tensor imaging and tractography. *NeuroImage.* 2007;36(1):64-68. DOI: 10.1016/j.neuroimage.2007.02.039

127. Dawe RJ, Bennett DA, Schneider JA, Vasireddi SK, Arfanakis K. Postmortem MRI of human brain hemispheres: T2 relaxation times during formaldehyde fixation. *Magnetic resonance in medicine.* 2009;61(4):810-818. DOI: 10.1002/mrm.21909

128. Eggen MD, Swingen CM, Iaizzo PA. Ex vivo diffusion tensor MRI of human hearts: Relative effects of specimen decomposition. *Magnetic resonance in medicine.* 2012;67(6):1703-1709. DOI: 10.1002/mrm.23194

129. Giannakidis A, Gullberg GT, Pennell DJ, Firmin DN. Value of Formalin Fixation for the Prolonged Preservation of Rodent Myocardial Microanatomical Organization: Evidence by MR Diffusion Tensor Imaging. *The Anatomical Record.* 2016;299(7):878-887. DOI: 10.1002/ar.23359

130. Helm PA, Younes L, Beg MF, Ennis DB, Leclercq C, Faris OP. Evidence of structural remodeling in the dyssynchronous failing heart. *Circ Res.* 2006;98. DOI: 10.1161/01.RES.0000199396.30688.eb

131. Jones DK. Determining and visualizing uncertainty in estimates of fiber orientation from diffusion tensor MRI. *Magnetic resonance in medicine.* 2003;49(1):7-12. DOI: 10.1002/mrm.10331

132. Kim S, Chi-Fishman G, Barnett AS, Pierpaoli C. Dependence on diffusion time of apparent diffusion tensor of ex vivo calf tongue and heart. *Magnetic resonance in medicine.* 2005;54(6):1387-1396. DOI: 10.1002/mrm.20676

133. Laule C, Vavasour IM, Kolind SH, Li DKB, Traboulsee TL, et al. Magnetic resonance imaging of myelin. *Neurotherapeutics.* July 01 2007;4(3):460-484. DOI: 10.1016/j.nurt.2007.05.004

134. Madi S, Hasan KM, Narayana PA. Diffusion tensor imaging of in vivo and excised rat spinal cord at 7 T with an icosahedral encoding scheme. *Magnetic resonance in medicine.* 2005;53(1):118-125. DOI: 10.1002/mrm.20304

135. Nagara H, Inoue T, Koga T, Kitaguchi T, Tateishi J, Goto I. Formalin fixed brains are useful for magnetic resonance imaging (MRI) study. *Journal of the Neurological Sciences.* 1987;81(1):67-77. DOI: 10.1016/0022-510X(87)90184-5

136. Nguyen C, Fan Z, Sharif B, He Y, Dharmakumar R, et al. In vivo three-dimensional high resolution cardiac diffusion-weighted MRI: A motion compensated diffusion-prepared balanced steady-state free precession approach. *Magnetic resonance in medicine.* 2014;72(5):1257-1267. DOI: 10.1002/mrm.25038

137. Pattany PM, Puckett WR, Klose KJ, Quencer RM, Bunge RP, et al. High-resolution diffusion-weighted MR of fresh and fixed cat spinal cords: evaluation of diffusion coefficients and anisotropy. *AJNR. American journal of neuroradiology.* Jun-Jul 1997;18(6):1049-1056.

138. Schmid P, Lunkenheimer PP, Redmann K, Rothaus K, Jiang X, et al. Statistical Analysis of the Angle of Intrusion of Porcine Ventricular Myocytes from Epicardium to Endocardium Using Diffusion Tensor Magnetic Resonance Imaging. *The Anatomical Record.* 2007;290(11):1413-1423. DOI: 10.1002/ar.20604

139. Shatil AS, Uddin MN, Matsuda KM, Figley CR. Quantitative Ex Vivo MRI Changes due to Progressive Formalin Fixation in Whole Human Brain Specimens: Longitudinal Characterization of Diffusion, Relaxometry, and Myelin Water Fraction Measurements at 3T. *Frontiers in Medicine.* 2018-February-20 2018;5(31). DOI: 10.3389/fmed.2018.00031

140. Shepherd TM, Flint JJ, Thelwall PE, Stanisz GJ, Mareci TH, et al. Postmortem interval alters the water relaxation and diffusion properties of rat nervous tissue--implications for MRI studies of human autopsy samples. *NeuroImage.* 2009;44(3):820-826. DOI: 10.1016/j.neuroimage.2008.09.054

141. Shepherd TM, Thelwall PE, Stanisz GJ, Blackband SJ. Aldehyde fixative solutions alter the water relaxation and diffusion properties of nervous tissue. *Magnetic resonance in medicine.* 2009;62(1):26-34. DOI: 10.1002/mrm.21977

142. Sosnovik DE, Mekkaoui C, Huang S, Chen HH, Dai G, et al. Microstructural impact of ischemia and bone marrow-derived cell therapy revealed with diffusion tensor magnetic resonance imaging tractography of the heart in vivo. *Circulation.* Apr 2014;129(17):1731-1741. DOI: 10.1161/CIRCULATIONAHA.113.005841

143. Sosnovik DE, Wang R, Dai G, Wang T, Aikawa E, et al. Diffusion spectrum MRI tractography reveals the presence of a complex network of residual myofibers in infarcted myocardium. *Circulation. Cardiovascular imaging.* May 2009;2(3):206-212. DOI: 10.1161/CIRCIMAGING.108.815050

144. Stoeck CT, von Deuster C, Genet M, Atkinson D, Kozerke S. Second order motion compensated spin-echo diffusion tensor imaging of the human heart. *Journal of Cardiovascular Magnetic Resonance.* 2015;17(Suppl 1):P81-P81. DOI: 10.1186/1532-429X-17-S1-P81

145. Thickman DI, Kundel HL, Wolf G. Nuclear magnetic resonance characteristics of fresh and fixed tissue: the effect of elapsed time. *Radiology.* Jul 1983;148(1):183-185. DOI: 10.1148/radiology.148.1.6856832

146. Tovi M, Ericsson A. Measurements of T1 and T2 over time in formalin-fixed human whole-brain specimens. *Acta Radiologica.* Sep 1992;33(5):400-404.

147. Wang C, Song L, Zhang R, Gao F. Impact of fixation, coil, and number of excitations on diffusion tensor imaging of rat brains at 7.0 T. *European radiology experimental.* Oct 2018;2(1):25. DOI: 10.1186/s41747-018-0057-2

148. Yong-Hing CJ, Obenaus A, Stryker R, Tong K, Sarty GE. Magnetic resonance imaging and mathematical modeling of progressive formalin fixation of the human brain. *Magnetic resonance in medicine.* 2005;54(2):324-332. DOI: 10.1002/mrm.20578

149. Bache RJ, Schwartz JS. Effect of perfusion pressure distal to a coronary stenosis on transmural myocardial blood flow. *Circulation.* 1982;65(5):928-935. DOI: 10.1161/01.CIR.65.5.928

150. Beyhoff N, Brix S, Betz IR, Klopfleisch R, Foryst-Ludwig A, et al. Application of Speckle-Tracking Echocardiography in an Experimental Model of Isolated Subendocardial Damage. *Journal of the American Society of Echocardiography.* 2017;30(12):1239-1250.e1232. DOI: 10.1016/j.echo.2017.08.006

151. Brooks WW, Conrad CH. Isoproterenol-Induced Myocardial Injury and Diastolic Dysfunction in Mice: Structural and Functional Correlates. *Comparative Medicine.* 2009;59(4):339-343.

152. Buckberg GD, Weisfeldt ML, Ballester M, Beyar R, Burkhoff D, et al. Left Ventricular Form and Function. *Circulation.* 2004;110(14):e333-e336. DOI: 10.1161/01.CIR.0000143625.56882.5C

153. Collins P, Billings CG, Barer GR, Daly JJ, Jolly A. Quantitation of isoprenaline-induced changes in the ventricular myocardium. *Cardiovascular Research.* 1975;9(6):797-806. DOI: 10.1093/cvr/9.6.797

154. de Boer RA, Daniels LB, Maisel AS, Januzzi Jr JL. State of the Art: Newer biomarkers in heart failure. *European Journal of Heart Failure.* 2015;17(6):559-569. DOI: 10.1002/ejhf.273

155. Fujii M, Nuno DW, Lamping KG, Dellsperger KC, Eastham CL, Harrison DG. Effect of hypertension and hypertrophy on coronary microvascular pressure. *Circulation Research.* 1992;71(1):120-126. DOI: 10.1161/01.RES.71.1.120

156. Geyer H, Caracciolo G, Abe H, Wilansky S, Carerj S, et al. Assessment of Myocardial Mechanics Using Speckle Tracking Echocardiography: Fundamentals and Clinical Applications. *Journal of the American Society of Echocardiography.* 2010;23(4):351-369. DOI: 10.1016/j.echo.2010.02.015

157. Goergen CJ, Chen HH, Sakadžić S, Srinivasan VJ, Sosnovik DE. Microstructural characterization of myocardial infarction with optical coherence tractography and two-photon microscopy. *Physiological Reports.* 2016;4(18):e12894. DOI: 10.14814/phy2.12894

158. Harrison DG, Florentine MS, Brooks LA, Cooper SM, Marcus ML. The effect of hypertension and left ventricular hypertrophy on the lower range of coronary autoregulation. *Circulation.* 1988;77(5):1108-1115. DOI: 10.1161/01.CIR.77.5.1108

159. Ikonomidis I, Tzortzis S, Triantafyllidi H, Parissis J, Papadopoulos C, et al. Association of impaired left ventricular twisting-untwisting with vascular dysfunction, neurohumoral activation and impaired exercise capacity in hypertensive heart disease. *European Journal of Heart Failure.* 2015;17(12):1240-1251. DOI: 10.1002/ejhf.403

160. Kane GC, Karon BL, Mahoney DW, Redfield MM, Roger VL, et al. Progression of Left Ventricular Diastolic Dysfunction and Risk of Heart Failure. *JAMA.* 2011;306(8):856-863. DOI: 10.1001/jama.2011.1201

161. Kang S-J, Lim H-S, Choi B-J, Choi S-Y, Hwang G-S, et al. Longitudinal Strain and Torsion Assessed by Two-Dimensional Speckle Tracking Correlate with the Serum Level of Tissue Inhibitor of Matrix Metalloproteinase-1, a Marker of Myocardial Fibrosis, in Patients with Hypertension. *Journal of the American Society of Echocardiography.* 2008;21(8):907-911. DOI: 10.1016/j.echo.2008.01.015

162. Lumens J, Delhaas T, Arts T, Cowan BR, Young AA. Impaired subendocardial contractile myofiber function in asymptomatic aged humans, as detected using MRI. *American Journal of Physiology-Heart and Circulatory Physiology.* 2006;291(4):H1573-H1579. DOI: 10.1152/ajpheart.00074.2006

163. Mizuguchi Y, Oishi Y, Miyoshi H, Iuchi A, Nagase N, Oki T. The Functional Role of Longitudinal, Circumferential, and Radial Myocardial Deformation for Regulating the Early Impairment of Left Ventricular Contraction and Relaxation in Patients With Cardiovascular Risk Factors: A Study With Two-Dimensional Strain Imaging. *Journal of the American Society of Echocardiography.* 2008;21(10):1138-1144. DOI: 10.1016/j.echo.2008.07.016

164. Mor-Avi V, Lang RM, Badano LP, Belohlavek M, Cardim NM, et al. Current and Evolving Echocardiographic Techniques for the Quantitative Evaluation of Cardiac Mechanics: ASE/EAE Consensus Statement on Methodology and Indications: Endorsed by the Japanese Society of Echocardiography. *Journal of the American Society of Echocardiography.* 2011;24(3):277-313. DOI: 10.1016/j.echo.2011.01.015

165. Mori H, Ishikawa S, Kojima S, Hayashi J, Watanabe Y, et al. Increased responsiveness of left ventricular apical myocardium to adrenergic stimuli. *Cardiovascular Research.* 1993;27(2):192-198. DOI: 10.1093/cvr/27.2.192

166. Palit A, Bhudia SK, Arvanitis TN, Turley GA, Williams MA. Computational modelling of left-ventricular diastolic mechanics: Effect of fibre orientation and right-ventricle topology. *Journal of Biomechanics.* 2015;48(4):604-612. DOI: 10.1016/j.jbiomech.2014.12.054

167. Parikh JD, Hollingsworth KG, Wallace D, Blamire AM, MacGowan GA. Normal age-related changes in left ventricular function: Role of afterload and subendocardial dysfunction. *International Journal of Cardiology.* 2016;223:306-312. DOI: 10.1016/j.ijcard.2016.07.252

168. Petrosino JM, Heiss VJ, Maurya SK, Kalyanasundaram A, Periasamy M, et al. Graded Maximal Exercise Testing to Assess Mouse Cardio-Metabolic Phenotypes. *PloS one.* 2016;11(2):e0148010. DOI: 10.1371/journal.pone.0148010

169. Pick R, Jalil JE, Janicki JS, Weber KT. The fibrillar nature and structure of isoproterenol-induced myocardial fibrosis in the rat. *Am J Pathol.* 1989;134(2):365-371.

170. Pop M, Ghugre NR, Ramanan V, Morikawa L, Stanisz G, et al. Quantification of fibrosis in infarcted swine hearts byex vivolate gadolinium-enhancement and diffusion-weighted MRI methods. *Physics in Medicine and Biology.* 2013;58(15):5009-5028. DOI: 10.1088/0031-9155/58/15/5009

171. Rona G. Catecholamine cardiotoxicity. *Journal of Molecular and Cellular Cardiology.* 1985;17(4):291-306. DOI: 10.1016/S0022-2828(85)80130-9

172. Samuel CS, Bodaragama H, Chew JY, Widdop RE, Royce SG, Hewitson TD. Serelaxin Is a More Efficacious Antifibrotic Than Enalapril in an Experimental Model of Heart Disease. *Hypertension.* 2014;64(2):315-322. DOI: 10.1161/HYPERTENSIONAHA.114.03594

173. Sengupta PP, Narula J. Reclassifying Heart Failure: Predominantly Subendocardial, Subepicardial, and Transmural. *Heart Failure Clinics.* 2008/07/01/ 2008;4(3):379-382. DOI: 10.1016/j.hfc.2008.03.013

174. Stanton T, Marwick TH. Assessment of Subendocardial Structure and Function. *JACC: Cardiovascular Imaging.* 2010;3(8):867-875. DOI: 10.1016/j.jcmg.2010.05.011

175. Strijkers GJ, Bouts A, Blankesteijn WM, Peeters THJM, Vilanova A, et al. Diffusion tensor imaging of left ventricular remodeling in response to myocardial infarction in the mouse. *NMR in biomedicine.* 2009;22(2):182-190. DOI: 10.1002/nbm.1299

176. Vogel MW, Slusser JP, Hodge DO, Chen HH. The Natural History of Preclinical Diastolic Dysfunction. *Circulation: Heart Failure.* 2012;5(2):144-151. DOI: 10.1161/CIRCHEARTFAILURE.110.959668

177. Watson SR, Dormer JD, Fei B. Imaging technologies for cardiac fiber and heart failure: a review. *Heart Failure Reviews.* 2018;23(2):273-289. DOI: 10.1007/s10741-018-9684-1

178. Wu MT, Tseng WY, Su MY, Liu CP, Chiou KR, Wedeen VJ. Diffusion tensor magnetic resonance imaging mapping the fiber architecture remodeling in human myocardium after infarction: correlation with viability and wall motion. *Circulation.* 2006;114. DOI: 10.1161/circulationaha.105.545863

179. Wu Y, Zhang L-J, Zou C, Tse H-F, Wu EX. Transmural heterogeneity of left ventricular myocardium remodeling in postinfarct porcine model revealed by MR diffusion tensor imaging. *Journal of Magnetic Resonance Imaging.* 2011;34(1):43-49. DOI: 10.1002/jmri.22589

180. Beyhoff N, Lohr D, Thiele A, Foryst-Ludwig A, Klopfleisch R, et al. Myocardial Infarction After High-Dose Catecholamine Application—A Case Report From an Experimental Imaging Study. *Frontiers in Cardiovascular Medicine.* 2020;7(247). DOI: 10.3389/fcvm.2020.580296

181. Abraham J, Mudd JO, Kapur N, Klein K, Champion HC, Wittstein IS. Stress Cardiomyopathy After Intravenous Administration of Catecholamines and Beta-Receptor Agonists. *Journal of the American College of Cardiology.* 2009;53(15):1320-1325. DOI: 10.1016/j.jacc.2009.02.020

182. Ghadri JR, Wittstein IS, Prasad A, Sharkey S, Dote K, et al. International Expert Consensus Document on Takotsubo Syndrome (Part I): Clinical Characteristics,

Diagnostic Criteria, and Pathophysiology. *Eur Heart J.* Jun 2018;39(22):2032-2046. DOI: 10.1093/eurheartj/ehy076

183. Kadish A, Shinnar M, Moore EN, Levine JH, Balke CW, Spear JF. Interaction of fiber orientation and direction of impulse propagation with anatomic barriers in anisotropic canine myocardium. *Circulation.* Dec 1988;78(6):1478-1494. DOI: 10.1161/01.cir.78.6.1478

184. Mekkaoui C, Reese TG, Jackowski MP, Bhat H, Sosnovik DE. Diffusion MRI in the heart. *NMR in biomedicine.* 2015. DOI: 10.1002/nbm.3426

185. Sachdeva J, Dai W, Kloner RA. Functional and histological assessment of an experimental model of Takotsubo's cardiomyopathy. *J Am Heart Assoc.* Jun 23 2014;3(3):e000921. DOI: 10.1161/jaha.114.000921

186. Taccardi B, Macchi E, Lux RL, Ershler PR, Spaggiari S, et al. Effect of myocardial fiber direction on epicardial potentials. *Circulation.* Dec 1994;90(6):3076-3090. DOI: 10.1161/01.cir.90.6.3076

187. Thygesen K, Alpert JS, Jaffe AS, Chaitman BR, Bax JJ, et al. Fourth universal definition of myocardial infarction (2018). *European Heart Journal.* 2018;40(3):237-269. DOI: 10.1093/eurheartj/ehy462

188. Wittstein IS, Thiemann DR, Lima JA, Baughman KL, Schulman SP, et al. Neurohumoral features of myocardial stunning due to sudden emotional stress. *The New England journal of medicine.* Feb 2005;352(6):539-548. DOI: 10.1056/NEJMoa043046

189. Elabyad IA, Terekhov M, Lohr D, Stefanescu MR, Baltes S, Schreiber LM. A Novel Mono-surface Antisymmetric 8Tx/16Rx Coil Array for Parallel Transmit Cardiac MRI in Pigs at 7T. *Scientific Reports.* 2020;10(1):3117. DOI: 10.1038/s41598-020-59949-6

190. Aussenhofer SA, Webb AG. An eight-channel transmit/receive array of TE01 mode high permittivity ceramic resonators for human imaging at 7T. *J Magn Reson.* Jun 2014;243:122-129. DOI: 10.1016/j.jmr.2014.04.001

191. Collins CM, Liu W, Swift BJ, Smith MB. Combination of optimized transmit arrays and some receive array reconstruction methods can yield homogeneous images at very high frequencies. *Magn Reson Med.* Dec 2005;54(6):1327-1332. DOI: 10.1002/mrm.20729

192. Dieringer MA, Renz W, Lindel T, Seifert F, Frauenrath T, et al. Design and application of a four-channel transmit/receive surface coil for functional cardiac imaging at 7T. *J Magn Reson Imaging.* Mar 2011;33(3):736-741. DOI: 10.1002/jmri.22451

193. Duan Q, Nair G, Gudino N, de Zwart JA, van Gelderen P, et al. A 7T spine array based on electric dipole transmitters. *Magn Reson Med.* Oct 2015;74(4):1189-1197. DOI: 10.1002/mrm.25817

194. Elabyad IA, Herrmann T, Bruns C, Bernarding J, Erni D. RF Shimming and Improved SAR Safety for MRI at 7 T With Combined Eight-Element Stepped Impedance Resonators and Traveling-Wave Antenna. *Ieee Transactions on Microwave Theory and Techniques.* Jan 2018;66(1):540-555. DOI: 10.1109/Tmtt.2017.2708707

195. Elabyad IA, Terekhov M, Stefanescu MR, Lohr D, Fischer M, Schreiber LM. Design and Evaluation of a Novel Symmetric Multichannel Transmit/Receive Coil Array for Cardiac MRI in Pigs at 7 T. *IEEE Transactions on Microwave Theory and Techniques.* 2019;67(9):3928-3945. DOI: 10.1109/TMTT.2019.2913636

196. Elabyad IA, Terekhov M, Stefanescu MR, Lohr D, Fischer M, Schreiber LM. Design of a novel antisymmetric coil array for parallel transmit cardiac MRI in pigs at 7 T. *Journal of magnetic resonance.* 2019;305:195-208. DOI: 10.1016/j.jmr.2019.07.004

197. Erturk MA, Raaijmakers AJ, Adriany G, Ugurbil K, Metzger GJ. A 16-channel combined loop-dipole transceiver array for 7 Tesla body MRI. *Magn Reson Med.* Feb 2017;77(2):884-894. DOI: 10.1002/mrm.26153

198. Erturk MA, Wu X, Eryaman Y, Van de Moortele PF, Auerbach EJ, et al. Toward imaging the body at 10.5 tesla. *Magn Reson Med.* Jan 2017;77(1):434-443. DOI: 10.1002/mrm.26487

199. Graessl A, Renz W, Hezel F, Dieringer MA, Winter L, et al. Modular 32-channel transceiver coil array for cardiac MRI at 7.0T. *Magn Reson Med.* Jul 2014;72(1):276-290. DOI: 10.1002/mrm.24903

200. Grassl A, Winter L, Thalhammer C, Renz W, Kellman P, et al. Design, evaluation and application of an eight channel transmit/receive coil array for cardiac MRI at 7.0 T. *Eur J Radiol.* May 2013;82(5):752-759. DOI: 10.1016/j.ejrad.2011.08.002

201. Ibrahim TS. Ultrahigh-Field MRI whole-slice and localized RF field excitations using the same RF transmit array. *Ieee Transactions on Medical Imaging.* Oct 2006;25(10):1341-1347. DOI: 10.1109/Tmi.2006.880666

202. Ibrahim TS, Kangarlu A, Chakeress DW. Design and performance issues of RF coils utilized in ultra high field MRI: experimental and numerical evaluations. *IEEE transactions on bio-medical engineering.* Jul 2005;52(7):1278-1284. DOI: 10.1109/tbme.2005.847564

203. Ibrahim TS, Lee R, Abduljalil AM, Baertlein BA, Robitaille PM. Dielectric resonances and B(1) field inhomogeneity in UHFMRI: computational analysis and experimental findings. *Magn Reson Imaging.* Feb 2001;19(2):219-226. DOI: 10.1016/s0730-725x(01)00300-9

204. Ipek O, Raaijmakers AJ, Klomp DW, Lagendijk JJ, Luijten PR, van den Berg CA. Characterization of transceive surface element designs for 7 tesla magnetic resonance imaging of the prostate: radiative antenna and microstrip. *Phys Med Biol.* Jan 21 2012;57(2):343-355. DOI: 10.1088/0031-9155/57/2/343

205. Kozlov M, Turner R. Fast MRI coil analysis based on 3-D electromagnetic and RF circuit co-simulation. *Journal of Magnetic Resonance.* 2009;200(1):147-152. DOI: 10.1016/j.jmr.2009.06.005

206. Krikken E, Steensma BR, Voogt IJ, Luijten PR, Klomp DWJ, et al. Homogeneous B1 (+) for bilateral breast imaging at 7 T using a five dipole transmit array merged with a high density receive loop array. *NMR Biomed.* Feb 2019;32(2):e4039. DOI: 10.1002/nbm.4039

207. Mao W, Smith MB, Collins CM. Exploring the limits of RF shimming for high-field MRI of the human head. *Magn Reson Med.* Oct 2006;56(4):918-922. DOI: 10.1002/mrm.21013

208. Niendorf T, Graessl A, Thalhammer C, Dieringer MA, Kraus O, et al. Progress and promises of human cardiac magnetic resonance at ultrahigh fields: a physics perspective. *J Magn Reson.* Apr 2013;229:208-222. DOI: 10.1016/j.jmr.2012.11.015

209. Niendorf T, Paul K, Oezerdem C, Graessl A, Klix S, et al. W(h)ither human cardiac and body magnetic resonance at ultrahigh fields? technical advances, practical considerations, applications, and clinical opportunities. *NMR Biomed.* Sep 2016;29(9):1173-1197. DOI: 10.1002/nbm.3268

210. Oezerdem C, Winter L, Graessl A, Paul K, Els A, et al. 16-channel bow tie antenna transceiver array for cardiac MR at 7.0 tesla. *Magn Reson Med.* Jun 2016;75(6):2553-2565. DOI: 10.1002/mrm.25840

211. Perrier A, Grenier D, Pouzin A, Esclassan F, Ravel N, et al. Design of a Two-Channel NMR Coil Using an Impedance Transformation Approach. *IEEE Sensors Journal.* 2012;12(6):1801-1808. DOI: 10.1109/JSEN.2011.2178237

212. Raaijmakers AJ, Ipek O, Klomp DW, Possanzini C, Harvey PR, et al. Design of a radiative surface coil array element at 7 T: the single-side adapted dipole antenna. *Magn Reson Med.* Nov 2011;66(5):1488-1497. DOI: 10.1002/mrm.22886

213. Raaijmakers AJ, Italiaander M, Voogt IJ, Luijten PR, Hoogduin JM, et al. The fractionated dipole antenna: A new antenna for body imaging at 7 Tesla. *Magn Reson Med.* Mar 2016;75(3):1366-1374. DOI: 10.1002/mrm.25596

214. Raaijmakers AJ, Luijten PR, van den Berg CA. Dipole antennas for ultrahigh-field body imaging: a comparison with loop coils. *NMR Biomed.* Sep 2016;29(9):1122-1130. DOI: 10.1002/nbm.3356

215. Schmitter S, DelaBarre L, Wu X, Greiser A, Wang D, et al. Cardiac imaging at 7 Tesla: Single- and two-spoke radiofrequency pulse design with 16-channel parallel excitation. *Magn Reson Med.* Nov 2013;70(5):1210-1219. DOI: 10.1002/mrm.24935

216. Snyder CJ, DelaBarre L, Metzger GJ, van de Moortele PF, Akgun C, et al. Initial results of cardiac imaging at 7 Tesla. *Magn Reson Med.* Mar 2009;61(3):517-524. DOI: 10.1002/mrm.21895

217. Steensma BR, Voogt IJ, Leiner T, Luijten PR, Habets J, et al. An 8-channel Tx/Rx dipole array combined with 16 Rx loops for high-resolution functional cardiac imaging at 7 T. *Magnetic Resonance Materials in Physics, Biology and Medicine.* 2018;31(1):7-18. DOI: 10.1007/s10334-017-0665-5

218. Terekhov M, Elabyad IA, Kögler C, Resmer F, Lanz T, et al. Customized B1+-shaping using multi-channel transceiver array prototype for 7T cardiac MRI with central elements symmetry. Paper presented at: Proc Intl Soc Mag Reson Med. 2020.

219. Thalhammer C, Renz W, Winter L, Hezel F, Rieger J, et al. Two-dimensional sixteen channel transmit/receive coil array for cardiac MRI at 7.0 T: design, evaluation, and application. *J Magn Reson Imaging.* Oct 2012;36(4):847-857. DOI: 10.1002/jmri.23724

220. Van de Moortele PF, Akgun C, Adriany G, Moeller S, Ritter J, et al. B(1) destructive interferences and spatial phase patterns at 7 T with a head transceiver array coil. *Magn Reson Med.* Dec 2005;54(6):1503-1518. DOI: 10.1002/mrm.20708

221. Vaughan JT, Garwood M, Collins CM, Liu W, DelaBarre L, et al. 7T vs. 4T: RF power, homogeneity, and signal-to-noise comparison in head images. *Magn Reson Med.* Jul 2001;46(1):24-30. DOI: 10.1002/mrm.1156

222. Vaughan JT, Snyder CJ, DelaBarre LJ, Bolan PJ, Tian J, et al. Whole-body imaging at 7T: preliminary results. *Magn Reson Med.* Jan 2009;61(1):244-248. DOI: 10.1002/mrm.21751

223. Versluis MJ, Tsekos N, Smith NB, Webb AG. Simple RF design for human functional and morphological cardiac imaging at 7tesla. *Journal of Magnetic Resonance.* 2009;200(1):161-166. DOI: 10.1016/j.jmr.2009.06.014

224. Winter L, Kellman P, Renz W, Gräßl A, Hezel F, et al. Comparison of three multichannel transmit/receive radiofrequency coil configurations for anatomic and functional cardiac MRI at 7.0T: implications for clinical imaging. *European Radiology.* 2012;22(10):2211-2220. DOI: 10.1007/s00330-012-2487-1

225. Xin SX, Huang QH, Gao Y, Li BG, Xu YK, Chen WF. Fetus MRI at 7 T: B-1 Shimming Strategy and SAR Safety Implications. *Ieee Transactions on Microwave Theory and Techniques.* May 2013;61(5):2146-2152. DOI: 10.1109/Tmtt.2013.2247053

226. Yacoub E, Shmuel A, Pfeuffer J, Van De Moortele PF, Adriany G, et al. Imaging brain function in humans at 7 Tesla. *Magn Reson Med.* Apr 2001;45(4):588-594. DOI: 10.1002/mrm.1080

227. Yang QX, Wang J, Zhang X, Collins CM, Smith MB, et al. Analysis of wave behavior in lossy dielectric samples at high field. *Magn Reson Med.* May 2002;47(5):982-989. DOI: 10.1002/mrm.10137

228. Yoo H, Gopinath A, Vaughan JT. A Method to Localize RF B-1 Field in High-Field Magnetic Resonance Imaging Systems. *Ieee Transactions on Biomedical Engineering.* Dec 2012;59(12):3365-3371. DOI: 10.1109/Tbme.2012.2208965

229. Akgun CE, DelaBarre L, Snyder CJ, Sohn S, Adriany G, et al. Alternating impedance multi-channel transmission line resonators for high field magnetic resonance imaging. Paper presented at: 2010 IEEE MTT-S International Microwave Symposium; May, 2010.

230. Akgun CE, DelaBarre L, Sohn S, Snyder C, Adriany G, et al. Novel multi-channel transmission line coil for high field magnetic resonance imaging. Paper presented at: IEEE MTT-S International Microwave Symposium Digest; June, 2009.

231. Akgun CE, DelaBarre L, Yoo H, Sohn S-M, Snyder CJ, et al. Stepped impedance resonators for high-field magnetic resonance imaging. *IEEE transactions on bio-medical engineering.* 2014;61(2):327-333. DOI: 10.1109/TBME.2013.2250973

232. Chen Z, Solbach K, Erni D, Rennings A. Electromagnetic Field Analysis of a Dipole Coil Element With Surface Impedance Characterized Shielding Plate for 7-T MRI. *IEEE Transactions on Microwave Theory and Techniques.* 2016;64(3):972-981. DOI: 10.1109/TMTT.2016.2518168

233. Chen Z, Solbach K, Erni D, Rennings A. Improving B1 Efficiency and Signal-to-Noise-Ratio of a Surface Coil by a High-Impedance-Surface RF Shield for 7-T Magnetic Resonance Imaging. *IEEE Transactions on Microwave Theory and Techniques.* 2017;65(3):988-997. DOI: 10.1109/TMTT.2016.2631169

234. Elabyad IA, Omar A. An investigation of alternating impedance microstrip transceiver coil arrays for MRI at 7T. Paper presented at: 2011 IEEE MTT-S International Microwave Symposium; June, 2011.

235. Sung-Min S, DelaBarre L, Vaughan JT, Gopinath A. RF multi-channel head coil design with improved B1+ Fields uniformity for high field MRI systems. Paper presented at: 2012 IEEE/MTT-S International Microwave Symposium Digest; June, 2012.

236. Vaughan JT, Hetherington HP, Otu JO, Pan JW, Pohost GM. High frequency volume coils for clinical NMR imaging and spectroscopy. *Magn Reson Med.* Aug 1994;32(2):206-218. DOI: 10.1002/mrm.1910320209

237. Wu B, Wang C, Kelley DA, Xu D, Vigneron DB, et al. Shielded microstrip array for 7T human MR imaging. *IEEE Trans Med Imaging.* Jan 2010;29(1):179-184. DOI: 10.1109/tmi.2009.2033597

238. Wu B, Wang C, Lu J, Pang Y, Nelson SJ, et al. Multi-channel microstrip transceiver arrays using harmonics for high field MR imaging in humans. *IEEE transactions on medical imaging.* 2012;31(2):183-191. DOI: 10.1109/TMI.2011.2166273

239. Zhang X, Ugurbil K, Chen W. Microstrip RF surface coil design for extremely high-field MRI and spectroscopy. *Magn Reson Med.* Sep 2001;46(3):443-450. DOI: 10.1002/mrm.1212

240. Zhang X, Ugurbil K, Chen W. A microstrip transmission line volume coil for human head MR imaging at 4T. *J Magn Reson.* Apr 2003;161(2):242-251. DOI: 10.1016/s1090-7807(03)00004-1

241. Zhang X, Ugurbil K, Sainati R, Chen W. An inverted-microstrip resonator for human head proton MR imaging at 7 tesla. *IEEE transactions on bio-medical engineering.* Mar 2005;52(3):495-504. DOI: 10.1109/tbme.2004.842968

242. Zhang X, Zhu XH, Chen W. Higher-order harmonic transmission-line RF coil design for MR applications. *Magn Reson Med.* May 2005;53(5):1234-1239. DOI: 10.1002/mrm.20462

243. Sohn S, DelaBarre L, Gopinath A, Vaughan JT. RF Head Coil Design With Improved RF Magnetic Near-Fields Uniformity for Magnetic Resonance Imaging (MRI) Systems. *IEEE Transactions on Microwave Theory and Techniques.* 2014;62(8):1784-1789. DOI: 10.1109/TMTT.2014.2331621

244. Abbasi-Sureshjani S, Amirrajab S, Lorenz C, Weese J, Pluim J, Breeuwer M. 4D Semantic Cardiac Magnetic Resonance Image Synthesis on XCAT Anatomical Model. *arXiv e-prints.* 2020. Accessed February 01, 2020.

245. Akkus Z, Galimzianova A, Hoogi A, Rubin DL, Erickson BJ. Deep Learning for Brain MRI Segmentation: State of the Art and Future Directions. *Journal of Digital Imaging.* 2017;30(4):449-459. DOI: 10.1007/s10278-017-9983-4

246. Baumgartner CF, Koch LM, Pollefeys M, Konukoglu E. An Exploration of 2D and 3D Deep Learning Techniques for Cardiac MR Image Segmentation. *arXiv e-prints.* 2017. Accessed September 01, 2017.

247. Bello GA, Dawes TJW, Duan J, Biffi C, de Marvao A, et al. Deep-learning cardiac motion analysis for human survival prediction. *Nature Machine Intelligence.* 2019;1(2):95-104. DOI: 10.1038/s42256-019-0019-2

248. Benou A, Veksler R, Friedman A, Riklin Raviv T. Ensemble of expert deep neural networks for spatio-temporal denoising of contrast-enhanced MRI sequences. *Med Image Anal.* Dec 2017;42:145-159. DOI: 10.1016/j.media.2017.07.006

249. Bermudez C, Plassard AJ, Davis TL, Newton AT, Resnick SM, Landman BA. Learning Implicit Brain MRI Manifolds with Deep Learning. *Proceedings of SPIE--the International Society for Optical Engineering.* Mar 2018;10574. DOI: 10.1117/12.2293515

250. Chen C, Qin C, Qiu H, Tarroni G, Duan J, et al. Deep learning for cardiac image segmentation: A review. *arXiv e-prints.* 2019. Accessed November 01, 2019.

251. Chen F, Taviani V, Malkiel I, Cheng JY, Tamir JI, et al. Variable-Density Single-Shot Fast Spin-Echo MRI with Deep Learning Reconstruction by Using Variational Networks. *Radiology.* Nov 2018;289(2):366-373. DOI: 10.1148/radiol.2018180445

252. Chen J, Li H, Zhang J, Menze B. Adversarial Convolutional Networks with Weak Domain-Transfer for Multi-Sequence Cardiac MR Images Segmentation. *arXiv e-prints.* 2019. Accessed August 01, 2019.

253. Curtis JP, Sokol SI, Wang Y, Rathore SS, Ko DT, et al. The association of left ventricular ejection fraction, mortality, and cause of death in stable outpatients with heart failure. *J Am Coll Cardiol.* Aug 2003;42(4):736-742. DOI: 10.1016/s0735-1097(03)00789-7

254. Dawes TJW, de Marvao A, Shi W, Fletcher T, Watson GMJ, et al. Machine Learning of Three-dimensional Right Ventricular Motion Enables Outcome Prediction in Pulmonary Hypertension: A Cardiac MR Imaging Study. *Radiology.* May 2017;283(2):381-390. DOI: 10.1148/radiol.2016161315

255. de Vos BD, Berendsen FF, Viergever MA, Sokooti H, Staring M, Isgum I. A Deep Learning Framework for Unsupervised Affine and Deformable Image Registration. *arXiv e-prints.* 2018. Accessed September 01, 2018.

256. Feng X, Yang J, Laine AF, Angelini ED. Discriminative Localization in CNNs for Weakly-Supervised Segmentation of Pulmonary Nodules. *arXiv e-prints.* 2017:arXiv:1707.01086. Accessed July 01, 2017.

257. He K, Zhang X, Ren S, Sun J. Deep Residual Learning for Image Recognition. *arXiv e-prints.* 2015:arXiv:1512.03385. Accessed December 01, 2015.

258. Hesamian MH, Jia W, He X, Kennedy P. Deep Learning Techniques for Medical Image Segmentation: Achievements and Challenges. *Journal of Digital Imaging.* 2019;32(4):582-596. DOI: 10.1007/s10278-019-00227-x

259. Jang Y, Hong Y, ha S, Kim S, Chang H-J. Automatic Segmentation of LV and RV in Cardiac MRI. *Statistical Atlases and Computational Models of the Heart.*2018:161-169.

260. Karamitsos TD, Francis JM, Myerson S, Selvanayagam JB, Neubauer S. The role of cardiovascular magnetic resonance imaging in heart failure. *J Am Coll Cardiol.* Oct 2009;54(15):1407-1424. DOI: 10.1016/j.jacc.2009.04.094

261. Liu F, Shen C. Learning Deep Convolutional Features for MRI Based Alzheimer's Disease Classification. *arXiv e-prints.* 2014. Accessed April 01, 2014.

262. Liu J, Pan Y, Li M, Chen Z, Tang L, et al. Applications of deep learning to MRI images: A survey. *Big Data Mining and Analytics.* 2018;1(1):1-18. DOI: 10.26599/BDMA.2018.9020001

263. Lohr D, Terekhov M, Kosmala A, Stefanescu MR, Hock M, Schreiber LM. Cardiac MRI with the Siemens Terra 7T System: Initial Experience and Optimization of Default Protocols. Paper presented at: Proc. of the 26th Annual Meeting of ISMRM; April, 2018; Paris, France.

264. Lundervold AS, Lundervold A. An overview of deep learning in medical imaging focusing on MRI. *Zeitschrift für Medizinische Physik.* 2019;29(2):102-127. DOI: 10.1016/j.zemedi.2018.11.002

265. Moon JC, Lorenz CH, Francis JM, Smith GC, Pennell DJ. Breath-hold FLASH and FISP cardiovascular MR imaging: left ventricular volume differences and reproducibility. *Radiology.* Jun 2002;223(3):789-797. DOI: 10.1148/radiol.2233011181

266. Paszke A, Gross S, Massa F, Lerer A, Bradbury J, et al. PyTorch: An Imperative Style, High-Performance Deep Learning Library. *arXiv e-prints.* 2019:arXiv:1912.01703. Accessed December 01, 2019.

267. Pinaya WHL, Gadelha A, Doyle OM, Noto C, Zugman A, et al. Using deep belief network modelling to characterize differences in brain morphometry in schizophrenia. *Scientific Reports.* 2016;6(1):38897. DOI: 10.1038/srep38897

268. Ronneberger O, Fischer P, Brox T. U-Net: Convolutional Networks for Biomedical Image Segmentation. *arXiv e-prints.* 2015:arXiv:1505.04597. Accessed May 01, 2015.

269. Ruijsink B, Puyol-Antón E, Oksuz I, Sinclair M, Bai W, et al. Fully Automated, Quality-Controlled Cardiac Analysis From CMR: Validation and Large-Scale Application to Characterize Cardiac Function. *JACC: Cardiovascular Imaging.* 2019. DOI: 10.1016/j.jcmg.2019.05.030

270. Schlemper J, Caballero J, Hajnal JV, Price AN, Rueckert D. A Deep Cascade of Convolutional Neural Networks for Dynamic MR Image Reconstruction. *IEEE transactions on medical imaging.* Feb 2018;37(2):491-503. DOI: 10.1109/tmi.2017.2760978

271. Simonyan K, Zisserman A. Very Deep Convolutional Networks for Large-Scale Image Recognition. *arXiv e-prints.* 2014:arXiv:1409.1556. Accessed September 01, 2014.

272. Smith LN. A disciplined approach to neural network hyper-parameters: Part 1 -- learning rate, batch size, momentum, and weight decay. *arXiv e-prints.* 2018:arXiv:1803.09820. Accessed March 01, 2018.

273. Sudlow C, Gallacher J, Allen N, Beral V, Burton P, et al. UK Biobank: An Open Access Resource for Identifying the Causes of a Wide Range of Complex Diseases of Middle and Old Age. *PLOS Medicine.* 2015;12(3):e1001779. DOI: 10.1371/journal.pmed.1001779

274. Sudre CH, Li W, Vercauteren T, Ourselin S, Jorge Cardoso M. Generalised Dice Overlap as a Deep Learning Loss Function for Highly Unbalanced Segmentations. 2017; Cham.

275. Tran PV. A Fully Convolutional Neural Network for Cardiac Segmentation in Short-Axis MRI. *arXiv e-prints.* 2016. Accessed April 01, 2016.

276. Vesal S, Ravikumar N, Maier A. Automated Multi-sequence Cardiac MRI Segmentation Using Supervised Domain Adaptation. *arXiv e-prints.* 2019. Accessed August 01, 2019.

277. Wang J, Huang H, Chen C, Ma W, Huang Y, Ding X. Multi-sequence Cardiac MR Segmentation with Adversarial Domain Adaptation Network. *arXiv e-prints.* 2019. Accessed October 01, 2019.

278. Wu G, Kim M, Wang Q, Munsell BC, Shen D. Scalable High-Performance Image Registration Framework by Unsupervised Deep Feature Representations Learning. *IEEE transactions on bio-medical engineering.* Jul 2016;63(7):1505-1516. DOI: 10.1109/tbme.2015.2496253

279. Zhu B, Liu JZ, Cauley SF, Rosen BR, Rosen MS. Image reconstruction by domain-transform manifold learning. *Nature.* 2018;555(7697):487-492. DOI: 10.1038/nature25988

280. Zijdenbos AP, Dawant BM, Margolin RA, Palmer AC. Morphometric analysis of white matter lesions in MR images: method and validation. *IEEE transactions on medical imaging.* 1994;13(4):716-724. DOI: 10.1109/42.363096

281. Bai W, Sinclair M, Tarroni G, Oktay O, Rajchl M, et al. Automated cardiovascular magnetic resonance image analysis with fully convolutional networks. *Journal of Cardiovascular Magnetic Resonance.* 2018;20. DOI: 10.1186/s12968-018-0471-x

282. Baumgartner CF, Koch LM, Pollefeys M, Konukoglu E. An Exploration of 2D and 3D Deep Learning Techniques for Cardiac MR Image Segmentation. 2018.

283. *nibabel* [computer program]. Version 3.2.1: Zenodo; 2020.

284. He K, Zhang X, Ren S, Sun J. Deep Residual Learning for Image Recognition. Paper presented at: 2016 IEEE Conference on Computer Vision and Pattern Recognition (CVPR); June, 2016.

285. Li L, Weng X, Schnabel JA, Zhuang XJA. Joint Left Atrial Segmentation and Scar Quantification Based on a DNN with Spatial Encoding and Shape Attention. 2020;abs/2006.13011.

286. Li L, Wu F, Yang G, Xu L, Wong T, et al. Atrial scar quantification via multi-scale CNN in the graph-cuts framework. *Med Image Anal.* Feb 2020;60:101595. DOI: 10.1016/j.media.2019.101595

287. Lin T-Y, Goyal P, Girshick R, He K, Dollár P. Focal Loss for Dense Object Detection. *arXiv:1708.02002.* 2017.

288. Pérez-García F, Sparks R, Ourselin S. TorchIO: a Python library for efficient loading, preprocessing, augmentation and patch-based sampling of medical images in deep learning. *arXiv:2003.04696.* 2020.

289. Pizer SM, Amburn EP, Austin JD, Cromartie R, Geselowitz A, et al. Adaptive Histogram Equalization and Its Variations. *Comput Vision Graph.* Sep 1987;39(3):355-368. DOI: 10.1016/S0734-189x(87)80186-X

290. Ronneberger O, Fischer P, Brox T. U-Net: Convolutional Networks for Biomedical Image Segmentation. 2015.

291. Russakovsky O, Deng J, Su H, Krause J, Satheesh S, et al. ImageNet Large Scale Visual Recognition Challenge. *International Journal of Computer Vision.* 2015;115(3):211-252. DOI: 10.1007/s11263-015-0816-y

292. Zabihollahy F, White JA, Ukwatta E. Convolutional neural network-based approach for segmentation of left ventricle myocardial scar from 3D late gadolinium enhancement MR images. *Med Phys.* Apr 2019;46(4):1740-1751. DOI: 10.1002/mp.13436

293. Geerts L, Bovendeerd P, Nicolay K, Arts T. Characterization of the normal cardiac myofiber field in goat measured with MR-diffusion tensor imaging. *American Journal of Physiology - Heart and Circulatory Physiology.* 2002;283(1):H139-H145. DOI: 10.1152/ajpheart.00968.2001

294. Milani-Nejad N, Janssen PML. Small and large animal models in cardiac contraction research: Advantages and disadvantages. *Pharmacology & Therapeutics.* 2014;141(3):235-249. DOI: 10.1016/j.pharmthera.2013.10.007

295. Cui J, Li J, Mathison M, Tondato F, Mulkey SP, et al. A clinically relevant large-animal model for evaluation of tissue-engineered cardiac surgical patch materials. *Cardiovascular Revascularization Medicine.* 2005;6(3):113-120. DOI: 10.1016/j.carrev.2005.07.006

296. Ugurbil K. Magnetic resonance imaging at ultrahigh fields. *IEEE transactions on bio-medical engineering.* 2014;61(5):1364-1379. DOI: 10.1109/TBME.2014.2313619

297. Vaughan JT, Garwood M, Collins CM, Liu W, DelaBarre L, et al. 7T vs. 4T: RF power, homogeneity, and signal-to-noise comparison in head images. *Magnetic resonance in medicine.* 2001;46(1):24-30. DOI: 10.1002/mrm.1156

298. Uğurbil K, Auerbach E, Moeller S, Grant A, Wu X, et al. Brain imaging with improved acceleration and SNR at 7 Tesla obtained with 64-channel receive array. *Magnetic resonance in medicine.* 2019;82(1):495-509. DOI: 10.1002/mrm.27695

299. Wiesinger F, Van de Moortele P-F, Adriany G, De Zanche N, Ugurbil K, Pruessmann KP. Parallel imaging performance as a function of field strength—An experimental investigation using electrodynamic scaling. *Magnetic resonance in medicine.* 2004;52(5):953-964. DOI: 10.1002/mrm.20281

300. Wiesinger F, Van de Moortele P-F, Adriany G, De Zanche N, Ugurbil K, Pruessmann KP. Potential and feasibility of parallel MRI at high field. *NMR in biomedicine.* 2006;19(3):368-378. DOI: 10.1002/nbm.1050

301. Vaidya MV, Sodickson DK, Lattanzi R. Approaching ultimate intrinsic SNR in a uniform spherical sample with finite arrays of loop coils. *Concepts in Magnetic Resonance Part B: Magnetic Resonance Engineering.* 2014;44(3):53-65. DOI: 10.1002/cmr.b.21268

302. Niendorf T, Schulz-Menger J, Paul K, Huelnhagen T, Ferrari VA, Hodge R. High Field Cardiac Magnetic Resonance Imaging. *Circulation: Cardiovascular Imaging.* 2017;10(6):e005460. DOI: 10.1161/CIRCIMAGING.116.005460

303. Reese TG, Weisskoff RM, Smith RN, Rosen BR, Dinsmore RE, Wedeen VJ. Imaging myocardial fiber architecture in vivo with magnetic resonance. *Magnetic resonance in medicine.* 1995;34(6):786-791. DOI: 10.1002/mrm.1910340603

304. Fagan AJ, Bitz AK, Björkman-Burtscher IM, Collins CM, Kimbrell V, et al. 7T MR Safety. *Journal of Magnetic Resonance Imaging.* DOI: 10.1002/jmri.27319

305. Fiedler TM, Ladd ME, Bitz AK. RF safety assessment of a bilateral four-channel transmit/receive 7 Tesla breast coil: SAR versus tissue temperature limits. *Med Phys.* Jan 2017;44(1):143-157. DOI: 10.1002/mp.12034

306. Terekhov M, Elabyad I, Kögler C, Reiter T, Schreiber L. SAR Safety Analysis for a 8Tx/16Rx Coil Array Prototype for Human Cardiac MRI at 7 T. *In Proceedings of the 28th Annual Meeting of ISMRM, virtual, 2020. p4167.*

307. Basser PJ, Jones DK. Diffusion-tensor MRI: theory, experimental design and data analysis - a technical review. *NMR in biomedicine.* 2002;15:456-467. DOI: 10.1002nbm.783

308. Andreopoulos A, Tsotsos JK. Efficient and generalizable statistical models of shape and appearance for analysis of cardiac MRI. *Med Image Anal.* Jun 2008;12(3):335-357. DOI: 10.1016/j.media.2007.12.003

309. Radau P, Lu Y, Connelly K, Paul G, Dick A, Wright G. Evaluation Framework for Algorithms Segmenting Short Axis Cardiac MRI. http://hdl.handle.net/10380/3070. 2009.

310. Suinesiaputra A, Cowan BR, Al-Agamy AO, Elattar MA, Ayache N, et al. A collaborative resource to build consensus for automated left ventricular segmentation of cardiac MR images. *Medical Image Analysis.* 2014;18(1):50-62. DOI: 10.1016/j.media.2013.09.001

311. Petitjean C, Zuluaga MA, Bai W, Dacher J-N, Grosgeorge D, et al. Right ventricle segmentation from cardiac MRI: A collation study. *Medical Image Analysis.* 2015;19(1):187-202. DOI: 10.1016/j.media.2014.10.004

312. Karim R, Bhagirath P, Claus P, James Housden R, Chen Z, et al. Evaluation of state-of-the-art segmentation algorithms for left ventricle infarct from late Gadolinium enhancement MR images. *Medical Image Analysis.* 2016;30:95-107. DOI: https://doi.org/10.1016/j.media.2016.01.004

313. Karim R, Housden RJ, Balasubramaniam M, Chen Z, Perry D, et al. Evaluation of current algorithms for segmentation of scar tissue from late gadolinium enhancement cardiovascular magnetic resonance of the left atrium: an open-access grand challenge. *Journal of Cardiovascular Magnetic Resonance.* 2013;15(1):105. DOI: 10.1186/1532-429x-15-105

314. Pace DF, Dalca AV, Geva T, Powell AJ, Moghari MH, Golland P. Interactive Whole-Heart Segmentation in Congenital Heart Disease. *Medical image computing and computer-assisted intervention : MICCAI ... International Conference on Medical Image Computing and Computer-Assisted Intervention.* Oct 2015;9351:80-88. DOI: 10.1007/978-3-319-24574-4_10

315. Bernard O, Lalande A, Zotti C, Cervenansky F, Yang X, et al. Deep Learning Techniques for Automatic MRI Cardiac Multi-Structures Segmentation and Diagnosis: Is the Problem Solved? *IEEE transactions on medical imaging.* 2018;37(11):2514-2525. DOI: 10.1109/TMI.2018.2837502

316. Ankenbrand MJ, Shainberg L, Hock M, Lohr D, Schreiber LM. Sensitivity Analysis for Interpretation of Machine Learning Based Segmentation Models in Cardiac MRI. *BMC Medical Imaging.* 2020. DOI: 10.21203/rs.3.rs-97535/v1

317. Bai W, Chen C, Tarroni G, Duan J, Guitton F, et al. Self-Supervised Learning for Cardiac MR Image Segmentation by Anatomical Position Prediction. *arXiv e-prints.* 2019:arXiv:1907.02757. Accessed July 01, 2019.

318. Joyce T, Chartsias A, Tsaftaris S. Deep Multi-Class Segmentation Without Ground-Truth Labels. Amsterdam2018.

319. Ouyang C, Kamnitsas K, Biffi C, Duan J, Rueckert D. Data Efficient Unsupervised Domain Adaptation for Cross-Modality Image Segmentation. 2019:arXiv:1907.02766. Accessed July 01, 2019.

320. Dou Q, Ouyang C, Chen C, Chen H, Glocker B, et al. PnP-AdaNet: Plug-and-Play Adversarial Domain Adaptation Network at Unpaired Cross-Modality Cardiac Segmentation. *IEEE Access.* 2019;7:99065-99076. DOI: 10.1109/ACCESS.2019.2929258

321. Dou Q, Ouyang C, Chen C, Chen H, Heng P-A. Unsupervised Cross-Modality Domain Adaptation of ConvNets for Biomedical Image Segmentations with Adversarial Loss. 2018:arXiv:1804.10916. Accessed April 01, 2018.

322. Chen C, Dou Q, Chen H, Qin J, Heng P-A. Synergistic Image and Feature Adaptation: Towards Cross-Modality Domain Adaptation for Medical Image Segmentation. 2019:arXiv:1901.08211. Accessed January 01, 2019.

323. https://www.fast.ai/. Accessed October 11, 2020.

324. Edelman RR, Gaa J, Wedeen VJ, Loh E, Hare JM, et al. In vivo measurement of water diffusion in the human heart. *Magnetic resonance in medicine.* 1994;32(3):423-428. DOI: 10.1002/mrm.1910320320

325. Teh I, Romero W, Dall'Armellina E, Ennis D, Ferreira PF, et al. Reproducibility of diffusion tensor imaging (DTI) on 12 clinical scanners: Towards validation of cardiac DTI sequences. *In Proceedings of the 28th Annual Meeting of ISMRM, virtual, 2020.*

326. Irvin J, Rajpurkar P, Ko M, Yu Y, Ciurea-Ilcus S, et al. CheXpert: A Large Chest Radiograph Dataset with Uncertainty Labels and Expert Comparison. 2019:arXiv:1901.07031. Accessed January 01, 2019.

327. Renard F, Guedria S, Palma ND, Vuillerme N. Variability and reproducibility in deep learning for medical image segmentation. *Scientific Reports.* 2020;10(1):13724. DOI: 10.1038/s41598-020-69920-0

328. Marrone S, Olivieri S, Piantadosi G, Sansone C. Reproducibility of Deep CNN for Biomedical Image Processing Across Frameworks and Architectures. Paper presented at: 2019 27th European Signal Processing Conference (EUSIPCO); September, 2019.

329. Rougier NP, Hinsen K, Alexandre F, Arildsen T, Barba LA, et al. Sustainable computational science: the ReScience initiative. *PeerJ Computer Science.* 2017;3:e142. DOI: 10.7717/peerj-cs.142

330. Sandve GK, Nekrutenko A, Taylor J, Hovig E. Ten Simple Rules for Reproducible Computational Research. *PLOS Computational Biology.* 2013;9(10):e1003285. DOI: 10.1371/journal.pcbi.1003285

331. Bartlett A, Penders B, Lewis J. Bioinformatics: indispensable, yet hidden in plain sight? *BMC Bioinformatics.* 2017;18(1):311. DOI: 10.1186/s12859-017-1730-9

332. Budd A, Corpas M, Brazas MD, Fuller JC, Goecks J, et al. A Quick Guide for Building a Successful Bioinformatics Community. *PLOS Computational Biology.* 2015;11(2):e1003972. DOI: 10.1371/journal.pcbi.1003972